UNIVERSITÀ DEGLI STUDI

DI MODENA E REGGIO EMILIA

PhD Course in "Models and Methods for Material and Environmental Sciences"

XXXVII Cycle

Lignin Depolymerization-Upgrading to Biomaterials

Candidate: Biagio Anderlini

Supervisor: Dr. Fabrizio Roncaglia

Director of the PhD Course: Prof. Stefano Lugli

UNIONE EUROPEA
Fondo Sociale Europeo
Ministero dell'Università e della Ricerca
PON RICERCA E INNOVAZIONE 2014 - 2020
REACT EU

Tesi di dottorato di ricerca co-finanziata nell'ambito del Programma Operativo Nazionale Ricerca e Innovazione 2014-2020 (CCI 2014IT16M2OP005), risorse FSE REACT-EU, Azione IV.4 “Dottorati e contratti di ricerca su tematiche dell’innovazione” e Azione IV.5 “Dottorati su tematiche Green”.

Contents

Abstract 7

List of Acronyms and Abbreviations 8

1. Introduction 10

1.1 General Regards 10

1.2 Catalytic Pyrolysis 12

1.3 Acid Catalyzed Hydrolysis 12

1.4 Base Catalyzed Hydrolysis 13

1.5 Catalytic Reductive Hydrogenolysis 14

1.6 Catalytic Oxidative Depolymerization 15

1.7 Lignin Depolymerization monomers 16

1.8 Aim of the thesis 17

1.8 Bibliography 18

2. Upgrading lignin monomers routes to aryl cored building blocks for polymers and resins 21

2.1 Introduction 21

2.2 Sustainable halogenation of BTX aromatics 24

2.3 Chloromethylation of bio-based electron-rich aromatics 32

2.4 Conclusion 38

2.5 Experimental 39

2.5.1 Materials and Methods 39

2.5.2 General procedure for benzylic bromination 39

2.5.3 General procedure for ring bromination 39

2.5.4 General procedure for one-pot first-ring-then-benzylic bromination 40

2.5.5 Characterization of brominated products 40

*2.5.6 Synthesis of **IV**[72]* 46

2.5.7 Synthesis of formiate/formamide mixture 46

*2.5.8 Synthesis of **Ia**[71]* 46

*2.5.9 Synthesis of **IIa*** 47

*2.5.10 Synthesis of **IIIa*** 47

*2.5.11 Synthesis of **IVa*** 47

*2.5.12 Synthesis of **Va**[53]* 47

*2.5.13 Synthesis of **VIa***[73] 48

*2.5.14 Synthesis of **VIam*** 48

2.5.15 Typical synthesis of amide derivatives 48

2.5.16 Characterization of amide derivatives 49

2.6 Bibliography 50

3. Synthesis and characterization of triphenolamines ligands and of their Vanadium complexes 54

3.1 Introduction 54

3.2 Synthesis of diphenolamines (DPAs) precursors 59

3.2.1 Characterization of 2,2'-[bis(methylene)imino]bis(4,6-dichlorophenol) ($DPA^{Cl,Cl}$) 60

3.2.2 Characterization of 2,2'-[bis(methylene)imino]bis(4,6-difluorophenol) ($DPA^{F,F}$) 67

3.3 Preliminary study of the coordination chemistry of $DPA^{Cl,Cl}$. 75

3.4 Synthesis of chlorometilated phenols (PhX_2CH_2Cls) precursors 90

3.4.1 Characterization of 2,4-dichloro-6-(chloromethyl)phenol ($PhCl_2CH_2Cl$) 93

3.4.2 Characterization of 2,4-difluoro-6-(chloromethyl)phenol (PhF_2CH_2Cl) 100

3.4.3 Characterization of 2-nitro-4-chloro-6-(chloromethyl)phenol ($PhClNO_2CH_2Cl$) 110

3.5 Synthesis of TPAs proligands 116

3.5.1 Characterization of 6,6',6''-(nitrilotris(methylene))tris(2,4-dichlorophenol) ($TPACl_6$) 118

3.5.2 Characterization of 6,6'-(((3,5-difluoro-2-hydroxybenzyl)azanediyl) bis(methylene))bis(2,4-dichlorophenol) ($TPACl_4F_2$) 126

3.5.3 Characterization of 6,6'-(((3-nitro-5-chloro-2-hydroxybenzyl)azanediyl) bis(methylene))bis(2,4-dichlorophenol) ($TPACl_5NO_2$) 135

3.5.4 Characterization of 6,6',6''-(nitrilotris(methylene))tris(2,4-difluorophenol) ($TPAF_6$) 142

3.5.5 Characterization of 6,6'-(((3,5-dichloro-2-hydroxybenzyl)azanediyl) bis(methylene))bis(2,4-difluorophenol) ($TPAF_4Cl_2$) 150

3.5.6 Characterization of 6,6'-(((3-nitro-5-chloro-2-hydroxybenzyl)azanediyl) bis(methylene))bis(2,4-difluorophenol) ($TPAF_4ClNO_2$) 158

3.6 Preliminary study of TPAs coordination chemistry 166

3.6.1 NMR Characterization of VOTPAs complexes 167

3.6.2 Electrochemical characterization of VOTPAs 170

3.6.3 UV-Vis Characterization of $VOTPACl_6$ 173

3.6.4 UV-Vis Characterization of $VOTPACl_4F_2$ 175

3.6.5 UV-Vis Characterization of $VOTPAF_4Cl_2$ 176
3.6.6 UV-Vis Characterization of $VOTPAF_6$ 177
3.6.7 UV-Vis Characterization of $VOTPACl_5NO_2$ 178
3.6.8 UV-Vis Characterization of $VOTPAF_4ClNO_2$ 179
3.6.9 UV-Vis Characterization Final Remarks and Comparisons 180
3.7 Conclusions and future outlooks 184
3.8 Experimental 185
3.8.1 Materials and Methods 185
3.8.2 Synthesis of $PhCl_2MeOH$ 186
3.8.3 Synthesis of PhF_2MeOH 186
3.8.4 Synthesis of $PhCl_2CH_2Cl$ starting from $PhCl_2MeOH$ 186
3.8.5 Synthesis of PhF_2CH_2Cl starting from PhF_2MeOH 187
3.8.6 Synthesis of $PhCl_2CH_2Cl$ starting from $PhCl_2$ 187
3.8.6 Synthesis of PhF_2CH_2Cl starting from PhF_2 187
3.8.7 Synthesis of $PhClNO_2CH_2Cl$ 188
3.8.8 Synthesis of $PhClNO_2CH_2Cl$-py adduct 188
3.8.9 Synthesis of $DPA^{Cl,Cl}$ 188
3.8.10 Synthesis of $DPA^{F,F}$ 189
3.8.11 Synthesis of $TPACl_6$ 189
3.8.12 Synthesis of $TPACl_4F_2$ 190
3.8.13 Synthesis of $TPACl_5NO_2$ 190
3.8.14 Synthesis of $TPAF_6$ 191
3.8.15 Synthesis of $TPAF_4Cl_2$ 191
3.8.16 Synthesis of $TPAF_4ClNO_2$ 192
3.8.17 Synthesis of oxo-isopropoxo Ti $DPA^{Cl,Cl}$ complex 192
3.8.18 Synthesis of Co $DPA^{Cl,Cl}$ monomer 192
3.8.22 Synthesis of $VOTPACl_5NO_2$ 194
3.8.23 Synthesis of $VOTPAF_6$ 194
3.8.24 Synthesis of $VOTPAF_4Cl_2$ 194
3.8.25 Synthesis of $VOTPAF_4ClNO_2$ 195
3.9 Bibliography 196

Abstract

Lignocellulosic biomass is primarily composed of carbohydrates cellulose and hemicellulose, and of lignin, a complex phenolic polymer. While the carbohydrates are processed to high-value products, lignin fraction is primarily burned for energy production. However, lignin is the main renewable resource of aromatic compounds. Native lignin present in biomass is a 3D amorphous macromolecule made up principally by the combination of three different phenylpropane monomer units: *p*-coumaryl alcohol, coniferyl alcohol and sinapyl alcohol, linked mainly by aryl ether bonds in a randomized way. Lignin is an abundant aromatic feedstock, but it is still largely considered as a source for heat and power from bio-refinery. The lack of well-established processes that add value to lignin can be largely attributed to its structural complexity and associated chemical inactivity. Lignin conversion to value-added products is governed by an interplay of three technological biorefinery aspects: (i) lignocellulosic biomass fractionation, (ii) lignin depolymerization, and (iii) upgrading towards targeted (intermediate or final) chemicals. Efficient lignin depolymerization could produce a wide range of fuels and chemicals (and/or their precursors). These molecules (especially alkylated phenols) could be used to produce chemicals and materials (polymers, antioxidants, resins, medicines, or pesticides) in substitution to fossil fuel resources. One of the most promising routes is the disassembling of the lignin structure into its phenolic building blocks, to further transform them into targeted end products. These units are connected through various ether and carbon–carbon bonds and *β*-O-4 ether bond is the most abundant linkage, at least in native lignin. Therefore, the oxidative conversion of lignin is of great interest because it enables the formation of highly functionalized, valuable compounds. Consequently, the design of more efficient and environmentally benign catalytic processes for the CC bond cleavage is a topic of key importance. Oxovanadium complexes are promising catalysts studied for the oxidation of dimeric lignin model compounds, using air or oxygen as an oxidant. In particular, triphenolamines (TPAs) ligands seems to be the most active ones. Catalyst's reactivity can be tuned by changing ligand structure and substituents. In particular, in this PhD thesis, we focused on ligand synthesis in order to improve poor yields, also obtaining asymmetric ones which were never described before. Fine control over ligand moieties can give much greater tuning capabilities upon catalysts properties, potentially changing their selectivity. Finally, we synthetized an array of complexes from the obtained ligands and characterized them through spectroscopy and voltammetry. These show small, yet significant differences in properties, as reduction potential and visible absorption. Future work should focus on catalytic activity tests, both in standard and photochemical conditions, starting from model compounds and then moving to actual lignin.

List of Acronyms and Abbreviations

1	*o*-xylene
1a	1,2-bis(bromomethyl)benzene
1b	1,2-dibromo-4,5-dimethylbenzene
1c	1,2-dibromo-4,5-bis(bromomethyl)benzene
2	*m*-xylene
2a	1,3-bis(bromomethyl)benzene
2b	1,5-dibromo-2,4-dimethylbenzene
3	*p*-xylene
3a	1,4-bis(bromomethyl)benzene
3am	1-(bromomethyl)-4-methylbenzene
3at	1-(bromomethyl)-4-(dibromomethyl)benzene
3b	1,4-dibromo-2,5-dimethylbenzene
3bm	2-bromo-1,4-dimethylbenzene
3c	1,4-dibromo-2,5-bis(bromomethyl)benzene
4	Mesitylene
4a	1,3,5-tris(bromomethyl)benzene
4b	1,3,5-tribromo-2,4,6-trimethylbenzene
4c	1,3,5-tribromo-2,4,6-tris(bromomethyl)benzene
I	Salicylaldehyde
Ia	3,5-bis(chloromethyl)-2-hydroxybenzaldehyde
Ib	N,N'-((5-formyl-4-hydroxy-1,3-phenylene)bis(methylene))diformamide
II	Vanillin
IIa	2-(chloromethyl)-4-hydroxy-5-methoxybenzaldehyde
IIb	N-(2-formyl-5-hydroxy-4-methoxybenzyl)formamide
III	Eugenol
IIIa	4-allyl-2,3-bis(chloromethyl)-6-methoxyphenol
IIIb	N,N'-((6-allyl-3-hydroxy-4-methoxy-1,2-phenylene)bis(methylene))diformamide
IV	2-methoxyphenyl acetate
IVa	2,3,4-tris(chloromethyl)-6-methoxyphenol
IVb	N,N',N''-((4-hydroxy-5-methoxybenzene-1,2,3-triyl)tris(methylene))triformamide
V	*p*-cresol
Va	2,6-bis(chloromethyl)-4-methylphenol
Vb	N,N'-((2-hydroxy-5-methyl-1,3-phenylene)bis(methylene))diformamide
VI	Piceol
VIa	1-(3-(chloromethyl)-4-hydroxyphenyl)ethanone
VIam	1-(3,5-bis(chloromethyl)-4-hydroxyphenyl)ethanone
VIb	N-(5-acetyl-2-hydroxybenzyl)formamide
VIbm	N,N'-((5-acetyl-2-hydroxy-1,3-phenylene)bis(methylene))diformamide
BPA	Bisphenol A
BTX	benzene, toluene, xylene
BVS	Bond-Valence Sum
COSY	Correlation Spectroscopy
CV	Cyclic Voltammetry
DBU	1,5-diazabiciclo(5.4.0)undec-7-ene
DCM	Dichloromethane
DMF	Dimethylformamide

DMSO	Dimethyl sulfoxide
DPA	Diphenolamine
$DPA^{Cl,Cl}$	2,2’-[bis(methylene)imino]bis(4,6-dichlorophenol)
$DPA^{F,F}$	2,2’-[bis(methylene)imino]bis(4,6-difluorophenol)
EPR	Electron Paramagnetic Resonance
ESI	Electron Spray Ionization
EtOAc	Ethyl acetate
EWG	Electron Withdrawing Group
FT-NMR	Fourier Transform Nuclear magnetic resonance spectroscopy
HMBC	Heteronuclear Multiple Bond Correlation spectroscopy
HMTA	Hexamethylenetetramine
HOMO	Highest Occupied Molecular Orbital
HSQC	Heteronuclear Single Quantum Coherence spectroscopy
IL	Ionic Liquid
LC	Liquid Chromatography
LMCT	Ligand to Metal Charge Transfer
MS	Mass Spectrometry
PF	Paraformaldehyde
$PhCl_2$	2,4-dichlorophenol
$PhCl_2CH_2Cl$	2,4-dichloro-6-(chloromethyl)phenol
$PhClNO_2$	4-chloro-2-nitrophenol
$PhClNO_2CH_2Cl$	2-nitro-4-chloro-6-(chloromethyl)phenol
PhF_2	2,4-difluorophenol
PhF_2CH_2Cl	2,4-difluoro-6-(chloromethyl)phenol
PTFE	Polytetrafluoroethylene
SC-XRD	Single Crystal X-Ray Diffraction
SHE	Standard Hydrogen Electrode
$TBABF_4$	Tetrabutylammonium tetrafluoroborate
TBACl	Tetrabutylammonium chloride
TEA	Triethylamine
THF	Tetrahydrofuran
TPA	Triphenolamine
$TPACl_4F_2$	6,6'-(((3,5-difluoro-2-hydroxybenzyl)azanediyl)bis(methylene))bis(2,4-dichlorophenol)
$TPACl_5NO_2$	6,6'-(((3-nitro-5-chloro-2-hydroxybenzyl)azanediyl)bis(methylene))bis(2,4-dichlorophenol)
$TPACl_6$	6,6',6"-(nitrilotris(methylene))tris(2,4-dichlorophenol)
$TPAF_4Cl_2$	6,6'-(((3,5-dichloro-2-hydroxybenzyl)azanediyl)bis(methylene))bis(2,4-difluorophenol)
$TPAF_4ClNO_2$	6,6'-(((3-nitro-5-chloro-2-hydroxybenzyl)azanediyl)bis(methylene))bis(2,4-difluorophenol)
$TPAF_6$	6,6',6"-(nitrilotris(methylene))tris(2,4-difluorophenol)
TPN	Triphenylene
UV-Vis-NIR	Ultraviolet-Visible-Near Infrared
VOTPA	Oxovanadium aminotriphenolates

Chapter 1

1. Introduction

1.1 General Regards

Lignin is an extremely abundant phenolic biopolymer whose valorization could lead to a renewable source of aromatic fine chemicals. However, lignin is primarily considered as a by-product and burnt to produce energy directly by producers, *i.e.*, pulping industry and bio-refineries[1]. Reasons for lignin underutilization are many and range from matrix complexity of lignocellulosic biomass to the absence of efficient industrializable processes to convert it to value added products. Lignocellulose composition can vary significantly in its three main components cellulose (40%–60%), hemicellulose (10%–40%) and lignin (15%–30%)[1]. Furthermore, lignin does not have a fixed structure and composition making general procedures development even harder. Lignin is composed of three main phenyl propene building-blocks or subunits, *p*-coumaryl, coniferyl and sinapyl alcohol, connected by many different kinds of linkages as shown in Figure 1.1.

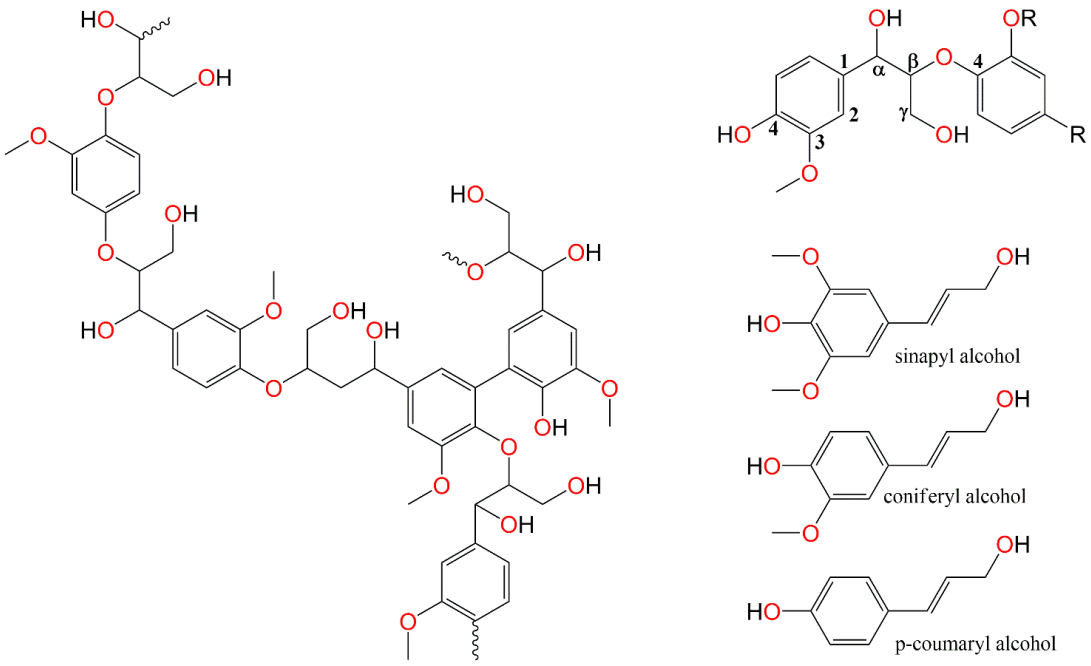

Figure 1.1: On the left: General example of lignin structure. On the right: Top, typical numeration of lignin subunits showing some of the most frequent linkage types. Bottom, structure of the three main subunits, namely sinapyl alcohol, coniferyl alcohol and *p*-coumaryl alcohol.

The main type of bonding is ethereal ranging between 55% and 80% of total connections and among these the most frequent are β-O-4 bonds[2]. Therefore, cleavage of β-O-4 bonds is one of the most studied topics in lignin depolymerization, because it would lead to soluble oligomers, a perfect starting point for further cleavage or upgrading[3]. Unfortunately, efficient ether cleavage usually requires the combination of strong alkali or acids with significantly high temperatures. These conditions applied to lignocellulose lead to the generation of active compounds which could degrade to unwanted molecules or, an even worse option, condense to more recalcitrant structures[4]. Also, it is demonstrated that even a small amount of condensation reactions can reduce significantly monomer yields[5]. Thus, milder processes for lignin separation from the carbohydrate part have been developed, in order to obtain it in high yield and purity with low condensation degree. This high-quality lignin is treated afterwards following many possible approaches, which will be discussed later in this Chapter. These processes focalized on lignin can be divided into two categories according to the adopted approach: passive stabilization and active stabilization[5]. The key concept of passive stabilization is preservation of lignin structure and activity reducing ether bond cleavage, and thus condensation-deactivation processes, performing extraction in mild conditions. Some examples of passive stabilization processes are ammonia-based fractionation[6], ionic liquid (IL)-assisted fractionation[7], γ-valerolactone-assisted hydrolysis[8,9], and mild organosolv techniques[10]. What these methods have in common is the use of alternative media in mild conditions to obtain biomass deconstruction and fractionation giving high purity lignin. The major setback of these methods is that lignin is recovered in low yield, due to the mild operating conditions. On the other hand, working in a harsher environment would lead to greater β-O-4 cleavage negatively affecting isolated lignin quality. To overcome these problems active stabilization processes have been developed, allowing to operate in conditions suitable for extensive delignification. This approach, also known as *lignin-first*, is based on the fact that cellulose and hemicellulose are less susceptible to degradation thanks to their semi-crystalline structure and thus can be valorized in later stages. Therefore, active stabilization is often considered a coupled process of biomass fractionation and lignin depolymerization, where the stabilization is due to the formation of low M_w products, namely monomers or small oligomers. Even though many active stabilization processes exist, they all share the same milestones: solvolytic extraction followed directly by *in-situ* lignin reductive depolymerization, stabilizing reactive intermediates in their reduced forms[11]. The main challenge of these kind of processes is to find a balance between lignin depolymerization and the preservation of the carbohydrate part. Furthermore, reduction usually requires an heterogenous catalyst whose separation from the mixture of lignin oils and carbohydrate pulp can be challenging. For these reasons *lignin-first* processes have not found yet major applications and multistep processes are still subject of extensive research, especially

considering the huge amount of technical lignin obtained as a by-product from biorefineries and pulp industry.

There are many strategies to depolymerize isolated lignin, some of the most studied (catalytic pyrolysis, acid catalyzed hydrolysis, base catalyzed hydrolysis, catalytic reductive hydrogenolysis and catalytic oxidative depolymerization) are going to be briefly discussed in following paragraphs[12].

1.2 Catalytic Pyrolysis

Lignin pyrolysis can be performed without the addition of any catalysts, as thermal energy, in absence of oxygen, can break almost every C–C bond. In pyrolysis processes working temperature starts from 200 °C and can be increased up to 900 °C. Unfortunately, even if almost all the bonds can be cracked in this way, yields and selectivity are always low, leading to complex mixtures with high amounts of chars[13]. Catalysts, ranging from zeolites to metals and metal oxides, can improve significantly pyrolysis performances increasing both yield and selectivity. Unfortunately, pyrolysis vapors contain significant amounts of phenolic polymers, which tend to form chars, quickly deactivating catalyst surface reducing significantly catalyst recyclability. Many catalysts exist, each with its own advantages and disadvantages. Zeolites are well tunable, give good results in terms of yield and selectivity, but cannot be recycled efficiently and are extremely sensible to coke deposition. On the other hand, metal oxides re-activation is usually feasible, but the lack of selectivity on target products makes them suitable for the production of bio-oils rather than fine chemicals[12].

1.3 Acid Catalyzed Hydrolysis

Lignin hydrolysis in acidic medium is a conventional depolymerization strategy whose origin comes from pulp industry pretreatments. Acid catalysts can be inorganic acids, organic acids or even Lewis acids, with the latter possessing two different active species, the metal center and the Brønsted acid generated by the protic medium interaction with Lewis acid. Lignin hydrolysis in acidic medium starts from the cleavage of aryl ether bonds. In particular, *β*-aryl ether bonds are hydrolyzed much faster when compared to other ether bonds in lignin[14]. The most abundant ether bonds in lignin, *β*-O-4, can be cleaved following different pathways leading to different products (Figure 1.2).

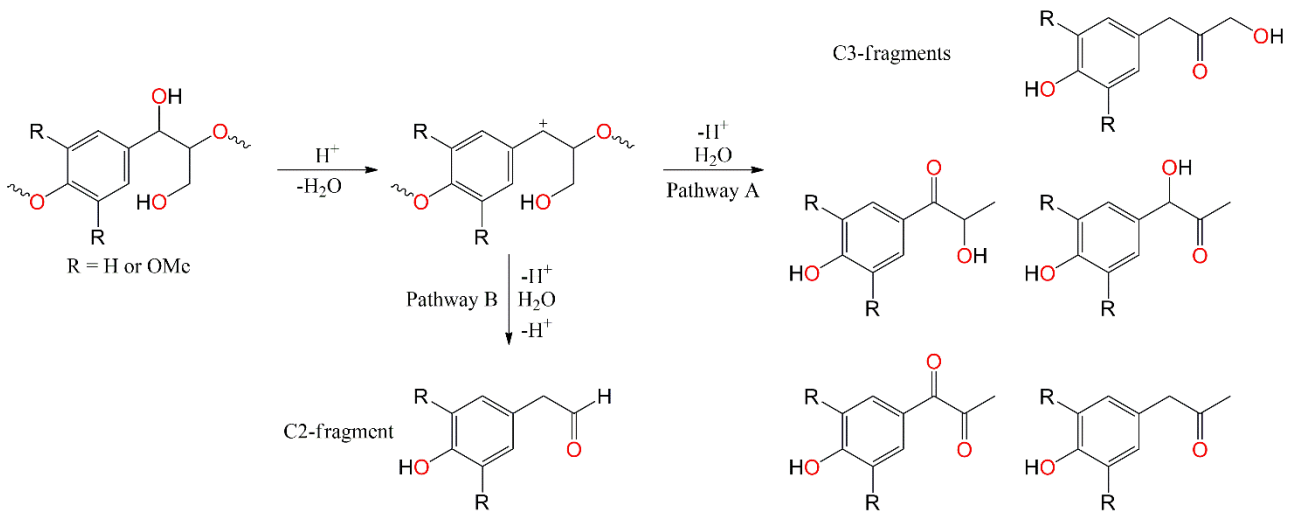

Figure 1.2: Schematic representation of lignin acidolysis pathways, and some possible general products.

Depending on the broken bond, ketones (C_3-fragments) or aldehydes (C_2-fragments) can be obtained. C_3-fragments are usually stable in the depolymerization conditions and can be isolated, while C_2-fragments tends to react giving chars and more recalcitrant condensation products, *de-facto* decreasing the overall yield of recovered monomers[15]. Furthermore, substrate and acid type can significantly modify reaction pathways. For example, hydrolysis of a model compound with phenolic hydroxyl substituents is way faster than hydrolysis of unsubstituted compound. This is due to the fact that side chain substituents and aromatic methoxy groups can stabilize generated carbocation heavily affecting hydrolysis kinetic[16].

1.4 Base Catalyzed Hydrolysis

In base promoted hydrolysis targeted linkages are still ether bonds, which can be cleaved using homogeneous catalysts, typically hydroxide of alkaline or alkaline-earth metals, or with heterogeneous bases such as CaO or layered double hydroxide[17]. Unfortunately, also in base catalyzed hydrolysis high temperatures are required. This means that reactive intermediates are formed leading to significant char production, decreasing obtainable monomers yields. The most popular approaches to minimize repolymerization include working in protic solvents or the addition of capping agents like boric acid or differently substituted phenols to block reactive species upon formation[18]. The cleavage of ether bonds involves a nucleophilic attack from a neighboring deprotonated hydroxyl, replacing the phenoxy group forming an epoxide which is readily opened by a hydroxide anion, as shown in Figure 1.3

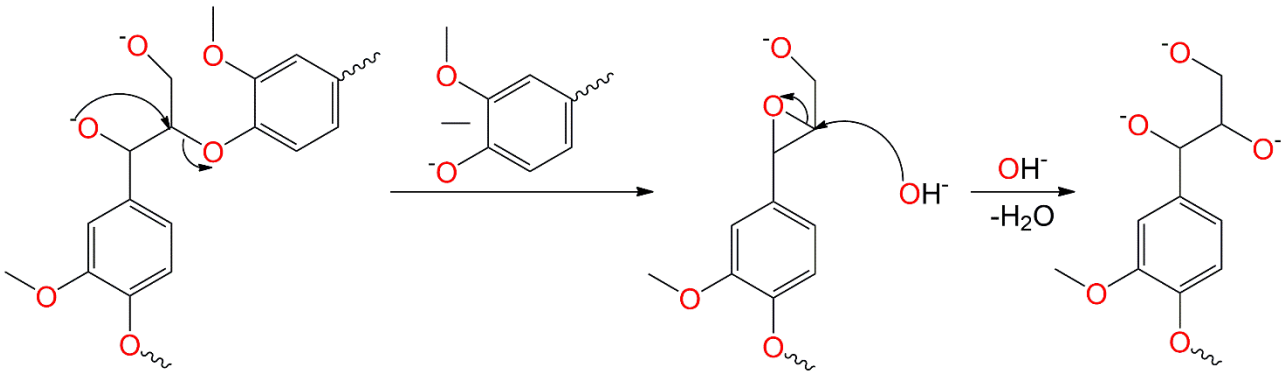

Figure 1.3: Reaction mechanism for base catalyzed ethereal bond cleavage.

1.5 Catalytic Reductive Hydrogenolysis

The chemical reactions through which hydrogen, or a hydrogen-donor, cleave carbon-carbon and carbon-heteroatom bond are referred to as Hydrogenolysis as shown in Figure 1.4.

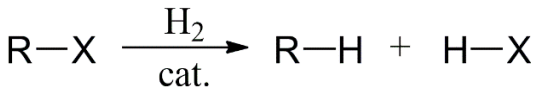

Figure 1.4: General schematic representation of hydrogenolysis reaction

Where X generally is an alkyl chain or other functional group containing heteroatoms (OH, SH, NH_2, OR, NR, etc.). This is a well-established and studied method to depolymerize lignin producing aromatic chemicals. If the conditions are adequate hydrogenolysis can be followed by hydrodeoxygenation, that is the removal of oxygen from the molecule to obtain hydrocarbons and represents the most important process in lignin upgrading to bio-oils[18]. Hydrogenolysis is performed in protic solvents, typically small-weight organic acids or alcohols, employing medium to high hydrogen pressure and a catalyst[19]. The most frequently used catalysts are heterogeneous, in particular metals of the "platinum group" (Pt, Pd, Ru, Rh and Ir) supported on an inert. These are generally prepared impregnating a carrier with a metal salt solution and subsequently thermally treating it in reducing conditions[20]. Monometallic catalysts are usually preferred thanks to their simplicity and generally high stability. In particular platinum and palladium supported on carbon (Pt/C - Pd/C) are extremely efficient and non-negligible amounts of hydrodeoxygenation and aromatic ring reduction products are usually obtained due to the harsh condition required for hydrogenolysis. Thus, other cheaper metals like Ni[21], Cu[22] and Fe[23], known to be less effective in hydrogenation conditions, have been studied both as homogeneous and heterogeneous catalysts. Non-commercial Ni catalysts can reach very good conversions, even if some additives, e.g. strong bases,

or atypical preparations are usually required[24]. Standard Ni/C is reported to successfully cleave aryl ether bonds without significant aromatic hydrogenation when proper conditions are used[23]. Significant improvement to catalyst performances can be obtained utilizing bimetallic systems. It is reported that specific metal couples have synergistic effects showing greater performances in lignin hydrogenolysis. This behavior comes from the chance to finely tune catalyst properties offering the possibility to increase the selectivity for a particular product. Mixed sulfides of Co, Ni, Mo, and W, as well as other bimetallic catalyst systems are often used for lignin hydrogenolysis[20]. Many different bimetallic systems exist, for example $LaNiO_3$ perovskite can be prepared on a mesoporous carrier forming a catalyst that gives particularly good yields in bio-oil[25]. Co/Mo sulfide catalysts due to their lower hydrogenation ability show higher selectivity for aromatic ether bonds and minor loss of aromaticity when compared to Ni catalysts, but with generally lower conversions[26]. Ru/Re alloys, even if quite expensive, show great activity on both ethereal and carbon-carbon bonds cleavage, giving high yields of monomeric compounds when applied either on model compounds or on real lignin[27].

1.6 Catalytic Oxidative Depolymerization

Catalytic oxidative depolymerization goal is to produce functional aromatic monomers such as vanillin, syringaldehyde and aromatic acids starting from lignin. Oxidative cleavage mainly focuses on C–C bonds, offering a way to crack them under mild conditions, giving complex mixtures of products depending on raw material nature and selected reaction conditions[28]. There are three possible pathways for oxidative cleavage:

- Oxidative cracking of C_1–C_α bond;
- Side chain oxidative cracking (C_α–C_β or C_β–C_γ bonds);
- Oxidative ring opening;

Different oxidants can be used, *e.g.*, nitrobenzene, metal oxides, O_2, H_2O_2, or O_3[12]. The activity and selectivity of catalytic oxidative depolymerization depends on the type and characteristics of both oxidant and catalyst, and on the severity of the reaction conditions[29]. Mild oxidants, *i.e.,* nitrobenzene, metal oxides and oxygen require an alkaline medium and produce mainly aldehydes preserving lignin's aromatic rings[29]. Oxygen is generally considered the most advantageous oxidant because it is inexpensive, green, it has a high efficiency per weight of oxidant, and it is a mild oxidant that does not affect aromatic rings[30]. Oxygen depolymerization mechanisms mainly proceed through radical chemistry, requiring basic conditions in order to ionize phenolic groups[30]. Harsh

depolymerization conditions can cause the cleavage of the aromatic ring, leading to the formation of unstable C6 acids that are quickly degraded to more stable C2-C4 acids[31]. The most abundantly produced acids from lignin harsh oxidation are succinic, malic and maleic acids. Most of these acids are valuable chemicals with many applications, from food to polymer industries. Obviously, if applied conditions are too harsh the oxidation proceeds to CO_2 and H_2O, completely mineralizing the matrix. For this reason, hydrogen peroxide has been studied a lot for ring-opening reactions as it is more reactive than O_2 and thus allowing milder reaction conditions[29]. Furthermore, using H_2O_2 helps to avoid typical mass transfer barriers between liquid and gas phases. On the other hand, H_2O_2 is a weak acid, and its reactivity strongly depends on the pH, being unstable in basic conditions. Therefore, it cannot be used in standard alkali conditions and dedicated protocols must be developed. Usually, a variety of catalysts, both homogeneous and heterogeneous can be employed, ranging from first transition metal complexes to noble metals, perovskites and zeolites. Nonetheless, oxidative depolymerization can be performed also without a catalyst, even tho selectivity and yield are lower and harsher reaction condition are required[12].

1.7 Lignin Depolymerization monomers

Lignin monomers are aromatic phenolic compounds that play crucial roles in both plant metabolism and industrial applications. These monomers are primarily derived from the phenylpropanoid pathway, a fundamental metabolic route in plants responsible for the biosynthesis of various phenolic compounds. The phenylpropanoid pathway begins with the conversion of phenylalanine to cinnamic acid. From cinnamic acid various derivatives are produced, including the three primary monomers that constitute the bulk of lignin: *p*-Coumaryl Alcohol, Coniferyl Alcohol, and Sinapyl Alcohol[32].

The depolymerization of lignin, whether through chemical, physical, or enzymatic processes, can break down the complex lignin polymer into its constituent monomers and smaller phenolic compounds. While the primary monomers surely are monolignols, lignin depolymerization can also yield a variety of other valuable compounds such as vanillin[33,34], guaiacol[35], syringol[36], catechol[37,38], vanillic[39] and syringic acids[40], eugenol[41], *p*-coumaric acid[42] and a variety of other phenols[43,44]. Among these, vanillin is probably the commercially most important chemical derived from lignin, widely used as a flavoring agent and as a building block in pharmaceutical industry. Guaiacol, syringol and catechol are mainly viewed as precursors for the synthesis of other fine chemicals. Eugenol can be produced from lignin in small amounts while it is easily extracted from clove-oils in good yields and thanks to its characteristic odor is widely used in perfume industry.

These compounds, derived from the breakdown of lignin could have a wide range of applications if reliable pathways to obtain them in good yield were available. Therefore, finding efficient pathways to depolymerize lignin into these valuable monomers is a key area of research for the development of sustainable biorefineries. In this way lignocellulosic biomass could be converted into bio-based chemicals, fuels, and materials, making industrial production more sustainable and reducing society's dependence on fossil fuels and their derivatives.

1.8 Aim of the thesis

In this project we worked on the upgrading of potentially biobased aromatic monomers to their halogenated corresponding products (Chapter 2). This kind of molecules could be of great use in green materials synthesis, in particular when it comes to resins and polymers. Furthermore, these aromatic cores could work as renewable and cheap starting materials for several pharmaceutical applications. The second part of the thesis (Chapter 3) focuses on the catalytic oxidative cleavage, in particular on the synthesis of molecular catalysts. Starting from ligands synthesis and optimization we aim to obtain several similar complexes and to characterize them expanding previous literature knowledge with spectroscopic and voltametric data, trying to demonstrate the correlation between ligand substitution and complex properties. As a final goal the most promising catalysts should be tested on the C–C cleavage of lignin model compounds.

1.8 Bibliography

[1] A. J. Ragauskas, G. T. Beckham, M. J. Biddy, R. Chandra, F. Chen, M. F. Davis, B. H. Davison, R. A. Dixon, P. Gilna, M. Keller, P. Langan, A. K. Naskar, J. N. Saddler, T. J. Tschaplinski, G. A. Tuskan, C. E. Wyman, *Science (1979)* **2014**, *344*, 709.

[2] M. Y. Balakshin, E. A. Capanema, H. Chang, in *Characterization of Lignocellulosic Materials*, Wiley, **2008**, pp. 148–170.

[3] C. Zhang, X. Shen, Y. Jin, J. Cheng, C. Cai, F. Wang, *Chem Rev* **2023**, *123*, 4510–4601.

[4] H. Wang, H. Ben, H. Ruan, L. Zhang, Y. Pu, M. Feng, A. J. Ragauskas, B. Yang, *ACS Sustain Chem Eng* **2017**, *5*, 1824–1830.

[5] T. Renders, S. Van den Bosch, S.-F. Koelewijn, W. Schutyser, B. F. Sels, *Energy Environ Sci* **2017**, *10*, 1551–1557.

[6] L. da Costa Sousa, M. Foston, V. Bokade, A. Azarpira, F. Lu, A. J. Ragauskas, J. Ralph, B. Dale, V. Balan, *Green Chemistry* **2016**, *18*, 4205–4215.

[7] K. H. Kim, B. A. Simmons, S. Singh, *Green Chemistry* **2017**, *19*, 215–224.

[8] J. S. Luterbacher, J. M. Rand, D. M. Alonso, J. Han, J. T. Youngquist, C. T. Maravelias, B. F. Pfleger, J. A. Dumesic, *Science (1979)* **2014**, *343*, 277–280.

[9] J. S. Luterbacher, A. Azarpira, A. H. Motagamwala, F. Lu, J. Ralph, J. A. Dumesic, *Energy Environ Sci* **2015**, *8*, 2657–2663.

[10] C. S. Lancefield, I. Panovic, P. J. Deuss, K. Barta, N. J. Westwood, *Green Chemistry* **2017**, *19*, 202–214.

[11] S. Van den Bosch, T. Renders, S. Kennis, S.-F. Koelewijn, G. Van den Bossche, T. Vangeel, A. Deneyer, D. Depuydt, C. M. Courtin, J. M. Thevelein, W. Schutyser, B. F. Sels, *Green Chemistry* **2017**, *19*, 3313–3326.

[12] Q. Tian, P. Xu, D. Huang, H. Wang, Z. Wang, H. Qin, Y. He, R. Li, L. Yin, S. Chen, Y. Zhao, *J Environ Chem Eng* **2023**, *11*, 109719.

[13] C. Bährle, V. Custodis, G. Jeschke, J. A. van Bokhoven, F. Vogel, *ChemSusChem* **2016**, *9*, 2397–2403.

[14] A. W. Pelzer, M. R. Sturgeon, A. J. Yanez, G. Chupka, M. H. O'Brien, R. Katahira, R. D. Cortright, L. Woods, G. T. Beckham, L. J. Broadbelt, *ACS Sustain Chem Eng* **2015**, *3*, 1339–1347.

[15] P. J. Deuss, M. Scott, F. Tran, N. J. Westwood, J. G. de Vries, K. Barta, *J Am Chem Soc* **2015**, *137*, 7456–7467.

[16] M. R. Sturgeon, S. Kim, K. Lawrence, R. S. Paton, S. C. Chmely, M. Nimlos, T. D. Foust, G. T. Beckham, *ACS Sustain Chem Eng* **2014**, *2*, 472–485.

[17] R. Katahira, A. Mittal, K. McKinney, X. Chen, M. P. Tucker, D. K. Johnson, G. T. Beckham, *ACS Sustain Chem Eng* **2016**, *4*, 1474–1486.

[18] C. Li, X. Zhao, A. Wang, G. W. Huber, T. Zhang, *Chem Rev* **2015**, *115*, 11559–11624.

[19] J. Zhang, *Green Energy & Environment* **2018**, *3*, 328–334.

[20] Z. Wan, H. Zhang, Y. Guo, H. Li, *ChemistrySelect* **2022**, *7*, DOI 10.1002/slct.202202582.

[21] J. M. Pepper, H. Hibbert, *J Am Chem Soc* **1948**, *70*, 67–71.

[22] K. Barta, G. R. Warner, E. S. Beach, P. T. Anastas, *Green Chem.* **2014**, *16*, 191–196.

[23] B. Duan, Q. Wang, Y. Zhao, N. Li, S. Zhang, Y. Du, *Biomass Bioenergy* **2019**, *131*, 105413.

[24] A. G. Sergeev, J. D. Webb, J. F. Hartwig, *J Am Chem Soc* **2012**, *134*, 20226–20229.

[25] J. Xu, Y. Yang, B. Liu, Y. Kong, B. Du, Y. Guo, J. Zhou, X. Wang, *Int J Biol Macromol* **2022**, *218*, 431–438.

[26] A. L. Jongerius, R. Jastrzebski, P. C. A. Bruijnincx, B. M. Weckhuysen, *J Catal* **2012**, *285*, 315–323.

[27] X. Li, Y. Ding, X. Pan, Y. Xing, B. Zhang, X. Liu, Y. Tan, H. Wang, C. Li, *Journal of Energy Chemistry* **2022**, *67*, 492–499.

[28] H. Lange, S. Decina, C. Crestini, *Eur Polym J* **2013**, *49*, 1151–1173.

[29] C. A. E. Costa, C. A. Vega-Aguilar, A. E. Rodrigues, *Molecules* **2021**, *26*, 4602.

[30] S. Gillet, M. Aguedo, L. Petitjean, A. R. C. Morais, A. M. da Costa Lopes, R. M. Łukasik, P. T. Anastas, *Green Chemistry* **2017**, *19*, 4200–4233.

[31] R. Rinaldi, R. Jastrzebski, M. T. Clough, J. Ralph, M. Kennema, P. C. A. Bruijnincx, B. M. Weckhuysen, *Angewandte Chemie International Edition* **2016**, *55*, 8164–8215.

[32] S. Dutta, in *Sustainable Catalytic Processes*, Elsevier, **2015**, pp. 125–155.

[33] Y. Wang, S. Sun, F. Li, X. Cao, R. Sun, *Ind Crops Prod* **2018**, *116*, 116–121.

[34] I. A. Pearl, *J Am Chem Soc* **1942**, *64*, 1429–1431.

[35] X. Shen, Q. Meng, Q. Mei, H. Liu, J. Yan, J. Song, D. Tan, B. Chen, Z. Zhang, G. Yang, B. Han, *Chem Sci* **2020**, *11*, 1347–1352.

[36] R. Panyadee, A. Saengsrichan, P. Posoknistakul, N. Laosiripojana, S. Ratchahat, B. M. Matsagar, K. C.-W. Wu, C. Sakdaronnarong, *Molecules* **2021**, *26*, 7444.

[37] A. Mabrouk, X. Erdocia, M. G. Alriols, J. Labidi, *J Clean Prod* **2018**, *198*, 133–142.

[38] S. Jeenpadiphat, I. Mongkolpichayarak, D. N. Tungasmita, *J Anal Appl Pyrolysis* **2016**, *121*, 318–328.

[39] Y. Higuchi, H. Ishimaru, T. Yoshikawa, T. Masuda, C. Sakamoto, N. Kamimura, E. Masai, D. Takeuchi, T. Sonoki, *Bioresour Technol* **2023**, *385*, 129450.

[40] C. Srinivasulu, M. Ramgopal, G. Ramanjaneyulu, C. M. Anuradha, C. Suresh Kumar, *Biomedicine & Pharmacotherapy* **2018**, *108*, 547–557.

[41] R. Morales-Cerrada, S. Molina-Gutierrez, P. Lacroix-Desmazes, S. Caillol, *Biomacromolecules* **2021**, *22*, 3625–3648.

[42] V. I. Timokhin, M. Regner, A. H. Motagamwala, C. Sener, S. D. Karlen, J. A. Dumesic, J. Ralph, *ACS Sustain Chem Eng* **2020**, *8*, 17427–17438.

[43] T. Yoshikawa, T. Yagi, S. Shinohara, T. Fukunaga, Y. Nakasaka, T. Tago, T. Masuda, *Fuel Processing Technology* **2013**, *108*, 69–75.

[44] M. Kleinert, T. Barth, *Chem Eng Technol* **2008**, *31*, 736–745.

Chapter 2

2. Upgrading lignin monomers routes to aryl cored building blocks for polymers and resins

2.1 Introduction

One of the most relevant challenges in modern polymer and resins market is to find a reliable and cheap alternative to bisphenol A (BPA), which is a chemical classified harmful from World Health Organization. BPA main applications are in polycarbonates synthesis, in which is reacted with phosgene to obtain the desired polymer, as shown in Figure 2.1,

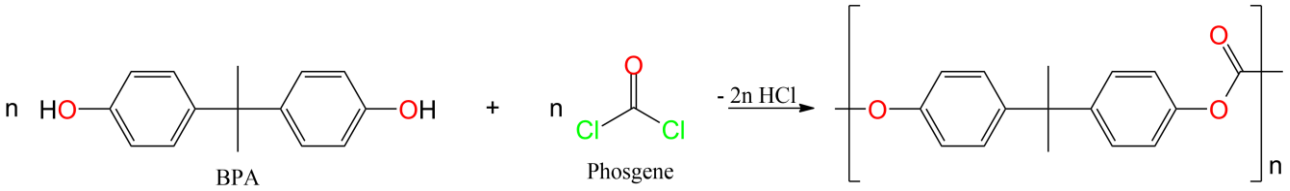

Figure 2.1: General synthesis of a BPA based polycarbonate

Bisphenols are also typically found as a core within epoxy resins, where the addition of the homonymous functional groups is obtained by the interaction with epichlorohydrin (Figure 2.2), which unfortunately, comes with additional dangers for the environment and human health.

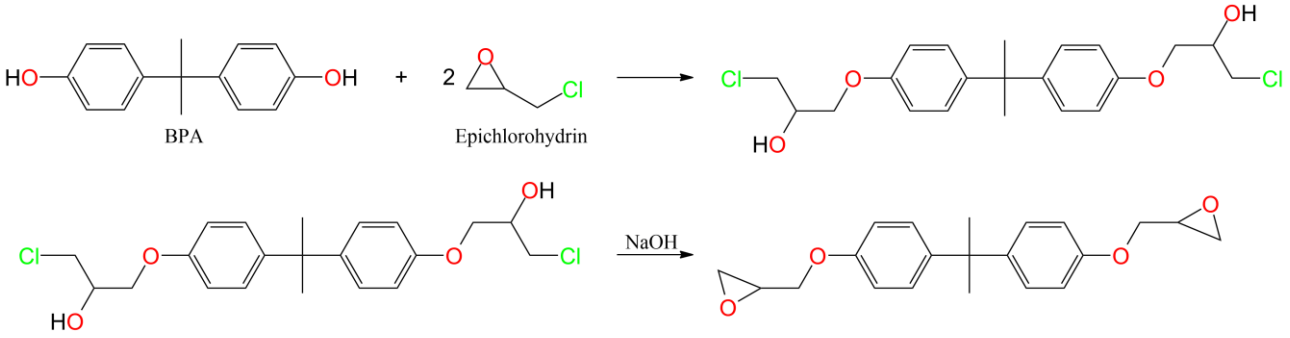

Figure 2.2: Reaction pathway to epoxy resins aromatic core starting from BPA and epichlorohydrin

On one side, bisphenols facilitate the production of technically stiff monomers and polymers, which are highly valued for their ability to deliver superior mechanical properties, including enhanced strength, durability, and stability. However, bisphenols, including BPA, are associated with various environmental and health concerns. These issues include their persistence in the environment,

potential to disrupt endocrine systems, and adverse effects on both human health and wildlife, raising significant challenges for their widespread use.

Lignin, one of the most abundant and widely distributed biopolymers (Chapter 1), holds significant potential as a sustainable source for bio-based bisphenol-like monomers. These lignin-derived compounds offer the promise of significantly reduced toxicity compared to traditional bisphenols, making them an environmentally friendly alternative for various industrial applications.

Certainly, monomers derived from lignin require appropriate chemical upgrading to transform them into forms that are directly suitable for use in industrial applications. A well-known upgrading example is the Dakin oxidation of vanillin [1,2], which converts it into methoxy hydroquinone (Figure 2.3). This monomer exhibits properties comparable to those of traditional bisphenols, making it a viable substitute when incorporated into materials such as epoxies and polyurethanes, where it contributes to desirable mechanical and chemical characteristics.

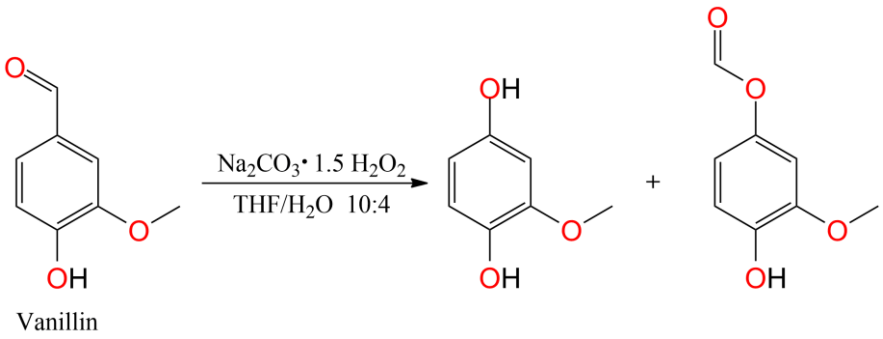

Figure 2.3: Dakin oxidation of vanillin

Another promising approach is the oxidative coupling of electron-rich lignin-derived arenes to produce oligoguaiacols, a process that could afford a number of dimeric or trimeric products, functionally linked to BPA. For example, enzymatic oxidation of guaiacol gives a number of biphenols and triphenols[3] (Figure 2.4).

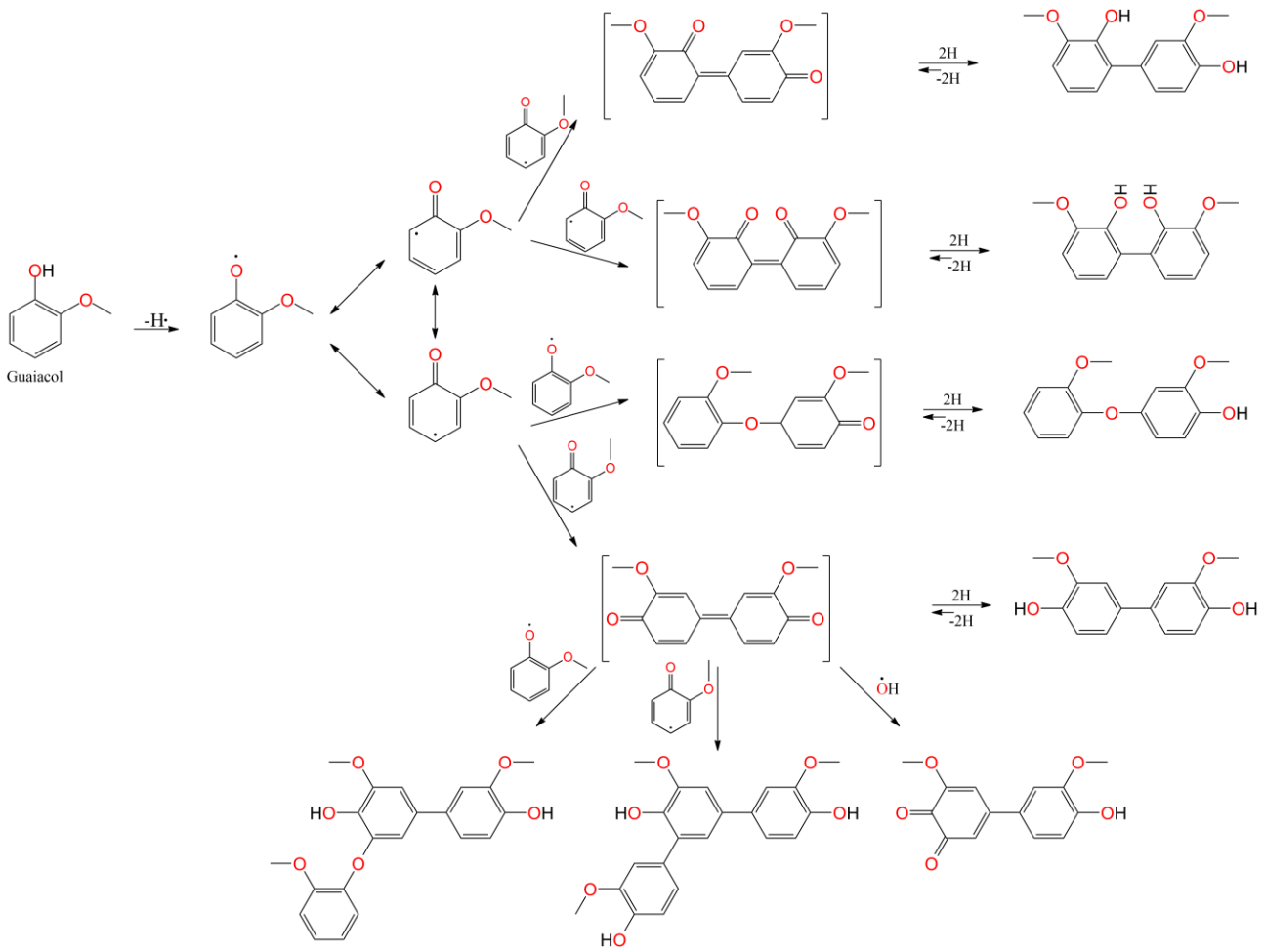

Figure 2.4: Oxidation of guaiacol leading to production of several different bi- and tri-phenols

In a similar approach, ferric chloride oxidation selectively converts guaiacol into an interesting triphenylenes (TPN)[4], which exhibits promising material properties.

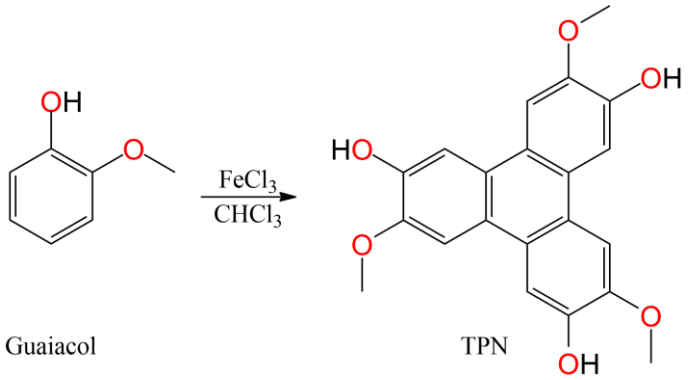

Figure 2.5: Oxidation of guaiacol to its corresponding triphenylene unit

TPN structures, capable of forming extended π-π stacking, typically self-assemble in column-shaped macrostructures, resulting in enhanced electron conduction and anisotropic conduction. This last property is of particular interest in organic semiconductors assembly, like field effect transistors, organic photovoltaic devices, and OLEDs[5].

An alternative approach to BPA-like monomers, involves the employment of electrophilic species, such as vanillyl alcohol, having the ability to alkylate guaiacol or other electron-rich arenes. Bisguaiacol (Figure 2.6) can thus be prepared, a compound that proved to have very less oestrogenic toxicity, compared to bisphenols[6].

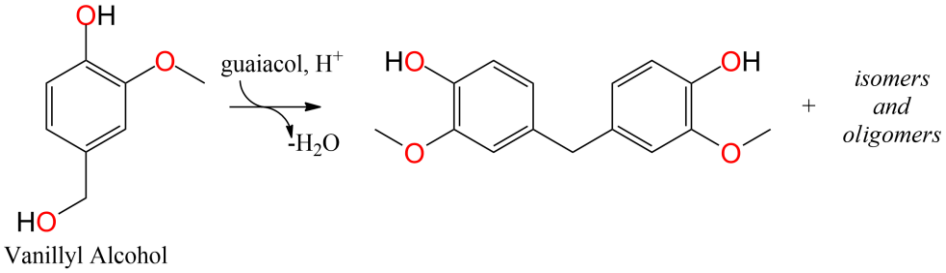

Figure 2.6: Electrophilic reaction of vanillyl alcohol with guaiacol to obtain BPA-like structures

The idea of having electrophilic reagents, possibly obtained from biomass and able to alkylate electron rich arenes, prompted us to study a sustainable halogenation method to functionalize benzylic positions.

2.2 Sustainable halogenation of BTX aromatics

Benzenes, toluenes, and xylenes (BTX aromatics) can be obtained from the thermochemical conversion of lignin through processes such as pyrolysis, hydrothermal liquefaction, and catalytic upgrading. These are usually obtained as mixtures, which can be purified through fractional distillation. Thus, the development of sustainable chemistry devoted to their upgrading becomes of central importance. Activation through halogens has become a key strategy in achieving desired reactivity. Substitution of a hydrogen atom with a halogen atom within an organic skeleton significantly increases the electrophilicity of the linked carbon center, enhancing concerted (S_N2) as well as carbenium ion-mediated (S_N1) substitutions, common – for instance – on benzylic positions. Additional opportunities offered by C(sp^3)–Hal bonds arise from the ease of their homolytic cleavage, leading to the formation of reactive carbon-centered radicals. C(sp2)–Hal bonds of aryl halides also exhibit high reactivity, particularly towards transition-metal-mediated cross-coupling processes or Ar-S_N reactions.

While C–H activation through halogens presents clear technical advantages, it also brings forth concerns about the toxicity of halo-compounds to both human health and environment[7]. Nevertheless, in line with the European Union's 'green new deal' guidelines[8], addressing two pivotal issues could facilitate the environmentally conscious utilization of halogenated compounds as intermediates in chemical processes:

1. The development of more sustainable production methods for halo compounds, potentially involving the use of eco-friendly halogenation reagents.

2. The development of methods for the efficient removal and recycle of halogens, advocating principles of a circular economy.

It is noteworthy that both aspects are influenced by the type of halogen employed. When considering the most atom-economical options, namely chlorine and bromine, the latter typically exhibits some advantages over the former. These include:

(i) better regioselectivity in radical processes, attributed to the lower bond enthalpy of H–Br (88 kcal/mol) compared to H–Cl (103 kcal/mol)[9],

(ii) greater electrophilicity of the halo compound due to better leaving group ability of the halide ion, reduced toxicity, presumably due to faster hydrolysis[10], and easier oxidation of the halide to molecular halogen (E^0 = 1.087 V (SHE) for Br_2/Br^-; E^0 = 1.358 V (SHE) for Cl_2/Cl^-)[11] resulting in easier recyclability.

Light irradiation often significantly influences the selectivity of halogenation processes. Photolytic cleavage of molecular halogens gives rise to radicals that are known to favor benzylic functionalization[9]. Conversely, the same molecular halogens exhibit prominent functionalization on the aromatic ring when used in the dark[12].

A classic example is the bromination of toluene with molecular bromine. When the system is exposed to light (right side of Figure 2.7), a radical mechanism is initiated by Br· coming from Br_2 homolysis. Propagation involves the reversible abstraction of a benzylic hydrogen atom from the substrate by Br·, to give HBr and a structure-stabilized carbon-centered radical, which may react with Br_2 to give the brominated product, thus regenerating Br· that is able to sustain the chain process. In absence of light (left side of Figure 2.7), the reaction follows a different mechanism, producing the *ortho* and *para*-bromoarenes through Ar-S_E, that involves cationic intermediates. In this case, a catalytic amount of iodine[13,14] or $FeCl_3$[15] is added to enhance the electrophilicity of bromine.

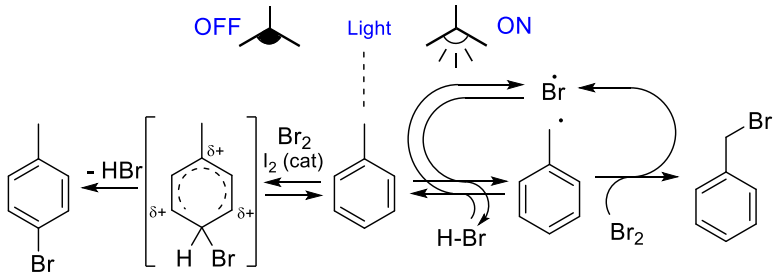

Figure 2.7: Comparison between the light initiated radical halogenation of toluene (right), and the Ar-S_E bromination in the dark (left). Reprinted from *Roncaglia et al.*[16]

While widely employed and capable of producing reliable results on various substrates, the direct use of molecular bromine poses sustainability challenges. Its innate reactivity requires stringent safety protocols during transportation, storage, and handling[17]. A related concern involves the stability of the diluting media, often requiring the use of toxic CCl_4 to prevent undesired solvent degradation. Furthermore, the direct use of Br_2, even if used in low concentration, exhibits limited selectivity towards benzylic bromination, primarily due to co-bromination occurring on the aromatic ring. This side process produces awkward halogenated byproducts that can complicate product separation, and will require disposal. Lastly, only one half of the halogen load is incorporated into the product, the other half being lost as bromide ion.

A solution for some of the aforementioned problems is the *in-situ* generation of bromine: firstly, the handling of Br_2 is no longer an issue, since it is formed inside the reaction vessel, secondly this approach allows enhanced selectivity of the bromination, as the amount and timing of the chemical generation can be modulated. In addition, in situ regeneration of bromine from bromide by-products improves the atom economy of the overall process.

Based on a literature review, we concluded that unparalleled efficiency and sustainability can be achieved through the well-established redox equilibria between hydrogen peroxide and halide ion in aqueous acidic media (Equation 1)[18]. Its practical implementation is surprisingly simple as standard aqueous HBr and H_2O_2 solutions are effective. The generated bromine can be involved in different chemical mechanisms, such as an Ar-SE (Equation 2)[19] or a radical substitution on activated positions (Equation 3). In the context of the radical process, it is noteworthy that a standard household LED lamp can serve as an efficient initiator, capable of triggering bromine photolysis (Equation 3, top)[20]. Hence, no oxidant-derived residues apart from water are formed and, at the end of the process, the residual halogen (if any) can decompose hydrogen peroxide into molecular oxygen (Equation 4)[20].

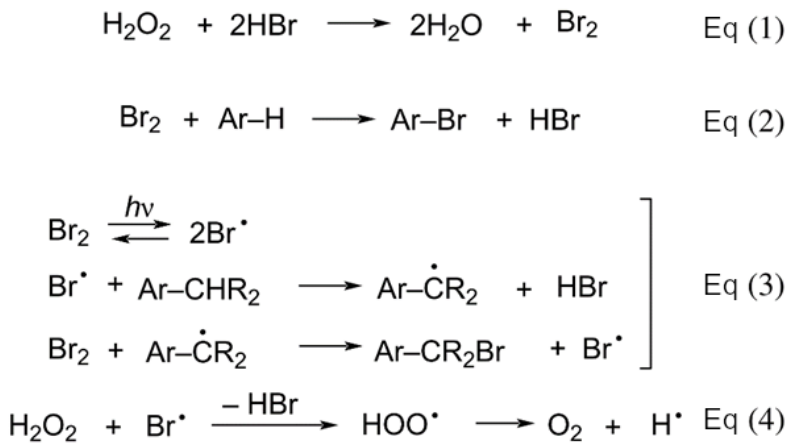

Over the years, various peroxide-bromide processes have been developed based on this chemistry. In particular, significant attention has been given to the preparation of benzyl (mono)bromides [21–24], which can be produced with high efficiency. The peroxide-bromide method appears to be especially suitable for obtaining aryl-cored dibromides, too. However, to the best of our knowledge, this option has been scarcely exploited, except for a few reports on some activated arenes[25,26]. We therefore investigated the application of the peroxide-bromide method to the synthesis of aryl-cored polybromides obtainable from xylenes or mesitylene[16].

Our investigation started (Table 2.1) with the conversion of **3** into **3a**, taking as "zero-point" conditions those reported for mono-bromides[23,24], with the only change of a double amount of brominating agent ($HBr/2H_2O_2$). A household white LED lamp was used as the activator, and hydrogen peroxide was slowly added, by means of a syringe pump. As the bromine color generated after each H_2O_2 drop disappeared quickly, the reaction time was reduced from 24 h to 8 h. In these conditions, the process exhibited complete conversion, but strong selectivity in favor of the monohalide **3am** (entry 1, Table 2.1).

Table 2.1: Light-mediated bromination of p-xylene with in-situ generated Br_2.[a] Adapted from *Roncaglia et al.*[16]

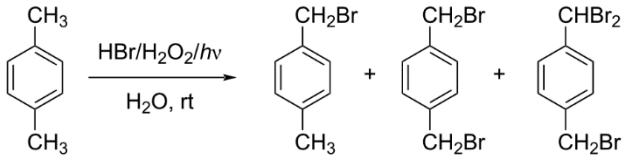

3 **3am** **3a** **3at**

entry	H_2O_2 dropping time (h)	post- dropping time (h)	H_2O (mL)	CH_2Cl_2 (mL)	**3am** (%)	**3a** (%)	**3at** (%)
1	8.0	–	4.0	–	78	22	traces
2	8.0	–	1.0	–	18	26	56
3	3.0	1.0	1.0	–	63	37	1
4	3.0	1.0	2.0	–	52	46	2
5	3.0	1.0	2.0	1.0	20	74	6
6	3.0	1.0	2.0	0.5	21	74	5
7	2.0	1.5	2.0	0.5	9	86	5
8	2.0	1.5	1.5	1.0	1	90	9

[a]Reaction conditions: *p*-xylene (531 mg, 5 mmol), H_2O (see Table), HBr (48 wt % aqueous solution, 1.25 mL, 11 mmol), white LED lamp, H_2O_2 (35 wt % aqueous solution, 2.00 mL, 23.3 mmol) slowly dropped by a syringe pump (see Table), CH_2Cl_2 (see Table). Yields are reported as molar % obtained from ^{1}H NMR spectra.

The reduction of the volume of the aqueous phase (Table 2.1, entry 2) resulted in a small shift towards the desired product **3a** but also in the predominant overreaction towards tribromide **3at**. Formation of **3at** was substantially controlled by reducing the reaction time (4 h overall, entries 3 and 4 in Table 2.1). In these last experiments a whitish solid appeared during addition of the oxidant, initially observed in the reaction with lower water amount (Table 2.1, entry 3). ^{1}H NMR experiments identified the solid as **3a**, making clear that phase separation was an important issue, resulting in a limitation of reagents' diffusion. The addition of a small amount of CH_2Cl_2 to solubilize this precipitate was thus considered (Table 2.1, entries 5 and 6) and resulted in a substantial selectivity improvement. The achievement of a better homogeneity made possible to further reduce the reaction time (Table 2.1, entry 7), giving total conversion and excellent selectivity toward **3a**. Water is an essential constituent of the system, as its polar nature favors the extraction of HBr from the organic phase, resulting in a useful shift of the reversible hydrogen abstraction from the substrate (Figure 2.1 and Equation 3, middle)[20]. This two-phase system is likely to benefit from efficient stirring as well as from a proper volume ratio between aqueous and organic phases, implemented in entry 8, which resulted in further enhancement of selectivity toward **3a**.

The application of the same protocol on *o*-xylene cleanly gave corresponding dibromide (**1a**, Figure 2.8) in almost quantitative yield. This product possesses a high lacrimatory activity[27,28], thus, it must be handled carefully when isolated and during the purification steps. On the other hand, **3a** lacks the same effect and therefore can be processed without any particular precautions.

Higher nucleophilic aromatic cores are affected by minor, yet inevitable, bromination on the ring. This is the case of dialkyl-substituted arenes having *o,p*-activated positions (*ortho* with respect to one alkyl substituent and *para* with respect to another alkyl substituent). For instance, bromination of *m*-xylene (**2**, Figure 2.8) resulted in lower selectivity for the benzyl *α,α'*-dibromide (**2a**) compared to **1a** or **3a**, due to the partial ring bromination[29]. The structure of mesitylene (**4**), featuring three *o,p*-activated positions, makes the selective halogenation of benzylic positions even more challenging. The conventional bromination with NBS in CCl_4 yields no more than 30% of the desired 1,3,5-tris(bromomethyl)benzene (**4a**)[30], due to the concurrent ring bromination[31]. A modified method working in refluxing benzene and benzoyl peroxide initiator was claimed to provide a clean conversion to **4a** with very high yields[32,33]. However, in our hands, this procedure resulted in significant amounts of ring bromination too. Using the peroxide bromide conditions developed for *p*-xylene, **4a** was obtained with a 42% yield. In this case, two chromatographic separations in sequence were necessary to remove most of the core brominated by-products, that were still detected in small amounts.

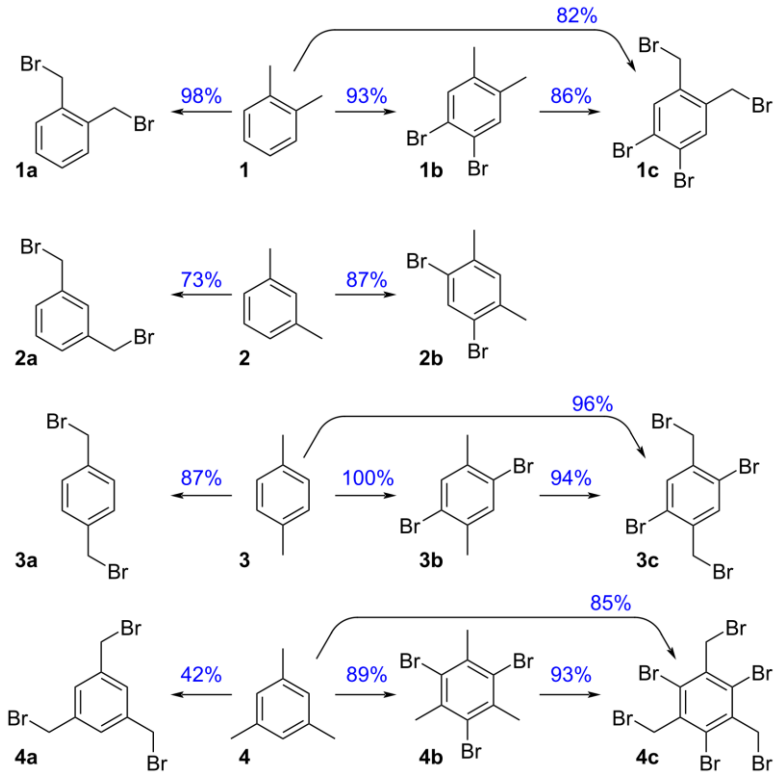

Figure 2.8: Yields obtained in the preparation of aryl-cored halides. Reprinted from *Roncaglia et al.*[16]

Ring bromination of xylenes is commonly carried out using molecular bromine in absence of light, along with the aforementioned catalytic promoters ($FeBr_3$ or I_2)[34,35]. Some reports of ring

bromination by means of NBS or the peroxide-bromide method are also known, but mainly for highly activated arenes (phenols or anisoles, for instance) or for the synthesis of monobromides[24,25,36]. Continuing our investigation on the subject, the ring bromination of *p*-xylene (**3**, Figure 2.8) towards **3b** was considered. The starting conditions were taken from procedures established for monobromides[24,37], adapting the molar amount of the brominating agent ($HBr/2H_2O_2$) and including a small amount of CH_2Cl_2, according to the previous discussion. A catalytic amount of iodine (≈1 mol %) was also included. Under these conditions, a first assessment of the reaction time was performed (entries 1, 2, 3 of Table 2.2), resulting in the predominant ring monobromination, even after 48 h. Considering the continuous conversion of HBr into Br_2 by means of the peroxide, we speculated on the decreasing acidity throughout the reaction progress. Since acidity was claimed to have a crucial role[38,39], we contemplated the addition of a small amount of sulfuric acid (Table 2.2, entry 4).

Table 2.2: *p*-Xylene bromination with in-situ generated Br_2 in absence of light.[a] Adapted from *Roncaglia et al.*[16]

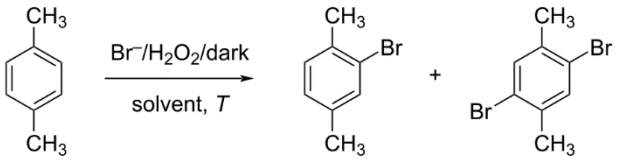

3 **3bm** **3b**

entry	CH_2Cl_2 (mL)	*T* (°C)	*t* (h)	H_2SO_4 (mmol)	**3bm** (%)	**3b** (%)
1	1.5	rt	16	–	90	10
2	1.5	rt	24	–	75	25
3	1.5	rt	48	–	73	27
4	1.5	rt	48	0.5	50	50
5	1.5	rt	168	0.5	43	57
6	1.5	60	72	0.5	40	60
7	–	60	72	0.5	78	22
8[b]	1.5	60	48	11.5	14	86
9[b,c]	1.5	60	48	11.5	0	100

[a]Reaction conditions: **3** (531 mg, 0.62 mL, 5 mmol), I_2 (15 mg, 0.07 mmol), HBr (48 wt % aqueous solution, 1.25 mL, 11 mmol), H_2SO_4 (98 wt %, see Table), H_2O_2 (35 wt % aqueous solution, 2.00 mL, 20.6 mmol) dropped in 2 h by a syringe pump, CH_2Cl_2 (see Table). Selectivity is reported as molar % obtained from ^1H NMR spectra. [b]NaBr (11 mmol) and H_2SO_4 (98 wt %, 11.5 mmol) instead of HBr (48 wt % aqueous solution). [c]Changed reagent order: NaBr (11 mmol) dissolved in H_2O_2 (35 wt % aqueous solution, 2.00 mL, 20.6 mmol) dropped in 15 min to a mixture of **3** (5 mmol, solution in CH_2Cl_2 (1.5 mL) and H_2SO_4 (98 wt %, 11.5 mmol).

This adjustment led to a significant enhancement towards **3b**, resulting in a respectable 57 mol % selectivity, after prolonged reaction time (Table 2.2, entry 5). Furthermore, a slight improvement was observed at higher temperatures (Table 2.2, entry 6), while the removal of CH_2Cl_2, possibly limiting the temperature inside the flask, had a negative impact (Table 2.2, entry 7). Nevertheless, yields and selectivity seemed to plateau around 60%.

Data available in literature suggested a beneficial effect coming from the reduction of the water amount[37]. As all the existing water originates from the employed reagents like aqueous HBr and H_2O_2, the combination of NaBr and H_2SO_4 was explored as a potential source of anhydrous HBr. A notable increase in selectivity towards **3b** was suddenly observed (Table 2.2, entry 8). However, this method led to the undesired, uncontrolled generation of Br_2 when neat H_2SO_4 was mixed with NaBr. This issue was addressed through an alternative reagent introduction scheme, where NaBr was dissolved in aqueous hydrogen peroxide and was gradually added to the reaction mixture, containing the remaining chemicals. The addition time of this aqueous reagent was also shortened to 15 minutes, to counteract the slow decomposition of H_2O_2 caused by NaBr. This modification ultimately resulted in nearly complete conversion of **3** into **3b** (Table 2.2, entry 9).

Such a peroxide-bromide halogenation method, originally developed for the monobromination of benzenoid structures, has been extended to synthesize aryl-cored polybromides with high yield and high atom economy. This method, when used with light irradiation as halogen initiator, is capable to selectively convert xylene isomers and mesitylene into their corresponding benzyl bromides, regardless the presence of halogen atoms on the core. Moreover, under dark conditions, a modification of the same method allows the preparation of aryl polybromides through ring halogenation. The two variants, tested on a 10-gram scale following the same synthetic protocols, can be telescoped to achieve polybromo derivatives that feature both core and side chain substitution, in high yield.

The aryl-cored bromides featuring both core and side chain halogens (**1c**, **3c**, and **4c** of Figure 2.8) could also be of some interest. The preparation of these polybromides can be ideally approached with two synthetic strategies: first-benzylic-then-ring or first-ring-then-benzylic halogenation. Of the two alternatives, the latter is more advantageous, due to three favorable features[40,41]: (i) Optimal control as each ring halogenation inhibits further ring halogenations, (ii) ring halogenation do not negatively affect benzylic bromination, and (iii) aryl bromides often display better solubility in organic solvents than benzyl bromides, reducing precipitation issues. Applying now the first-ring-then-benzylic halogenation strategy to *p*-xylene, dibromide **3b** was successfully converted into **3c**, by means of the method herein developed for the benzylic bromination. The process was then telescoped, resulting in a one-pot, two-step synthesis of **3c** from **3**, with improved operativity and yield (see Section 2.5,

Experimental). The same strategies were followed for the preparation of **1c** (from **1b** or from **1**), as well as for **4c** (from **4b** or from **4**).

The nucleophilicity of **4** provides useful support for its ring bromination towards **4b**, resulting in an excellent isolated yield of 89%. Moreover, the intermediacy of **4b** is advantageous for obtaining **4c**, thus avoiding the selectivity issues observed during the benzylic bromination of **4**. As a result, **4c** was obtained from **4** (in a one-pot, two-step process) with an 85% isolated yield. The particular cleanliness of the conversion of **4b** into **4c**, featuring negligible formation of gem dihalides, could arise from the useful steric hindrance given by the halogen bound to the core. Figure 2.8 collects the results obtained in the preparation of aryl-cored halides by means of the peroxide-bromide process. For products featuring bromine on both the aromatic core and the side chain, the "direct" one-pot two-stage and the "indirect" first-ring-then-benzylic halogenation methods are compared.

The peroxide-bromide halogenation method, originally developed for the monobromination of benzenoid structures, can thus be extended to synthesize aryl-cored polybromides with high yield and high atom economy. This method, when used with light irradiation as halogen initiator, is capable to selectively convert xylene isomers and mesitylene into their corresponding benzyl bromides, regardless the presence of halogen atoms on the core. Moreover, under dark conditions, a modification of the same method allows the preparation of aryl polybromides through ring halogenation. The two variants, tested on a 10-gram scale following the same synthetic protocols, can be telescoped to achieve polybromo derivatives that feature both core and side chain substitution, in high yield. For example, one possible application of these polybromo derivatives is the alkylation of electron-rich biobased arenes such as guaiacol, giving rise to valuable adducts[42,43].

2.3 Chloromethylation of bio-based electron-rich aromatics

Benzenoid compounds from natural sources often contain oxygen atoms on the aromatic ring, endowing them with electron-rich characteristics. This electron density makes these compounds particularly reactive in electrophilic aromatic substitution reactions. Aldehydes, which can be naturally occurring or readily synthesized (e.g., through alcohol oxidation), are effective electrophiles and are expected to interact efficiently with bio-sourced arenes. The reaction between aldehydes and phenols is well-established; it often leads to the coupling of two arene units, where the initial substitution product alkylates a second arene molecule.

Interestingly, the presence of chloride ions alters this reaction pathway. First described by Grassi-Cristaldi and Maselli in 1898[44,45] and later expanded upon by Stephen[46], Blanc in 1923[47], and

Quelet in 1932[48], this effect is attributed to a significant interaction between the halide and the aldehyde, resulting in the formation of a chlorinated intermediate, such as a Cl,O-acetal[44,49], which acts as the true electrophilic species in the reaction with the aromatic partner.

Despite the long history of the Blanc-Quelet reaction, only a few studies have explored its application to bio-based phenols. Therefore, we proceeded to investigate the application of the Blanc–Quelet procedure for the selective chloromethylation of representative bio-based phenols, including guaiacol, eugenol, *p*-cresol, piceol, vanillin, and salicylaldehyde.

The resulting benzyl halides (**Ia**–**VIa**, Figures 2.9 and 2.10) serve as valuable building blocks for the production of bio-based materials and chemicals[16,50–52]. One particularly interesting application we developed is the selective amidation of these benzyl chlorides to form benzyl formamides (**Ib**–**VIb**, Figures 2.9 and 2.10). These compounds exhibit significant synthetic versatility, as they can be transformed into a variety of functional groups.

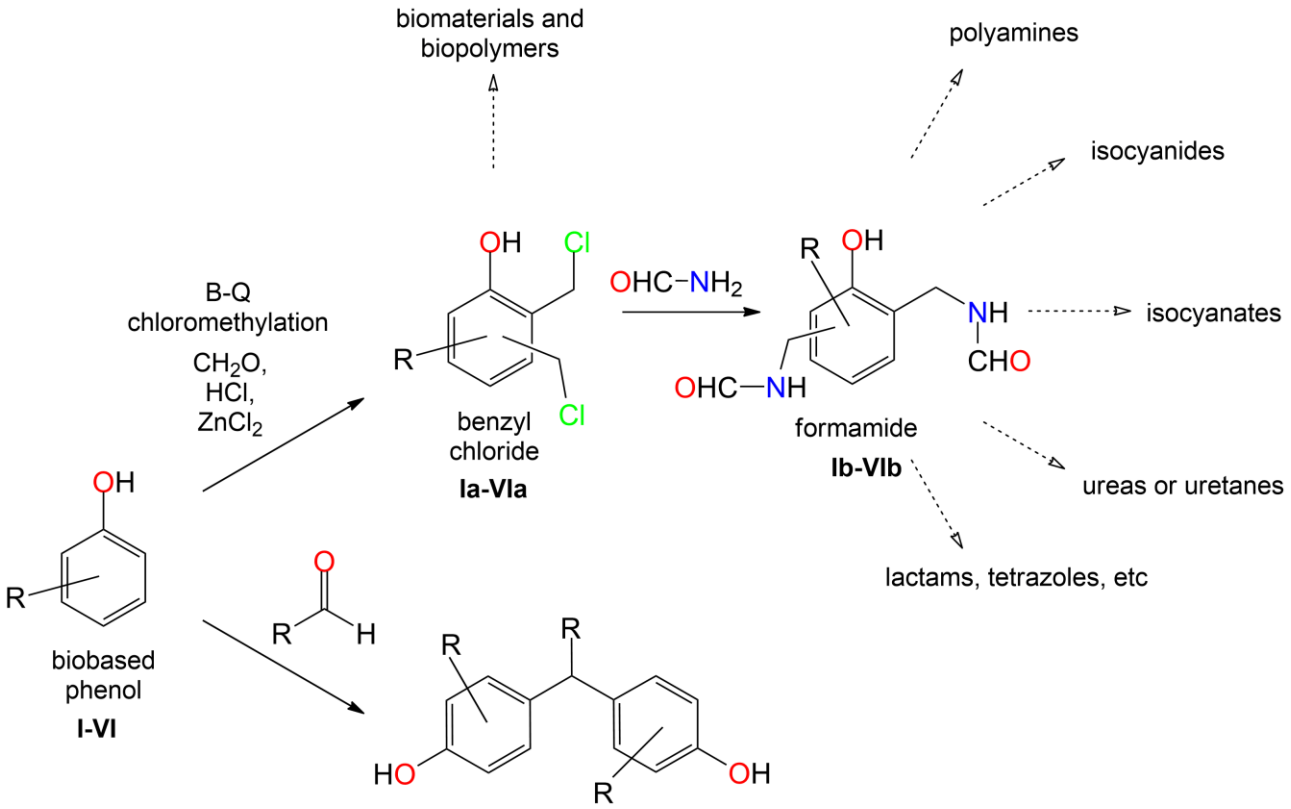

Figure 2.9: General scheme of upgrading of biobased phenols through Blanc-Quelet reaction to benzyl chloride and formamides, or directly to a BPA-like structure reacting them with a proper aldehyde.

For example, formamides can be reduced to amines[53–57] or dehydrated to isocyanides. Additionally, it is possible to convert formamides into isocyanates[58], enabling the synthesis of urethanes[59], ureas[60,61], and thiocarbamates[62]. Moreover, specialized methods have been developed for coupling formamides with other synthons to produce structures such as aminonitriles[63], tetrazoles[64] or

lactams[65], which may act as essential structural motifs in low molecular weight active pharmaceutical ingredients.

Our goal was to develop synthetic procedures with reduced environmental impact, which led our decisions in synthesis design. First, paraformaldehyde (PF) was chosen over aqueous formaldehyde to reduce the amount of aqueous waste produced. Second, acidic metal catalysts were ditched in favor of concentrated sulfuric acid[66] for ease of purification and cost reduction. The choice of solvents was made so that they could be considered renewable, or at least as less environmentally impactful as possible. Also, it was chosen to operate at the lowest temperature possible that would grant the obtainment of the desired product.

Adjustments to the synthetic procedures were made necessary by the great difference in reactivity between the substrates due to their different substitution and chemical structure. Various reaction parameters had to be optimized, and our preliminary studies showed that a five- to eight-fold excess of hydrochloric acid with respect to PF was necessary to ensure chlorination of the resulting carbocation and avoiding the production of the corresponding alcohol.

The first substrate which we focused our synthetic endeavors on was vanillin for the production of derivative **IIa** (Figure 2.10). At first, experiments were performed at room temperature in concentrated hydrochloric acid with equimolar amounts of substrate and alkylating agent. Small amounts of CH_2Cl_2 were employed as solvent for the organic solid. Even long reaction times, spanning from 16 to 24 hours, led to limited conversion of the substrate. Equimolar amounts of sulfuric acid were then added to the reaction mixture, which lead to a considerable increase of conversion values, up to 90 %. An increase in temperature was experimented to offset the tendency of PF to undergo limited decomposition producing formalin oligomers, unfortunately leading to a non-significant increase in conversion. It was then decided to operate with a small excess of paraformaldehyde, which proved to be successful as conversion increased up to 95 %. Despite our efforts to push the reaction further, no trace of the di-chloromethylation product was found, even when large amounts of PF were employed. Finally, a solventless approach was tested, suspending the organic solids directly in HCl conc. under vigorous stirring at 60 °C. Pleasantly, the reaction proceeded way faster than expected, reaching complete conversion of the substrate after six hours, with no side-products detected through ^{1}H NMR.

The same procedure was applied to the successive substrates. Salicylaldehyde proved to be more challenging, as the reaction operated at low temperatures resulted in a mixture of mono- and di-alkylation products, even when performed with over-stoichiometric amounts of PF. To increase selectivity toward the di-alkylation product, the amount of PF was increased, and the reaction

temperature was set to 70 °C, coherently with procedures found in literature for similar substrates[66]. This change led to quantitative conversions, followed by an increase in selectivity as the mono-chloromethylation product was not detected through ^{1}H NMR.

In an attempt to reduce the amount of wastewater produced, a brine solution was used as source of chloride ions, substituting HCl conc. with an equivalent amount of H_2SO_4 conc. in order to generate HCl *in-situ*. Given the much higher concentration of the solution, it was possible to reduce the Cl:PF ratio to 2. Surprisingly, the reaction afforded the desired product **Ia** (Figure 2.10) in almost quantitative conversion, albeit with significant unidentified impurities found through ^{1}H NMR analysis.

Eugenol's main challenge was to achieve control over the functionalization site. Mono-chloromethylation could only be achieved when sub-stoichiometric amounts of paraformaldehyde were employed, giving mixtures of products and undefined impurities, making ^{1}H NMR interpretation even harder. This phenomenon was attributed to polymerization reactions occurring on the highly activated aromatic ring. Therefore, acidity of the system was decreased allowing to avoid side-reactions, yielding usable products. The reaction selectively afforded product **IIIa** (Figure 2.10) when a large excess of alkylating agent was employed. The reaction mixture required the addition of an organic solvent, as the product stuck to the stirring bar forming a glue, halting further conversion. Among the reaction products, this proved to be the hardest to employ in the following amidation step due to its viscosity.

Reactions performed on guaiacol led to the production of resinous products which proved impossible to be identified by ^{1}H NMR due to random oligomerization. As for Eugenol, this behavior was attributed to both the activation of the aromatic ring which made the compound prone to electrophilic aromatic substitution and to the abundance of active sites. Therefore, some means of cleavable protection were made necessary to limit its reactivity. The acetylated derivative **IV** (Figure 2.10) was chosen due to ease of production. To our surprise, despite using sub-stoichiometric amounts of PF, only derivative **IVa** (Figure 2.10) was produced, with traces of the acetylated derivative still present in the reaction mixture. This led us to assume that a consistent part of guaiacol underwent degradation, while the remaining fraction took part in reaction, hence explaining the stoichiometry of the product. As for successive attempts to replicate the result, the PF:**IV** ratio was raised to 4.0, so to exploit the substrate reactivity, which led unambiguously to quantitative conversion to **IVa** (Figure 2.10).

As for *p*-cresol, its alkylation products are well-known. It is employed in electrophilic aromatic substitution for the production of antioxidants, namely di-*t*-butyl hydroxy toluene[67], and resol resins. On the other hand, its use to produce benzyl chlorides was not deeply explored, therefore we decided

to test it as a possible building block. Reactions went smoothly, as even in the first trials the compound showed high conversions to **Va**, reaching approximately 75%. Nonetheless, subsequent attempts were made to evaluate effects of reaction time, temperature and catalyst quantity, unfortunately giving no significant increase in conversion. Such behavior was attributed to the inherent heterogeneity of the reaction system, made of a liquid and a wax-like solid which tends to clot, therefore halting the reaction progression. Piceol proved to be a peculiar substrate, as it yielded two very different products depending on the reaction conditions, products **VIa** (Figure 2.10) and **VIam** (Figure 2.10). To the best of our knowledge, no reports of Piceol chloromethylation under standard reaction conditions were found. Therefore, we conducted a series of experiments in which we varied the ratio between alkylating agent and substrate, then temperature and reaction time. At first, we performed the reactions at room temperature with an excess of PF (1.5 eq) for 6 hours, resulting only in derivative **VIa** (Figure 2.10). An increase in the ratio (2.0 first, then 3.0), keeping temperature and reaction time constant, resulted in the same product. Temperature was then increased to 60 °C for the same reaction time, keeping the ratio at 2.0 leading to generation of traces of product **VIam** (Figure 2.10), observed in the ^{1}H NMR spectra. Increasing the ratio to 3.0 led to the same result, thus temperature was raised to 100 °C keeping reaction time at 6 h and ratio at 3.0. To our delight, only **VIam** (Figure 2.10) was formed so the reaction was further optimized decreasing the ratio to 2.5, the bare minimum, and the reaction time to 4 hours.

This procedure has been also described in Chapter 3, Section 3.4 for deactivated non-biobased phenols allowing to obtain the direct chloromethylation of tough substrate as nitro-phenols. These findings are going to be published soon, along with a modified Leuckart-Wallach reaction protocol, described in Section 2.5 (Experimental), used for further upgrading to the corresponding formamides, whose value and versatility were discussed in the beginning of this Section.

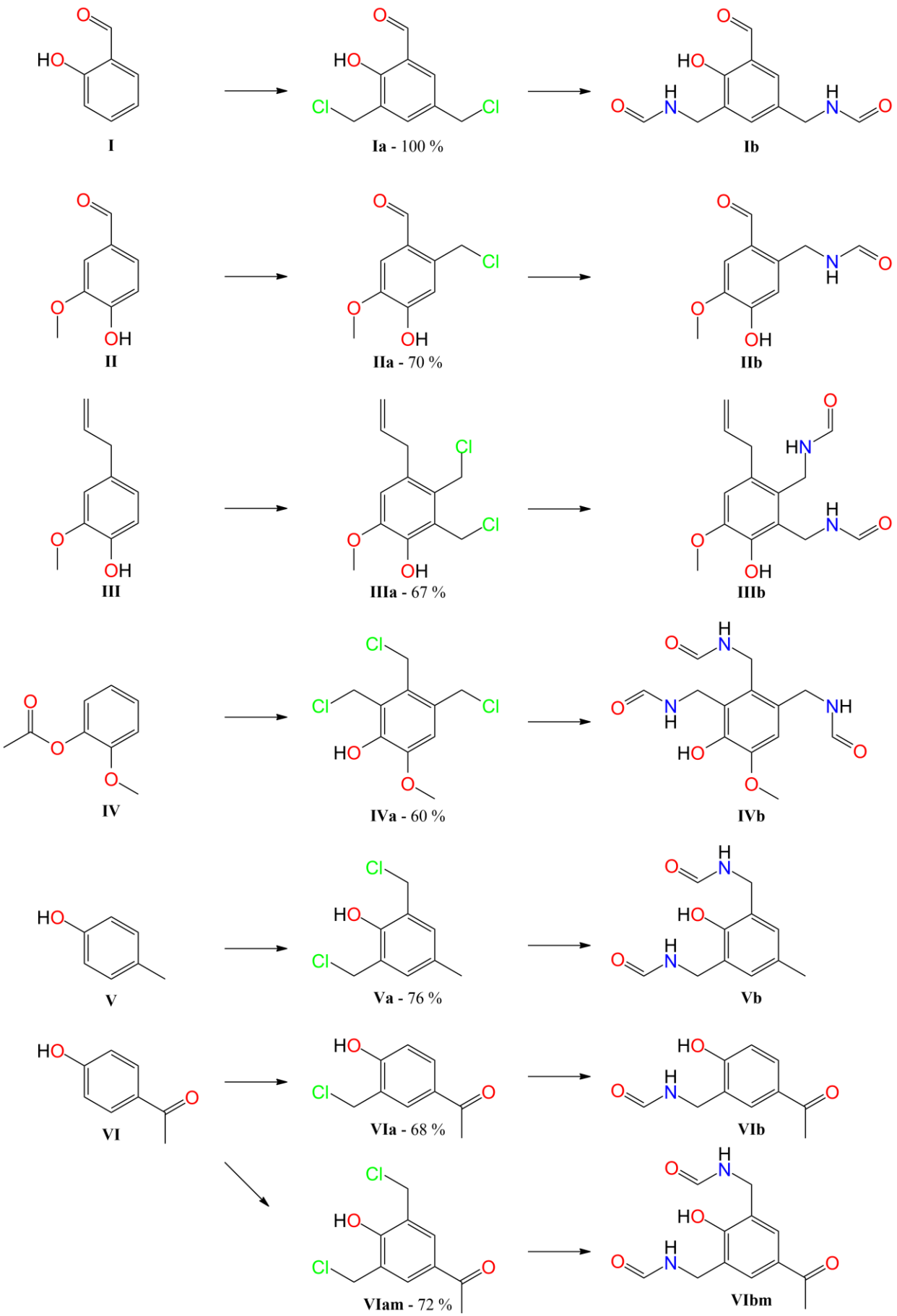

Figure 2.10: Schematic representation of phenols starting material and of the obtained benzyl chlorides and formamides products

2.4 Conclusion

In summary, the peroxide-bromide halogenation method, originally developed for the monobromination of benzenoid structures, has been extended to synthesize aryl-cored polybromides with high yield and optimal atom economy. This method, when used with light irradiation as halogen initiator, is capable of selectively convert xylene isomers and mesitylene into their corresponding benzyl bromides, regardless the presence of halogen atoms on the core. Moreover, under dark conditions, a modification of the same method allows the preparation of aryl polybromides through ring halogenation. The two variants, tested in a 10-gram scale, can be telescoped to achieve polybromo derivatives that features both core and side chain substitution, in high yield.

Furthermore, a series of chloro-methylated derivatives of a variety of bio-based phenolic compounds characterized by different functions on the aromatic ring were successfully synthesized with simple, straightforward procedures. Some of those compounds were unknown in literature and hold considerable potential as possible building blocks due to their versatility. These chloro-methylated derivatives were then successfully converted into the corresponding mono-, di- and tri-amides by a simple, fast and straightforward procedure, leading to the corresponding amides in quantitative yields.

2.5 Experimental

2.5.1 Materials and Methods

Solvents and reagents were commercial grade and used as received. ^{1}H NMR spectra were acquired with a Bruker Avance 400 spectrometer. The lighting was achieved by means of a standard household white LED bulb (OSRAM 6.5 W, 2700 K, 806 lm). The H_2O_2 solution was dispensed by means of a syringe pump, mod. SyringeOne NE-300, from NewEra Instruments. All the aryl-cored halides and some of the chloromethylated products here prepared are known, and thoroughly characterized in literature: **1a**, **2a**, **3a**[67]; **1b**, **3b**, **4b**[68]; **2b**, **3b**, **3c**[35]; **1c**[69]; **4a**[30]; **4c**[70]; **Ia**[71]; **IV**[72]; **Va**[53] and **VIa**[73].

2.5.2 General procedure for benzylic bromination

In a 15 mL Schlenk tube with screw cap, equipped with a magnetic stirring bar, the substrate (5 mmol, 1.0 equiv), solvent (either CH_2Cl_2 or chlorobenzene, 1.0–4.0 mL), H_2O (1.5 mL), and HBr (48 wt % aqueous solution, d = 1.49 g/mL, 1.25 mL, 11 mmol, 2.2 equiv) were inserted. The mixture was kept under stirring at rt and irradiated with a LED lightbulb placed at 10 cm from the side of the reaction tube. Aqueous H_2O_2 (35 wt % solution, d = 1.13 g/mL, 2.00 mL, 23.3 mmol, 4.7 equiv) was added over 2 h using a syringe pump, through a small PTFE tube inserted through the side arm of the Schlenk tube. After the addition was complete, the mixture was left under stirring for 1 h and 30 min. Once the mixture was neutralised with solid $NaHCO_3$, the product was extracted with CH_2Cl_2 (3 × 5 mL). The combined organic layers were concentrated to dryness to give the crude product.

2.5.3 General procedure for ring bromination

In a 25 mL round-bottomed flask, equipped with a magnetic stirring bar, the substrate (12 mmol, 1.0 equiv), H_2SO_4 (96 wt %, 3.00 g, 30 mmol, 2.5 equiv), I_2 (0.04 g, 0.16 mmol, 0.01 equiv), and CH_2Cl_2 (1.50 mL) were inserted. The flask, kept under stirring at room temperature (rt), was light-shielded with aluminium foil and a water-cooled condenser was installed on its top. A solution of NaBr (2.88 g, 28 mmol, 2.33 equiv) in H_2O_2 (35 wt % aqueous solution, 4.8 mL, 56 mmol, 4.67 equiv) was added to the mixture over 15 min with a syringe pump, through a PTFE tube inserted in the top of the condenser. The system was then refluxed for 48 h. Once cooled to rt, the reaction mixture was neutralised with solid $NaHCO_3$, and the product was extracted with CH_2Cl_2 (3 × 5 mL). The combined organic layers were concentrated to dryness to give the crude product.

2.5.4 General procedure for one-pot first-ring-then-benzylic bromination

In a 25 mL round-bottomed flask, equipped with a magnetic stirring bar, the substrate (12 mmol, 1.0 equiv), H_2SO_4 (96 wt %, 3.00 g, 30 mmol, 2.5 equiv), I_2 (0.04 g, 0.16 mmol, 0.01 equiv), and chlorobenzene (8.0 mL) were inserted at rt. The flask was shielded from light by means of an aluminium foil and a water-cooled condenser was installed on its top. Once the stirring was started, a solution of NaBr (2.88 g, 28 mmol, 2.33 equiv) in H_2O_2 (35 wt % aqueous solution, 4.8 mL, 56 mmol, 4.67 equiv) was added over 15 min through a PTFE tube inserted at the top of the condenser, by means of a syringe pump. The flask was then heated to 50 °C for 48 h, cooled to rt, and unwrapped. Under stirring at rt, H_2O (3.6 mL) and HBr (48 wt % aqueous solution, 3.00 mL, 26.5 mmol, 2.2 equiv) were inserted. The mixture was then irradiated with a LED lightbulb, placed at 10 cm from the side of the flask and aqueous H_2O_2 (35 wt % solution, 4.8 mL, 56 mmol, 4.7 equiv) was added over 2 h using a syringe pump, through a PTFE tube inserted at the top of the condenser. After the addition was complete, the mixture was left under stirring for 1 h and 30 min. The reaction mixture was then neutralised with solid NaHCO3 and the product was extracted with CH_2Cl_2 (3 × 10 mL). The combined organic layers were concentrated to dryness to give the crude product.

2.5.5 Characterization of brominated products

1,2-bis-bromomethyl-benzene (**1a**)[67]: white solid, yield: 98%, ^{1}H NMR (400 MHz, 298 K, $CDCl_3$): δ 7.37 (m, 2H), 7.31 (m, 2H), 4.67 (s, 4H) ppm.

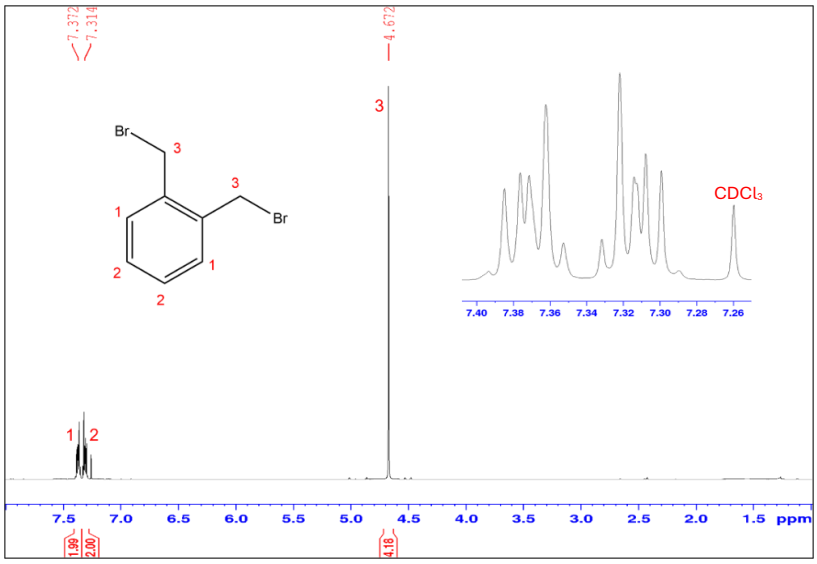

1,2-dibromo-4,5-dimethylbenzene (1b)[68]: brown solid, yield: 93%. ^{1}H NMR (400 MHz, 298 K, $CDCl_3$) δ 7.37 (s, 2H), 2.19 (s, 6H) ppm.

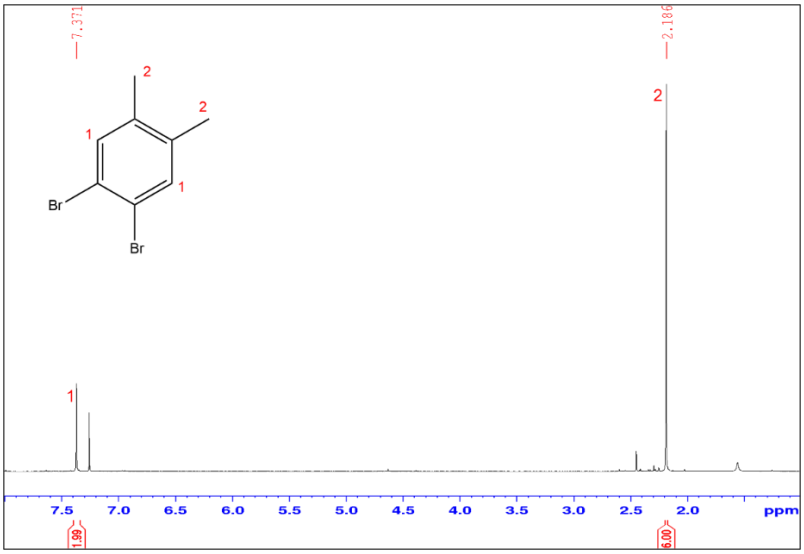

1,2-dibromo-4,5-bis(bromomethyl)benzene (1c)[69]: From **1b**: chlorobenzene (4.0 mL) was used as the solvent instead of CH_2Cl_2 (1 mL). Brown solid, yield: 86%. From **1** (two-step, one pot): Brown solid, yield: 82%. Recrystallisation from hot hexane gave the pure product. White solid, ^{1}H NMR (400 MHz, 298 K, $CDCl_3$): δ 7.62 (m, 2H), 4.53 (s, 4H) ppm.

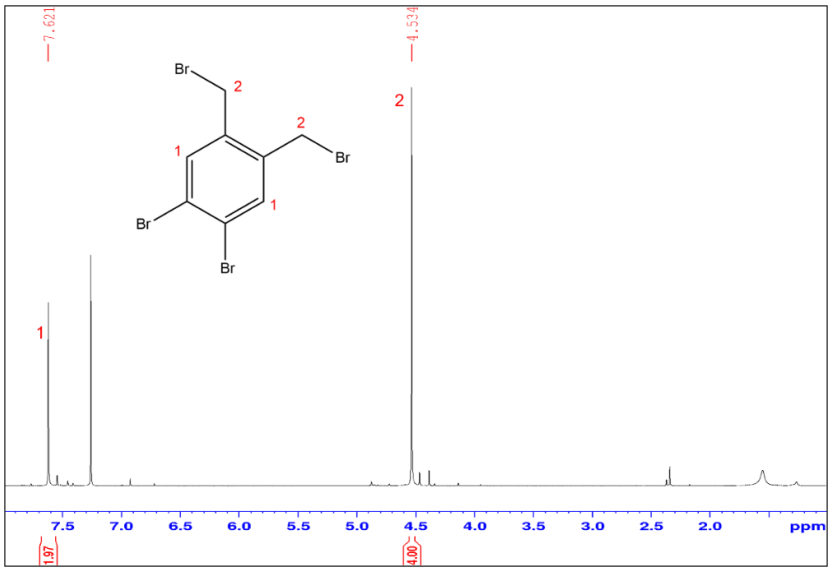

1,3-bis-bromomethyl-benzene (2a)[67]: Petroleum ether (1.5 mL) was used as the solvent instead of CH_2Cl_2. The reaction mixture was kept at 5 °C instead of rt and time was extended by 15% (2 h 20 min for H_2O_2 dropping and 2 h after the addition). The title product was obtained as pale-yellow solid,

yield: 73%. Recrystallisation from hot petroleum ether gave the pure product as white solid. ^{1}H NMR (400 MHz, 298 K, $CDCl_3$): δ 7.42 (m, 1H), 7.33 (m, 1H), 7.32 (m, 2H), 4.48 (s, 4H) ppm.

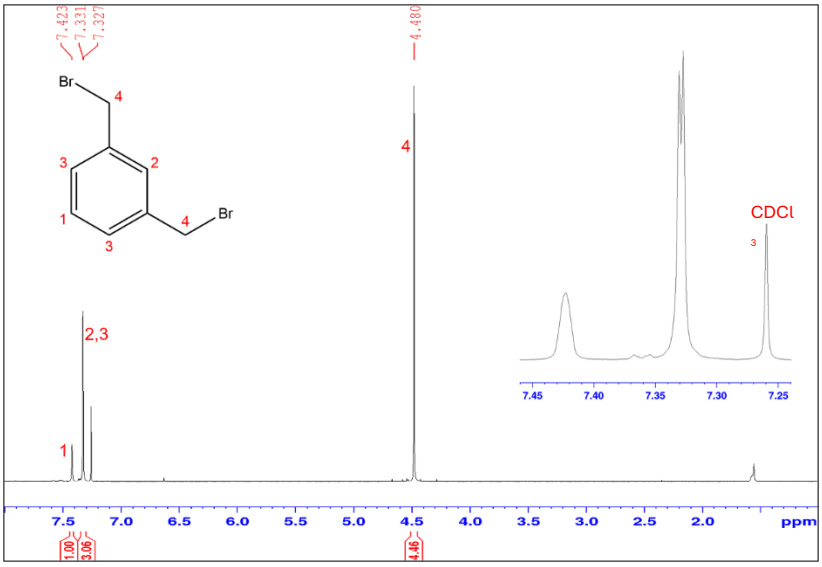

1,5-dibromo-2,4-dimethylbenzene (2b)[35]: Brown solid, yield: 87%. Recrystallisation from hot ethanol gave the pure product as pale-yellow solid. ^{1}H NMR (400 MHz, 298 K, $CDCl_3$): δ 7.68 (s, 1H), 7.10(s, 1H), 2.31 (s, 6H) ppm.

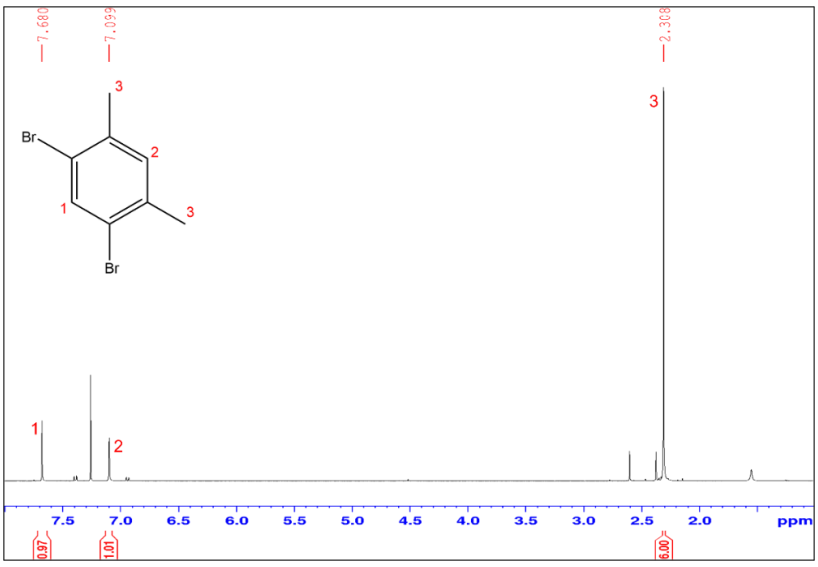

1,4-bis-bromomethyl-benzene (3a)[67]: White-yellowish solid, yield: 87%. Recrystallisation from hot toluene gave the pure product as white solid. ^{1}H NMR (400 MHz, 298 K, $CDCl_3$): δ 7.37 (s, 4H), 4.48 (s, 4H) ppm.

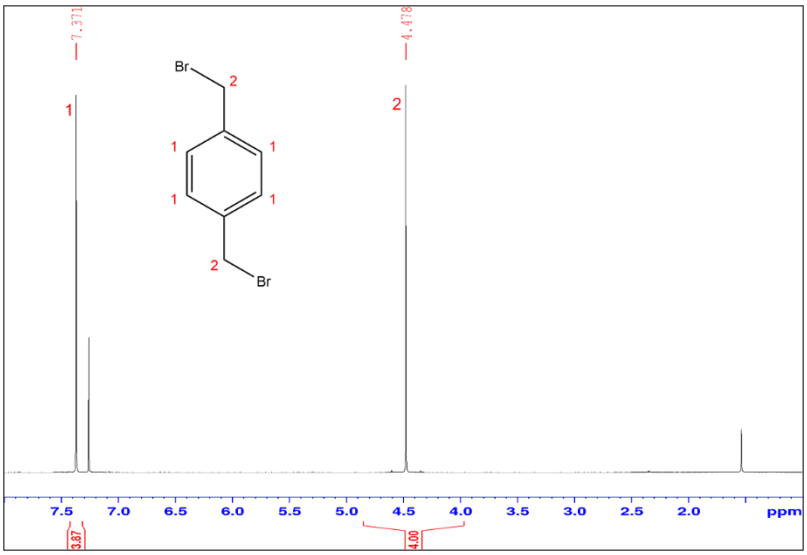

1,4-dibromo-2,5-dimethylbenzene (**3b**)[35][68]: pale orange solid, yield: quantitative. Recrystallisation from hot hexane gave the pure product as pale-yellow solid. ^{1}H NMR (400 MHz, 298 K, $CDCl_3$): δ 7.39 (s, 2H), 2.33 (s, 6H) ppm.

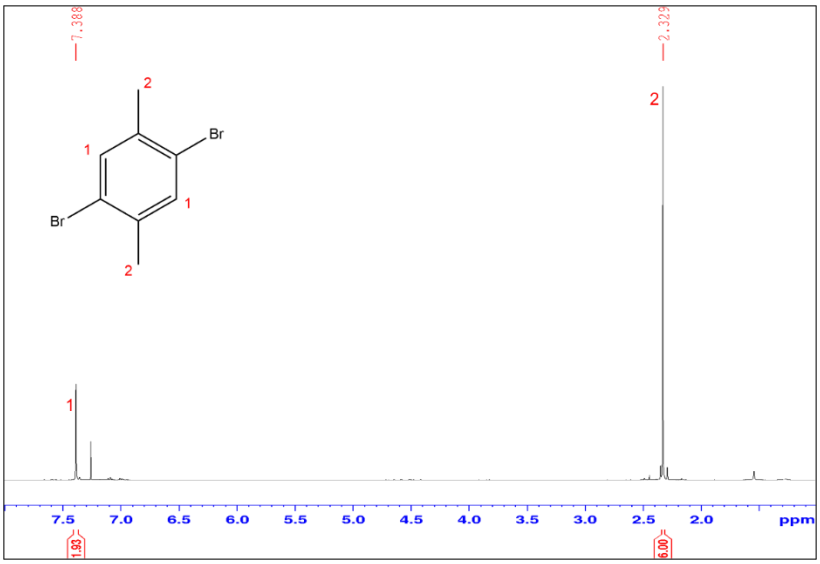

1,4-dibromo-2,5-bis(bromomethyl)benzene (**3c**)[35]: From **3b**: chlorobenzene (4.0 mL) was used as the solvent instead of CH_2Cl_2 (1.0 mL). Pale-yellow solid, yield: 94%. From **3** (two-step, one pot): yellow solid, yield 96%. Recrystallisation from hot petroleum ether gave the pure product as white solid.^{1}H NMR (400 MHz, 298 K, $CDCl_3$): δ 7.66 (s, 2H), 4.51 (s, 4H) ppm.

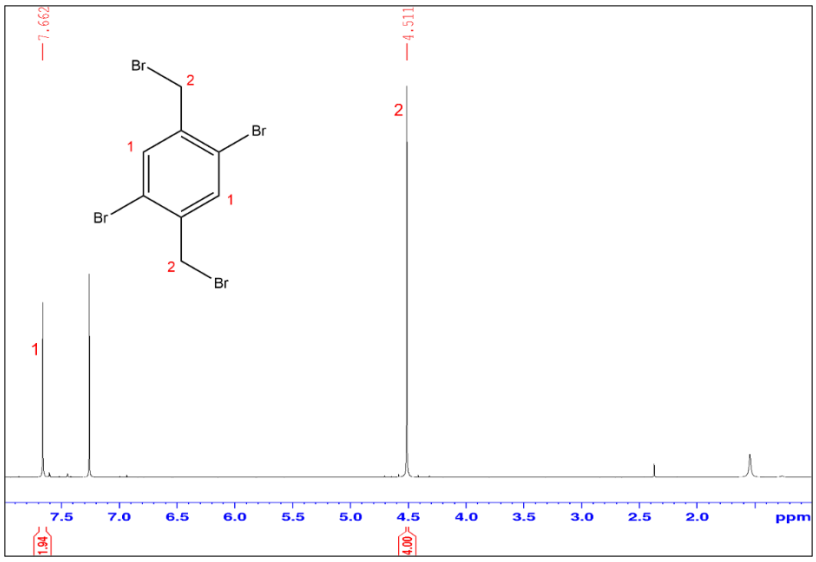

1,3,5-tris(bromomethyl)benzene (**4a**)[30]: The general procedure was adapted considering the three benzylic positions. In a 15 mL Schlenk tube with screw cap, equipped with a magnetic stirring bar, substrate **4** (5 mmol, 1.0 equiv), CH_2Cl_2 (2.0 mL), H_2O (2.0 mL), and HBr (48 wt % aqueous solution, d = 1.49 g/mL, 1.87 mL, 16.5 mmol, 3.3 equiv) were inserted. The mixture was kept under stirring at rt and irradiated with a LED lightbulb placed at 10 cm from the side of the reaction tube. Aqueous H_2O_2 (35 wt % solution, 3.0 mL, 23.3 mmol, 4.7 equiv) was added over 2 h using a syringe pump, through a small PTFE tube inserted through the side arm of the Schlenk. After the addition was complete, the mixture was left under stirring for 1 h and 30 min. Yield: 42%. The crude product was purified via column chromatography on silica gel 60, eluting with petroleum ether. The pure product appears as a white solid. ^{1}H NMR (400 MHz, 298 K, $CDCl_3$): δ 7.35 (s, 3H), 4.45 (s, 6H) ppm.

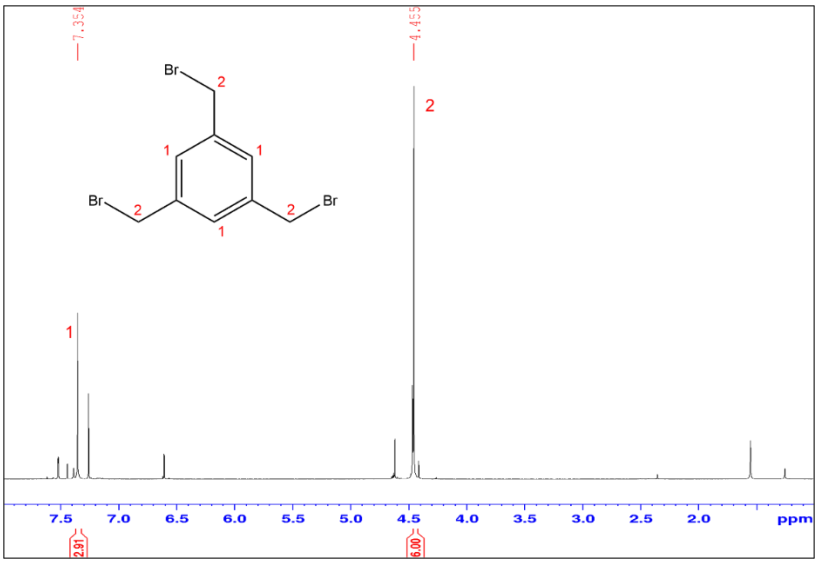

1,3,5-tribromo-2,4,6-trimethylbenzene (4b)[68]: The general procedure was adapted considering the three ring positions to be halogenated (3.5 equiv of NaBr were used instead of 2.33 equiv). The raw product appears as pale-yellow solid, yield: 89%. Recrystallisation from hot chloroform gave the pure product as white solid. ^{1}H NMR (400 MHz, 298 K, $CDCl_3$): δ 2.65 (s, 9H) ppm.

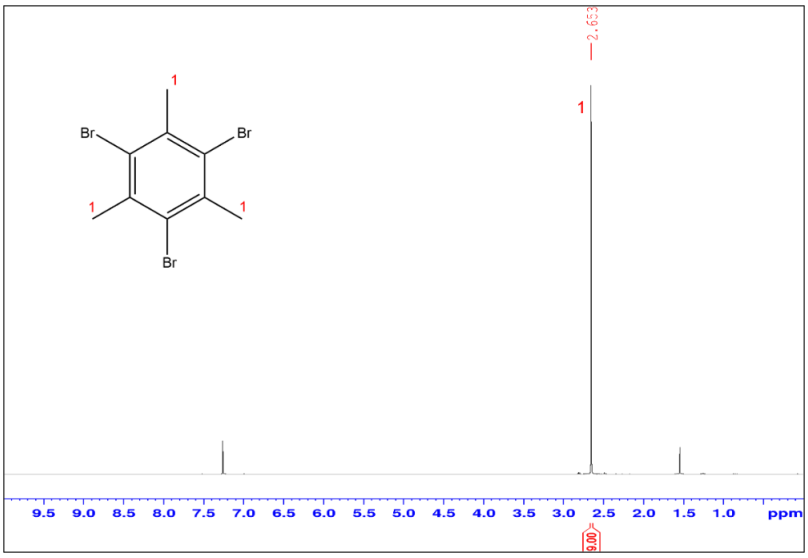

1,3,5-tribromo-2,4,6-tris(bromomethyl)benzene (4c)[70]: The general procedure was adapted considering the three ring and the three benzylic positions. From 4b: White solid, yield: 93%. From 4 (two-step, one pot): Pale yellow solid, yield 85%. ^{1}H NMR (400 MHz, 298 K, $CDCl_3$): δ 4.92 (s, 6H) ppm.

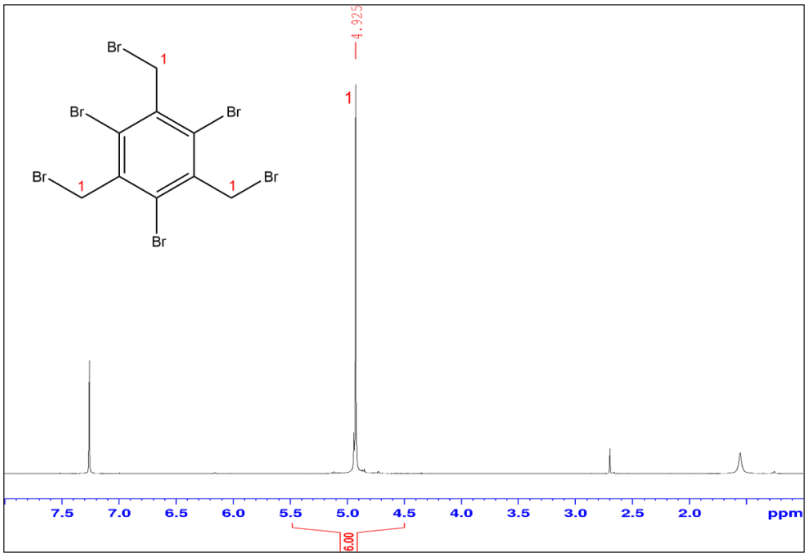

*2.5.6 Synthesis of **IV***[72]

The synthetic procedure was adapted from others found in the literature[72]. Guaiacol (2.20 mL, 20 mmol), AA (2.85 mL, 30 mmol) and TEA (3.07 mL, 22 mmol) were mixed at 0 °C, then the reaction mixture was brought to 60 °C inside an oil bath and left stirring for two hours. The reaction mixture was diluted with distilled water (10 mmol) and left stirring vigorously for 10 minutes. The reaction mixture was diluted with ethyl acetate (20 mL) and the organic phase was washed with a 2M H_2SO_4 acqueous solution (3 x 5 mL), 10 % m/v aq. $NaHCO_3$ solution (3x10 mL) and saturated NaCl acqueous solution (3 x 10 mL), then anhydrified over $MgSO_4$ and dried at the rotavapor. Pale yellow liquid, quantitative. *1H NMR (400 MHz, CDCl3) δ (ppm):* 7.20 (dd, *J* = 1.80; 7.50 Hz, 1H, Ar-*H*), 7.04 (dd, *J* = 1.68; 7.82 Hz, 1H, Ar-*H*), 6.96 (dd, 1.20 Hz, *J* = 8.17; 15.76; 2H, Ar-*H*), 3,83 (s, 3H, -OC*H₃*), 2,32 (s, 3H, -OC(=O)C*H₃*).

2.5.7 Synthesis of formiate/formamide mixture

The procedure was adapted from the literature[74]. Ammonium formate (10 g, 0.159 mol) was placed in a round bottom flask with a Dean-Stark apparatus mounted on top of it. It was heated up to 150 °C, then slowly to 180 °C. Collection of water was used to measure conversion, and the reaction was stopped when production reached 2,8 mL. The product was used as is.

*2.5.8 Synthesis of **Ia***[71]

I (1.221 g, 1.05 mL, 10 mmol), PF (750 mg, 25 mmol), HCl 37 % (17 mL, 0.2 mol) and H_2SO_4 96 % (1.0 g, 20 mmol) were poured into a sealed round bottom flask and left stirring overnight at 70 °C. The reaction product was extracted in EtOAc and the organic layer was thoroughly washed with $NaHCO_3$ solution (10 % m/v, 3 x 10 mL), and brine (3 x 10 mL) and the product was dried at the rotary evaporator. Pale pink solid, quantitative.

^{1}H NMR (400 MHz, $CDCl_3$) δ (ppm): 11.49 (s, 1H, Ar-OH), 9.91 (s, 1H, Ar-C(=O)H), 7.68 (d, 1H, *J* = 1.00, Ar–H), 7.59 (d, 1H, *J* = 0.99, Ar–H), 4.68 (s, 2H, Ar–oCH2-Cl), 4.59 (s, 2H, Ar–pCH2-Cl).

*2.5.9 Synthesis of **IIa***

II (1.512 g, 10 mmol), PF (360 mg, 12 mmol), HCl 37 % (6.5 mL, 96 mmol) and H_2SO_4 96 % (0.5 mL, 10 mmol) were poured into a sealed round bottom flask and left vigorously stirring for 6 hours at room temperature. The reaction product was filtered on a P3 glass filter and washed thoroughly with water. The product was dried *in vacuo* overnight at 50 °C. 70 %, brown solid.

^{1}H NMR (400 MHz, $CDCl_3$) δ (ppm): 9.84 (s, 1H, Ar-C(=O)H), 7.53 (s, 1H, Ar–H), 7.40 (s, 1H, Ar–H), 6.43 (s, 1H, Ar–OH), 4.72 (s, 2H, Ar–CH2-Cl), 3.99 (s, 3H, O-CH3).

*2.5.10 Synthesis of **IIIa***

III (1.642 g, 1,54 mL, 10 mmol), PF (900 mg, 30 mmol), HCl 37 % (20 mL, 0.24 mol) and CH_2Cl_2 (2 mL) were poured into a sealed round bottom flask and left vigorously stirring at room temperature for 4 hours. The reaction product was extracted in EtOAc and the organic layer was thoroughly washed with $NaHCO_3$ solution (10 % m/v, 3 x 10 mL), and brine (3 x 10 mL) and the product was dried at the rotary evaporator giving a viscous black liquid in a 67 % yield.

^{1}H NMR (600 MHz, $CDCl_3$) δ (ppm): 6.91 (s, H, mOCH_3), 6.68 (s, H, pOCH_3), 6.67 (s, H, oOCH_3), 4.87 (s, H, Ar-CH_2-Cl), 4.74 (s, H, Ar-CH_2-Cl), 4.54 (s, H, Ar-CH_2-Cl).

*2.5.11 Synthesis of **IVa***

IV (0.322 g, 2 mmol), PF (240 mg, 8 mmol), HCl 37 % (5.4 mL, 64 mmol) and CH_2Cl_2 (0.5 mL) were poured into a sealed round bottom flask and left vigorously stirring at 40 °C for 6 hours. The reaction product was extracted in EtOAc and the organic layer was thoroughly washed with $NaHCO_3$ solution (10 % m/v, 3 x 10 mL), and brine (3 x 10 mL) and the product was dried at the rotary evaporator. It presented itself as a dark brown/black liquor which crystallized overnight in 60 % yield.

^{1}H NMR (400 MHz, $CDCl_3$) δ (ppm): 6.87 (s, H, oOCH_3), 6.03 (s, H, OH), 4.85 (s, H, Ar-CH_2-Cl), 4.84 (s, H, Ar-CH_2-Cl), 4.68 (s, H, Ar-CH_2-Cl), 3.93 (s, H, OCH_3).

*2.5.12 Synthesis of **Va***[53]

V (1.08 g, 10 mmol), PF (660 mg, 22 mmol), HCl 37% (5.4 mL, 64 mmol) and CH_2Cl_2 (0.5 mL) were poured into a sealed round bottom flask and left vigorously stirring at 40 °C for 6 hours. The

reaction product was extracted in EtOAc and the organic layer was thoroughly washed with $NaHCO_3$ solution (10 % m/v, 3 x 10 mL), and brine (3 x 10 mL) and the product was dried at the rotary evaporator. White waxy solid, 76 %.

^{1}H NMR (600 MHz, $CDCl_3$) δ (ppm): 7.09 (s, 2H, mAr-H), 4.66 (s, 4H, Ar-CH_2-Cl), 2.28 (s, 3H, Ar-CH_3).

*2.5.13 Synthesis of **VIa***[73]

VI (1.362 g, 10 mmol), PF (360 mg, 12 mmol), HCl 37 % (6.5 mL, 96 mmol) and H_2SO_4 96% (0.25 mL, 5 mmol) were poured into a sealed round bottom flask and left vigorously stirring for 6 hours at room temperature. The reaction product was filtered on a P3 glass filter and washed thoroughly with water. The product was dried *in vacuo* overnight at 50 °C. 68 %, coral pink solid.

^{1}H NMR (600 MHz, $CDCl_3$) δ (ppm): 7.95 (d, 1,8 Hz, 1H, Ar-H), 7.88 (dd, J = 2.10; 8.44 Hz, 1H, Ar-H), 6.91 (d, J = 8.39 Hz, 1H, Ar-H), 5.81 (s, 1H, Ar-OH), 4,70 (s, 2H, Ar-CH_2-Cl) e 2.57 (s, 3H, Ar-C(O)CH_3);

*2.5.14 Synthesis of **VIam***

VI (1.362 g, 10 mmol), PF (750 mg, 25 mmol), HCl 37 % (13 mL, 0.2 mol) and sulfuric acid 96% (0.25 mL, 5 mmol) were poured into a sealed round bottom flask and left vigorously stirring for 6 hours at room temperature. The reaction product was filtered on a P3 glass filter and washed thoroughly with water. The product was dried *in vacuo* overnight at 50 °C. 72 %, magenta solid.

^{1}H NMR (400 MHz, $CDCl_3$) δ (ppm): 7.93 (s, 2H, Ar-H), 6.28 (s, 1H, Ar-OH), 4.72 (s, 4H, Ar-CH_2-Cl) e 2.58 (s, 3H, Ar-C(O)CH_3);

2.5.15 Typical synthesis of amide derivatives

The proper chloro-methylated derivative (10 mmol) was dissolved in 10 mL of THF and added dropwise to 4 equivalents of formamide in the case of **IIb**, 8 equivalents for **Ib**, **IIIb**, **Vb** and **VIb**, and 12 equivalents for **IVb** kept at 60 °C. The reaction temperature was raised to reflux and left stirring for 30 minutes. It was then washed with brine (3 x 10 mL), dried over sodium sulfate and the solvent was eliminated at the rotavapor yielding the desired product quantitatively.

2.5.16 Characterization of amide derivatives

Ib: ^{1}H NMR (400 MHz, $CDCl_3$) δ (ppm): 11.43 (s, 1H, Ar-OH), 9.92 (s, 1H, Ar-C(=O)H), 8.17 (s, H, o-N-C(=O)H), 8.13 (s, H, pC-N-C(=O)H), 7.65 (d, 1H, J = 1.00, Ar–H), 7.61 (d, 1H, J = 0.99, Ar–H), 5.31 (s, 2H, Ar–oCH2-N), 5.19 (s, 2H, Ar–pCH2-N).

IIb: ^{1}H NMR (400 MHz, $CDCl_3$) δ (ppm): 9.84 (s, 1H, Ar-C(=O)H), 8.17 (s, 1H, N-C(=O)H), 7.51 (d, 1H, Ar–H), 7.42 (d, 1H, Ar–H), 6.47 (s, 1H, Ar–OH), 5,33 (s, 2H, Ar–CH2-N), 3.99 (s, 3H, O-CH3).

IIIb: ^{1}H NMR (400 MHz, $CDCl_3$) δ (ppm): 8.10 (s, 2H, N-C(=O)H), 8.06 (t, H, N-C(=O)H), 5.43 (s, 2H, Ar-CH_2-N), 5.28 (d, 2H, Ar-CH_2-N), 5.12 (s, 2H, Ar-CH_2-N).

IVb: ^{1}H NMR (400 MHz, $CDCl_3$) δ (ppm): 8.10 (s, 2H, N-C(=O)H), 8.06 (s, 1H, N-C(=O)H), 5.43 (s, 2H, Ar-CH_2-N), 5.28 (s, 2H, Ar-CH_2-N), 5.12 (s, 2H, Ar-CH_2-N).

Vb: ^{1}H NMR (400 MHz, $CDCl_3$) δ (ppm): 8.13 (s, 2H, N-C(=O)H), 7.70 (s, 1H, Ar-OH), 7.14 (s, 2H, Ar-H), 5.22 (s, 4H, Ar-CH_2-N) e 2.28 (s, 3H, Ar-CH_3).

VIb: ^{1}H NMR (400 MHz, $CDCl_3$) δ (ppm): 8.16 (s, 1H, N-C(=O)H), 7.96 (d, J = 2.40 Hz, 1H, Ar-H), 7.88 (dd, J = 2.16; 8.53 Hz, 1H, Ar-H), 6.97 (d, J = 8.50 Hz, 1H, Ar-H), 5.27 (s, 2H, Ar-CH_2-N) e 2.56 (s, 3H, Ar-C(O)CH_3);

VIbm: ^{1}H NMR (400 MHz, $CDCl_3$) δ (ppm):8.16 (s, 2H, N-C(=O)H), 7.98 (s, 2H, Ar-H), 5,28(s, 4H, Ar-CH_2-Cl) e 2.57 (s, 3H, Ar-C(O)CH_3).

2.6 Bibliography

[1] S. Nikafshar, O. Zabihi, S. Hamidi, Y. Moradi, S. Barzegar, M. Ahmadi, M. Naebe, *RSC Adv.* **2017**, *7*, 8694–8701.

[2] M. Fache, B. Boutevin, S. Caillol, *Green Chem.* **2016**, *18*, 712–725.

[3] K. E. Simmons, R. D. Minard, J. Bollag, *Soil Science Society of America Journal* **1988**, *52*, 1356–1360.

[4] S. Ishihara, Y. Furuki, J. P. Hill, K. Ariga, S. Takeoka, *J. Nanosci. Nanotechnol.* **2014**, *14*, 5130–5137.

[5] T. Wöhrle, I. Wurzbach, J. Kirres, A. Kostidou, N. Kapernaum, J. Litterscheidt, J. C. Haenle, P. Staffeld, A. Baro, F. Giesselmann, S. Laschat, *Chem. Rev.* **2016**, *116*, 1139–1241.

[6] S.-F. Koelewijn, D. Ruijten, L. Trullemans, T. Renders, P. Van Puyvelde, H. Witters, B. F. Sels, *Green Chem.* **2019**, *21*, 6622–6633.

[7] Y. F. Sasaki, A. Saga, M. Akasaka, S. Ishibashi, K. Yoshida, Y. Q. Su, N. Matsusaka, S. Tsuda, *Mutation Research/Genetic Toxicology and Environmental Mutagenesis* **1998**, *419*, 13–20.

[8] *European Commission; Directorate-General for Communication; European Green Deal – Delivering on Our Targets. Publications Office of the European Union: 2021. Https://Data.Europa.Eu/Doi/10.2775/373022*.

[9] R. Bruckner, Radical Halogenation of Hydrocarbons. In Organic Mechanisms Reactions Stereochemistry and Synthesis, **2010**, Harmata, M., Ed.; Springer: Berlin, Heidelberg,.

[10] Compare, for Example, the SDS of Benzyl Chloride with That of Benzyl Bromide. Source: Sigma-Aldrich® Site. SDS Are up to Date at 05/12/2023. Https://Www.Sigmaaldrich.Com/IT/Ru/Sds/Aldrich/185558?UserType=undefined, Https://Www.Sigmaaldrich.Com/IT/En/Sds/Aldrich/B17905?UserType=undefined.

[11] M. Sun, G. V. Lowry, K. B. Gregory, *Water Res.* **2013**, *47*, 3723–3731.

[12] Bruckner, R. Ar-SE Reactions via Sigma Complexes: Individual Reactions. In Organic Mechanisms Reactions Stereochemistry and Synthesis; Harmata, M., Ed.; Springer: Berlin, Heidelberg, 2010; Pp 215–233.

[13] N. Tang, X. Song, T. Yang, R. Qiu, S.-F. Yin, *J. Organomet. Chem.* **2021**, *942*, 121820.

[14] Z. Xie, B. Yang, L. Liu, M. Li, D. Lin, Y. Ma, G. Cheng, S. Liu, *J. Phys. Org. Chem.* **2005**, *18*, 962–973.

[15] J. A. Mikroyannidis, *Macromolecules* **2002**, *35*, 9289–9295.

[16] F. Roncaglia, A. Ughetti, N. Porcelli, B. Anderlini, A. Severini, L. Rigamonti, *Beilstein Journal of Organic Chemistry* **2024**, *20*, 1076–1087.

[17] I. Saikia, A. J. Borah, P. Phukan, *Chem. Rev.* **2016**, *116*, 6837–7042.

[18] W. C. Bray, R. S. Livingston, *J. Am. Chem. Soc.* **1923**, *45*, 1251–1271.

[19] Leulier, A. Bull. Soc. Chim. Fr. 1924, 35, 1325–1330.

[20] A. Amati, G. Dosualdo, L. Zhao, A. Bravo, F. Fontana, F. Minisci, H.-R. Bjørsvik, *Org. Process. Res. Dev.* **1998**, *2*, 261–269.

[21] Eur. Pat. Appl. EP0336567A1, Oct 11, 1989.

[22] R. Mestres, J. Palenzuela, *Green Chem.* **2002**, *4*, 314–316.

[23] A. Podgoršek, S. Stavber, M. Zupan, J. Iskra, *Tetrahedron Lett.* **2006**, *47*, 7245–7247.

[24] A. Podgoršek, S. Stavber, M. Zupan, J. Iskra, *Tetrahedron* **2009**, *65*, 4429–4439.

[25] H. H. L. B. Lima, G. R. da Silva, J. M. Pena, R. Cella, *ChemistrySelect* **2017**, *2*, 9624–9627.

[26] A. Podgoršek, M. Zupan, J. Iskra, *Angew Chem. Int. Ed.* **2009**, *48*, 8424–8450.

[27] E. F. M. Stephenson, *Organic Syntheses* **1954**, *34*, 100.

[28] G. S. Pearson, R. S. Magee, *Pure and Applied Chemistry* **2002**, *74*, 187–316.

[29] H. Shaw, H. D. Perlmutter, C. Gu, S. D. Arco, T. O. Quibuyen, *J Org Chem* **1997**, *62*, 236–237.

[30] G. R. Newkome, Zhongqi. Yao, G. R. Baker, V. K. Gupta, P. S. Russo, M. Jane. Saunders, *J Am Chem Soc* **1986**, *108*, 849–850.

[31] D. M. Tal, S. J. D. Karlish, *Tetrahedron* **1995**, *51*, 3823–3830.

[32] J. Li, D. Liu, Y. Li, C.-S. Lee, H.-L. Kwong, S. Lee, *Chemistry of Materials* **2005**, *17*, 1208–1212.

[33] Q. Shang, T. Zeng, K. Gao, N. Liu, Q. Cheng, G. Liao, Z. Pan, H. Zhou, *New Journal of Chemistry* **2019**, *43*, 16595–16603.

[34] X. Yang, D. Liu, Q. Miao, *Angew Chem. Int. Ed.* **2014**, *53*, 6786–6790.

[35] M. C. Bonifacio, C. R. Robertson, J.-Y. Jung, B. T. King, *J. Org. Chem.* **2005**, *70*, 8522–8526.

[36] M. Naresh, M. Arun Kumar, M. Mahender Reddy, P. Swamy, J. Nanubolu, N. Narender, *Synthesis (Stuttg)* **2013**, *45*, 1497–1504.

[37] J. K. Kajorinne, J. C. M. Steers, M. E. Merchant, C. D. MacKinnon, *Can. J. Chem.* **2018**, *96*, 1087–1091.

[38] P. V. Vyas, A. K. Bhatt, G. Ramachandraiah, A. V. Bedekar, *Tetrahedron Lett.* **2003**, *44*, 4085–4088.

[39] F. Sabuzi, G. Pomarico, B. Floris, F. Valentini, P. Galloni, V. Conte, *Coord. Chem. Rev.* **2019**, *385*, 100–136.

[40] H. Dai, Z.-B. Cai, Q.-X. Lou, S.-L. Li, Y.-P. Tian, *Tetrahedron* **2021**, *96*, 132359.

[41] M. Auffray, F. Charra, L. Sosa Vargas, F. Mathevet, A.-J. Attias, D. Kreher, *New Journal of Chemistry* **2020**, *44*, 7665–7674.

[42] Z.-J. Jiang, S.-Y. Zhong, Y.-H. Chen, Q. Liao, M.-J. Lin, *Dyes and Pigments* **2024**, *227*, 112158.

[43] W. Fu, J. Tian, Y. Ding, X. Wang, M. Wang, Z. Wang, *Org. Lett.* **2024**, *26*, 2546–2551.

[44] S. Moulay, *Des Monomers Polym.* **2011**, *14*, 179–220.

[45] G. Grassi-Cristaldi and C. Maselli, Gazz. Chim. Ital. 28, 477 (1898).

[46] H. Stephen, W. F. Short, G. Gladding, *J. Chem. Soc., Trans.* **1920**, *117*, 510–527.

[47] G. L. Blanc, Sur La Préparation de Dérivés Chlorométhyléniques Aromatiques. Bulletin de La Société Chimique de France. Série 4. (1923) 33: 313–319.

[48] R. Quelet, Preparation d'un Derive Chloro-Methyl Du Para-Bromo-Anisol Methoxy-2 Bromo-2 α-Chlorotoluene). Compt. Rend. (1932) (T195): 155.

[49] K. K. Laali, in *Encyclopedia of Reagents for Organic Synthesis*, John Wiley & Sons, Ltd, Chichester, UK, **2001**.

[50] P. R. Sarika, P. Nancarrow, A. Khansaheb, T. Ibrahim, *Polymers (Basel)* **2020**, *12*, 2237.

[51] L. Zhu, P. Cheng, Z. Xiao, C. Lu, B. Li, X. Jiang, Z. Shen, N. Qian, W. Zhong, Y. He, *Chemical Engineering Journal* **2024**, *481*, 148359.

[52] H. Jin, X. Chen, C. Qian, X. Ge, S. Zhou, *European J. Org. Chem.* **2021**, *2021*, 3403–3406.

[53] N. Iranpoor, F. Panahi, *Org. Lett.* **2015**, *17*, 214–217.

[54] S. Kar, M. Rauch, A. Kumar, G. Leitus, Y. Ben-David, D. Milstein, *ACS Catal.* **2020**, *10*, 5511–5515.

[55] M. Bhunia, S. R. Sahoo, A. Das, J. Ahmed, S. P., S. K. Mandal, *Chem. Sci.* **2020**, *11*, 1848–1854.

[56] P. V. Ramachandran, A. A. Alawaed, A. Singh, *Molecules* **2023**, *28*, 4575.

[57] J. Li, C. Huang, D. Wen, Q. Zheng, B. Tu, T. Tu, *Org. Lett.* **2021**, *23*, 687–691.

[58] J. Bruffaerts, N. von Wolff, Y. Diskin-Posner, Y. Ben-David, D. Milstein, *J. Am. Chem. Soc.* **2019**, *141*, 16486–16493.

[59] T. M. Townsend, W. H. Bernskoetter, N. Hazari, B. Q. Mercado, *ACS Catal.* **2021**, *11*, 10614–10624.

[60] A. E. Owen, A. Preiss, A. McLuskie, C. Gao, G. Peters, M. Bühl, A. Kumar, *ACS Catal.* **2022**, *12*, 6923–6933.

[61] C. R. Langsted, S. W. Paulson, B. H. Bomann, S. Suhail, J. A. Aguirre, E. J. Saumer, A. R. Baclasky, K. H. Salmon, A. C. Law, R. J. Farmer, C. J. Furchtenicht, D. S. Stankowski, M. L.

Johnson, L. G. Corcoran, C. C. Dolan, M. J. Carney, N. J. Robertson, *J. Appl. Polym. Sci.* **2022**, *139*.

[62] K. A. Waibel, D. Barther, T. Malliaridou, D. Moatsou, M. A. R. Meier, *European J. Org. Chem.* **2021**, *2021*, 4508–4516.

[63] F. Yan, Z. Huang, C.-X. Du, J.-F. Bai, Y. Li, *J. Catal.* **2021**, *395*, 188–194.

[64] K. Ishihara, K. Ishihara, Y. Tanaka, T. Shioiri, M. Matsugi, *Tetrahedron* **2022**, *108*, 132642.

[65] H. Li, H. Wu, H. Zhang, Y. Su, S. Yang, E. J. M. Hensen, *ChemSusChem* **2019**, *12*, 3778–3784.

[66] Q. Wang, C. Wilson, A. J. Blake, S. R. Collinson, P. A. Tasker, M. Schröder, *Tetrahedron Lett.* **2006**, *47*, 8983–8987.

[67] K. Kondamudi, P. Elavarasan, P. J. Dyson, S. Upadhyayula, *J. Mol. Catal. A Chem.* **2010**, *321*, 34–41.

[68] A. Bose, P. Mal, *Tetrahedron Lett.* **2014**, *55*, 2154–2156.

[69] J. M. Rivera, T. Martín, J. Rebek, *J. Am. Chem. Soc.* **2001**, *123*, 5213–5220.

[70] G. Hennrich, V. M. Lynch, E. V. Anslyn, *Chemistry - A European Journal* **2002**, *8*, 2274.

[71] A. T. Carpenter, R. F. Hunter, *Journal of the Chemical Society (Resumed)* **1954**, 2731.

[72] Y. Takashima, Y. Isogawa, A. Tsuboi, N. Ogawa, Y. Kobayashi, *Org. Biomol. Chem.* **2021**, *19*, 9906–9909.

[73] T. Yanagi, K. Kikuchi, H. Takeuchi, T. Ishikawa, T. Nishimura, I. Yamamoto, *Chem. Pharm. Bull. (Tokyo)* **2001**, *49*, 1018–1023.

[74] F. Pietrucci, A. M. Saitta, *Proceedings of the National Academy of Sciences* **2015**, *112*, 15030–15035.

Chapter 3

3. Synthesis and characterization of triphenolamines ligands and of their Vanadium complexes

3.1 Introduction

Among the previously described depolymerization techniques (Chapter 1) we decided to work on catalytic oxidative cleavage, focalizing on homogeneous catalysts. The most studied homogeneous catalysts for oxidative cleavage are salen-type complexes, metalloporphyrins and oxovanadium complexes. These are usually studied on model compounds or on isolated native lignin, as technical lignin coming from pulping processes is too recalcitrant to oxidation. Salen-type complexes (Figure 3.1) are a class of complexes made by a bis-Schiff's base chelating ligand and a metal.

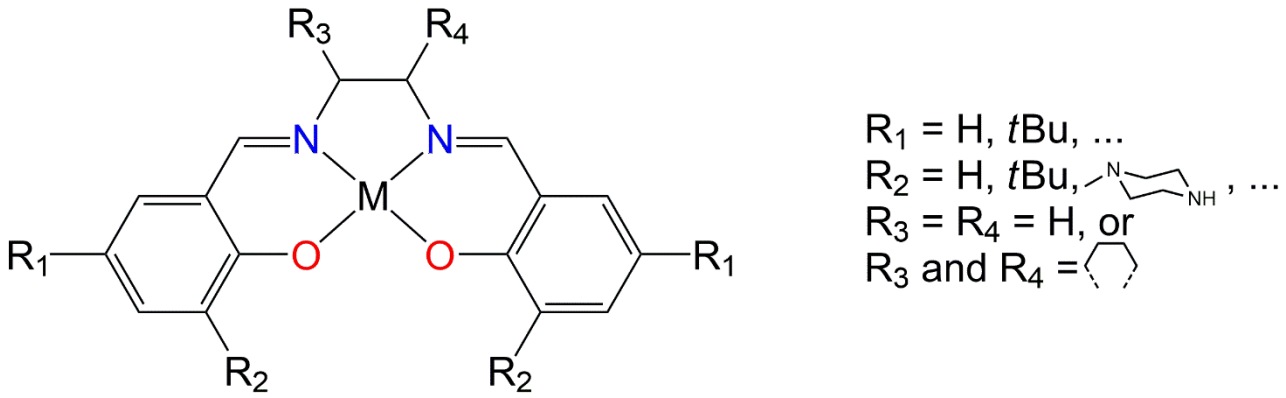

Figure 3.1: General structure of a Salen-type complex

The most studied are Co complexes[1–4] but also V[5,6], Mn[4,7], Cu[4,8], Fe[4] found some space. Their activity is influenced by many parameters such as the amount of carbohydrates present in the system[9], oxygen[10] and NaOH[11] concentration, the presence of nitrogen axial ligands like imidazoles[12] or pyridine[13].

Synthetic metalloporphyrins are usually designed to mimic enzymes activity, their properties can be modulated modifying R_1 and R_2 substituents[14] (Figure 3.2).

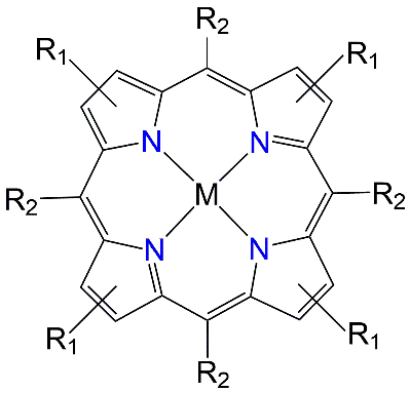

Figure 3.2: General structure of a metalloporphyrin complex

The most investigated are Fe- and Mn-porphyrins[14–16] whose activity can be tuned modifying the reaction medium ranging from aqueous buffer solutions to organic solvents[15,16]. These catalysts react with the oxidant, usually O_2 or H_2O_2, to form highly oxidized metallo-oxo complexes which then proceed to oxidize the substrate.

Oxovanadium complexes generally work using oxygen or air as oxidants giving many possible products. Selectivity and reactivity can be changed modifying ligand structure and/or substituents[17]. Many ligands have been studied, some of the most popular complexes are shown in Figure 3.3

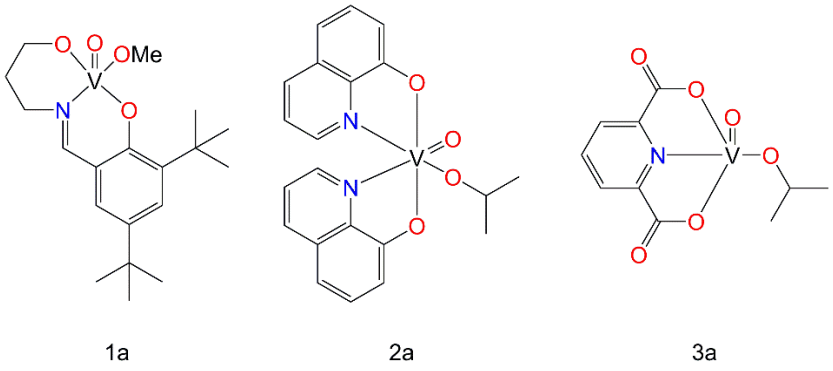

Figure 3.3: Representation of most studied VO complexes

As an example of different selectivity according to the ligand structure, complex 1a catalyzes the cleavage of both phenolic and non-phenolic *β*-O-4 model compounds, giving aryl enones[17,18]. Complex 2a showed a really different selectivity oxidizing non-phenolic to C_α ketones, while the phenolic analogues were converted to *p*-quinones[17,18]. Finally, complex 3a catalyze oxidation of non-phenolic to a complicate mixture of C_α ketones, aryl enones and aromatic acids, while phenolic substrates were converted into C_γ aldehydes[19].

In this PhD Thesis we decided to focalize on a class of oxovanadium complexes in our opinion understudied for oxidative cleavage, oxovanadium aminotriphenolates (VOTPA) (Figure 3.4) that performed well in C–C cleavage of vicinal diols under aerobic conditions[20].

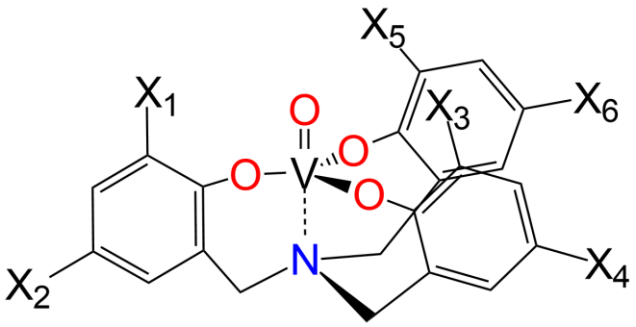

Figure 3.4: Generic VOTPA complex

TPA complexes have been synthesized with many different metals, basically from each transition group. The two mostly studied are surely Ti and V complexes, even if also Zr, Hf, Cr, Mo and W are reported[21]. Ti TPA complexes can be used as catalysts in many different applications[21]:

- Oxygen atom transfer in sulfoxidation of different substrates,
- C–C bond formation working as a Lewis acid in Diels-Alder, syn aldol, allylation and alkylation reactions,
- Deprotection of ethers, acetals and carbamates and ring-opening of epoxides,
- Ethylene polymerization, ligand structure influences obtained polymers average molecular weight and distribution,

V TPA complexes are used in many reactions, mainly in oxidation and halogenation, such as sulfoxidations, epoxidations[22] and epoxide coupling with CO_2[23], electrophilic brominations and chlorinations[24], finally, as stated before, they are active in C–C oxidative cleavage[20]. V TPA can be used too for ethylene polymerization[25] giving similar results to Ti catalysts. Vanadium in TPA complexes is usually coordinated as oxo-V^{+5}, these complexes are typically synthetized adding the precursor $VO(OiPr)_3$ directly to the desired ligand. Ligands can be differently substituted, modifying complexes electronic properties and allowing to tune catalysts reactivity. V^{+4}[26] and V^{+3}[24] complexes can be obtained from VCl_3 and a base, but they are usually extremely air sensitive going to the oxo-V^{+5} form immediately when exposed to air.

The proposed mechanism for C–C bond oxidative cleavage with VOTPA complexes [20] (Figure 3.5) can be summarized in the following steps: diol deprotonation and water formation, followed by C–C bond cleavage and reduction from V^{+5} to V^{+3} and finally restoration of the V^{+5} complex mediated by O_2.

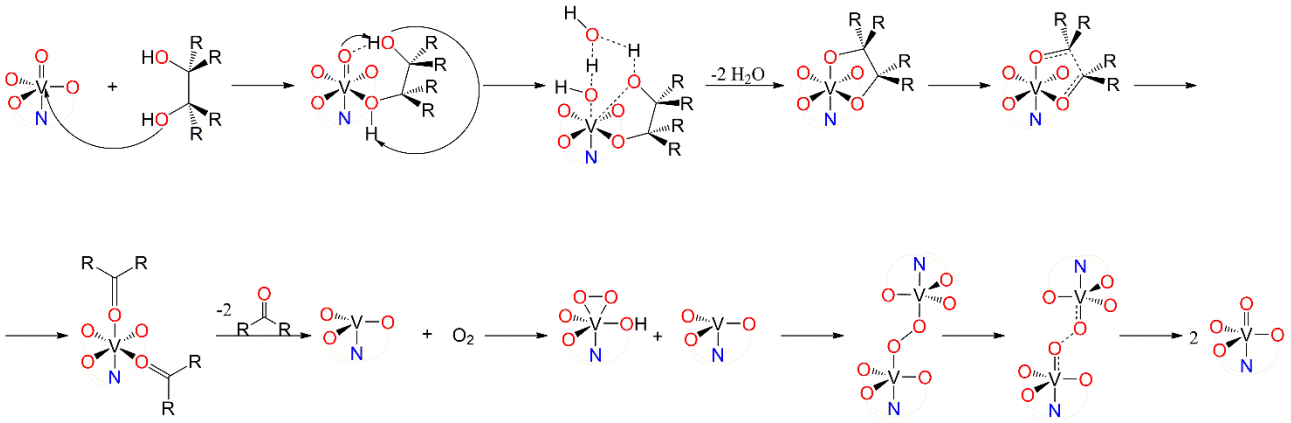

Figure 3.5: Catalytic cycle for oxidative cleavage mediated by VOTPA complexes, adapted from Amadio et al. [20]

The mechanism starts with one of the diol oxygens coordinating the VO, followed by the formation of a hydrogen bond between the other OH and the axial oxide. This leads to the first deprotonation step, forming an alkoxide and leaving a hydroxo-group in catalyst axial position. Then, the second proton of the diol substrate is ceded to the hydroxide, forming a non-oxo diol chelate V^{+5} intermediate and releasing a water molecule. Two one-electron processes occur forming two carbonyl moieties, leading to C–C bond cleavage and to formal reduction to V^{+3}. This V^{+3} intermediates are quite unstable, and quickly re-oxidized to the V^{+5} catalyst by an oxygen molecule. This is a two step-process starting with a peroxo-intermediate which is attacked by another V^{+3} entity leading to a bimetallic V^{+4} adduct that rapidly breaks yielding the starting V^{+5} catalyst.

Considering the proposed mechanism, the critical step is probably the reduction step from V^{+5} to V^{+3}. This energy barrier could be decreased adding electron-withdrawing groups to the ligand as they should significantly stabilize HOMO energy level increasing their reduction potential *i.e.*, making them better oxidants[27]. This hypothesis is supported by literature data on VOTPA catalysts efficiency[20] showing a strong influence of ligand electronic properties over required reaction time. In particular, electron-poor $VOTPA^{Cl,Cl}$ completely converted the substrate in 40 minutes, while $VOTPA^{tBu,H}$ and $VOTPA^{tBu,tBu}$ required 4 and 5 hours respectively. This become even more obvious taking into consideration the electron-richer $VOTPA^{tBu,OMe}$ which gave complete conversion only after 10 hours. Based on these considerations our idea was to synthesize ligands and corresponding complexes with even more electron-withdrawing groups to increase catalyst efficiency.

When it comes to ligand synthesis several procedures exist, many of them are variations of the classical synthesis with hexamethylenetetramine (HMTA) on *orto*-, *para*-substituted phenols (Figure 3.6).

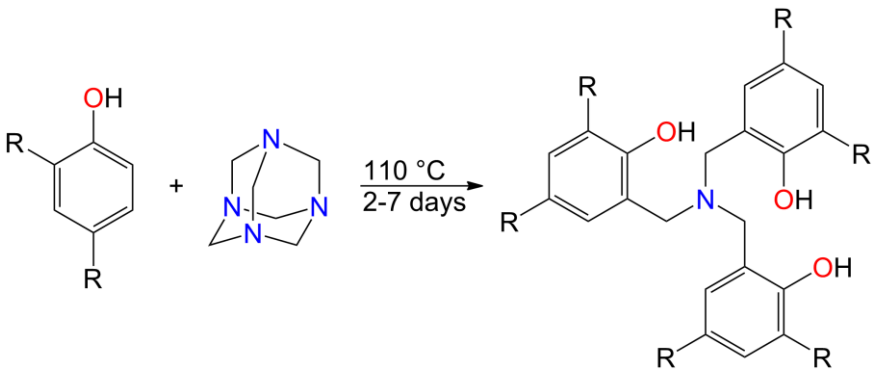

Figure 3.6: General representation of typical synthesis of TPA symmetric ligands

This procedure requires generally long reaction times, giving low to medium yields of the trimeric desired ligand[28], mixed with the dimeric adduct when electron-poor phenols are used[29]. Other reaction pathways exist, also enabling the synthesis of asymmetrical TPA ligands (Figure 3.7), but, to the best of our knowledge, they all need multi-step reactions, often requiring to work on protected phenols adding a further deprotection step, leading to overall medium to low yields.

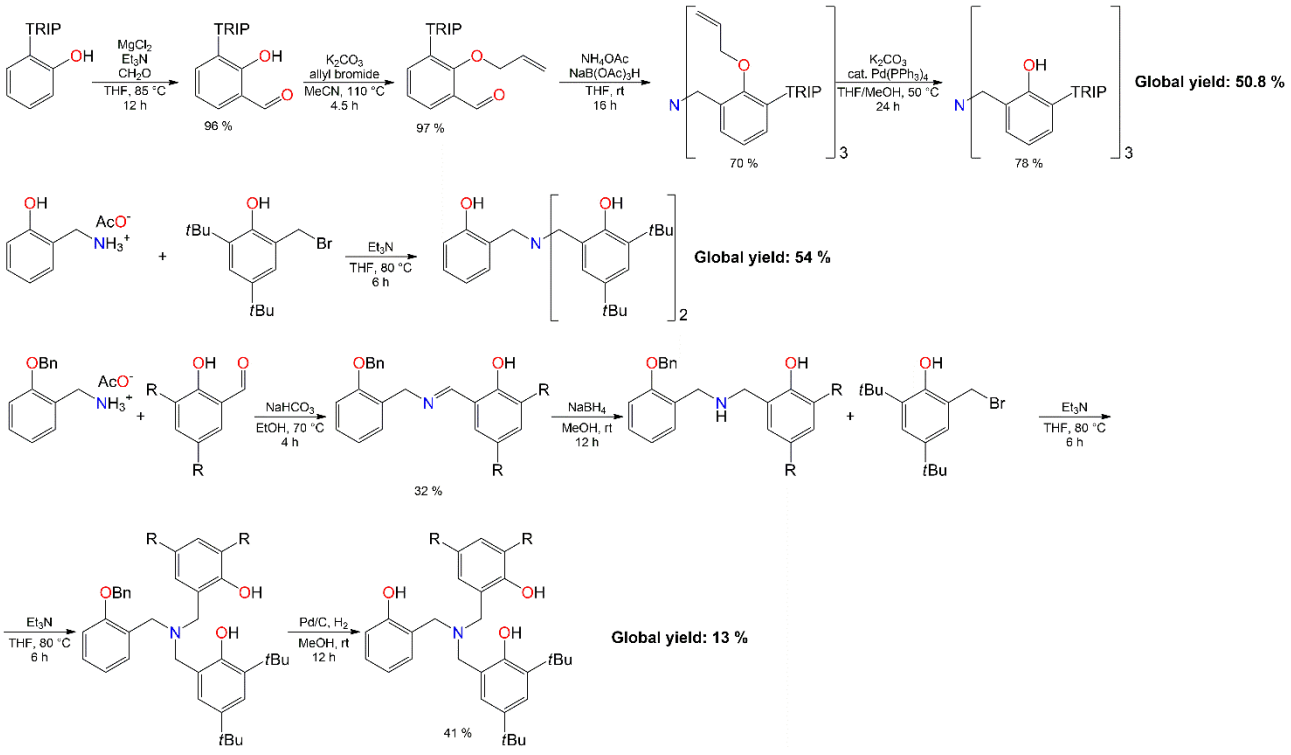

Figure 3.7: Different synthetic pathways to obtain symmetric and asymmetric TPA ligands. TRIP = 1,3,5-triisopropyl phenyl, R = methyl, t-butyl or methoxy. Top was adapted from Bae et al. [30]. Middle and bottom were adapted from Forder et al. [31]

We decided to stick to the classical HMTA synthesis, working on 2,4-dichlorophenol ($PhCl_2$), 2,4-difluorophenol (PhF_2) and on 4-chloro-2-nitrophenol ($PhClNO_2$). Unfortunately, in our hands none of the tested procedures for TPAs gave the expected ligands, even if reported for the same $PhCl_2$ substrate[29], thus we optimized our own synthetic pathway to these target molecules.

3.2 Synthesis of diphenolamines (DPAs) precursors

As stated just before, performing the classical HMTA synthesis (Figure 3.6) we never detected the expected TPA ligands, not even in low amount, always obtaining as the main products diphenolamines (DPAs) in varying yields and conversions. Therefore, given the impossibility to obtain directly TPAs we decided as a first step to optimize DPA synthesis, planning a subsequent alkylation in a similar way to second and third procedures shown in Figure 3.7. Yield and conversion strictly following the reported procedure[29] were very low, after several attempts and slightly modifying the protocol, we identified four major issues. First of all, HMTA reactivity is low, as it proceeds through a sort of slow thermal decomposition, thus longer reaction time are required, similar to syntheses of non-deactivated TPA ligands[28,32]. Second, the ratio phenol : HMTA should be increased from the reported 3 to 6, to avoid formation of by-products and DPA·HMTA and TPA·HMTA adducts[29,33]. This also allows to fully exploit the 3 HMTA dimethylenamino groups, leaving as a by-product only ammonia, greatly increasing the overall atomic efficiency, theoretically allowing to obtain 3 DPA molecules for each HMTA unit. The third consideration is that generally phenols have a slight tendency to sublimate, this can be ignored when solvents are used or if reaction time is low. On the other hand, when working with melted reagents in long solventless reactions it should be taken into consideration to avoid reagent sequestration causing yield loss. The easiest solution to this problem would be to increase the amount of phenol, but in our hands that did not give good results. We were able to bypass this problem working with only a slight excess of phenols, performing the synthesis in a Schlenk tube with a tight screwcap and heating the whole system to the desired temperature. Finally, the addition of an acidic catalyst can greatly enhance the reaction speed, in particular following the literature[28] we employed *p*-toluensulfonic acid decreasing the reaction time from one week to 40 hours. Also work-up was not completely straight forward, as the raw product is a bulky extremely hard solid mass, not soluble in the vast majority of solvents. The best results were obtained when the solid was triturated with boiling chloroform obtaining a powder that was furtherly purified by reprecipitation in water, *i.e.*, solubilizing it in strongly basic water and slowly increasing the pH until complete precipitation. Reversing the procedure would be more practical, but unfortunately gave lower purity products when compared to the previous one. We have been able to obtain the desired DPAs in very high yield and purity from both $PhCl_2$ and PhF_2, but unfortunately not from $PhClNO_2$. Despite our attempts to modify the reaction condition we always recovered unreacted $PhClNO_2$ or charred material, confirming that selectivity and obtainable products can change significantly with the electronic properties of the phenol. Both 2,2'-[bis(methylene)imino]bis(4,6-dichlorophenol) ($DPA^{Cl,Cl}$) and 2,2'-[bis(methylene)imino]bis(4,6-difluorophenol) ($DPA^{F,F}$) were fully characterized through NMR spectroscopy and ESI-MS spectrometry as shown in Figures 3.8–3.20. Assignments were determined

through careful analysis of 1D (^{1}H, ^{13}C and ^{19}F when applicable) and 2D (^{1}H–^{1}H COSY, ^{1}H–^{13}C HSQC, ^{1}H–^{13}C HMBC) spectra.

3.2.1 Characterization of 2,2'-[bis(methylene)imino]bis(4,6-dichlorophenol) (DPA^{Cl,Cl})

DMSO-d_6 is required for NMR as solubility in other solvents is too low to reach the concentrations necessary for this technique. Figure 3.8 shows the typical ^{1}H NMR spectrum of DPA^{Cl,Cl}, with two aromatic doublets at 7.48 ppm and 7.32 ppm with a small coupling constant (*J*) of 2.03 Hz, a quite typical value for aromatic *meta* couplings. The aminomethylene groups are clearly visible as a singlet at 4.01 ppm while the amine and phenols protons are not visible. The broad signal at 6 ppm was assigned to water as DMSO is very hygroscopic and the typical water signal at 3.33 ppm is missing, also, the area of the signal does not fit well with other peaks. We do not know the reason for this shift of water signal always observed in DPA^{Cl,Cl} products.

Figure 3.9 shows DPA^{Cl,Cl} ^{13}C NMR spectrum with all the 7 expected signals visible, even if intensity of quaternary carbons signals are unusually high when compared to non-quaternary *C3*, *C5* and *C7*. All the aromatic signals are located between 130 and 120 ppm, apart from *C1* that bears a hydroxide and therefore is way more deshielded reaching 151 ppm, while the aliphatic *C7* being both aminic and benzylic stands at about 47 ppm. Looking at Figure 3.12 showing the ^{1}H–^{13}C HMBC spectrum it can be noted a coupling at 4.01-46.75 ppm, these are the signals belonging to the methylenic bridge. This coupling does not arise from an instrumental error, as ^{1}H–^{13}C HMBC pulse programme suppresses short range interactions, but is due to symmetry and an actual coupling between the two methylene groups, *i.e.*, *H7-C7'* and *H7'-C7*.

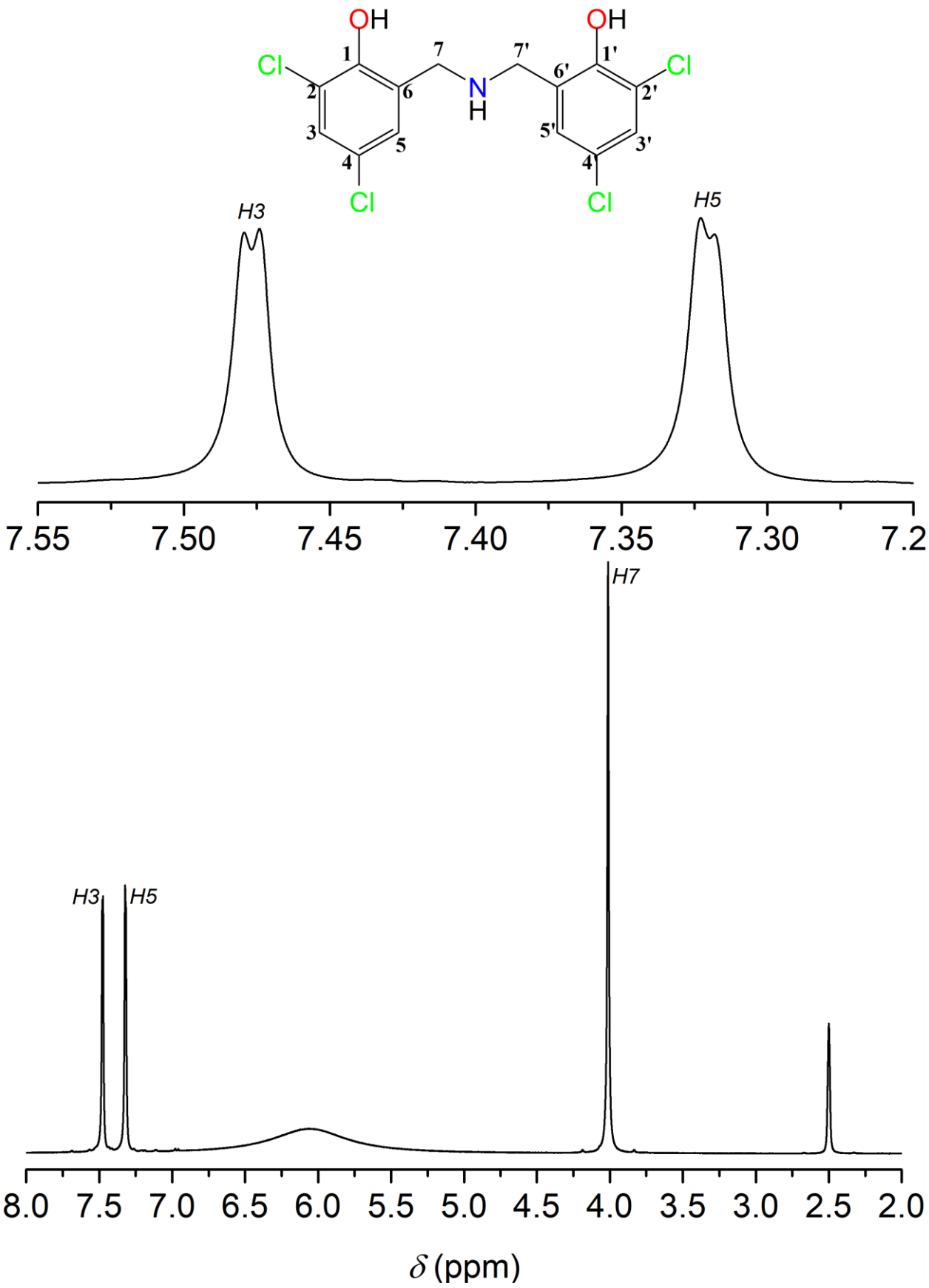

Figure 3.8: Bottom: ^{1}H NMR spectrum of $DPA^{Cl,Cl}$ in DMSO-d_6 (298 K, 400.13 MHz). Top: structure of $DPA^{Cl,Cl}$ and magnification of the spectrum between 7.55 ppm and 7.2 ppm. Processing parameters (TopSpin 4.3.0): SI = TD, LB = 0.30 Hz. δ_H (ppm) = 2.50 (residual protons in DMSO-d_6)

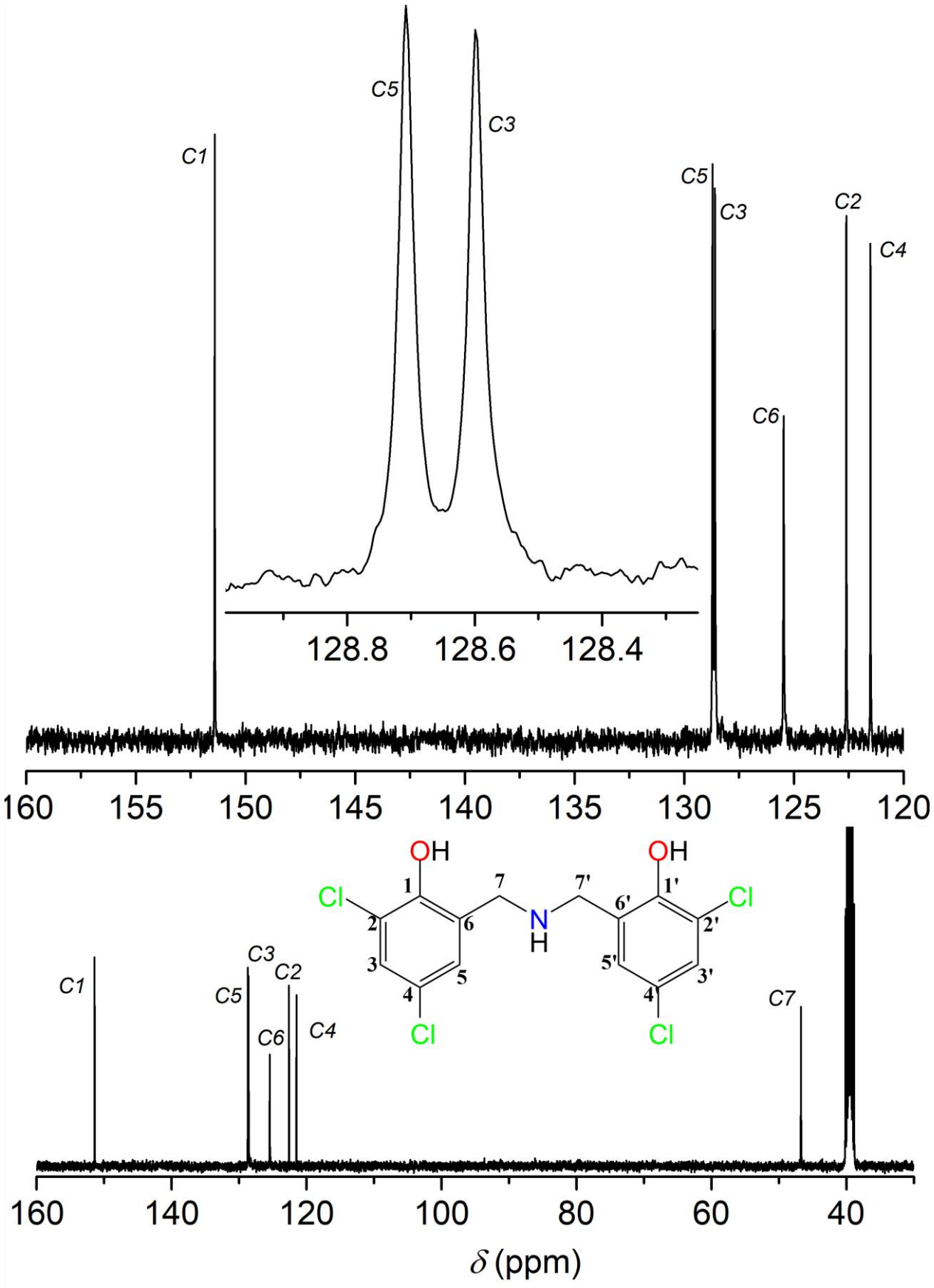

Figure 3.9: Bottom: ^{13}C NMR spectrum of $DPA^{Cl,Cl}$ in DMSO-d_6 (298 K, 400.13 MHz) and structure of $DPA^{Cl,Cl}$. Top: Magnification of the spectrum between 160–120 ppm and 129.0–128.2 ppm. Processing parameters (TopSpin 4.3.0): SI = TD, LB = 0.30 Hz. δ_C (ppm) = 39.52 (residual carbons in DMSO-d_6)

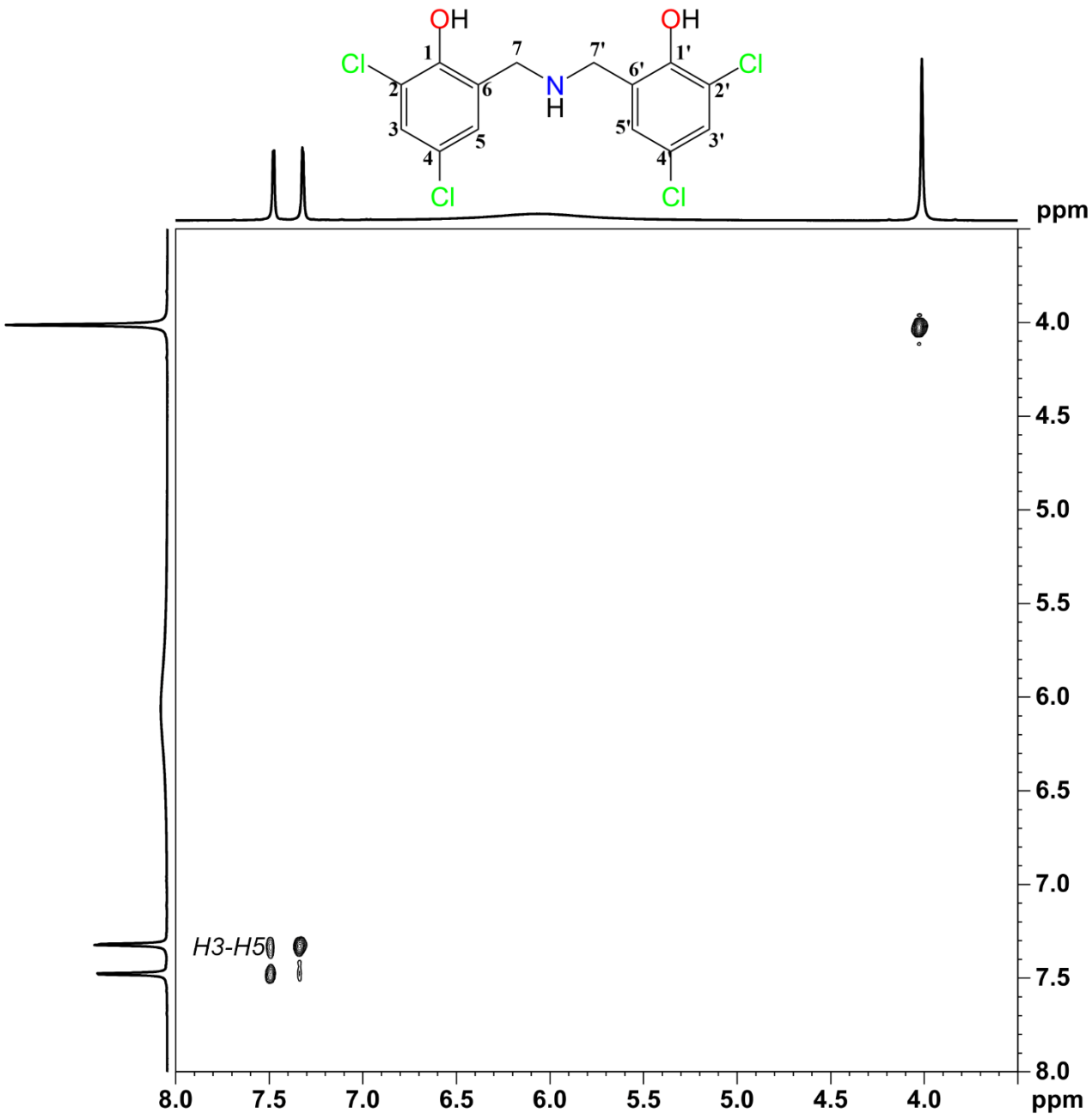

Figure 3.10: Structure and $^{1}H–^{1}H$ COSY spectrum of $DPA^{Cl,Cl}$ in DMSO-d_6 between 8.0 and 3.5 ppm (298 K, 400.13 MHz). The labelling of the cross-peaks indicates the $^{1}H–^{1}H$ coupling (F2,F1). Processing parameters (TopSpin 4.3.0) for F2 (x axis): SI = TD, LB = 1.00 Hz. Processing parameters for F1 (y axis): SI = 2·TD, LB = 0.30 Hz.

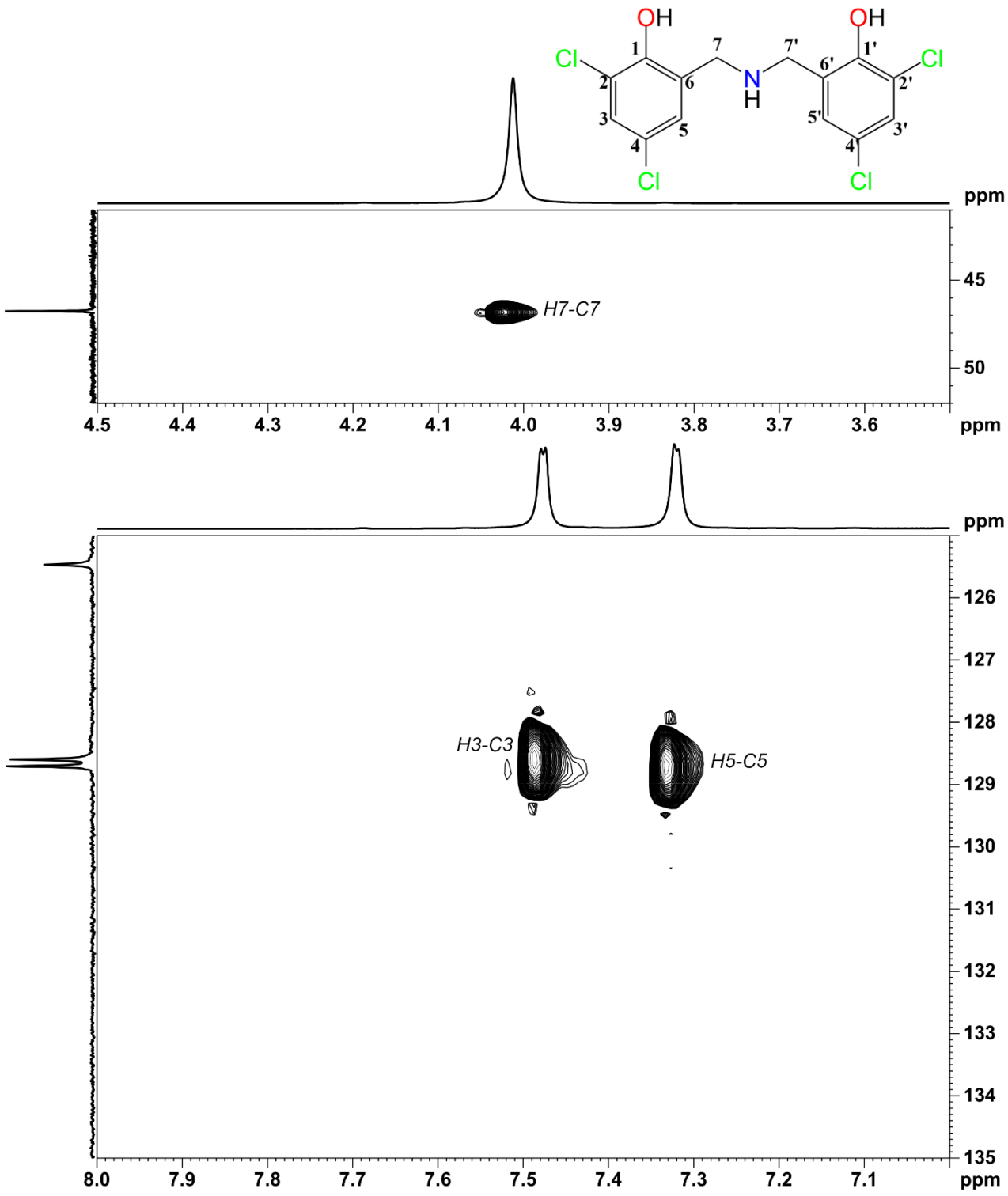

Figure 3.11: Structure and $^{1}H–^{13}C$ HSQC spectrum of $DPA^{Cl,Cl}$ in DMSO-d_6 for: bottom δ_H = 8.0–6.3 ppm and δ_C =135–125 ppm, top δ_H = 4.5–3.5 ppm and δ_C = 52–41 ppm (298 K, 400.13 MHz). The labelling of the cross-peaks indicates the $^{1}H–^{13}C$ coupling (F2,F1). Processing parameters (TopSpin 4.3.0) for F2 (x axis): SI = 2·TD, LB = 1.00 Hz. Processing parameters for F1 (y axis): SI = 3·TD, LB = 0.30 Hz

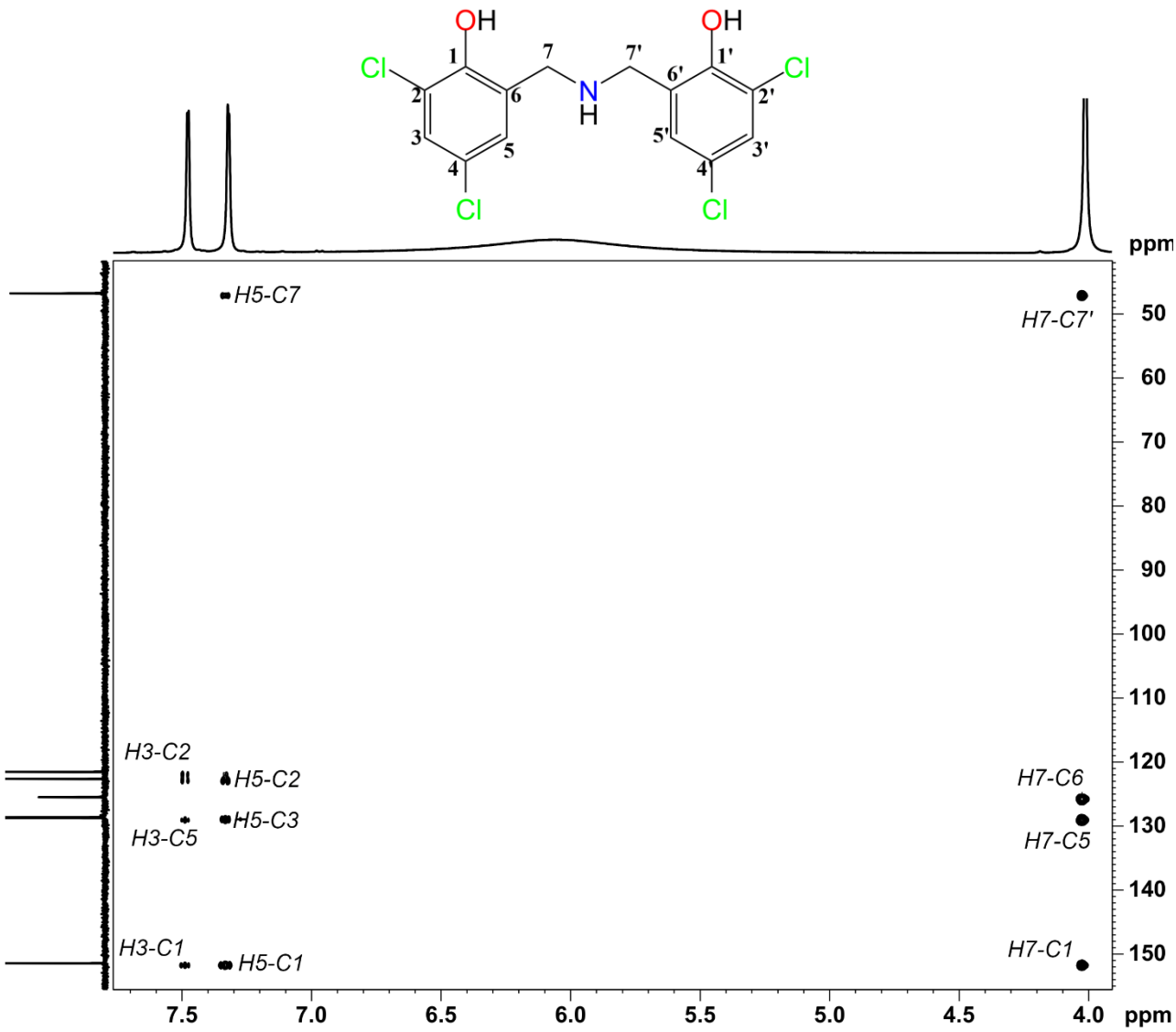

Figure 3.12: Structure and $^{1}H–^{13}C$ HMBC spectrum of $DPA^{Cl,Cl}$ in DMSO-d_6 for δ_H = 7.8–3.9 ppm and δ_C =156–43 ppm (298 K, 400.13 MHz). The labelling of the cross-peaks indicates the $^{1}H–^{13}C$ coupling (F2,F1). Processing parameters (TopSpin 4.3.0) for F2 (x axis): SI = 2·TD, LB = 1.00 Hz. Processing parameters for F1 (y axis): SI = 3·TD, LB = 0.30 Hz

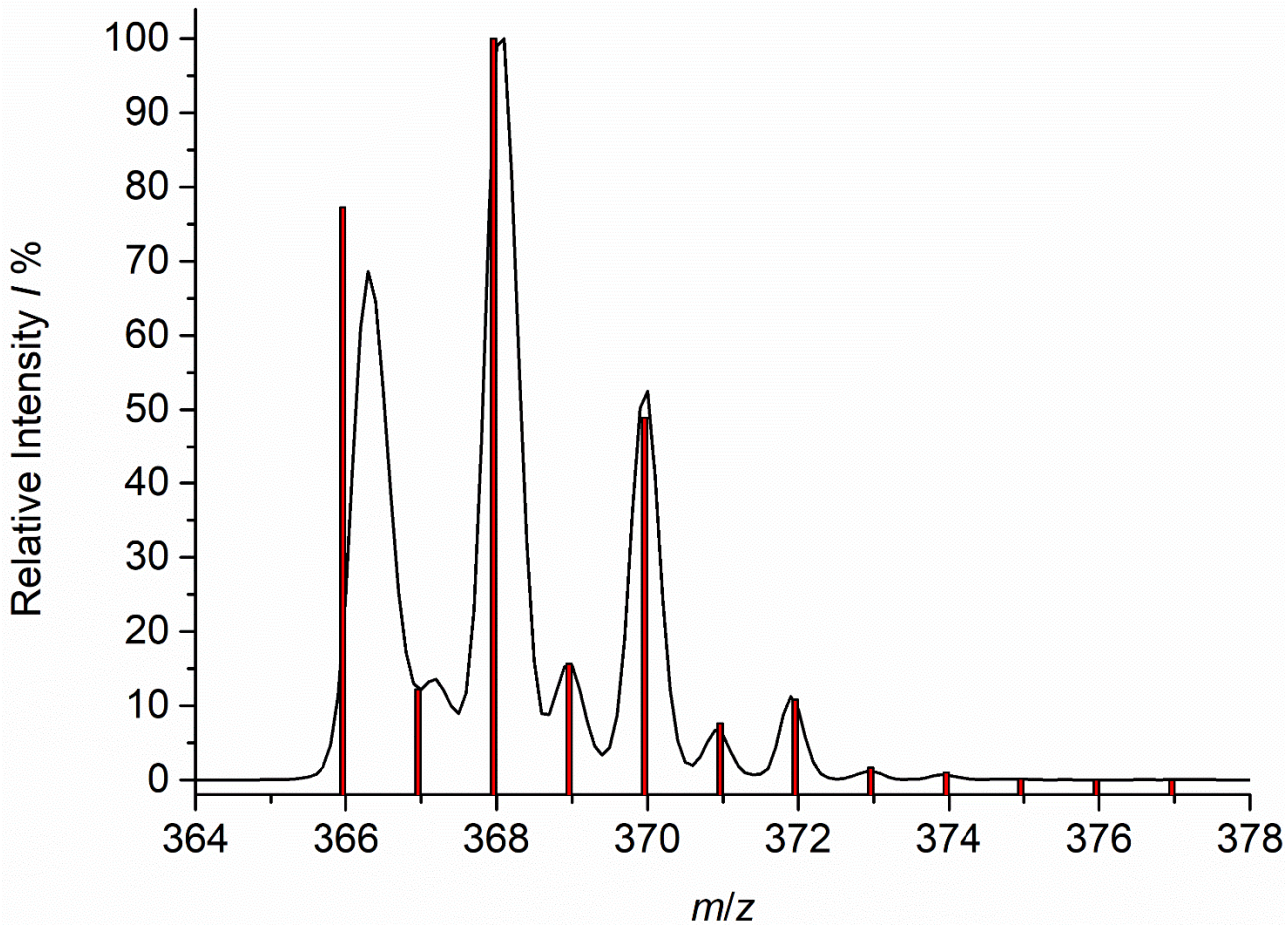

Figure 3.13: Black line: ESI-MS spectrum of $DPA^{Cl,Cl}$ (isocratic LC at 80:20 CH_3CN:H_2O (0.1% HCOOH)/Zorbax 30x4.6 mm column, positive ion mode). Red bars: simulated isotopic pattern for $[DPA^{Cl,Cl}+H]^+$.

Figure 3.13 displays the experimental ESI-MS spectra of $DPA^{Cl,Cl}$ in black, and the simulated isotopic pattern for $[DPA^{Cl,Cl}+H]^+$ as red bars, showing a good fit. Concentrations required for ESI-MS are extremely low compared to those needed for NMR, thus it was possible to use CH_3CN even if substrates are not very soluble in it. This characterization was necessary to define surely if TPAs or DPAs were obtained in the first place. In fact, the NMR spectra of pure samples of symmetric DPA or TPA would be extremely similar, with slightly different chemical shifts and no difference in peak area ratios. Furthermore, even through Elemental Analysis (EA) it would be impossible to distinguish them as the variations in the percentage of C, H and N going from DPA to TPA are extremely close to the typically accepted measurement error. On the other hand MS leaves no doubt, as $[TPACl_6+H]^+$ would have a m/z = 539.92 instead of the $[DPA^{Cl,Cl}+H]^+$ m/z = 365.96. Moreover, the isotopic pattern allows to establish with decent precision the number of Cl atoms in a molecule further confirming that $DPA^{Cl,Cl}$ was obtained.

3.2.2 Characterization of 2,2'-[bis(methylene)imino]bis(4,6-difluorophenol) ($DPA^{F,F}$)

Similarly to $DPA^{Cl,Cl}$ also $DPA^{F,F}$ has very low solubility in organic solvents, thus for NMR analysis DMSO-d_6 is required. Figure 3.14 shows the typical ^{1}H NMR spectrum of $DPA^{F,F}$, with two multiplets similar to overlapped double double doublets. These peculiars multiplicities arise from the combination of *H–H* and *H–F* couplings. In particular, *H3* has two *H–F* couplings in *ortho-* positions with similar coupling constants (^{3}J) of 11.20 and 8.92 Hz and a smaller *H–H meta-* coupling (^{4}J) of 3.20 Hz, while *H5* has two different *H–F* couplings coming from *ortho-* (^{3}J) and *para-* (^{5}J) positions, respectively of 9.32 Hz and 1.52 Hz. As far as concern the methylene protons they generate a sharp singlet at 3.58 ppm, even if at proper distance for long range (^{5}J) interactions. Surprisingly, $DPA^{F,F}$ has lower proton chemical shifts when compared to $DPA^{Cl,Cl}$. This observation was unexpected because the higher electronegativity of fluoride should make the aromatic electron-poorer, causing an overall greater deshielding of the molecule.

Figure 3.15 displays the ^{13}C NMR spectrum of $DPA^{F,F}$, all the signals, except *C7* and *C1*, show 2 *C–F* couplings giving splitted signals, therefore lowering the intensity making harder to detect quaternary carbons. In particular, *C2* and *C4* are barely visible in ^{13}C NMR and actual detection required combined inspection of it and ^{1}H–^{13}C HMBC spectra. *C1* signal is a doublet with a ^{2}J of 23.0 Hz, probably, the intensity is too low to appreciate also the four bond coupling (^{4}J) with *F4* that should be of ~2–3 Hz. *C2* and *C4* have similar multiplicity looking as double doublets. They both have an *ipso*-F, which generates a wide splitting because of the extremely high coupling constants *C–F* (^{1}J) respectively of 205 Hz and 233 Hz while the smaller ^{3}J are 10.3 Hz and 10.4 Hz. *C3* has two couplings (^{2}J) of ~25 Hz resulting in a pseudo-triplet signal. *C5* and *C6* are both double doublets, *C5* with two quite different coupling constants of 20.8 Hz (^{2}J) and 2.8 Hz (^{4}J) while *C6* has two similar ^{3}J of 7.6 Hz and 5.2 Hz giving partial overlap on the "central" peak. Finally, *C7* stands as a singlet even if at four bonds distance from both *F2* and *F4*. Similarly to $DPA^{Cl,Cl}$ also in $DPA^{F,F}$ ^{1}H–^{13}C HMBC spectra (Figure 3.19) it is detected, at 3.58-47.7 ppm, a coupling between *H7–C7'* due to molecule symmetry.

Figure 3.16 shows the ^{19}F NMR of $DPA^{F,F}$. Two signals are clearly visible, a broad singlet at −130.0 ppm and a doublet at −133.5 ppm with a splitting of 10.2 Hz. It should be noted that usually ^{19}F NMR yields sharp and well resolved peaks where it is possible to detect both *F–H* and *F–F* couplings. The lack of resolution, probably due to the usage of DMSO-d_6, is reasonably responsible for the broadening of both peaks. In fact, *F4* should be a double triplet with two very similar $^{3}J_{H-F}$ of ~10 Hz and a smaller $^{4}J_{F-F}$ of ~2–3 Hz, while *F2* should be a sort of triple doublet with a big $^{3}J_{H-F}$ of ~10 Hz and two smaller constants $^{4}J_{F-F}$ and $^{5}J_{H-F}$ of ~2–3 Hz and ~1–2 Hz respectively. These considerations

led to assigning the broad singlet at −130.0 ppm to *F4* and the broad doublet at −133.5 ppm to *F2*. *C–F* couplings are not detectable in ^{19}F NMR due to the relative abundance of carbon isotopes, with the NMR active ^{13}C being only ~1% of the total, *i.e.*, a quantity too low to significantly affect ^{19}F signal shape.

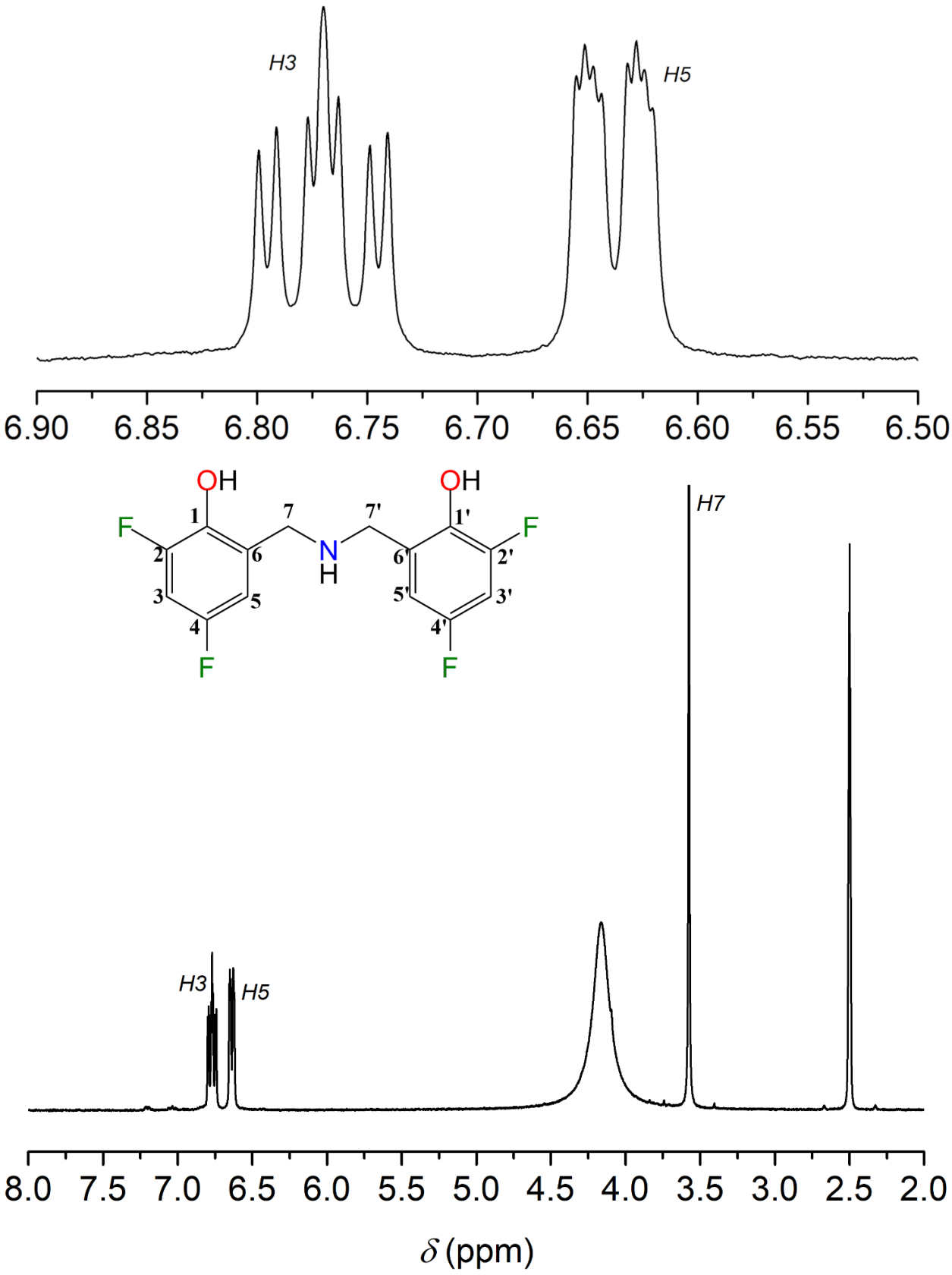

Figure 3.14: Bottom: ^{1}H NMR spectrum of DPA^{F,F} in DMSO-d_6 (298 K, 400.13 MHz). Top: structure of DPA^{F,F} and magnification of the spectrum between 6.90 ppm and 6.50 ppm. Processing parameters (TopSpin 4.3.0): SI = TD, LB = 0.30 Hz. δ_H (ppm) = 2.50 (residual protons in DMSO-d_6)

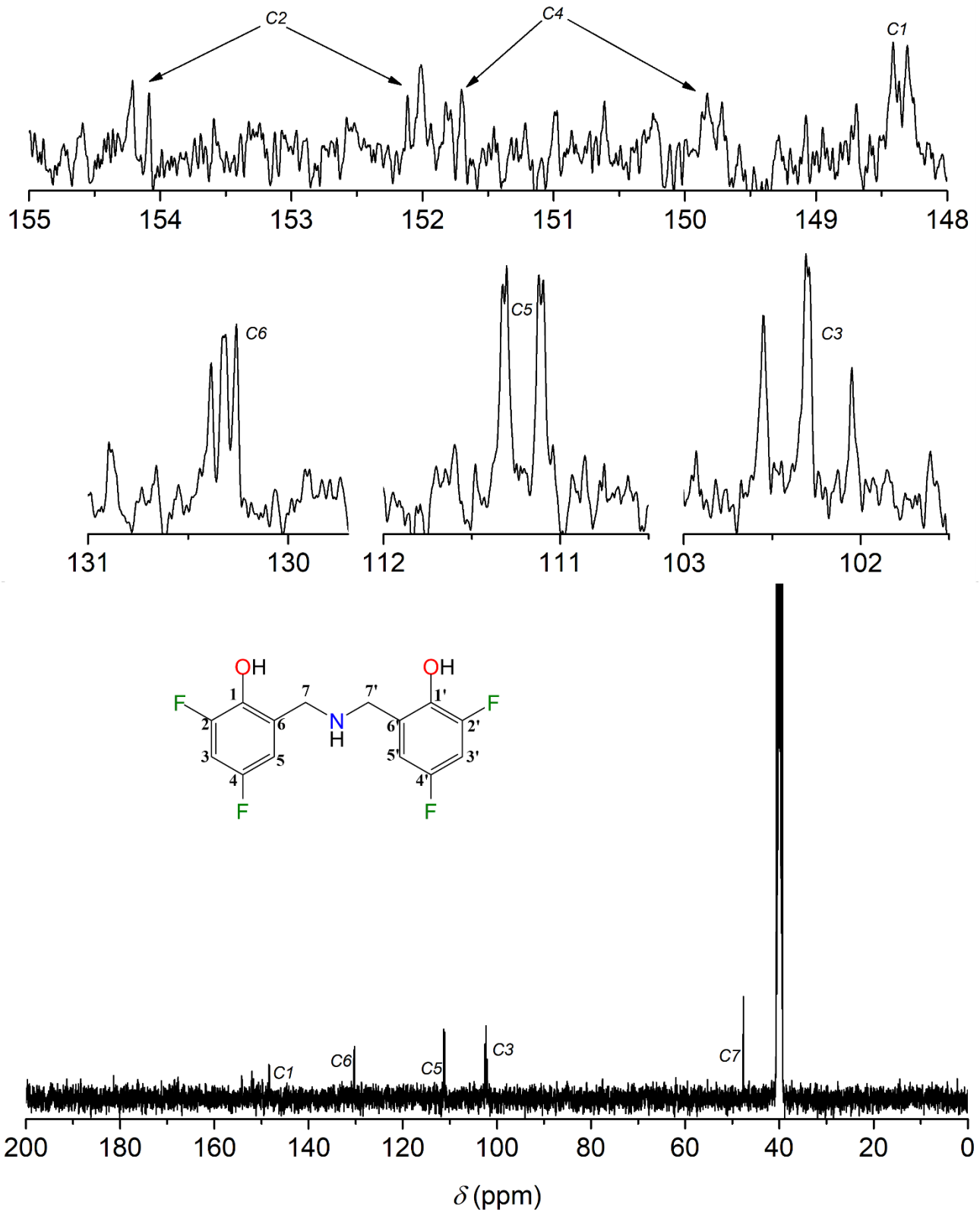

Figure 3.15: Bottom: ^{13}C NMR spectrum of $DPA^{F,F}$ in DMSO-d_6 (298 K, 400.13 MHz) and structure of $DPA^{F,F}$. Top: Magnifications of the spectrum between 155–148 ppm, 131.0–129.7 ppm, 112.0–110.5 ppm, 103.0–101.5 ppm. Processing parameters (TopSpin 4.3.0): SI = TD, LB = 0.30 Hz. δ_C (ppm) = 39.52 (residual carbons in DMSO-d_6)

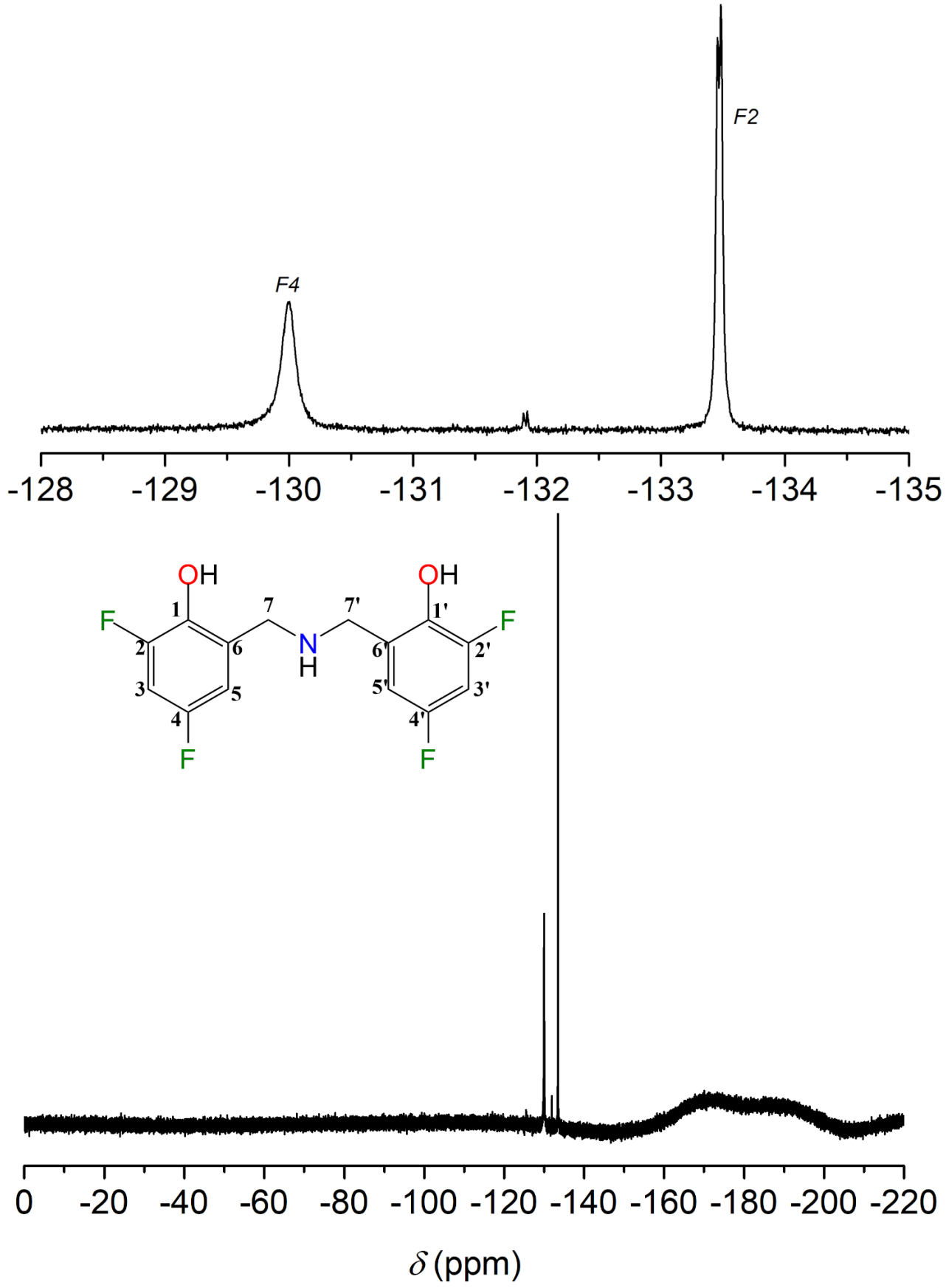

Figure 3.16: Bottom: ^{19}F NMR spectrum of $DPA^{F,F}$ in DMSO-d_6 (298 K, 400.13 MHz) and structure of $DPA^{F,F}$. Top: Magnification of the spectrum between −128 ppm and −135 ppm. Processing parameters (TopSpin 4.3.0): SI = TD, LB = 0.30 Hz.

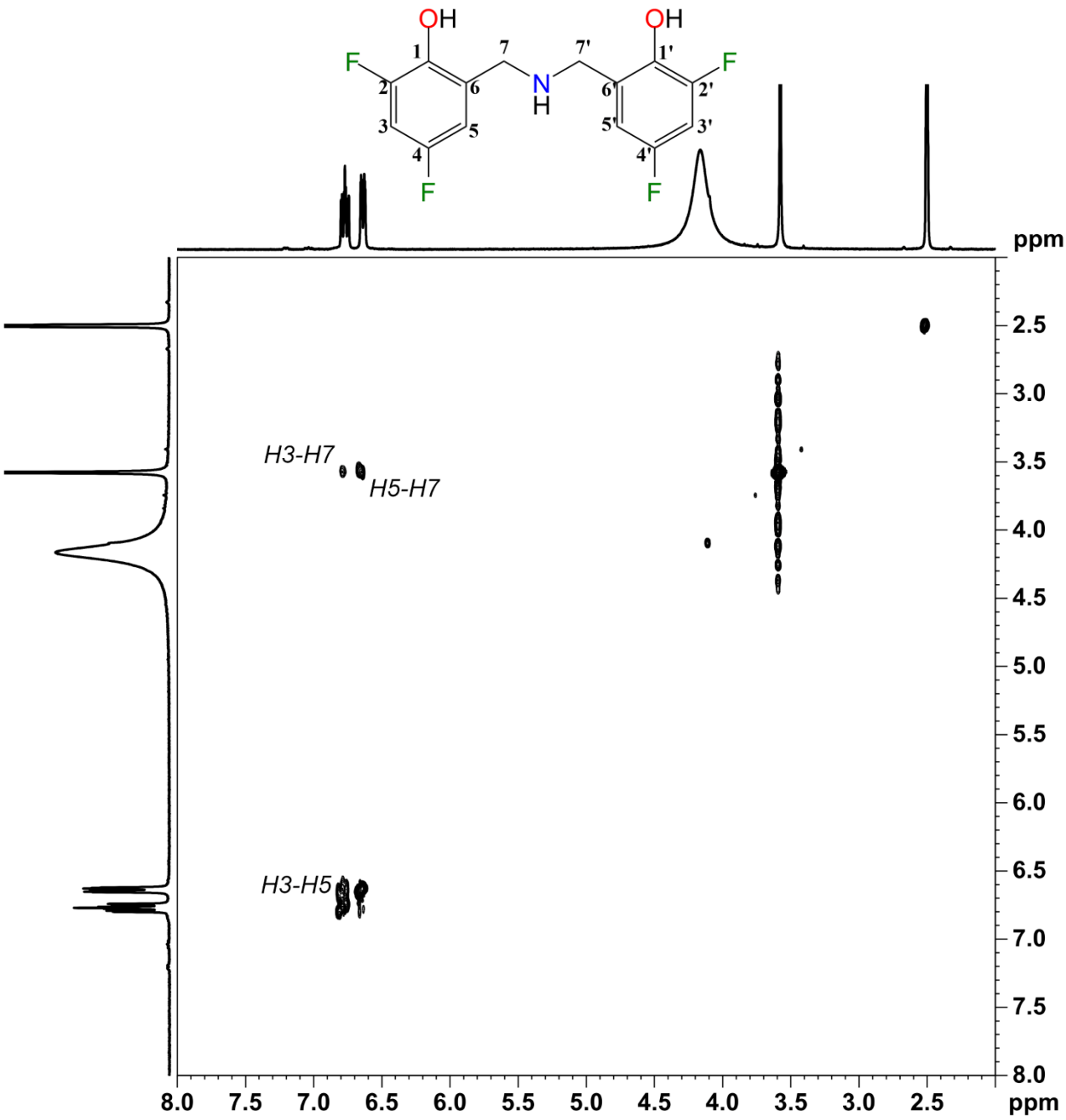

Figure 3.17: Structure and $^{1}H–^{1}H$ COSY spectrum of $DPA^{F,F}$ in DMSO-d_6 between 8.0 and 2.0 ppm (298 K, 400.13 MHz). The labelling of the cross-peaks indicates the $^{1}H–^{1}H$ coupling (F2,F1). Processing parameters (TopSpin 4.3.0) for F2 (x axis): SI = TD, LB = 1.00 Hz. Processing parameters for F1 (y axis): SI = 2·TD, LB = 0.30 Hz.

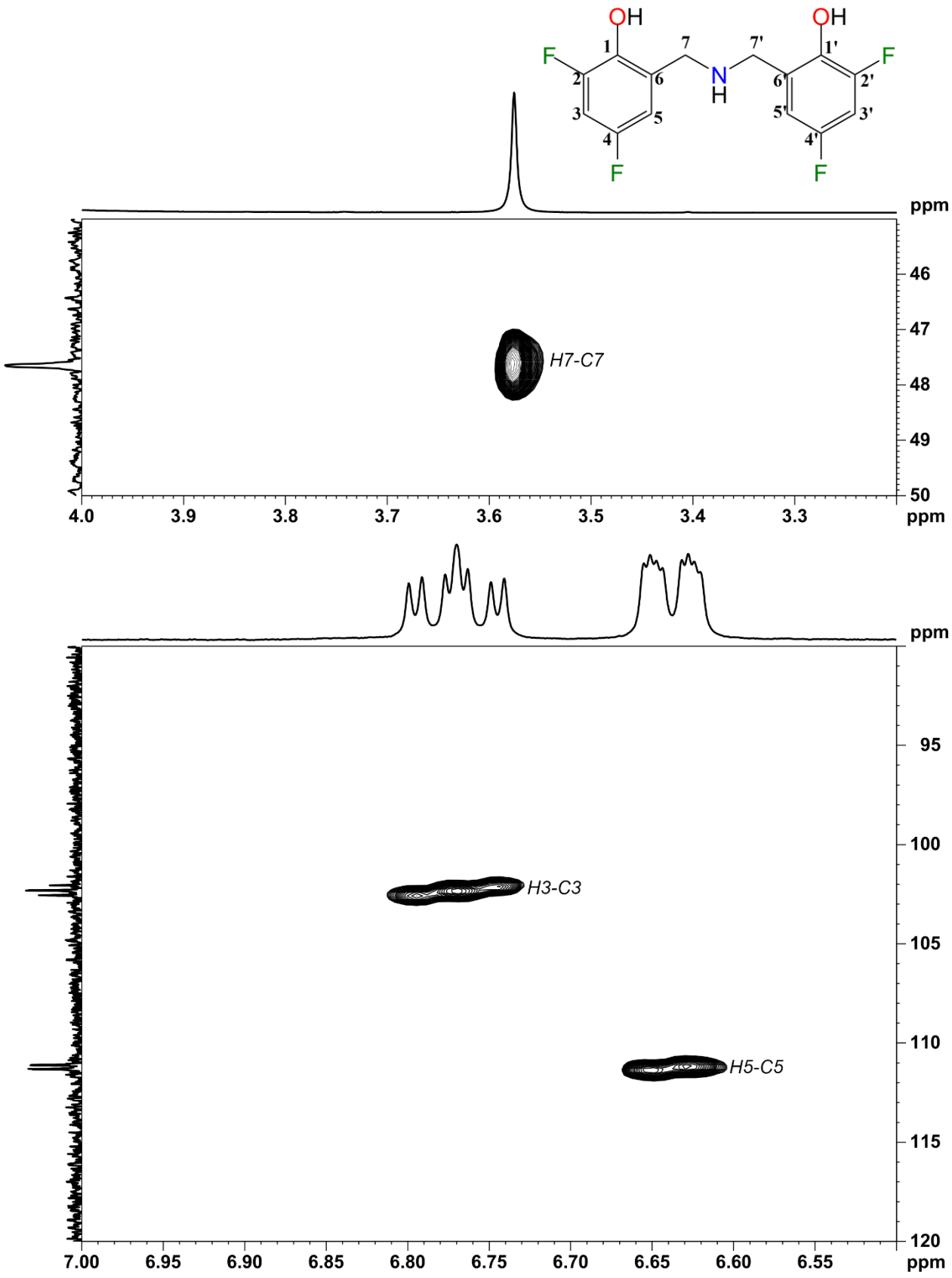

Figure 3.18: Structure and ^{1}H–^{13}C HSQC spectrum of $DPA^{F,F}$ in DMSO-d_6 for: bottom δ_H = 7.0–6.5 ppm and δ_C =120–90 ppm, top δ_H = 4.0–3.2 ppm and δ_C = 50–45 ppm (298 K, 400.13 MHz). The labelling of the cross-peaks indicates the ^{1}H–^{13}C coupling (F2,F1). Processing parameters (TopSpin 4.3.0) for F2 (x axis): SI = 2·TD, LB = 1.00 Hz. Processing parameters for F1 (y axis): SI = 3·TD, LB = 0.30 Hz

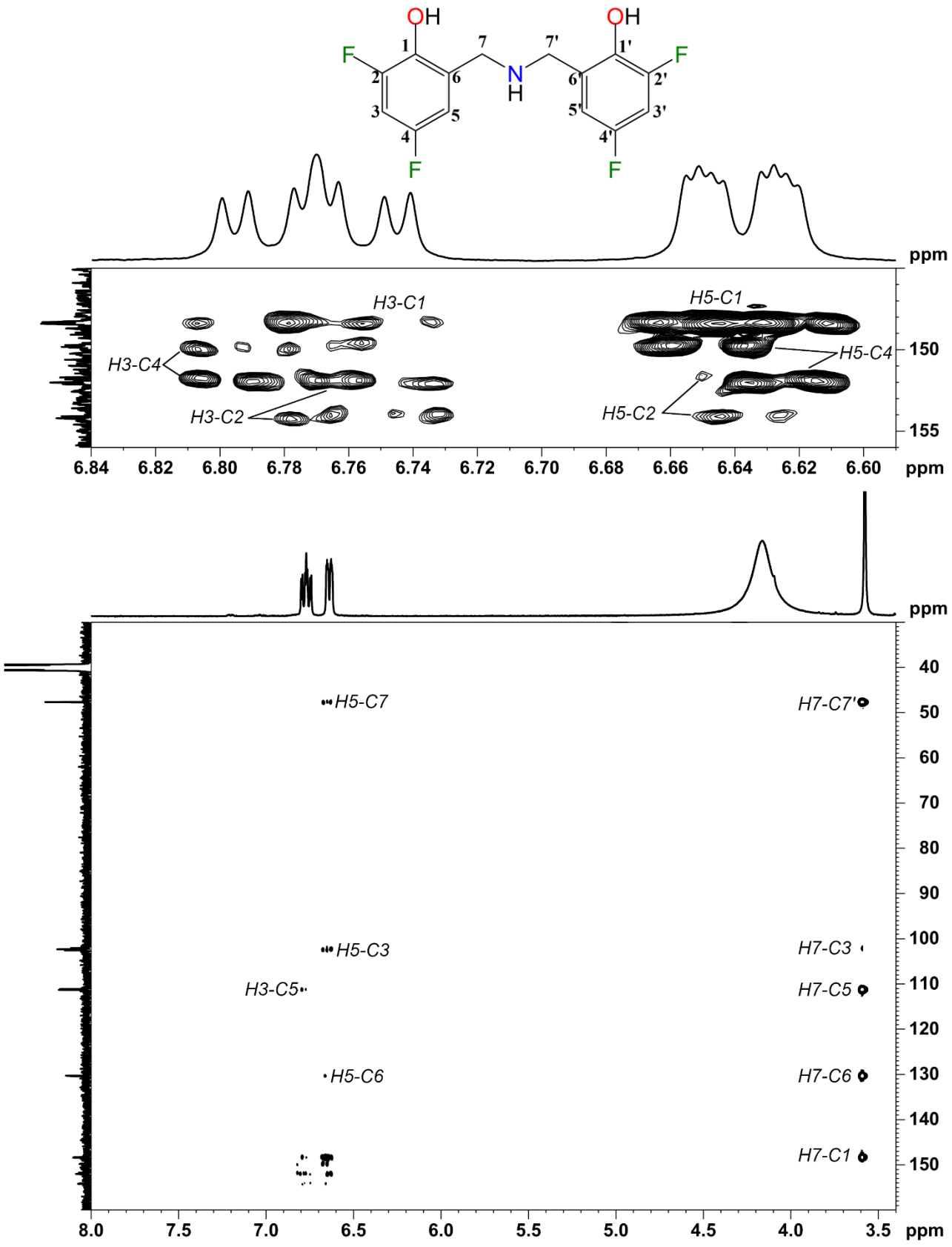

Figure 3.19: Structure and ^{1}H–^{13}C HMBC spectrum of $DPA^{F,F}$ in DMSO-d_6 for: bottom δ_H = 8.0–3.4 ppm and δ_C =155–35 ppm, top δ_H = 6.84–6.59 ppm and δ_C = 156–145 ppm (298 K, 400.13 MHz). The labelling of the cross-peaks indicates the ^{1}H–^{13}C coupling (F2,F1). Processing parameters (TopSpin 4.3.0) for F2 (x axis): SI = 2·TD, LB = 1.00 Hz. Processing parameters for F1 (y axis): SI = 3·TD, LB = 0.30 Hz

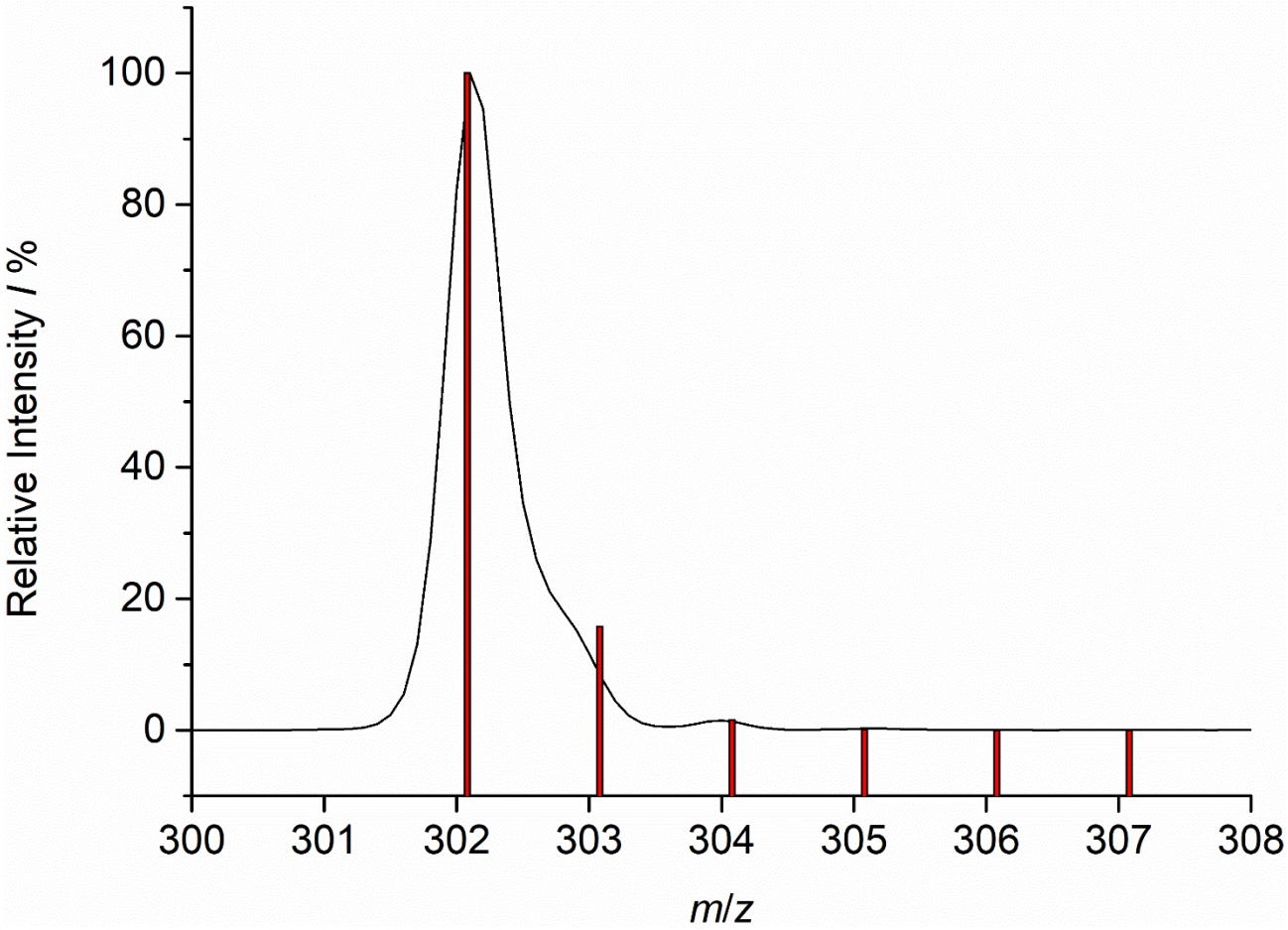

Figure 3.20: Black line: ESI-MS spectrum of $DPA^{F,F}$ (isocratic LC at 80:20 $CH_3CN:H_2O$ (0.1% HCOOH)/Zorbax 30x4.6 mm column, positive ion mode). Red bars: simulated isotopic pattern for $[DPA^{F,F}+H]^+$.

Figure 3.20 displays the experimental ESI-MS spectra of $DPA^{F,F}$ in black, and the simulated isotopic pattern for $[DPA^{F,F}+H]^+$ as red bars, showing a decent fit. It is quite common when low resolution spectra are recorded to see slightly broad signals with shoulders instead of a proper isotopic pattern peak. Nevertheless, the experimental signal at m/z = 302.1 is very close to the calculated m/z = 302.080 for $[DPA^{F,F}+H]^+$, a further confirmation that $DPA^{F,F}$ was obtained.

3.3 Preliminary study of the coordination chemistry of $DPA^{Cl,Cl}$.

While working on the DPAs to TPAs steps we also started to evaluate the coordination chemistry of DPAs.

Generally, DPAs ligands are synthetized through double alkylation of a primary amine (Figure 3.21). This leads to tertiary amines with two phenolic moieties and a variety of third substituents, ranging from simple alkyl groups[34,35] to neutral nitrogen or oxygen coordinating groups, *i.e.*, tertiary amines, THF- or pyridine-like arms[34,36–38].

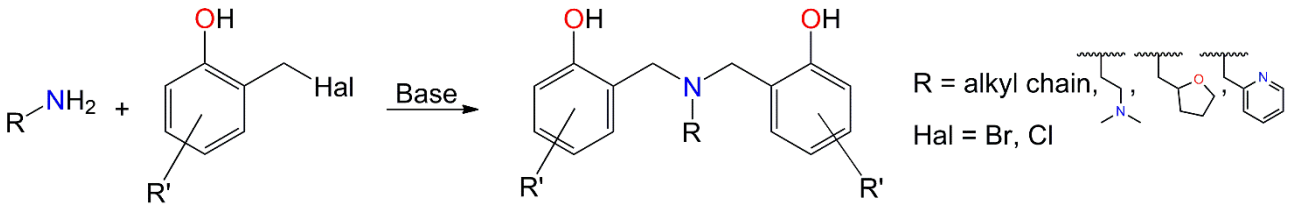

Figure 3.21: General typical synthesis of DPA ligands

These DPAs ligands are used to chelate a wide array of metals, spanning across first, second and third transition groups[34,36–40], find applications mainly in catalysis[35,39] and are studied for their magnetic behavior[37,38]. The tungsten alkylidyne complex reported by *VenkatRamani et al.*[41] is the only complex of a secondary DPA we are aware of. They show that the ligand can properly coordinate in both the di- and tri-anionic forms, the aminic nitrogen was removed after complexation by the addition of a strong base (Methylenetriphenylphosphorane) aiming to increase the nucleophilicity of the alkylidyne α-carbon.

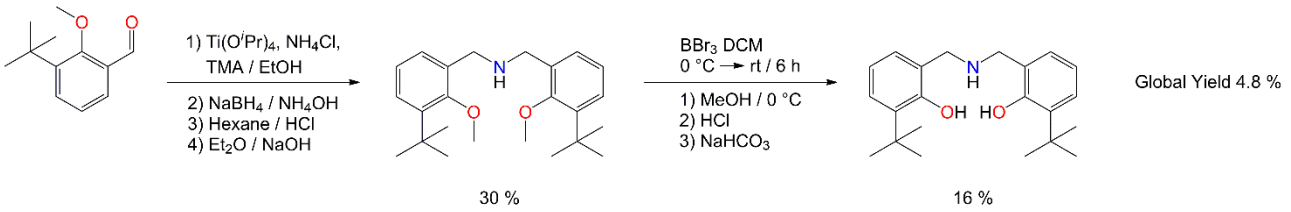

Figure 3.22: Synthesis of a secondary amine DPA ligand, adapted from *VenkatRamani et al.* [41]

The reaction pathway proposed[41] for this secondary DPA (Figure 3.22) uses as a substrate a substituted 2-methoxybenzaldehyde which is reacted over night with NH_4Cl in presence of equimolar amounts of both titanium isopropoxide ($Ti(OiPr)_4$) and trimethylamine in ethanol, under an inert atmosphere. Then $NaBH_4$ is added to the mixture and stirred for several hours and subsequently quenched with NH_4OH, extracted with EtOAc, vacuum dried, redissolved in hexane and stirred with 2 M HCl, to give a solid precipitate that is the corresponding amine hydrochloride. This is then treated with 1 M NaOH to give the neutral desired amine with a global yield of 30 %. The second step for phenols deprotection uses an excess of BBr_3 in DCM followed by three subsequential quenching with methanol, 1 M HCl and saturated $NaHCO_3$ giving the desired DPA after recrystallization in 16 % yield. This procedure gives a global yield in DPA of ~5%, requires several steps, many of which must be performed in carefully dried and inert atmosphere, employing in its last step a particularly corrosive and dangerous reagent, BBr_3 which is a H300 + H330 (Fatal if swallowed or inhaled). This procedure allow to synthetize secondary DPAs with phenols *o*- and *p*- free positions. On the other hand, even if our procedure requires *o*-, *p*-substituted phenols gives the product in a single step with high yield, working with not dangerous reagents, making it a viable alternative.

As far as concern coordination study we decided to test the $DPA^{Cl,Cl}$ on Ti using $Ti(OiPr)_4$ as a source of titanium, and on Co using $CoCl_2$ as a source of cobalt. Co coordination was tested under different conditions, *i.e.*, in an organic solvent with an organic base, namely THF and 1,5-diazabiciclo(5.4.0)undec-7-ene (DBU), and in water using NaOH as a base. These three different syntheses gave different complexes that were characterized through SC-XRD. Synthesis of the Ti complex was performed slightly modifying a reported procedure[34]. Crystals obtained by layering technique were of deep yellow-orange color and quite air sensitive, the structure obtained after refinement is shown in Figure 3.23, right. Unexpectedly, the complex obtained is very different from the reported one[34], shown in Figure 3.23, left. The reported complex has an octahedral coordination given by 2 DPA ligands both in a *mer*-geometry (occupying an axial position and two *trans* equatorial positions). This geometry implies that aromatic rings of the same ligand lay on planes with an angle of ~140° while the two ligand molecules are rotated of ~70° embedding the central metal ion, setting the ratio DPA : M on 2 : 1. Our complex crystallizes in a monoclinic ($P2_1/n$) group laying on an inversion center, making only half of the molecule the asymmetric unit, thus even if two ligands and four Ti ions are present only half of them are actually independent. So, the ratio DPA : M is 1 : 2 and there are two different Ti ions which possess different coordination geometries. Ti1 has a octahedral coordination with $DPA^{Cl,Cl}$ in a *fac*-geometry (occupying an axial and two *cis* equatorial position), causing a significant bend in the ligand bringing the aromatic rings onto two planes with an angle of 19.8°. This geometry is stabilized by π-stacking interactions, in fact aromatic rings centroids are at a distance of ~3.6 Å, with typical distance values for these interactions ranging from 3.3 to 3.8 Å[42]. The other three positions are occupied by two bridging oxides and an $i\text{PrO}^-$. Ti2 has a trigonal bipyramidal coordination with three positions occupied by isopropoxides, a bridging oxide and a bridging phenoxide. The four Ti ions, the two bridging oxides and one $i\text{PrO}^-$ lay on the same plane, the two phenoxides are tilted by ~20° and on the same side of one $i\text{PrO}^-$, while the remaining two independent isopropoxides coordinate from the other side of the plane. Obviously, the complex is really air sensitive, as the four independent isopropoxides can be easily protonated by moisture. Crystal data and refinement parameters can be found in Table 3.1, while bond distances and angles are shown in Tables 3.2 and 3.3. It should be noted that distances of ~3 Å between Ti1–Ti2 and Ti1–Ti'1 are compatible with single Ti–Ti bonds[43]. Bond-Valence Sum (BVS) calculations (Table 3.4) show that both Ti ions are in a +4 oxidation state making the overall molecule neutral. The formation of this peculiar complex rather than a more predictable system like the reported one[34] could be due to partial hydrolysis of $Ti(OiPr)_4$ reagent to a low nuclearity titanium oxo-isopropoxide[44]. Furthermore, the extremely low solubility of $DPA^{Cl,Cl}$ makes the Ti source always in a wide excess regardless of used ratios.

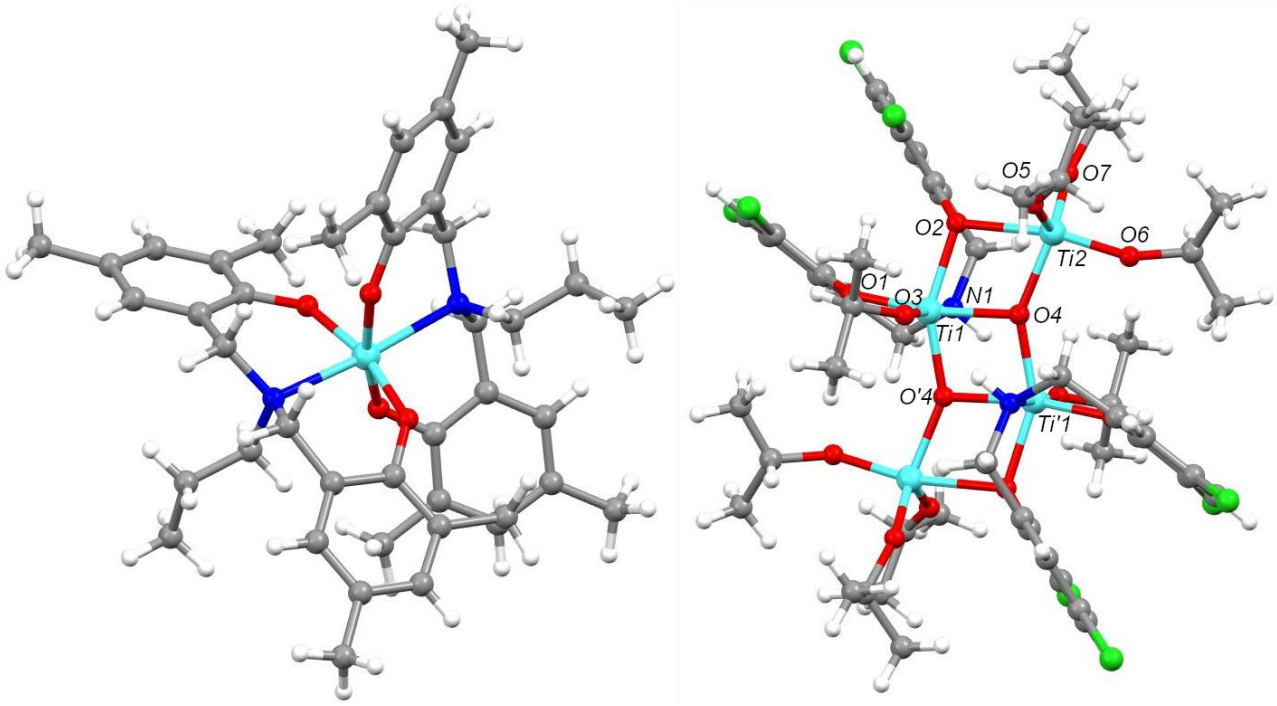

Figure 3.23: Left: Molecular structure of DPA-Ti reported monomer [34] Right: Molecular structure of the obtained Ti-oxoisopropoxo-DPA complex, drawn using a ball-and-stick model. Color code: cyan, Ti; blue, N; dark gray, C; red, O; green, Cl; white, H. Minority disordered components are omitted for clarity.

Table 3.1: Crystal data and refinement parameters for Ti-oxoisopropoxo-DPA^{Cl,Cl} complex

Empirical formula	$C_{52}H_{74}N_2O_{14}Cl_8Ti_4$
Formula weight (g/mol)	1426.33
Temperature/K	298(2)
Radiation	Mo-Kα (λ = 0.71073 Å)
Crystal system	monoclinic
Space group	$P2_1/n$
a (Å)	13.158(5)
b (Å)	16.756(5)
c (Å)	16.010(5)
α (deg)	90.000(5)
β (deg)	105.936(5)
γ (deg)	90.000(5)
V (Å^3)	3394(2)
Z	2
ρ_{calc} (g/cm^3)	1.396
$2\theta_{min}/2\theta_{max}$ (deg)	6.44/53.998
Reflections collected/independent	23093/7326
R_1/wR_2 ($I \geq 2\sigma(I)$)	0.0489/0.1259
R_1/wR_2 (all data)	0.0920/0.1430
Largest diff. peak/hole (e Å^{-3})	0.57/-0.38

Table 3.2: Selected interatomic distances (Å) in Ti-oxoisopropoxo-DPA^{Cl,Cl} complex

Distance	(Å)	Distance	(Å)	Distance	(Å)
Ti1−Ti'1	3.0085(12)	Ti1−O4	1.9144(19)	Ti2−O4	1.961(2)
Ti1− Ti2	3.2590(12)	Ti1−O'4	1.9974(19)	Ti2−O5	1.772(2)
Ti1−O1	1.871(2)	Ti1−N1	2.314(2)	Ti2−O6	1.777(2)
Ti1−O2	2.006(2)	Ti2−O2	2.218(2)	Ti2−O7	1.779(2)
Ti1−O3	1.795(2)				

Table 3.3: Selected interatomic angles (°) in Ti-oxoisopropoxo-DPA^{Cl,Cl} complex

Angles	(°)	Angles	(°)	Angles	(°)
Ti'1−Ti1−Ti'2	72.89(3)	O3−Ti1−Ti'1	99.85(7)	Ti1−O2−Ti'2	100.87(8)
O1−Ti1−Ti'1	145.81(7)	O3−Ti1−Ti'2	94.84(7)	Ti2−O4−Ti'1	110.85(9)
O1−Ti1−Ti'2	136.32(7)	O3−Ti1−O1	95.12(10)	N1−Ti1−Ti'2	89.33(7)
O1−Ti1−O2	94.42(9)	O3−Ti1−O2	100.03(9)	O5−Ti2−O2	92.02(10)
O1−Ti1−O4	107.00(9)	O3−Ti1−O4	97.64(9)	O5−Ti2−O4	111.82(11)
O1−Ti1−O'4	164.93(9)	O3−Ti1−O'4	97.49(9)	O5−Ti2−O6	100.16(13)
O1−Ti1−N1	81.07(9)	O6−Ti2−O7	98.63(12)	O5−Ti2−O7	113.25(13)
O2−Ti1−Ti'1	112.76(6)	O7−Ti2−Ti'1	113.97(8)	O6−Ti2−Ti'1	130.85(9)
O2−Ti1−Ti'2	41.94(6)	O7−Ti2−O4	128.91(10)	O6−Ti2−Ti'1	95.93(11)
O2−Ti1−N1	82.35(8)	C1−O1−Ti1	139.3(2)		

Table 3.4: Bond-Valence Sum calculations on Ti-oxoisopropoxo-DPA^{Cl,Cl} complex

Atom	Ti^{+3}	Ti^{+4}	General Parameters
Ti1	3.121	3.888	3.988
Ti2	3.324	4.345	4.061

As stated before, Co complexes were obtained following two different procedures, working in water or in organic solvent. We chose THF as it is typically used in combination with transition metal chlorides as it is a coordinating solvent and usually able to form more soluble intermediate complexes[45]. We followed a two-step procedure, firstly mixing DPA^{Cl,Cl} and DBU as a base in THF until complete solubilization, supposedly associated to deprotonation, and then slowly adding $CoCl_2$. Dark orange-red crystals obtained from liquid-liquid diffusion were analyzed by SC-XRD, revealing the structure showed in Figure 3.24, while crystal data and refinement parameters can be found in Table 3.5, bond distances and angles are shown in Tables 3.6 and 3.7. This is a monocobalt complex, with a regular octahedral coordination, very similar to the Ti[34] one previously discussed. The two

DPA^{Cl,Cl} ligands are rotated by ~90° both coordinating with a *mer*-geometry, embedding the Co ion in an octahedral cavity. BVS (Table 3.8) clearly shows a Co^{3+}, thus, given the ligands 4 negative charges, electroneutrality is granted by a protonated DBU counterion. DBU acquired proton (H4) is at ~2.1 Å from one of the coordinating oxygens (O2), establishing a quite strong and short H-bond[46], causing an increase in the coordination bond (Co−O2) of 0.027 Å (from 1.899 Å to 1.926 Å)

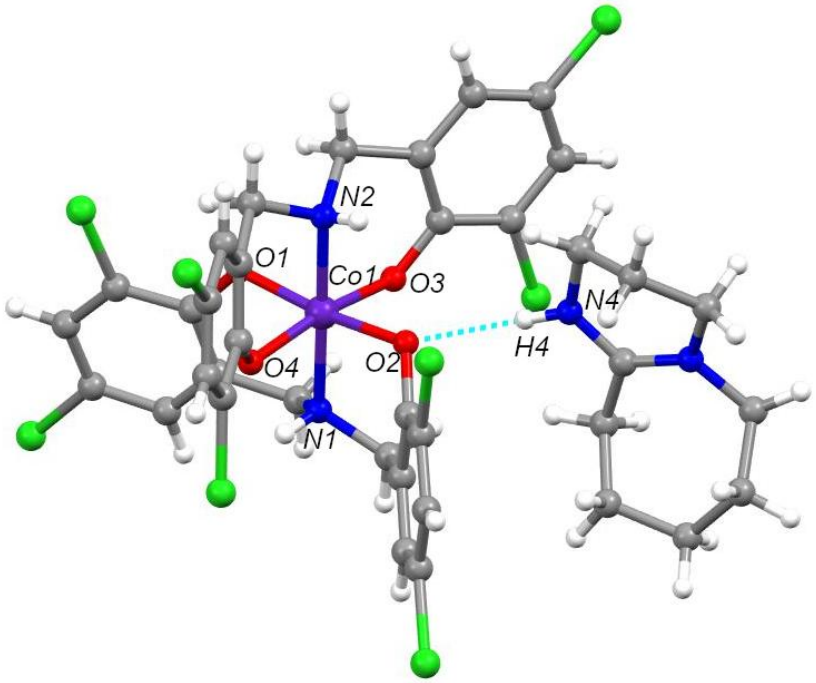

Figure 3.24: Molecular structure of the obtained Co-DPA^{Cl,Cl} monomer, with a protonated DBU counter-ion drawn using a ball-and-stick model. Hydrogen bond is represented as a cyan dotted line. Color code: dark violet, Co; blue, N; dark gray, C; red, O; green, Cl; white, H. Minority disordered components are omitted for clarity.

Table 3.5: Crystal data and refinement parameters for Co-DPA^{Cl,Cl} monomer

Empirical formula	$C_{37}H_{35}N_4O_4Cl_8Co$
Formula weight	942.22
Temperature (K)	298(2)
Crystal system	monoclinic
Space group	$P2_1/c$
a (Å)	11.901(5)
b (Å)	19.260(5)
c (Å)	17.583(5)
α (deg)	90.000(5)
β (deg)	93.705(5)
γ (deg)	90.000(5)
V (Å^3)	4022(2)
Z	4
ρ_{calc} (g/cm^3)	1.556
Radiation	MoKα (λ = 0.71073)
$2\theta_{min}/2\theta_{max}$ (deg)	3.14/51.056
GOF	0.982
R_1/wR_2 ($I \geq 2\sigma(I)$)	0.0402/0.0826
R_1/wR_2 (all data)	0.0849/0.0948
Largest diff. peak/hole / e Å^{-3}	0.32/-0.34

Table 3.6: Selected interatomic distances (Å) in Co-DPA^{Cl,Cl} monomer

Distance	(Å)	Distance	(Å)	Distance	(Å)
Co1−O1	1.8990(19)	Co1−O3	1.899(2)	Co1−N1	1.952(2)
Co1−O2	1.9257(19)	Co1−O4	1.8982(19)	Co1−N2	1.954(2)

Table 3.7: Selected interatomic angles (°) in Co-DPA^{Cl,Cl} monomer

Angles	(°)	Angles	(°)	Angles	(°)
O1−Co1−O2	172.21(7)	O3−Co1−O1	91.31(9)	O4−Co1−O2	91.04(9)
O1−Co1−N1	93.82(8)	O3−Co1−O2	89.36(9)	O4−Co1−O3	170.23(7)
O1−Co1−N2	86.59(10)	O3−Co1−N1	87.04(10)	O4−Co1−N1	83.19(10)
O2−Co1−N1	93.97(8)	O3−Co1−N2	94.57(9)	O4−Co1−N2	95.19(9)
O2−Co1−N2	85.62(10)	O4−Co1−O1	89.62(9)	N1−Co1−N2	178.33(11)

Table 3.8: Bond-Valence Sum calculations on Co-DPA^{Cl,Cl} monomer

Atom	Co^{+2}	Co^{+3}	Co^{+4}	General Parameters
Co1	3.313	2.919	2.445	3.677

Synthesis in water was performed using NaOH as a base and $CoCl_2$ as a source of cobalt. Unfortunately, the 2-step approach did not gave good results, in fact adding $CoCl_2$ to a completely deprotonated ligand always gave brown solutions from which only colorless crystals of DPA^{Cl,Cl} sodium salt were isolated. Changing hydroxide, *i.e.*, working with LiOH or KOH gave similar results. This behavior could be due to the typically great affinity of phenoxides for alkali metal cations that could hamper the formation of a Co complex. Thus a one pot procedure in NaOH defect was tested, working with a ratio DPA^{Cl,Cl} : $CoCl_2$: NaOH of 1 : 1 : 1 giving a bright green solution, that turned brown in a few hours at room temperature, or quickly upon heating. Given this observation we decided to perform a sort of discontinuous titration to establish the amount of NaOH required to obtain a stable green color. The ratio DPA^{Cl,Cl} : $CoCl_2$ was set to 1 : 1, while NaOH equivalents were varied between 0 and 1. All the experiments were then heated to 80 °C for 2 h, and visually inspected to detect macroscopic color changes. When 0.7–1.0 eq of NaOH were added the system turned brown during the heating phase, while below 0.6 eq the green coloration was retained. Working with 0.6 eq of base means that only 30% of the ligand can be fully deprotonated, heavily affecting maximum crystals yields, nonetheless this is the only way we found to isolate bright green prisms instead of colorless plates. These green crystals were obtained from liquid-liquid diffusion and analyzed through SC-XRD revealing the structure showed in Figure 3.25, while crystal data and refinement parameters

can be found in Table 3.9, bond distances and angles are shown in Tables 3.10 and 3.11. The asymmetric unit is made by two independent clusters of 4 ligand molecules and 4 cobalt ions each. The 4 Co lays on the same plane forming a square with an oxide anion in the center of it which is sandwiched between two axial Na cations. Each Co is in a square planar coordination, made by two phenoxides and the amine of a single $DPA^{Cl,Cl}$ molecule plus the central oxide anion, the planes described by coordinating atoms are all tilted by ~51° from the 4Co plane. Both axial Na ions strongly interact with two Cl at ~2.9 Å, a shorter distance than the sum of van der Waals radii. Distances between Co ions is of ~2.8 Å, too long to consider them bonded[47]. BVS (Table 3.12) indicates 4 Co^{2+} in both clusters, thus, considering 4 phenoxides and an oxide each cluster is neutral thanks to Na cations. The structure has very large solvent accessible cavities and channels, showed in Figure 3.26, corresponding to ~1/4 of total cell volume (4380/16071 $Å^3$), in which disordered and non-modellable residual electron density is equal to 461 electrons, that is ~11 molecules of DCM or ~9 molecules of *n*-hexane (solvents used for layering).

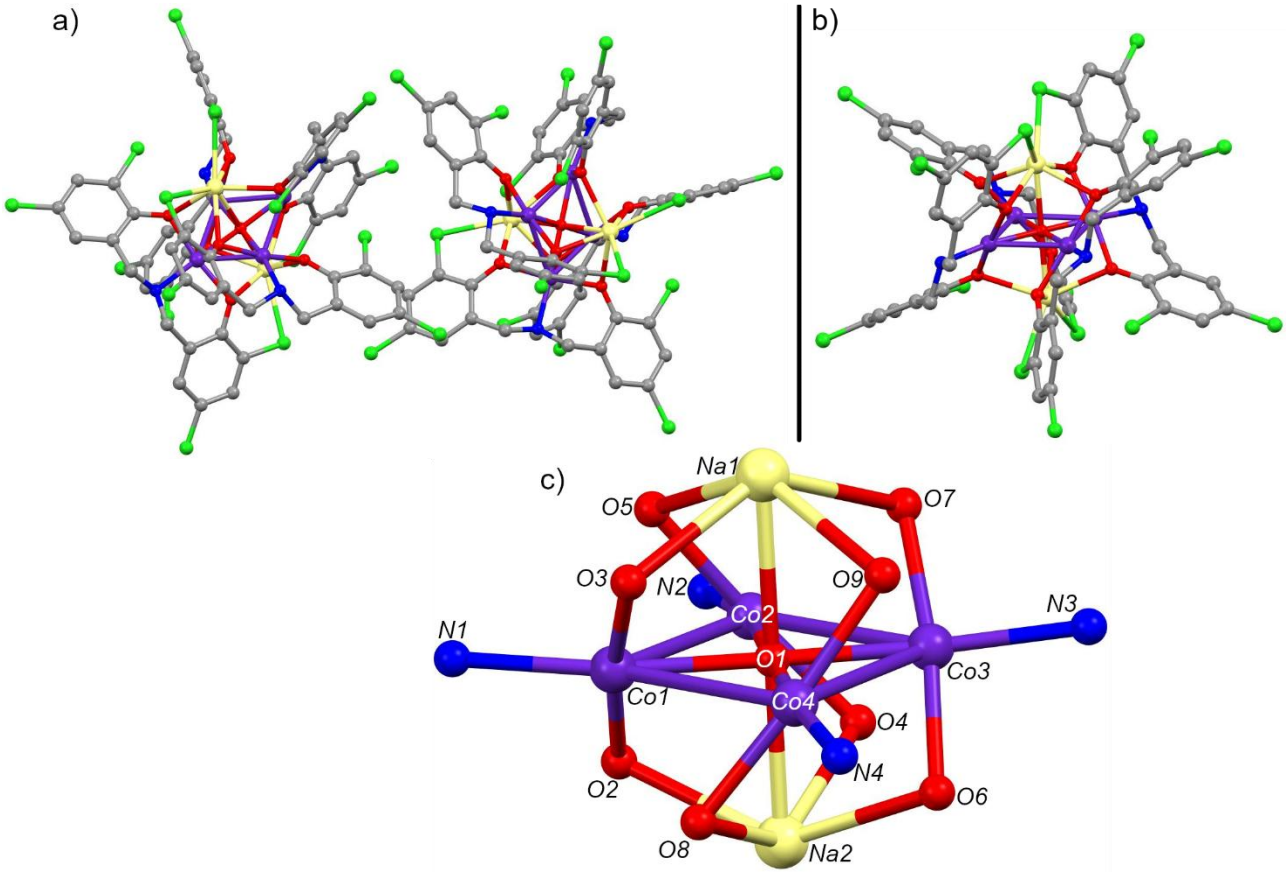

Figure 3.25: a) Molecular structure of the obtained Co-$DPA^{Cl,Cl}$ tetramer; b) Magnification and rotation of one molecule to highlight the cluster; c) Magnification of core cluster to highlight metal coordination; each drawn using a ball-and-stick model. Color code: dark violet, Co; blue, N; dark gray, C; red, O; green, Cl; yellow, Na. Hydrogen atoms and minority disordered components are omitted for clarity.

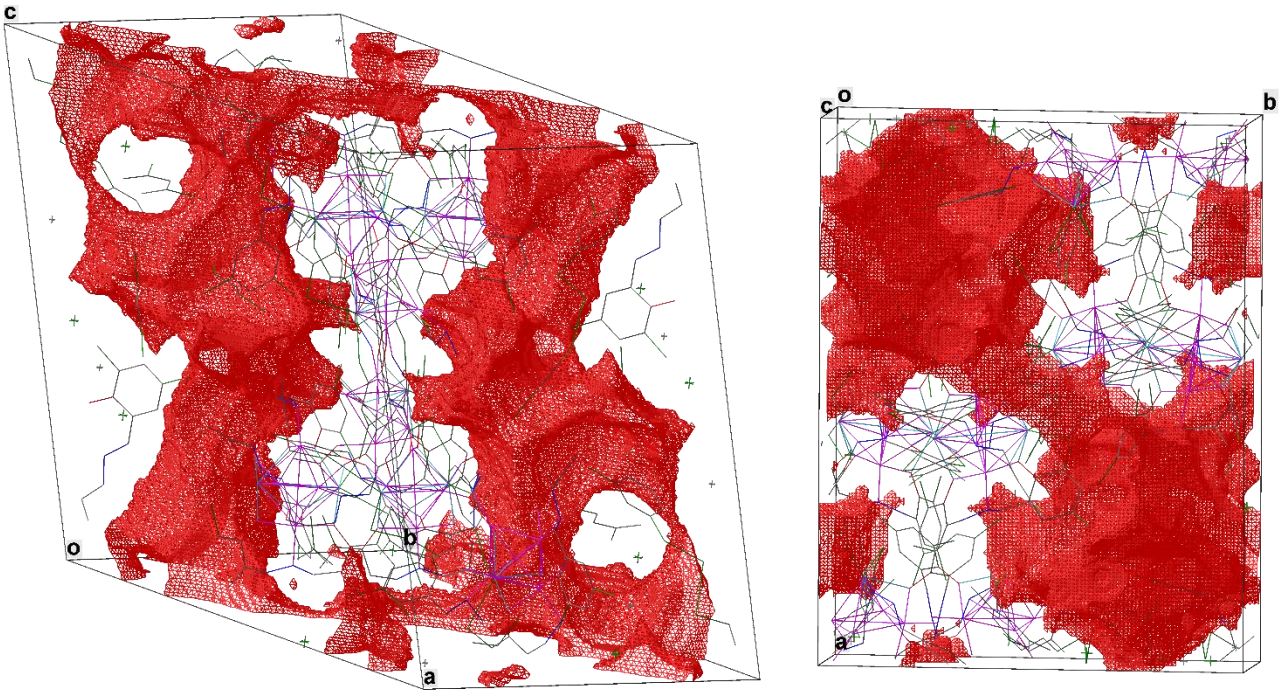

Figure 3.26: Crystal cells with solvent accessible cavities highlighted in red. Left: Side-view; Right: C-axis view.

Table 3.9: Crystal data and refinement parameters for Co-DPA^{Cl,Cl} tetramer

Empirical formula	$C_{112}H_{72}N_8O_{18}Cl_{32}Co_8Na_4$
Formula weight	3515.57
Temperature (K)	298(2)
Crystal system	monoclinic
Space group	$P2_1/c$
a (Å)	29.801(5)
b (Å)	21.328(5)
c (Å)	27.225(5)
α (deg)	90.000(5)
β (deg)	111.761(5)
γ (deg)	90.000(5)
V (Å^3)	16071(6)
Z	4
ρ_{calc} (g/cm^3)	1.453
Radiation	MoKα (λ = 0.71073)
$2\theta_{min}/2\theta_{max}$ (deg)	3.746/52.066
GOF	1.031
R_1/wR_2 ($I \geq 2\sigma(I)$)	0.0448/0.1119
R_1/wR_2 (all data)	0.0905/0.1294
Largest diff. peak/hole / e Å^{-3}	0.59/-0.53

Table 3.10: Selected interatomic distances (Å) in Co-DPA^{Cl,Cl} tetramer

Distance	(Å)	Distance	(Å)	Distance	(Å)
Co1−Co2	2.8152(8)	Co2−N2	2.007(3)	Cl1−Na2	2.841(2)
Co1−Co4	2.8832(7)	Co3−Co4	2.8106(8)	Na1−O1	2.397(3)
Co1−Na1	3.1019(16)	Co3−Na1	3.1268(17)	Na1−O3	2.438(3)
Co1−Na2	3.1315(17)	Co3−Na2	3.1004(16)	Na1−05	2.385(3)
Co1−O1	2.003(2)	Co3−O1	1.999(2)	Na1−O7	2.431(3)
Co1−O2	1.945(3)	Co3−O6	1.971(3)	Na1−O9	2.409(3)
Co1−O3	1.945(3)	Co3−O7	1.965(3)	Na2−O1	2.379(3)
Co1−N1	2.019(3)	Co3−N3	2.000(3)	Na2−O2	2.379(3)
Co2−Co3	2.8650(7)	Co4−Na1	3.1485(16)	Na2−O4	2.474(3)
Co2−Na1	3.1267(16)	Co4−Na2	3.1124(17)	Na2−O6	2.370(3)
Co2−Na2	3.1246(17)	Co4−O1	2.023(2)	Na2−O8	2.468(3)
Co2−O1	2.018(2)	Co4−O8	1.949(2)	Cl15−Na1	2.8537(19)
Co2−O4	1.944(3)	Co4−O9	1.942(2)	Cl9−Na2	2.875(2)
Co2−O5	1.943(3)	Co4−N4	2.021(3)	Cl7−Na1	2.933(2)

Table 3.11: Selected interatomic angles (°) in Co-DPA^{Cl,Cl} tetramer

Angles	(°)	Angles	(°)	Angles	(°)
Co2−Co1−Co4	90.34(2)	N3−Co3−Na1	124.07(10)	O9−Na1−Cl15	67.35(7)
Co2−Co1−Na1	63.58(3)	N3−Co3−Na2	134.85(10)	O9−Na1−O3	82.28(10)
Co2−Co1−Na2	63.13(3)	Co1−Co4−Na1	61.71(3)	O9−Na1−O7	81.79(10)
Co4−Co1−Na1	63.36(3)	Co1−Co4−Na2	62.84(3)	Co2−Na2−Co1	53.49(3)
Co4−Co1−Na2	62.16(3)	Co3−Co4−Co1	89.29(2)	Co3−Na2−Co1	79.89(4)
Na1−Co1−Na2	100.01(4)	Co3−Co4−Na1	63.00(3)	Co3−Na2−Co2	54.80(3)
O1−Co1−Co2	45.79(7)	Co3−Co4−Na2	62.89(3)	Co3−Na2−Co4	53.79(3)
O1−Co1−Co4	44.55(7)	Na2−Co4−Na1	99.41(5)	Co4−Na2−Co1	55.00(3)
O1−Co1−Na1	50.60(7)	O1−Co4−Co1	43.98(6)	Co4−Na2−Co2	80.78(4)
O1−Co1−Na2	49.42(7)	O1−Co4−Co3	45.31(7)	Cl1−Na2−Co1	105.12(5)
O1−Co1−N1	169.62(12)	O1−Co4−Na1	49.58(7)	Cl1−Na2−Co2	99.01(6)
O2−Co1−Co2	60.59(8)	O1−Co4−Na2	49.84(7)	Cl1−Na2−Co3	144.06(7)
O2−Co1−Co4	111.56(8)	O8−Co4−Co1	61.17(8)	Cl1−Na2−Co4	155.44(6)
O2−Co1−Na1	123.92(8)	O8−Co4−Co3	115.29(8)	Cl1−Na2−Cl9	91.40(6)
O2−Co1−Na2	49.40(8)	O8−Co4−Na1	122.87(8)	Cl9−Na2−Co1	142.72(7)
O2−Co1−O1	85.42(10)	O8−Co4−Na2	52.45(8)	Cl9−Na2−Co2	156.92(6)
O2−Co1−O3	171.90(11)	O8−Co4−O1	87.13(10)	Cl9−Na2−Co3	105.98(6)

O2−Co1−N1	93.30(12)	O8−Co4−N4	94.64(11)	Cl9−Na2−Co4	98.12(6)
O3−Co1−Co2	115.34(8)	O9−Co4−Co1	111.55(8)	O1−Na2−Co1	39.76(6)
O3−Co1−Co4	60.67(8)	O9−Co4−Co3	60.33(8)	O1−Na2−Co2	40.23(6)
O3−Co1−Na1	51.81(8)	O9−Co4−Na1	49.87(8)	O1−Na2−Co3	40.14(6)
O3−Co1−Na2	122.80(9)	O9−Co4−Na2	123.02(8)	O1−Na2−Co4	40.55(6)
O3−Co1−O1	87.01(10)	O9−Co4−O1	85.49(10)	O1−Na2−Cl1	134.21(9)
O3−Co1−N1	94.66(12)	O9−Co4−O8	172.27(11)	O1−Na2−Cl9	134.37(9)
N1−Co1−Co2	125.10(10)	O9−Co4−N4	93.01(11)	O1−Na2−O2	68.51(9)
N1−Co1−Co4	144.07(10)	N4−Co4−Co1	143.92(9)	O1−Na2−O4	68.21(9)
N1−Co1−Na1	123.54(10)	N4−Co4−Co3	126.46(9)	O1−Na2−O8	68.77(9)
N1−Co1−Na2	135.27(10)	N4−Co4−Na1	134.46(9)	O2−Na2−Co1	38.36(6)
Co1−Co2−Co3	89.57(2)	N4−Co4−Na2	125.16(9)	O2−Na2−Co2	52.30(7)
Co1−Co2−Na1	62.68(3)	N4−Co4−O1	170.73(12)	O2−Na2−Co3	103.04(8)
Co1−Co2−Na2	63.38(3)	Co1−Na1−Co2	53.74(3)	O2−Na2−Co4	93.36(8)
Co3−Co2−Na1	62.73(3)	Co1−Na1−Co3	79.95(4)	O2−Na2−Cl1	68.38(8)
Co3−Co2−Na2	62.17(3)	Co1−Na1−Co4	54.93(3)	O2−Na2−Cl9	150.16(9)
Na2−Co2−Na1	99.62(4)	Co2−Na1−Co4	80.19(4)	O2−Na2−O4	82.24(10)
O1−Co2−Co1	45.34(7)	Co3−Na1−Co2	54.53(3)	O2−Na2−O8	82.59(10)
O1−Co2−Co3	44.23(7)	Co3−Na1−Co4	53.22(3)	O4−Na2−Co1	91.91(8)
O1−Co2−Na1	50.05(7)	Cl7−Na1−Co1	96.57(5)	O4−Na2−Co2	38.46(6)
O1−Co2−Na2	49.57(7)	Cl7−Na1−Co2	104.01(5)	O4−Na2−Co3	52.69(7)
O4−Co2−Co1	115.67(8)	Cl7−Na1−Co3	155.67(6)	O4−Na2−Co4	102.64(8)
O4−Co2−Co3	60.11(8)	Cl7−Na1−Co4	141.93(6)	O4−Na2−Cl1	91.37(9)
O4−Co2−Na1	122.84(8)	Cl15−Na1−Co1	156.35(6)	O4−Na2−Cl9	121.38(9)
O4−Co2−Na2	52.35(8)	Cl15−Na1−Co2	140.75(6)	O6−Na2−Co1	103.65(8)
O4−Co2−O1	86.78(10)	Cl15−Na1−Co3	96.39(5)	O6−Na2−Co2	94.27(8)
O4−Co2−N2	94.76(12)	Cl15−Na1−Co4	104.20(5)	O6−Na2−Co3	39.47(7)
O5−Co2−Co1	60.73(8)	Cl15−Na1−Cl7	95.91(6)	O6−Na2−Co4	52.51(7)
O5−Co2−Co3	112.39(8)	O1−Na1−Co1	40.21(6)	O6−Na2−Cl1	150.84(9)
O5−Co2−Na1	49.67(8)	O1−Na1−Co2	40.20(6)	O6−Na2−Cl9	67.93(8)
O5−Co2−Na2	123.90(8)	O1−Na1−Co3	39.73(6)	O6−Na2−O1	69.68(9)
O5−Co2−O1	86.21(10)	O1−Na1−Co4	39.99(6)	O6−Na2−O2	138.18(11)
O5−Co2−O4	172.31(11)	O1−Na1−Cl7	132.23(9)	O6−Na2−O4	83.05(10)
O5−Co2−N2	92.71(11)	O1−Na1−Cl15	131.85(9)	O6−Na2−O8	82.05(10)
N2−Co2−Co1	125.64(9)	O1−Na1−O3	68.42(9)	O8−Na2−Co1	53.45(7)
N2−Co2−Co3	144.26(9)	O1−Na1−O7	68.42(9)	O8−Na2−Co2	103.12(8)
N2−Co2−Na1	134.87(9)	O1−Na1−O9	68.14(9)	O8−Na2−Co3	92.53(7)

N2−Co2−Na2	124.35(9)	O3−Na1−Co1	38.84(7)	O8−Na2−Co4	38.76(6)
N2−Co2−O1	169.53(11)	O3−Na1−Co2	92.55(8)	O8−Na2−Cl1	119.44(9)
Co2−Co3−Na1	62.73(3)	O3−Na1−Co3	102.17(8)	O8−Na2−Cl9	89.29(8)
Co2−Co3−Na2	63.03(3)	O3−Na1−Co4	52.92(7)	O8−Na2−O4	136.99(11)
Co4−Co3−Co2	90.80(2)	O3−Na1−Cl7	89.01(9)	Co1−O1−Co2	88.87(9)
Co4−Co3−Na1	63.79(3)	O3−Na1−Cl15	121.63(9)	Co1−O1−Co4	91.47(9)
Co4−Co3−Na2	63.32(3)	O5−Na1−Co1	52.74(7)	Co1−O1−Na1	89.19(9)
Na2−Co3−Na1	100.15(4)	O5−Na1−Co2	38.39(6)	Co1−O1−Na2	90.83(9)
O1−Co3−Co2	44.77(7)	O5−Na1−Co3	92.91(8)	Co2−O1−Co4	179.62(15)
O1−Co3−Co4	46.03(7)	O5−Na1−Co4	103.54(8)	Co2−O1−Na1	89.75(9)
O1−Co3−Na1	50.05(7)	O5−Na1−Cl7	66.80(7)	Co2−O1−Na2	90.20(9)
O1−Co3−Na2	50.10(7)	O5−Na1−Cl15	150.80(9)	Co3−O1−Co1	179.40(14)
O1−Co3−N3	170.31(12)	O5−Na1−O1	68.96(9)	Co3−O1−Co2	91.00(9)
O6−Co3−Co2	112.85(8)	O5−Na1−O3	82.94(10)	Co3−O1−Co4	88.66(9)
O6−Co3−Co4	60.47(8)	O5−Na1−O7	82.07(10)	Co3−O1−Na1	90.22(9)
O6−Co3−Na1	124.04(8)	O5−Na1−O9	137.09(11)	Co3−O1−Na2	89.76(9)
O6−Co3−Na2	49.84(8)	O7−Na1−Co1	102.61(8)	Co4−O1−Na1	90.44(9)
O6−Co3−O1	86.20(10)	O7−Na1−Co2	52.80(7)	Co4−O1−Na2	89.62(9)
O6−Co3−N3	93.13(12)	O7−Na1−Co3	38.94(7)	Na2−O1−Na1	179.9(2)
O7−Co3−Co2	60.33(8)	O7−Na1−Co4	92.14(8)	Co1−O2−Na2	92.24(11)
O7−Co3−Co4	114.81(8)	O7−Na1−Cl7	120.94(9)	Co1−O3−Na1	89.35(11)
O7−Co3−Na1	51.04(8)	O7−Na1−Cl15	87.95(8)	Co2−O4−Na2	89.18(10)
O7−Co3−Na2	123.31(8)	O7−Na1−O3	136.83(11)	Co2−O5−Na1	91.94(11)
O7−Co3−O1	86.45(10)	O9−Na1−Co1	92.97(7)	Co3−O6−Na2	90.69(11)
O7−Co3−O6	172.47(11)	O9−Na1−Co2	102.59(8)	Co3−O7−Na1	90.02(10)
O7−Co3−N3	94.40(12)	O9−Na1−Co3	51.82(7)	Co4−O8−Na2	88.79(10)
N3−Co3−Co2	142.88(10)	O9−Na1−Co4	38.06(6)	Co4−O9−Na1	92.07(10)
N3−Co3−Co4	125.79(10)	O9−Na1−Cl7	152.32(9)		

Table 3.12: Bond-Valence Sum calculations on Co-DPA^{Cl,Cl} tetramer

Atom	Co^{2+}	Co^{3+}	Co^{4+}	General Parameters
Co1	1.887	1.653	1.559	2.056
Co2	1.888	1.655	1.545	2.064
Co3	1.854	1.626	1.497	2.039
Co4	1.859	1.629	1.532	2.030
Co5	1.861	1.632	1.514	2.041
Co6	1.883	1.651	1.531	2.064
Co7	1.859	1.630	1.505	2.042
Co8	1.909	1.672	1.575	2.079

3.4 Synthesis of chlorometilated phenols (PhX_2CH_2Cls) precursors

Given the reliable pathway to DPAs described in Section 3.2 we started considering potential methods to upgrade DPAs to TPAs. The most straightforward method, as previously reported[21,31], would be to perform an electrophilic attack with a halo-methylated phenol to the amine. Thus, a method to obtain these from our three deactivated phenols is required. This step may seem easy as different procedures exist to add a halo-methylene group to a phenol, *i.e.* Blanc reactions[48–51]. Unfortunately, these methods are usually well described for electron-rich substrate and known to work poorly on deactivated aromatics due to the formaldehyde electrophilic attack step. Thus, we considered a different two step approach, shown in Figure 3.27, starting with the addition of a hydroxy-methylene group. This first step is similar to the typical synthesis of phenol-formaldehyde polymers in basic medium. In our conditions self-condensation should be minimized to avoid yield loss, this can be done working in an excess of base rather than with a catalytic amount. This process is known to be poorly selective, giving mixtures of *o*- and *p*- products, luckily our substrates possess only one free *o*- position making the procedure usable. The second step consists of chlorination with thionyl chloride, which is a quite typical method to obtain alkyl and acyl chlorides from acids and alcohols[52–58].

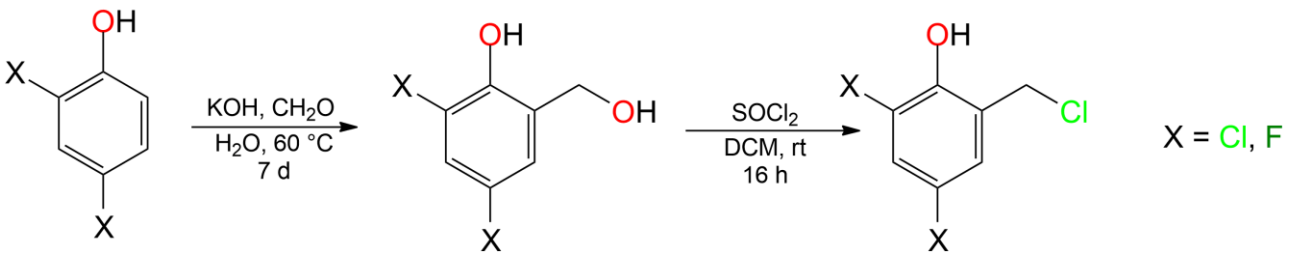

Figure 3.27: Two-step reaction pathway to $PhCl_2CH_2Cl$ and PhF_2CH_2Cl. First step: base-catalyzed nucleophilic attack to CH_2O; Second step: Chlorination with $SOCl_2$

The first step is surely the most critical as electron-poor phenols can be easily deprotonated stabilizing the negative charge on the ring and therefore decreasing their reactivity, increasing the amount of possible side products. In fact, before performing the second step that proceeded smoothly, both $PhCl_2$ and PhF_2 required a difficult chromatography purification giving average yields. Unfortunately, $PhClNO_2$ proved to be completely unreactive in these conditions, always yielding only the starting materials. This is possibly due to the higher electron-withdrawing character of NO_2 when compared to a halogen, that causes the phenol to be much more deactivated. This is probably reducing the partial negative charge on the *o*-position useful for nucleophilic attack, making the substrate completely unreactive in these conditions.

At this point, given the general unsuccessfulness of this two-step approach we started delving into reported literature of Blanc reaction modifications, searching for applications on not-so-active substrates. Luckily, we found the work of Wang *et al.*[59] describing halo-methylation of substituted salicylaldehydes using H_2SO_4 as a catalyst, as shown in Figure 3.28.

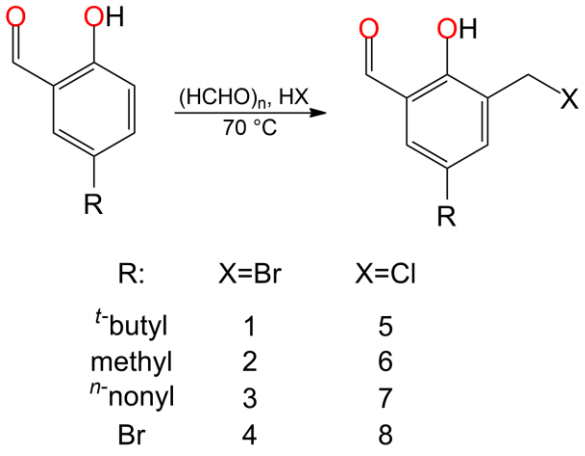

Product	Reaction time	Yield (%)
1	20 h	98
2	2 h	95
3	9 days	93
4	66 h	85
5	45 h	93
6	4 h	97
7	10 days	~50
8	6.5 days	~40

Figure 3.28: Reported pseudo-Blanc reaction on deactivated substrates, adapted from *Wang et al.* [59]

Reported yields are generally high, while reaction times are quite long. Direct application of this procedure with HCl to $PhCl_2$ and PhF_2 gave decent results, thus we worked on optimization to minimize by-products and reaction time (Figure 3.29). In particular, best results were obtained by increasing the amount of H_2SO_4 and decreasing temperature and reaction time, giving the chloromethylated products in high yield with no need of further purifications after solvent extraction.

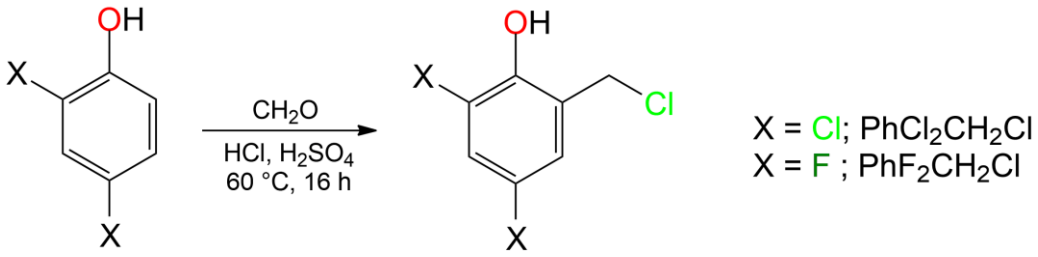

Figure 3.29: Pseudo-Blanc reaction optimized on $PhCl_2$ and PhF_2 to give $PhCl_2CH_2Cl$ and PhF_2CH_2Cl in a single step

$PhClNO_2$ proved to be recalcitrant also in these conditions, even when higher amount of H_2SO_4 and higher temperature were employed. Thus, a different approach was tested, completely removing water from the system, *i.e.*, mixing solids $PhClNO_2$, paraformaldehyde and NaCl in excess, then adding H_2SO_4 as a solvent. The first attempts revealed through ^1H NMR complete conversion after a week to the desired product, contaminated by 25% of the self-condensation by-product shown in Figure 3.30.

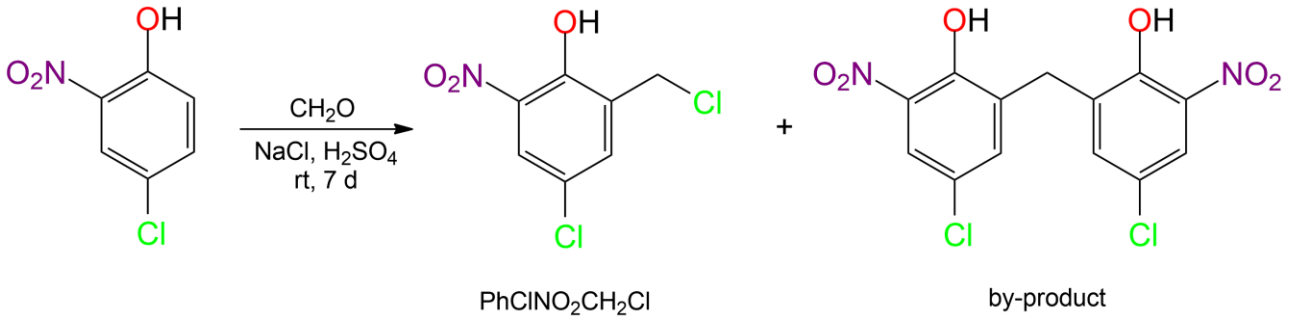

Figure 3.30: Direct chloromethylation of $PhClNO_2$. On the left the desired product ($PhClNO_2CH_2Cl$), on the right an unwanted self-condensation by-product

Separation of these two substances proved to be extremely difficult, therefore we decided to work on reaction conditions to minimize by-product formation. In particular, using even bigger excesses of NaCl did not affect significantly the products ratio. On the other hand, we found that the amount of water is crucial in determining selectivity for this reaction. As stated before, when the reaction is performed in HCl conc. the amount of water is too high, and unreacted $PhClNO_2$ is recovered. A similar behavior was observed also working with H_2SO_4 50% showing low conversion to $PhClNO_2CH_2Cl$. However, when the proper amount of water is added to H_2SO_4 conc., the formation of this impurity can be reduced to ~2% (estimated through ^1H NMR) without affecting conversion.

$PhCl_2CH_2Cl$, PhF_2CH_2Cl and $PhClNO_2CH_2Cl$ are novel compounds, therefore they were fully characterized through NMR spectroscopy as shown in Figures 3.31–3.50. Assignments were determined through careful analysis of 1D (^1H, ^{13}C and ^{19}F when applicable) and 2D (^1H–^1H COSY, ^1H–^{13}C HSQC, ^1H–^{13}C HMBC and ^1H–^{19}F HMBC when applicable) spectra. Unfortunately, soft-

ionization systems, like ESI, frequently fail on phenols as their ionization typically is hard both in positive and negative mode, thus no mass spectrum is available for these compounds.

3.4.1 Characterization of 2,4-dichloro-6-(chloromethyl)phenol ($PhCl_2CH_2Cl$)

Both $PhCl_2CH_2Cl$ and $PhCl_2CH_2OH$ possess good solubility in organic solvents, thus NMR experiments were performed in $CDCl_3$. Figure 3.31 shows the ^1H NMR spectrum of $PhCl_2CH_2OH$, full characterization for this compound has not been recorded as the two-step pathway was discarded. The typical $PhCl_2CH_2OH$ spectra has 4 signals, 2 aromatic pseudo-doublets, at 7.29 and 7.13 ppm split by similar coupling constants of ~2.5 Hz, a broad OH signal at 6.61 ppm and an area 2 singlet at 4.78 ppm. Assignations for the aromatic part are based on the hypothesis that deshielding of two *o*-chloride should be higher than that of one *o*- and one *p*-chloride, while regarding OH it comes from *δ*, as a benzylic OH should be expected in 1.5–3.5 ppm region.

Figure 3.32 shows ^1H NMR spectrum of $PhCl_2CH_2Cl$, which is very similar in signals shape and positions to the $PhCl_2CH_2OH$ one, as it should be given the small differences between the two molecules. In particular, aromatic signals shift to slightly higher *δ* of 7.32 and 7.28 ppm, while OH and methylene signals shift to lower ones, namely 5.77 and 4.62 ppm. In Figure 3.33 is represented the typical ^{13}C NMR $PhCl_2CH_2Cl$ spectrum, with the 7 expected signals all visible, 5 aromatic signals are clustered between 130 and 120 ppm while the phenolic one lays at 148.32 ppm. The aliphatic carbon stands at 40.50 ppm, being both benzylic and chlorinated. Figure 3.36 represents ^1H–^{13}C HMBC interestingly showing couplings between *OH* proton and *C1, C2* and *C6*, this is quite unusual as usually correlations through heteroatoms cannot be seen.

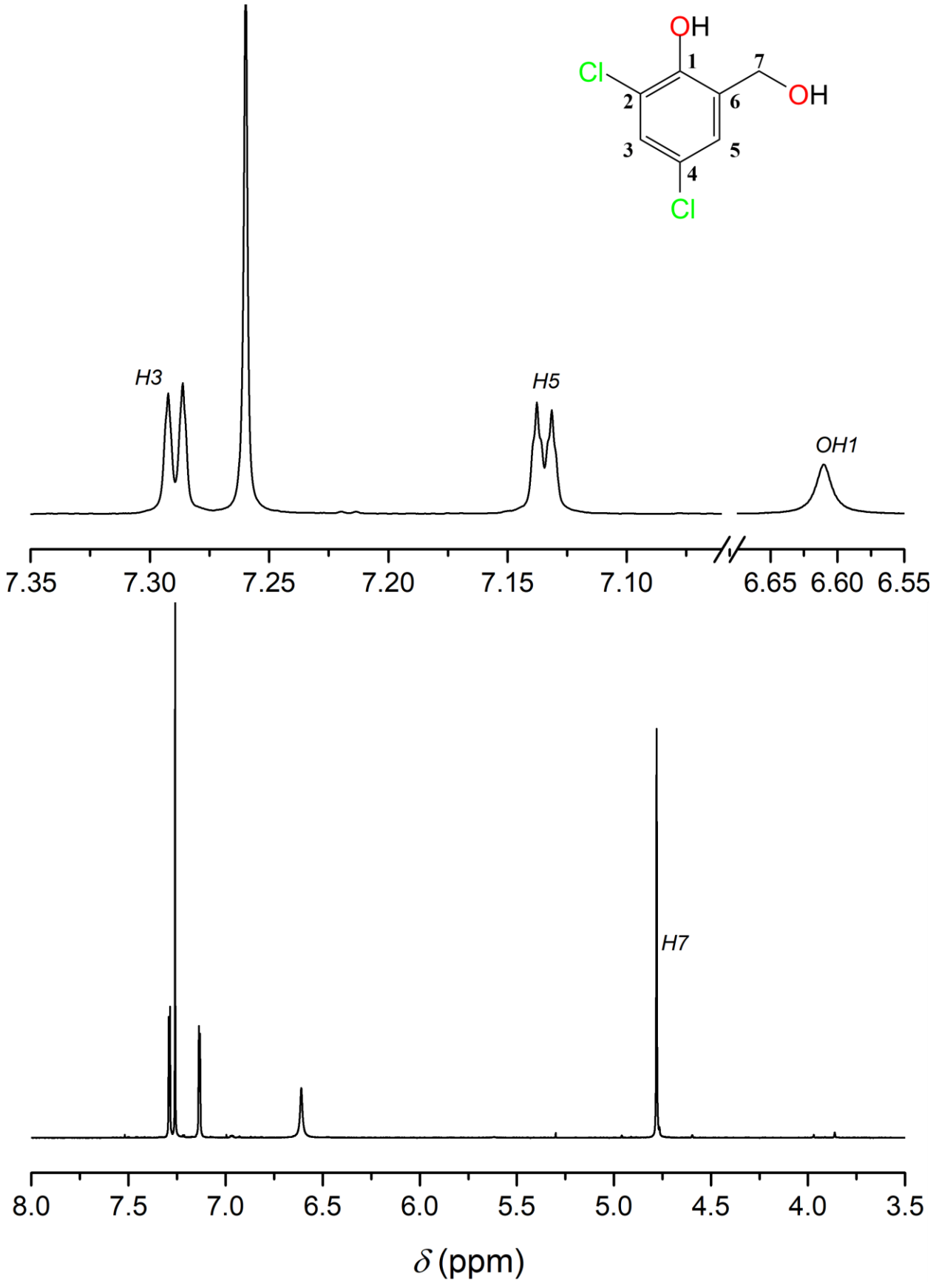

Figure 3.31: Bottom: ^{1}H NMR spectrum of $PhCl_2MeOH$ in $CDCl_3$ (298 K, 400.13 MHz). Top: structure of $PhCl_2MeOH$ and magnification of the spectrum in 7.35–7.05 ppm and 6.70–6.55 ppm ranges. Processing parameters (TopSpin 4.3.0): SI = TD, LB = 0.30 Hz. δ_H (ppm) = 7.26 (residual protons in $CDCl_3$)

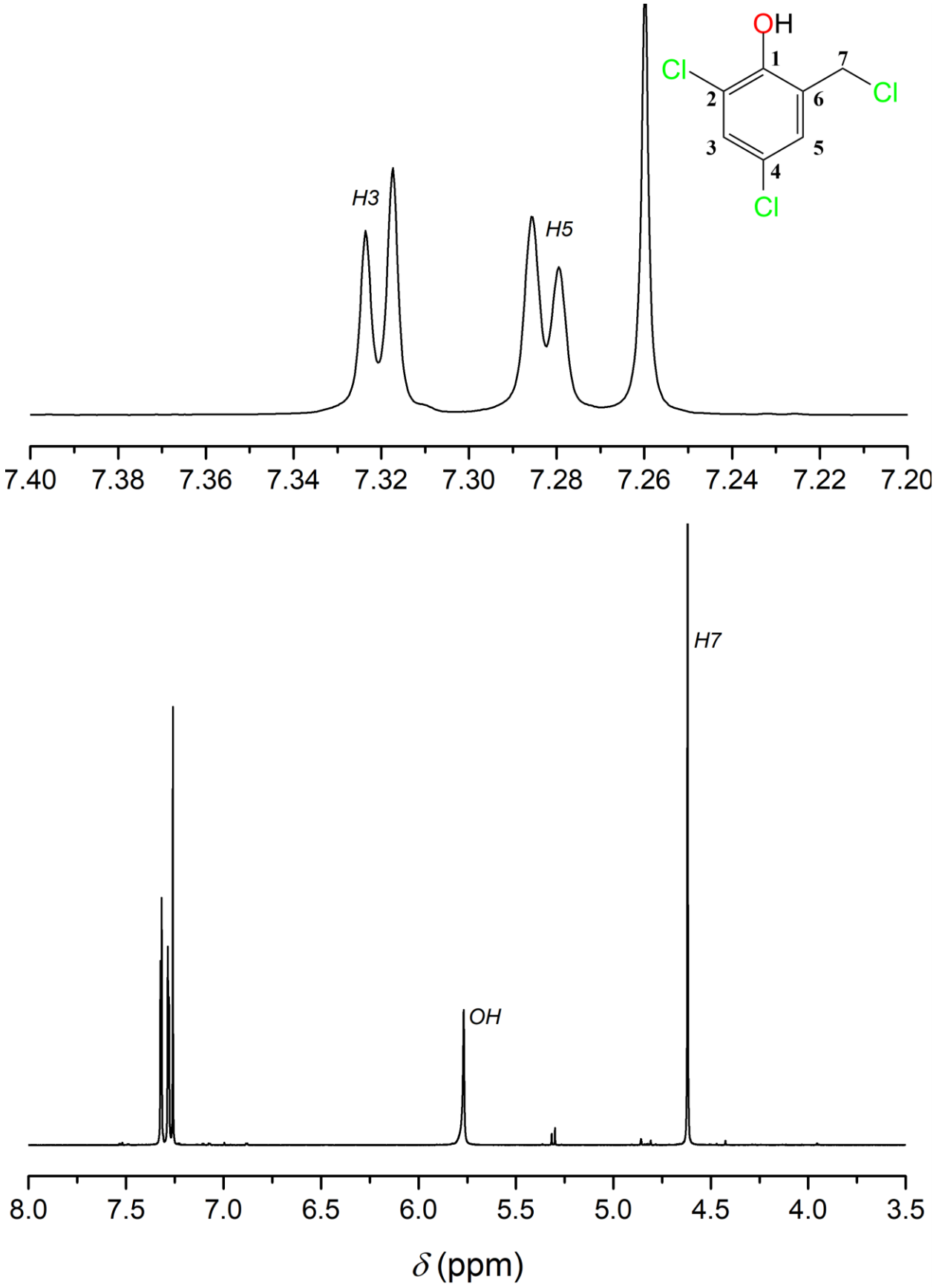

Figure 3.32: Bottom: ^{1}H NMR spectrum of $PhCl_2CH_2Cl$ in $CDCl_3$ (298 K, 400.13 MHz). Top: structure of $PhCl_2CH_2Cl$ and magnification of the spectrum between 7.40 ppm and 7.20 ppm. Processing parameters (TopSpin 4.3.0): SI = TD, LB = 0.30 Hz. δ_H (ppm) = 7.26 (residual protons in $CDCl_3$)

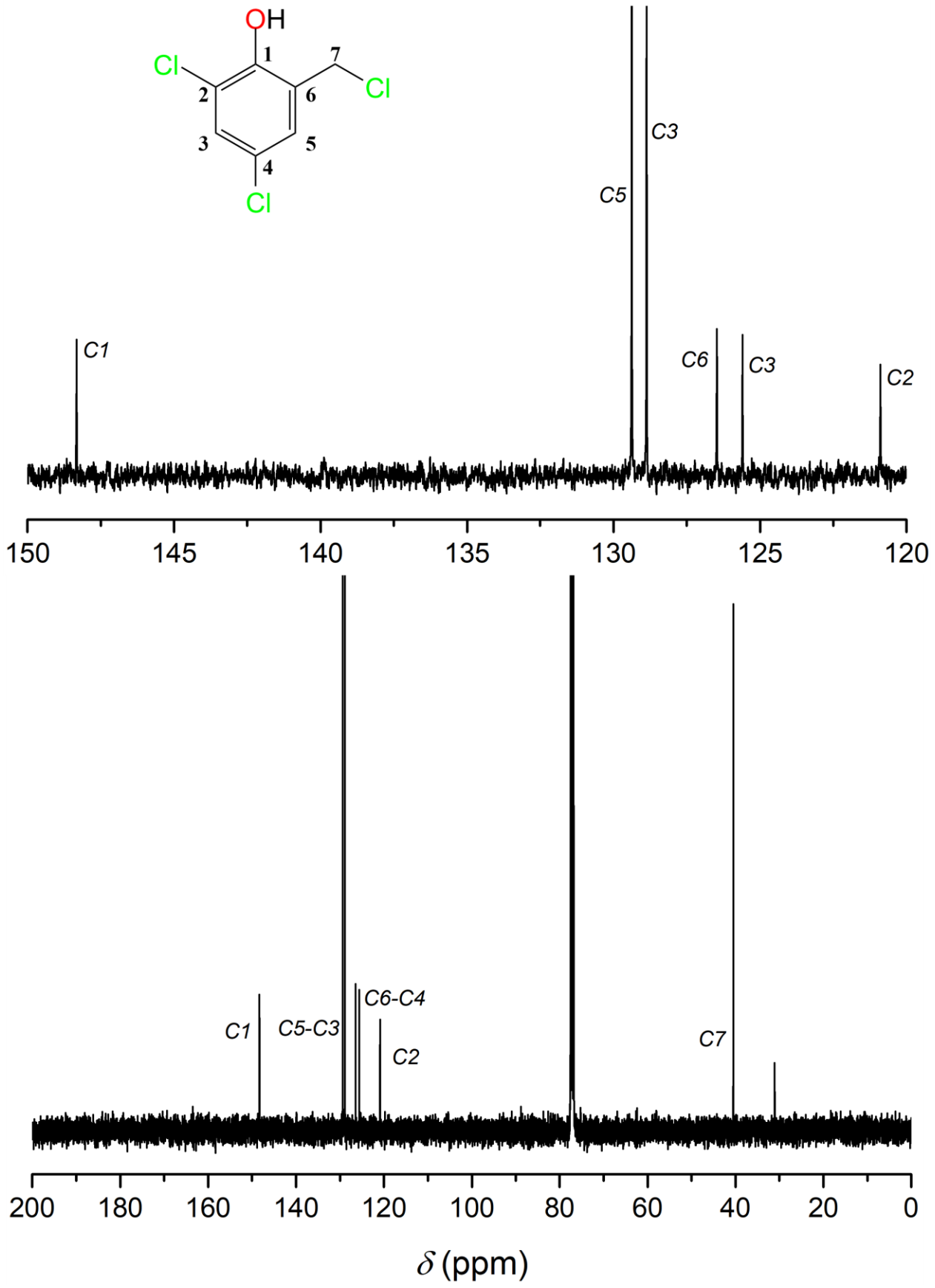

Figure 3.33: Bottom: ^{13}C NMR spectrum of $PhCl_2CH_2Cl$ in $CDCl_3$ (298 K, 400.13 MHz). Top: Structure of $PhCl_2CH_2Cl$ and magnification of the spectrum between 150 ppm and 120 ppm. Processing parameters (TopSpin 4.3.0): SI = TD, LB = 0.30 Hz. δ_C (ppm) = 77.16 (residual carbon in $CDCl_3$)

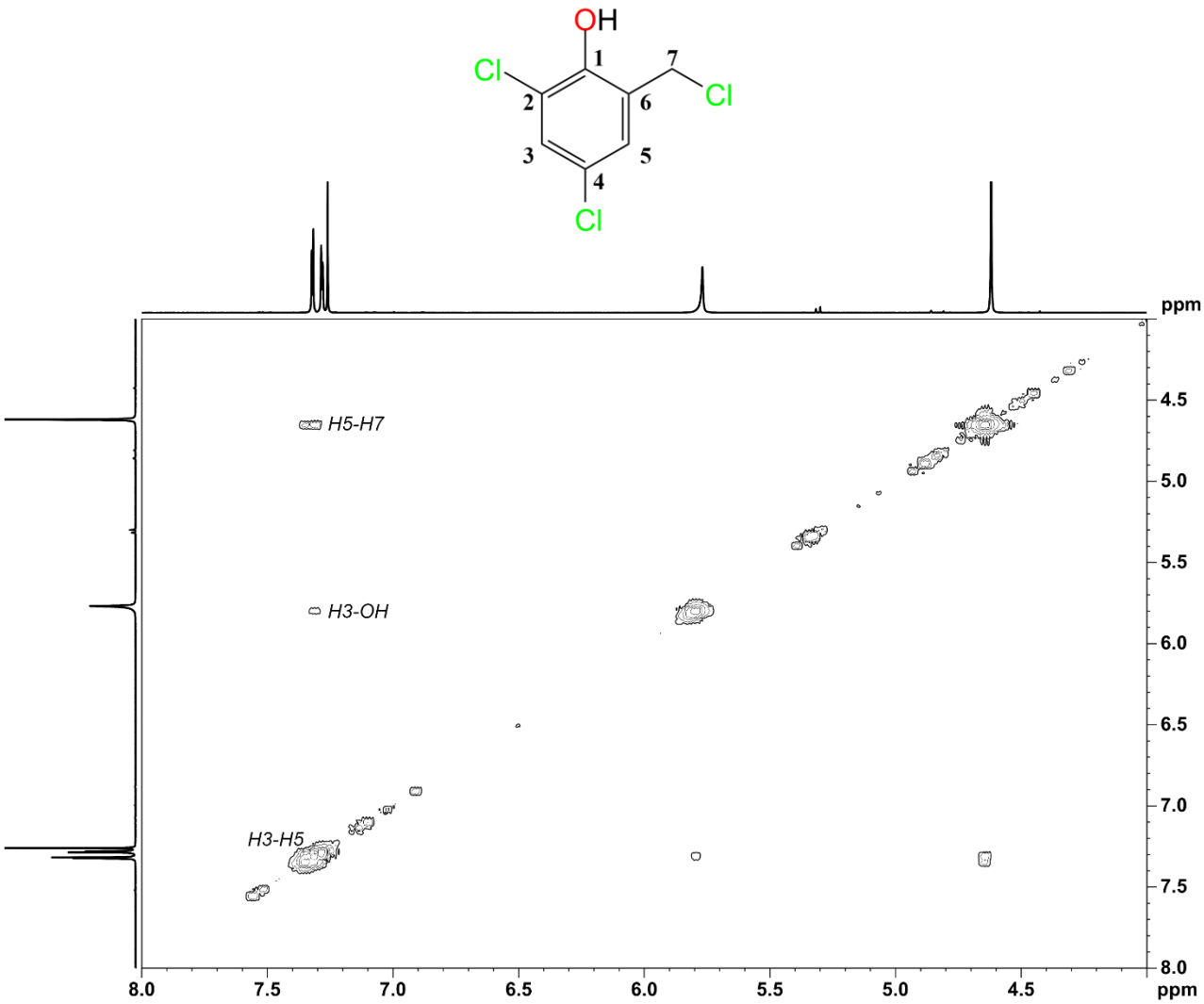

Figure 3.34: Structure and $^{1}H–^{1}H$ COSY spectrum of $PhCl_2CH_2Cl$ in $CDCl_3$ between 8.0 and 4.0 ppm (298 K, 400.13 MHz). The labelling of the cross-peaks indicates the $^{1}H–^{1}H$ coupling (F2,F1). Processing parameters (TopSpin 4.3.0) for F2 (x axis): SI = TD, LB = 1.00 Hz. Processing parameters for F1 (y axis): SI = 2·TD, LB = 0.30 Hz.

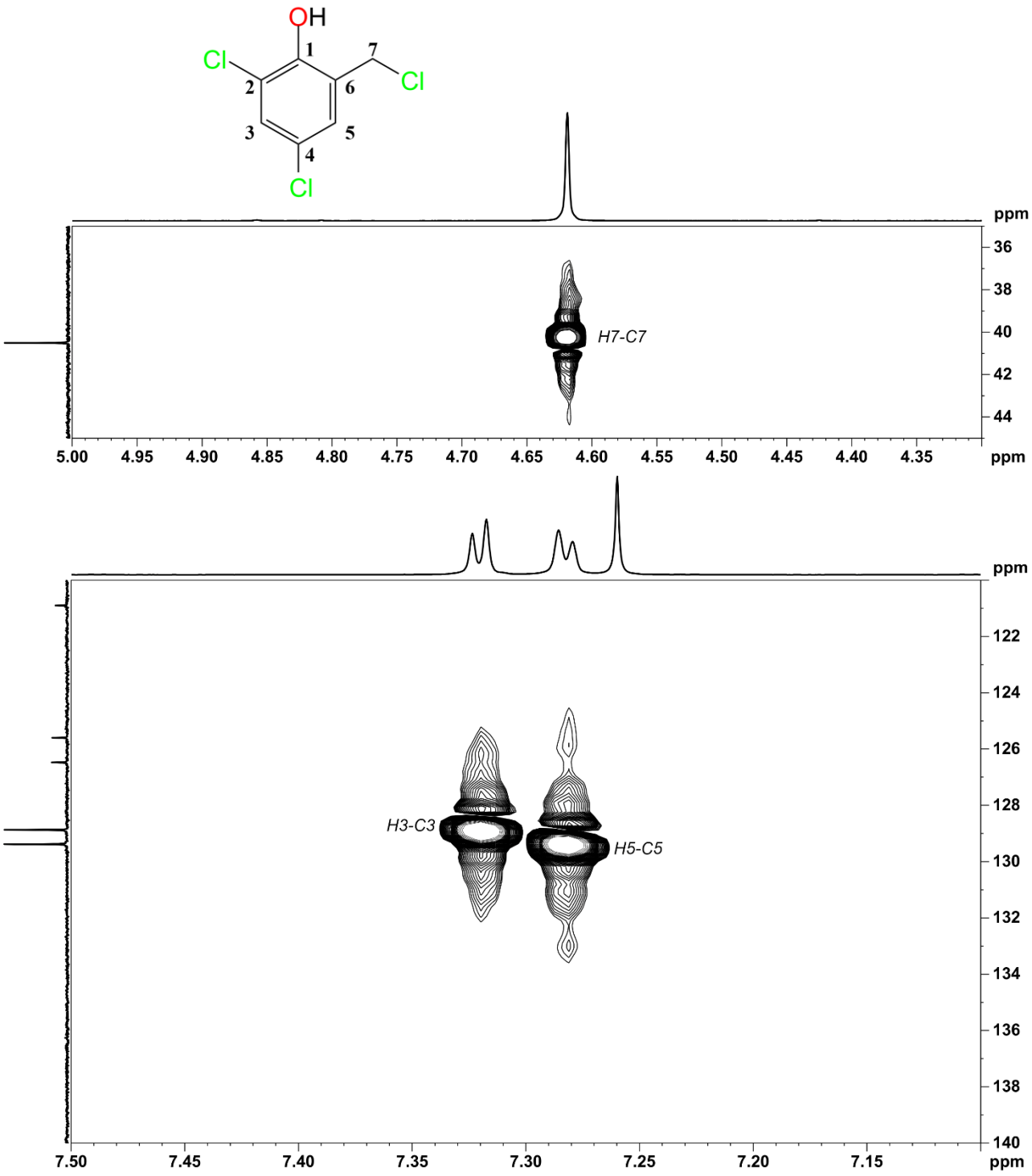

Figure 3.35: Structure and $^{1}H–^{13}C$ HSQC spectrum of $PhCl_2CH_2Cl$ in $CDCl_3$ for: bottom δ_H = 7.5–7.1 ppm and δ_C =140–120 ppm, top δ_H = 5.0–4.3 ppm and δ_C = 45–35 ppm (298 K, 400.13 MHz). The labelling of the cross-peaks indicates the $^{1}H–^{13}C$ coupling (F2,F1). Processing parameters (TopSpin 4.3.0) for F2 (x axis): SI = 2·TD, LB = 1.00 Hz. Processing parameters for F1 (y axis): SI = 3·TD, LB = 0.30 Hz

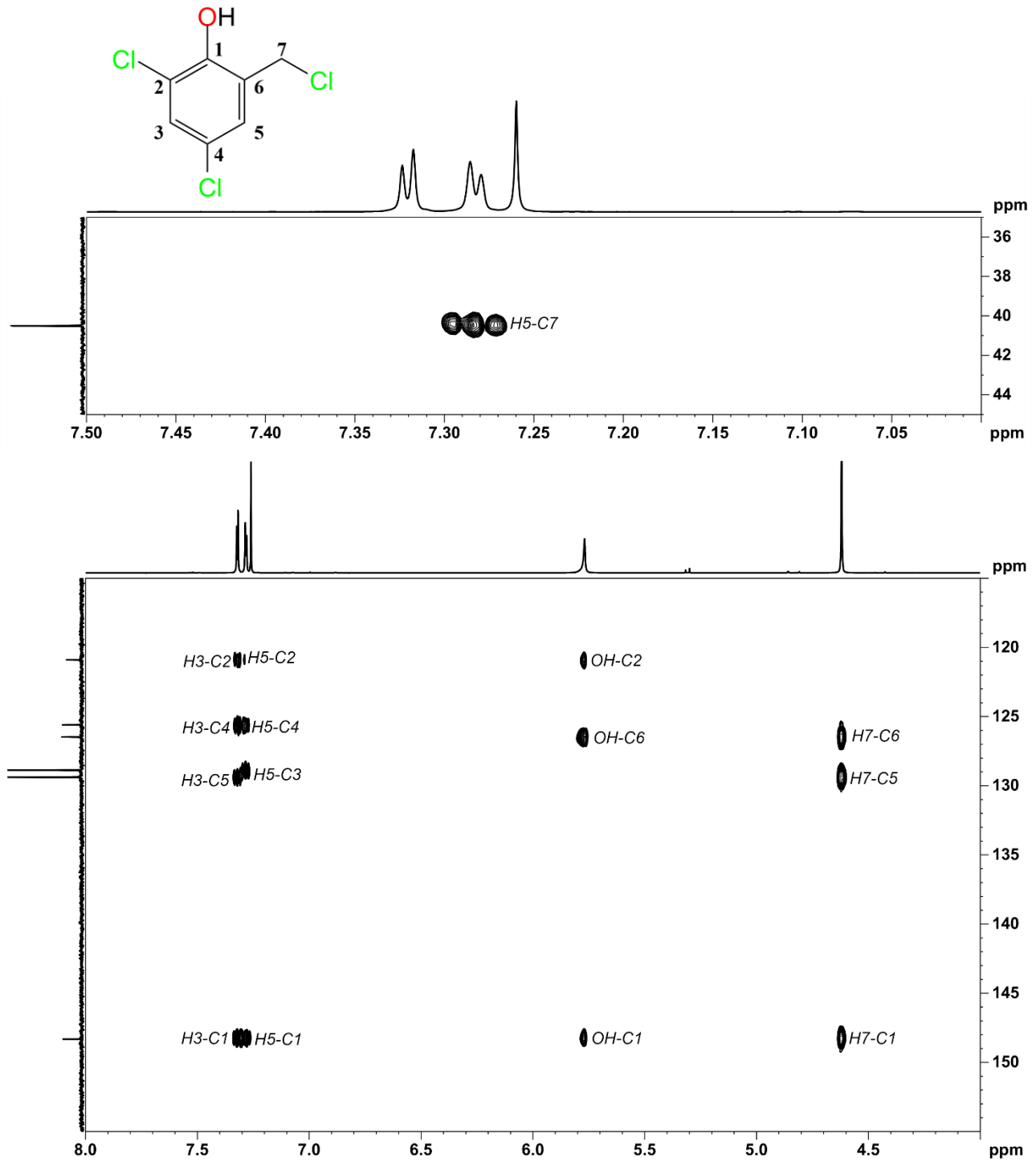

Figure 3.36: Structure and $^{1}H–^{13}C$ HMBC spectrum of $PhCl_2CH_2Cl$ in $CDCl_3$ for: bottom δ_H = 8.0–4.0 ppm and δ_C =155–115 ppm, top δ_H = 7.5–7.0 ppm and δ_C = 45–35 ppm (298 K, 400.13 MHz). The labelling of the cross-peaks indicates the $^{1}H–^{13}C$ coupling (F2,F1). Processing parameters (TopSpin 4.3.0) for F2 (x axis): SI = 2·TD, LB = 1.00 Hz. Processing parameters for F1 (y axis): SI = 3·TD, LB = 0.30 Hz

3.4.2 Characterization of 2,4-difluoro-6-(chloromethyl)phenol (PhF_2CH_2Cl)

Both PhF_2CH_2Cl and PhF_2CH_2OH possess good solubility in organic solvents, thus NMR experiments were performed in $CDCl_3$. Figure 3.38 shows the ^1H NMR spectrum of PhF_2CH_2OH, full characterization for this compound has not been recorded as the two-step pathway was discarded. The typical PhF_2CH_2OH spectra has two aromatic signals, resembling two poorly resolved overlying double double doublets at 6.80 and 6.73 ppm while phenolic OH and methylene signals stand at 6.39 and 4.81 ppm respectively. Assignments were based on multiplicity. In fact, even if poorly resolved, it can be seen that signal at 6.81 ppm has 2 bigger similar coupling constants, and a smaller one, fitting well with *H3* (2 $^3J_{H-F}$ ~8 Hz, $^4J_{H-H}$ ~2.5 Hz), while the signal at 6.73 ppm has 2 small coupling constants and a bigger one, as it should be for *H5* ($^3J_{H-F}$ ~8 Hz, $^4J_{H-H}$ ~2.5 Hz, $^5J_{H-F}$ ~1.5 Hz). As far as concern OH, it comes from δ, as a benzylic OH should be expected in 1.5–3.5 ppm region. Even if the crude was purified through chromatography the spectrum shows the presence of significant unidentified impurities clearly visible in the methylene region that we were unable to remove by any means.

Figure 3.39 shows PhF_2CH_2Cl ^1H NMR spectrum which is very similar in signals shape and positions to the $PhCl_2CH_2OH$ one, as it should be given the small differences between the two molecules. In particular, aromatic signals shift to slightly higher δ of 6.91 and 6.84 ppm, with an inversion of *H3*/*H5* signals relative positions, OH shifts to lower ones, namely 5.46 ppm, while methylene does not shift significantly. It should be noted that OH signal has an unusual sharp and resolved shape, showing a doublet multiplicity with a coupling constant ($^4J_{H-F}$) of ~4.2 Hz. This is a quite remarkable observation as generally couplings through heteroatoms are disfavored, furthermore OH signals are typically too broad due to rapid proton exchange to appreciate usually small ^4J. Figure 3.40 shows ^{19}F NMR highlighting two different fluorides signals at −135.8 ppm and −120.1 ppm, both in decent resolution that allow to appreciate signal multiplicity. Signal at −120.1 ppm is a double triplet with two similar large coupling constants ($^3J_{H-F}$) and a smaller one ($^4J_{F-F}$), this fits well with *F4*. −135.8 ppm signal shape is quite peculiar as *F2* expected multiplicity would be a double triplet or a double double doublet with two similar small coupling constants ($^4J_{F-F}$, $^5J_{H-F}$) and a bigger one ($^3J_{H-F}$), while it appears as a pseudo-double quintet. This can be explained by considering what was previously noted for OH signal in ^1H NMR spectrum, *i.e.*, an unexpected coupling ($^4J_{H-F}$) of medium intensity significantly changing the predictable signal shape, as schematically shown in Figure 3.37.

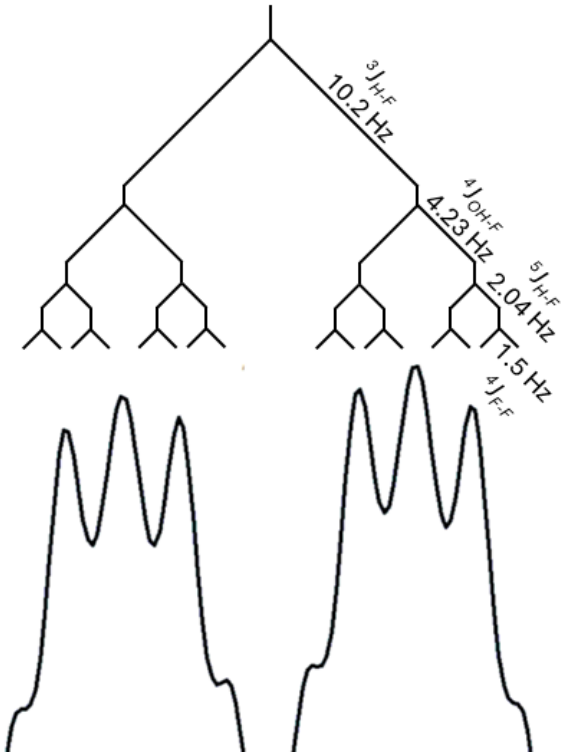

Figure 3.37: Schematic representation of the predicted signal shape including also the coupling constant with hydroxide proton, showing a good fit with the experimental signal, partially reported below

These considerations were also validated by $^{1}H–^{19}F$ HMBC (Figure 3.41) clearly showing all H–F couplings, confirming the fluoride assignments. *J* values were all measured where easier to pick rather than directly on *F2* multiplet.

Figure 3.42 shows ^{13}C NMR of PhF_2CH_2Cl all the signals possess 2 *C–F* couplings giving a set of 7 double doublet signals. *C1* signal has a ^{2}J of 15.0 Hz ^{4}J of 3.6 Hz. *C2* and *C4* both have an *ipso*-F, which generates a wide splitting because of the extremely high coupling constants $^{1}J_{C–F}$ respectively of 240.2 Hz and 242.0 Hz while the smaller ^{3}J are 12.5 Hz and 11.6 Hz. *C3* has two couplings (^{2}J) of 27.2 Hz and 22.5 Hz, this is quite surprising as from 2 similar $^{2}J_{C–F}$ a triplet would be predicted. Also *C6* and *C7* have two quite different ^{3}J (8.7 Hz and 2.8 Hz) and ^{4}J (3.65 Hz and 1.59 Hz) respectively, making it reasonable to hypothesize quite different electronic properties for *F2* and *F4*. Finally, *C5* has two quite different coupling constants of 23.5 Hz (^{2}J) and 3.5 Hz (^{4}J).

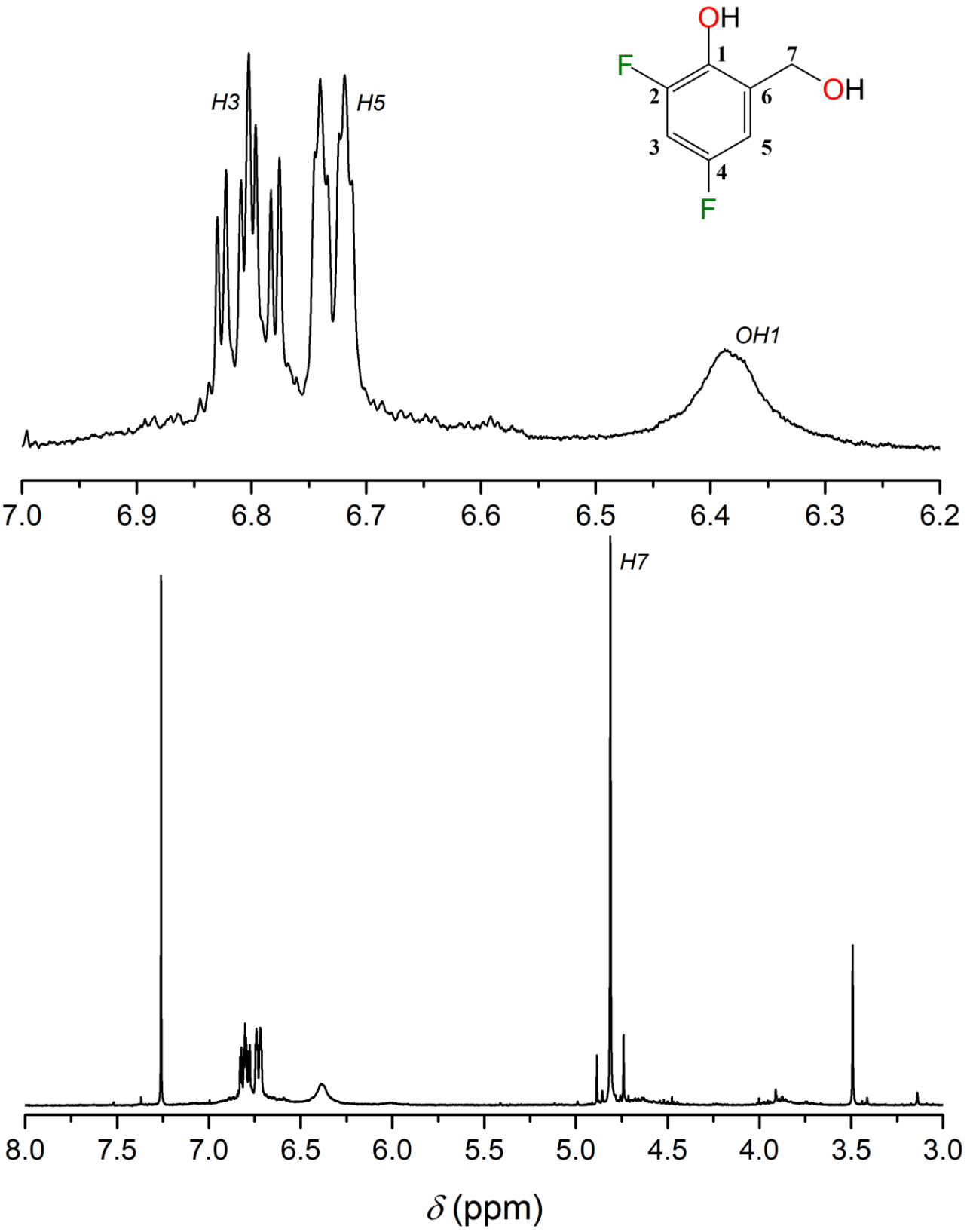

Figure 3.38: Bottom: ^{1}H NMR spectrum of PhF_2MeOH in $CDCl_3$ (298 K, 400.13 MHz). Top: structure of PhF_2MeOH and magnification of the spectrum in 7.0–6.2 ppm range. Processing parameters (TopSpin 4.3.0): SI = TD, LB = 0.30 Hz. δ_H (ppm) = 7.26 (residual protons in $CDCl_3$)

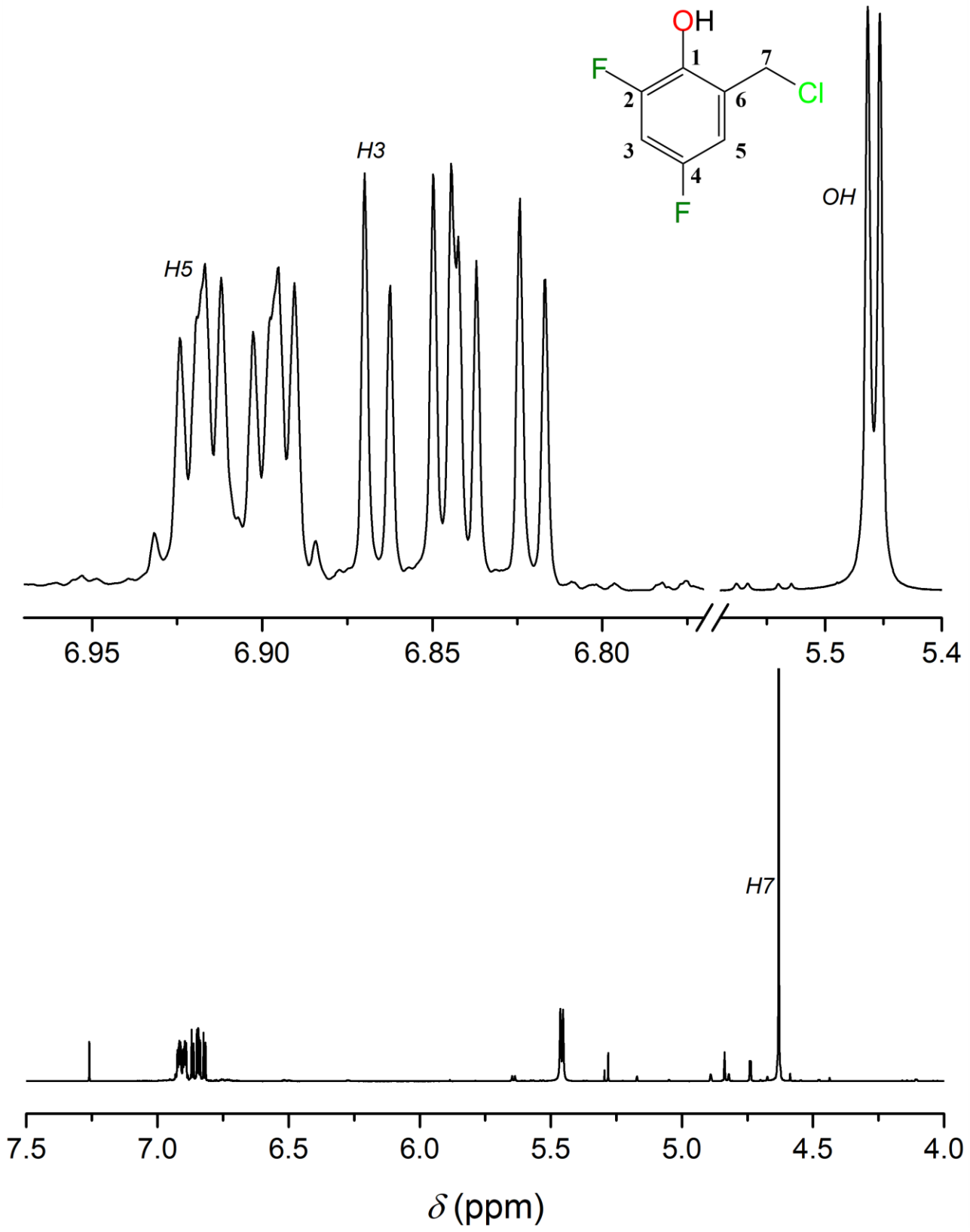

Figure 3.39: Bottom: ^{1}H NMR spectrum of PhF_2CH_2Cl in $CDCl_3$ (298 K, 400.13 MHz). Top: structure of PhF_2CH_2Cl and magnification of the spectrum in 6.95–6.75 ppm and 5.6–5.4 ppm ranges. Processing parameters (TopSpin 4.3.0): SI = TD, LB = 0.30 Hz. δ_H (ppm) = 7.26 (residual protons in $CDCl_3$)

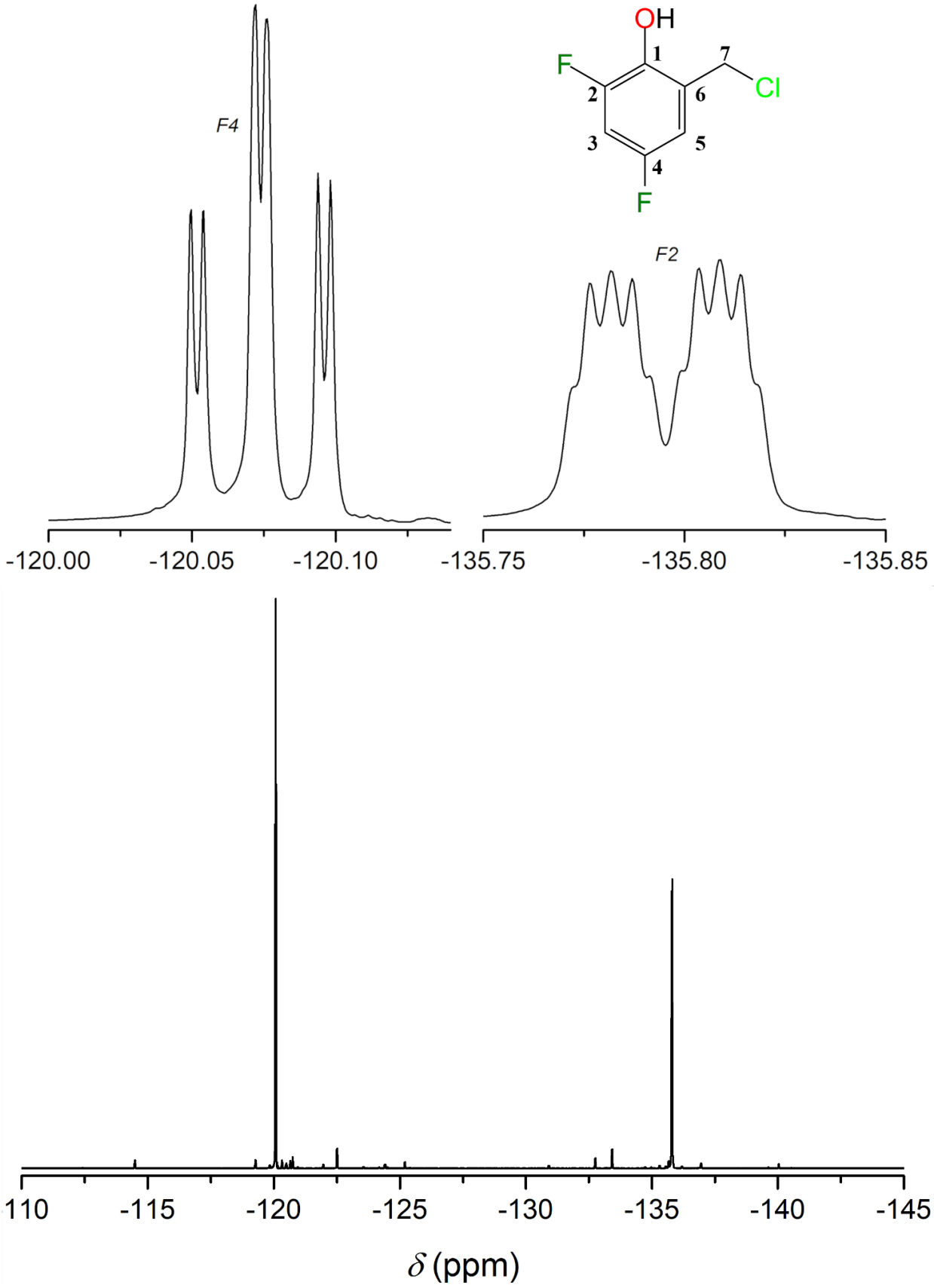

Figure 3.40: Bottom: ^{19}F NMR spectrum of PhF_2CH_2Cl in $CDCl_3$ (298 K, 400.13 MHz) and structure of PhF_2CH_2Cl. Top: Magnification of the spectrum on the signals. Processing parameters (TopSpin 4.3.0): SI = TD, LB = 0.30 Hz.

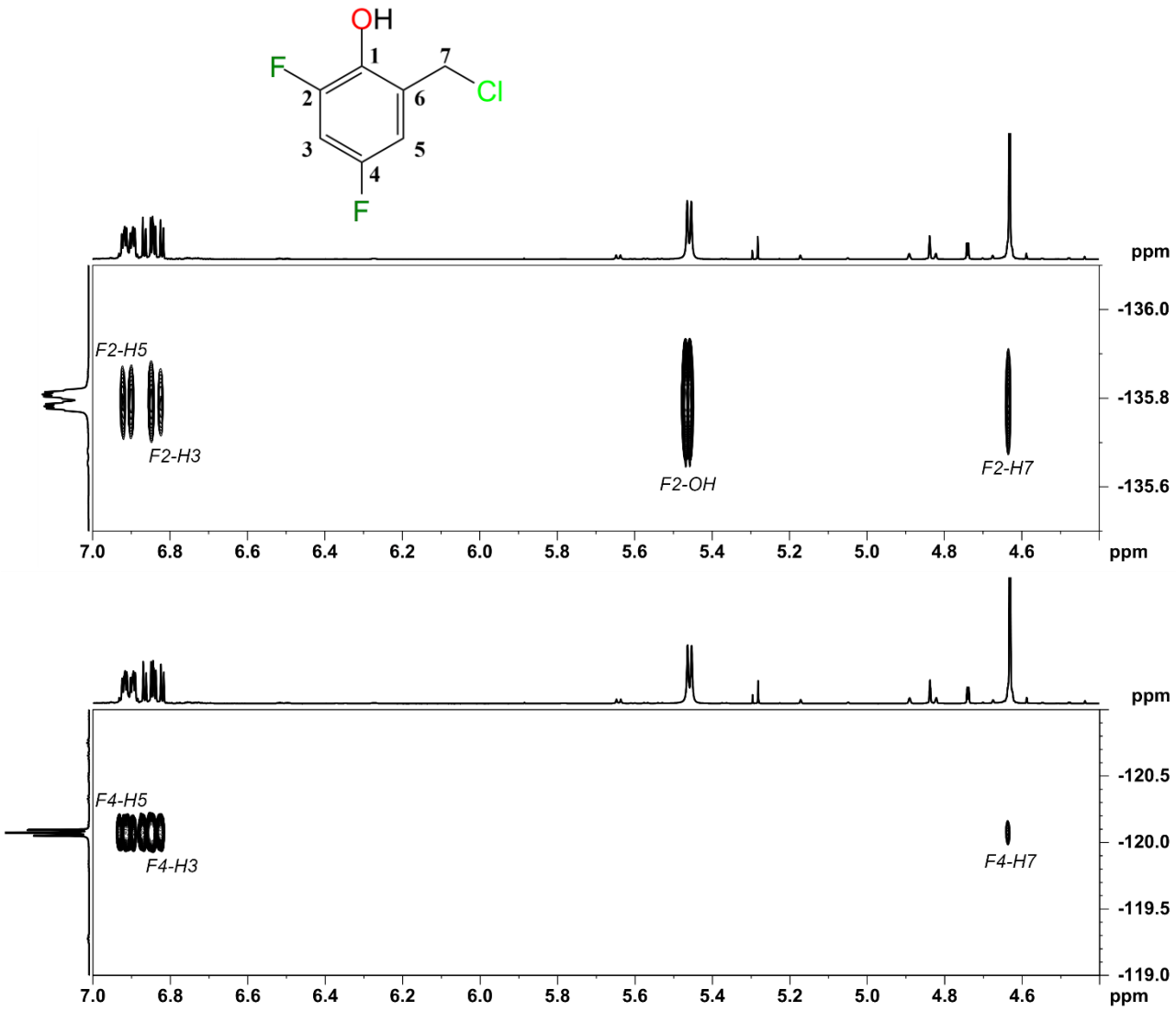

Figure 3.41: Structure and ^{1}H–^{19}F HMBC spectrum of PhF_2CH_2Cl in $CDCl_3$ for: bottom δ_H = 7.0–4.4 ppm and δ_C =−121–−119 ppm, top δ_H = 7.0–4.4 ppm and δ_C = −136.1–−135.5 ppm (298 K, 400.13 MHz). The labelling of the cross-peaks indicates the ^{1}H–^{19}F coupling (F2,F1). Processing parameters (TopSpin 4.3.0) for F2 (x axis): SI = 2·TD, LB = 1.00 Hz. Processing parameters for F1 (y axis): SI = 3·TD, LB = 0.30 Hz

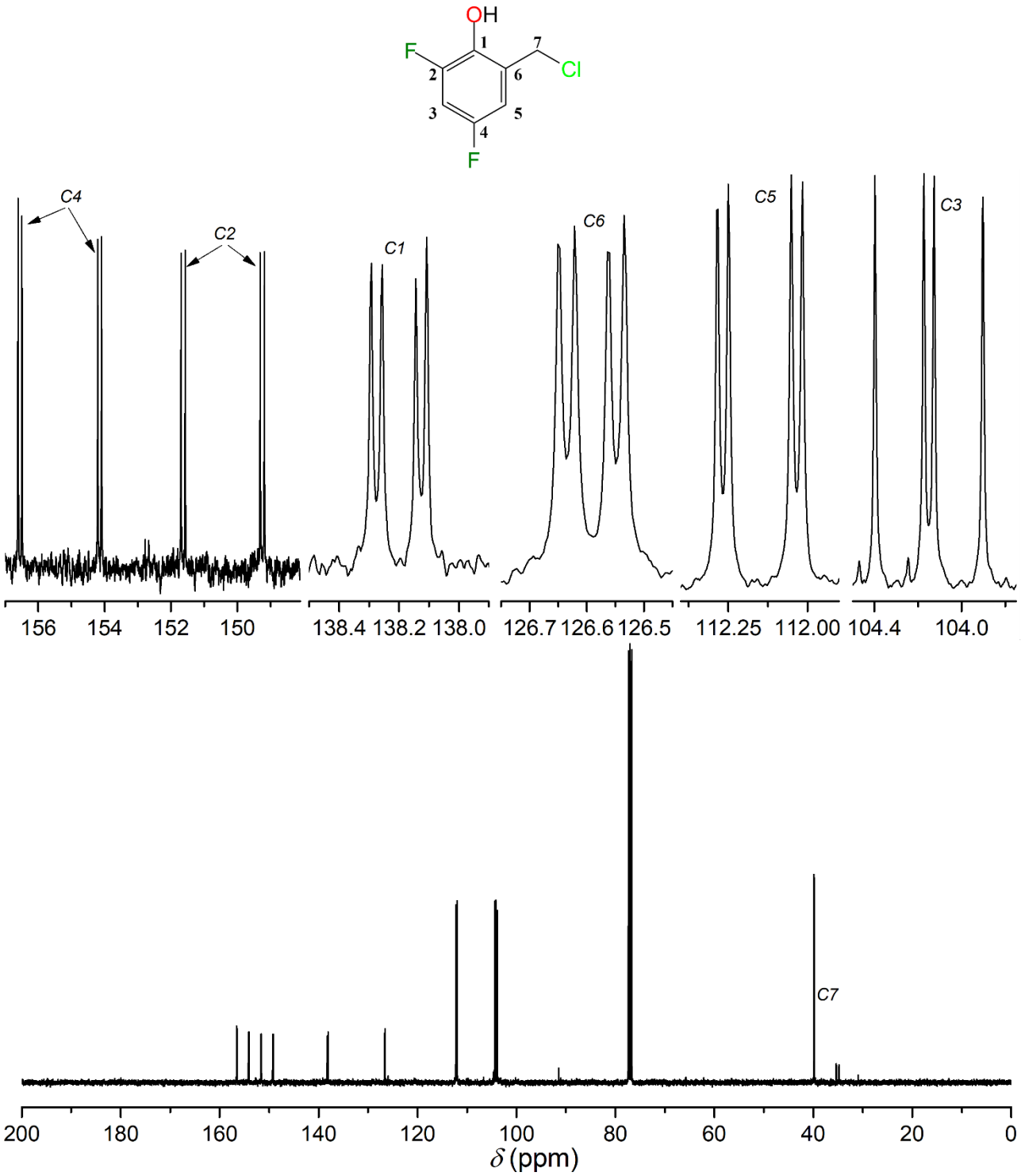

Figure 3.42: Bottom: ^{13}C NMR spectrum of PhF_2CH_2Cl in $CDCl_3$ (298 K, 400.13 MHz). Top: Structure of PhF_2CH_2Cl and magnifications of the spectrum in 157–148 ppm, 138.5–137.9 ppm, 126.8–126.4 ppm, 112.3–111.9 ppm and 104.5–103.8 ppm. Processing parameters (TopSpin 4.3.0): SI = TD, LB = 0.30 Hz. δ_C (ppm) = 77.16 (residual carbon in $CDCl_3$)

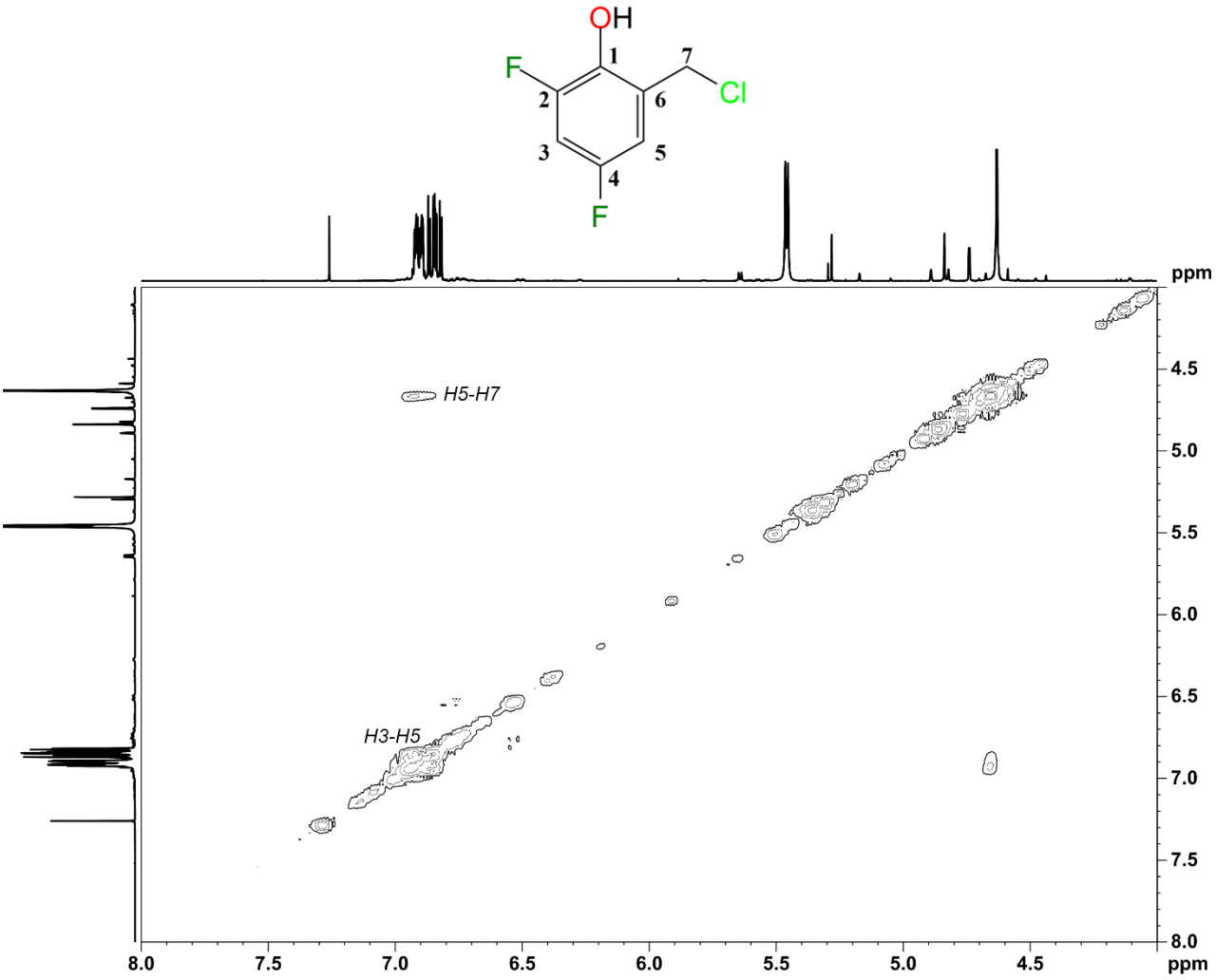

Figure 3.43: Structure and $^{1}H–^{1}H$ COSY spectrum of PhF_2CH_2Cl in $CDCl_3$ between 8.0 and 4.0 ppm (298 K, 400.13 MHz). The labelling of the cross-peaks indicates the $^{1}H–^{1}H$ coupling (F2,F1). Processing parameters (TopSpin 4.3.0) for F2 (x axis): SI = TD, LB = 1.00 Hz. Processing parameters for F1 (y axis): SI = 2·TD, LB = 0.30 Hz.

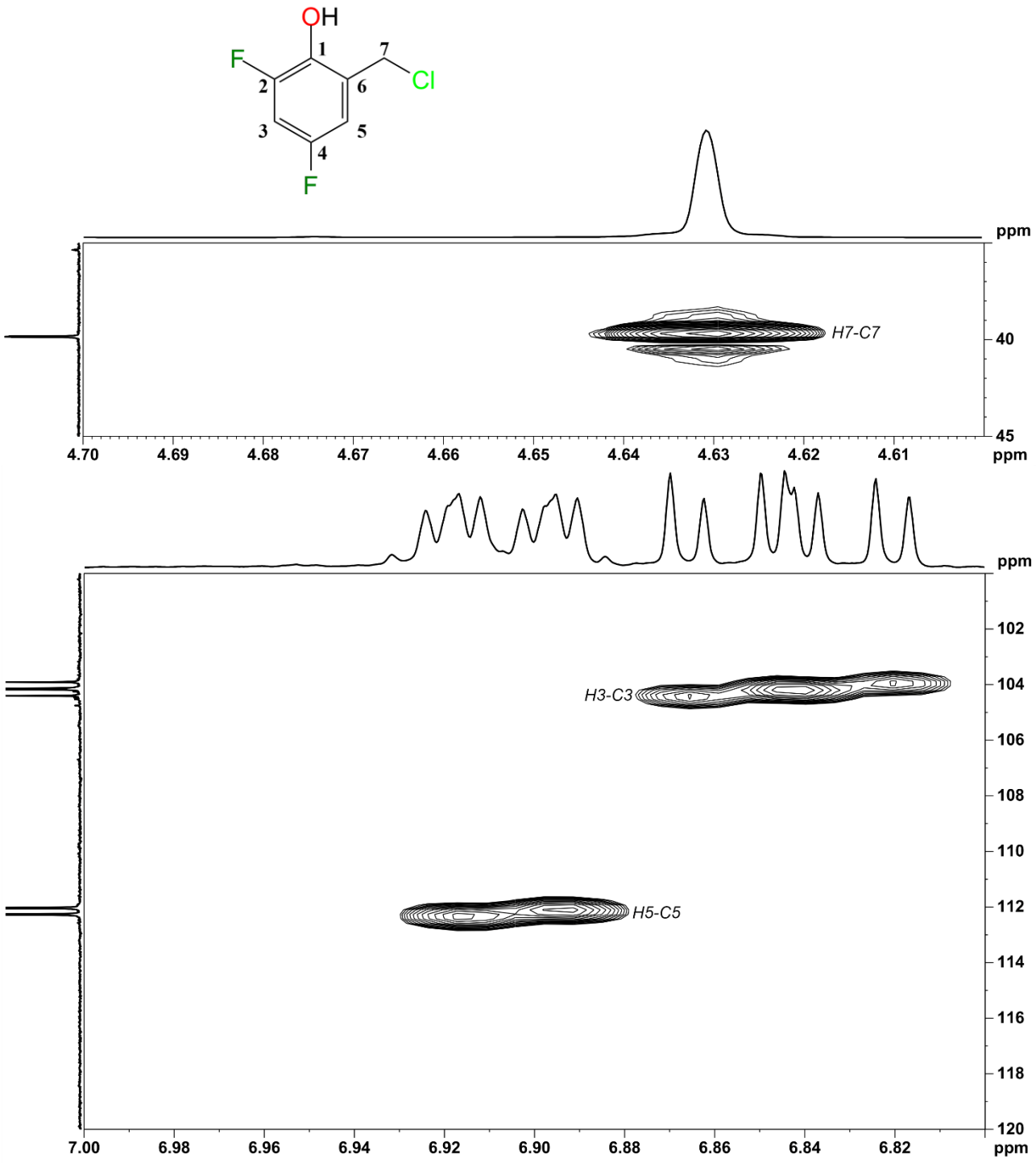

Figure 3.44: Structure and $^{1}H–^{13}C$ HSQC spectrum of PhF_2CH_2Cl in $CDCl_3$ for: bottom δ_H = 7.0–6.8 ppm and δ_C =120–100 ppm, top δ_H = 4.7–4.6 ppm and δ_C = 45–35 ppm (298 K, 400.13 MHz). The labelling of the cross-peaks indicates the $^{1}H–^{13}C$ coupling (F2,F1). Processing parameters (TopSpin 4.3.0) for F2 (x axis): SI = 2·TD, LB = 1.00 Hz. Processing parameters for F1 (y axis): SI = 3·TD, LB = 0.30 Hz

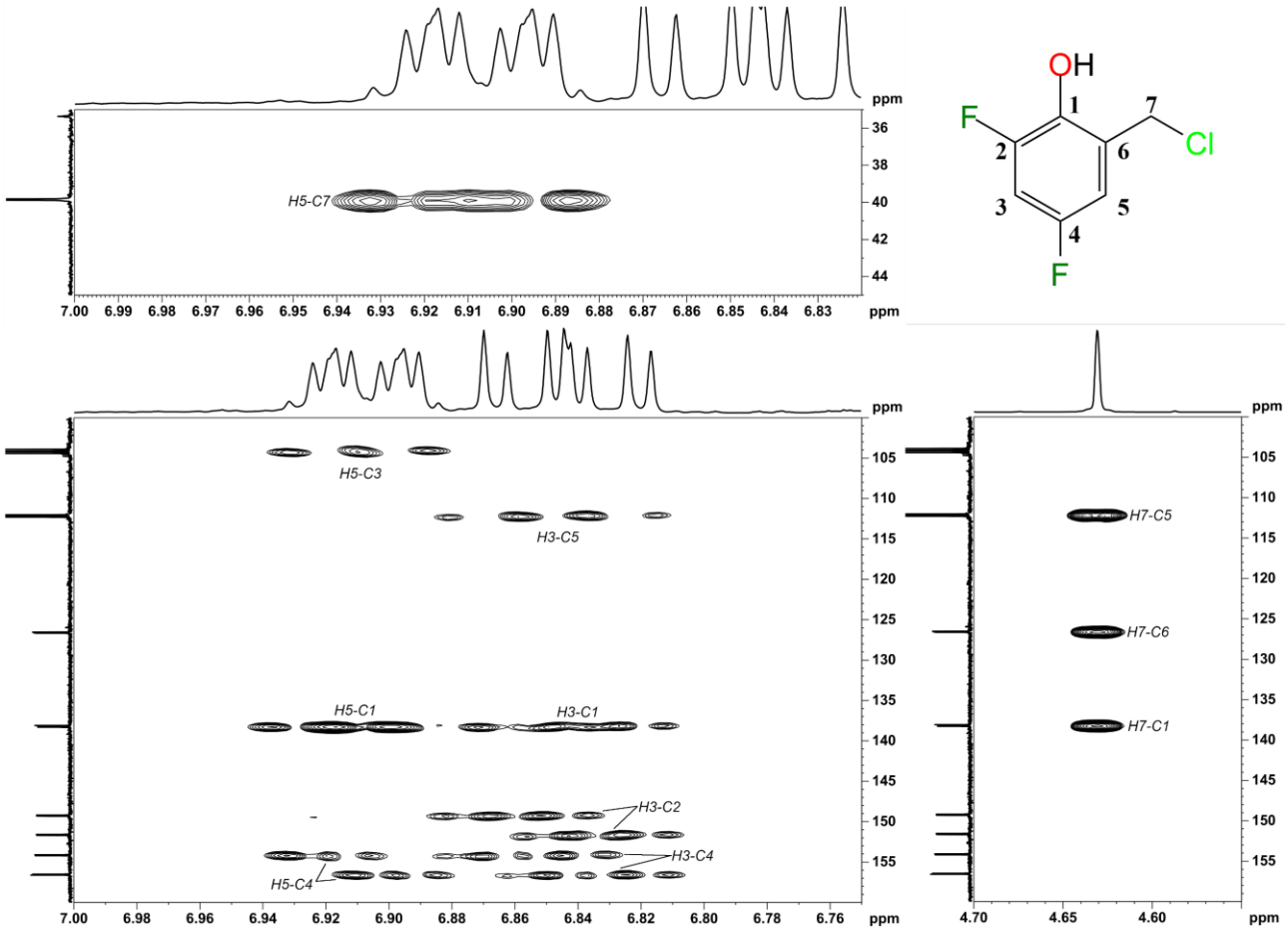

Figure 3.45: Structure and $^{1}H–^{13}C$ HMBC spectrum of PhF_2CH_2Cl in $CDCl_3$ for: bottom δ_H = 7.0–6.75 ppm and δ_C =160–100 ppm, top δ_H = 7.0–6.82 ppm and δ_C = 45–35 ppm (298 K, 400.13 MHz), right δ_H = 4.70–4.55 ppm and δ_C =160–100 ppm. The labelling of the cross-peaks indicates the $^{1}H–^{13}C$ coupling (F2,F1). Processing parameters (TopSpin 4.3.0) for F2 (x axis): SI = 2·TD, LB = 1.00 Hz. Processing parameters for F1 (y axis): SI = 3·TD, LB = 0.30 Hz

3.4.3 Characterization of 2-nitro-4-chloro-6-(chloromethyl)phenol ($PhClNO_2CH_2Cl$)

$PhClNO_2CH_2Cl$ possesses good solubility in organic solvents, thus NMR experiments were performed in $CDCl_3$. Figure 3.46 shows the typical ^1H NMR spectrum of $PhClNO_2CH_2Cl$ with 4 well defined and sharp peaks. The methylenic protons of $PhClNO_2CH_2Cl$ give a singlet at 4.68 ppm while aromatics fall at 7.71 ppm and 8.10 ppm, both forming a doublet with a *J* of 2.6 Hz. The hydroxide proton has two peculiar characteristics, first, it is quite sharp and appears as a well-defined singlet, second, it is located at 10.92 ppm, a position typical for carboxylic acids and aldehyde protons. Even if unusual, this behavior is well-known for acid phenols bearing electron-withdrawing substituents, as they tend to aggregate through H-bonding giving sharp shifted signals[60]. As major impurity it can be noted a ~1.5% of the condensation by-product both in the aromatic and benzylic part at 4.11 ppm, 7.56 ppm and 8.03 ppm.

In Figure 3.47 is represented the typical ^{13}C NMR $PhClNO_2CH_2Cl$ spectrum, with the 7 expected signals all visible, 5 aromatic signals are located between 138 ppm and 124 ppm, with *C2* barely visible at 133.9 ppm, while the phenolic one lays at 151.8 ppm. The aliphatic carbon stands at 39.30 ppm, being both benzylic and chlorinated. Figure 3.48 represents ^1H–^{13}C HMBC interestingly showing couplings between *OH* proton and *C1, C2*, *C5* and *C6*, this is quite unusual as usually correlations through heteroatoms cannot be seen.

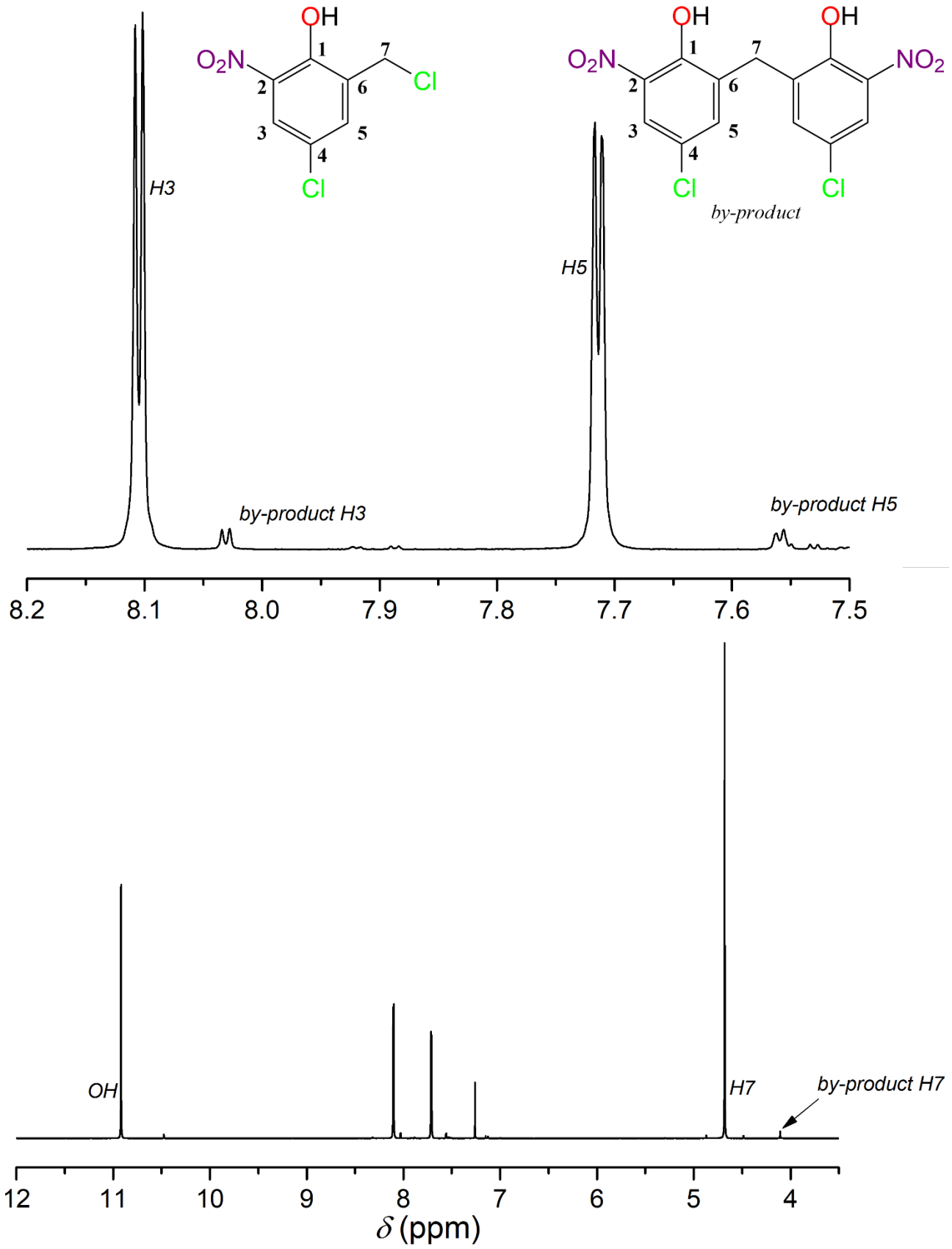

Figure 3.46: Bottom: ^{1}H NMR spectrum of $PhClNO_2CH_2Cl$ in $CDCl_3$ (298 K, 400.13 MHz). Top: structure of $PhClNO_2CH_2Cl$, of the self-condensation by-product and magnification of the spectrum between 8.2 ppm and 7.5 ppm. Processing parameters (TopSpin 4.3.0): SI = TD, LB = 0.30 Hz. δ_H (ppm) = 7.26 (residual protons in $CDCl_3$)

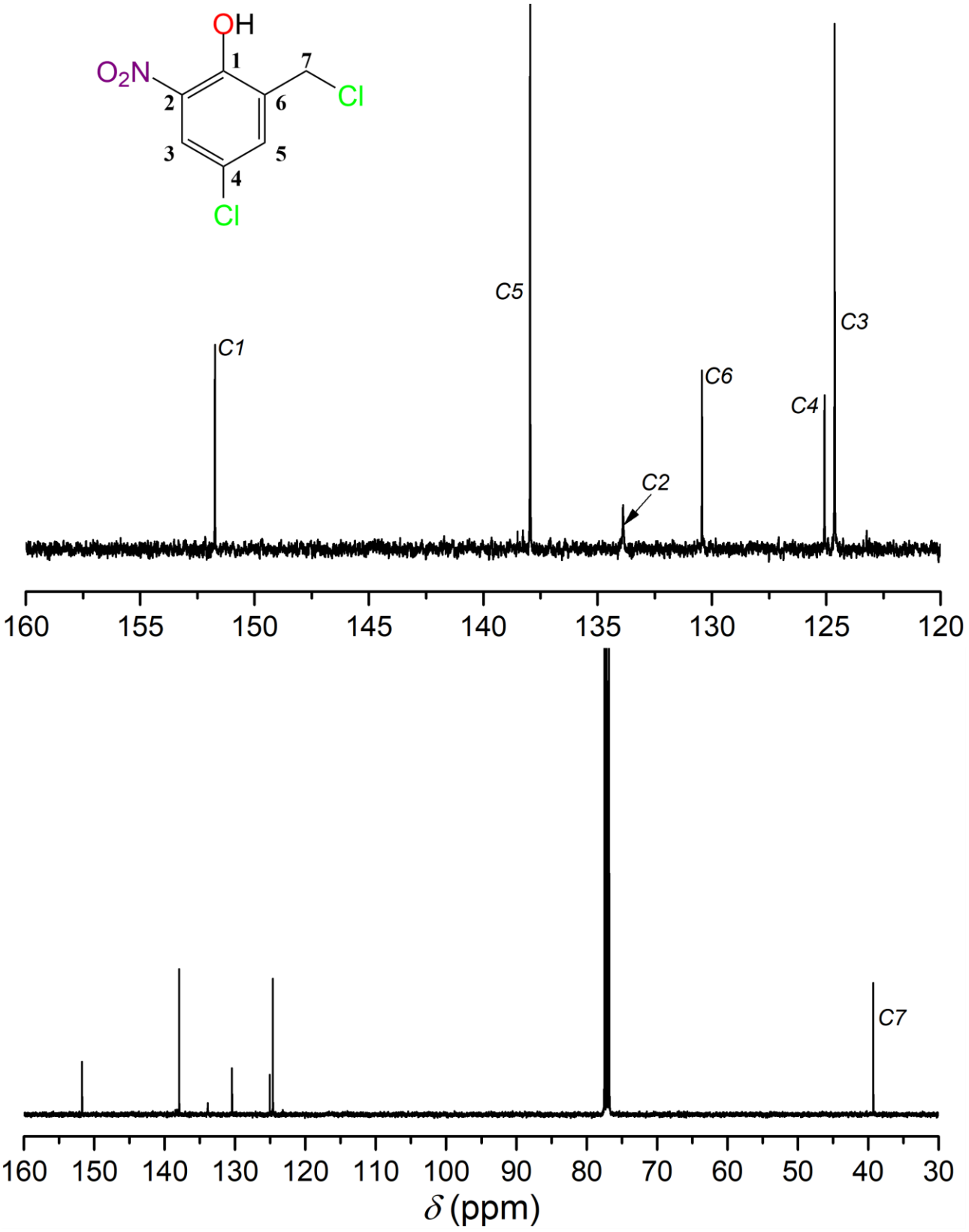

Figure 3.47: Bottom: ^{13}C NMR spectrum of $PhClNO_2CH_2Cl$ in $CDCl_3$ (298 K, 400.13 MHz). Top: structure of $PhClNO_2CH_2Cl$ and magnification of the spectrum between 160 ppm and 120 ppm. Processing parameters (TopSpin 4.3.0): SI = TD, LB = 0.30 Hz. δ_C (ppm) = 77.16 (residual carbon in $CDCl_3$)

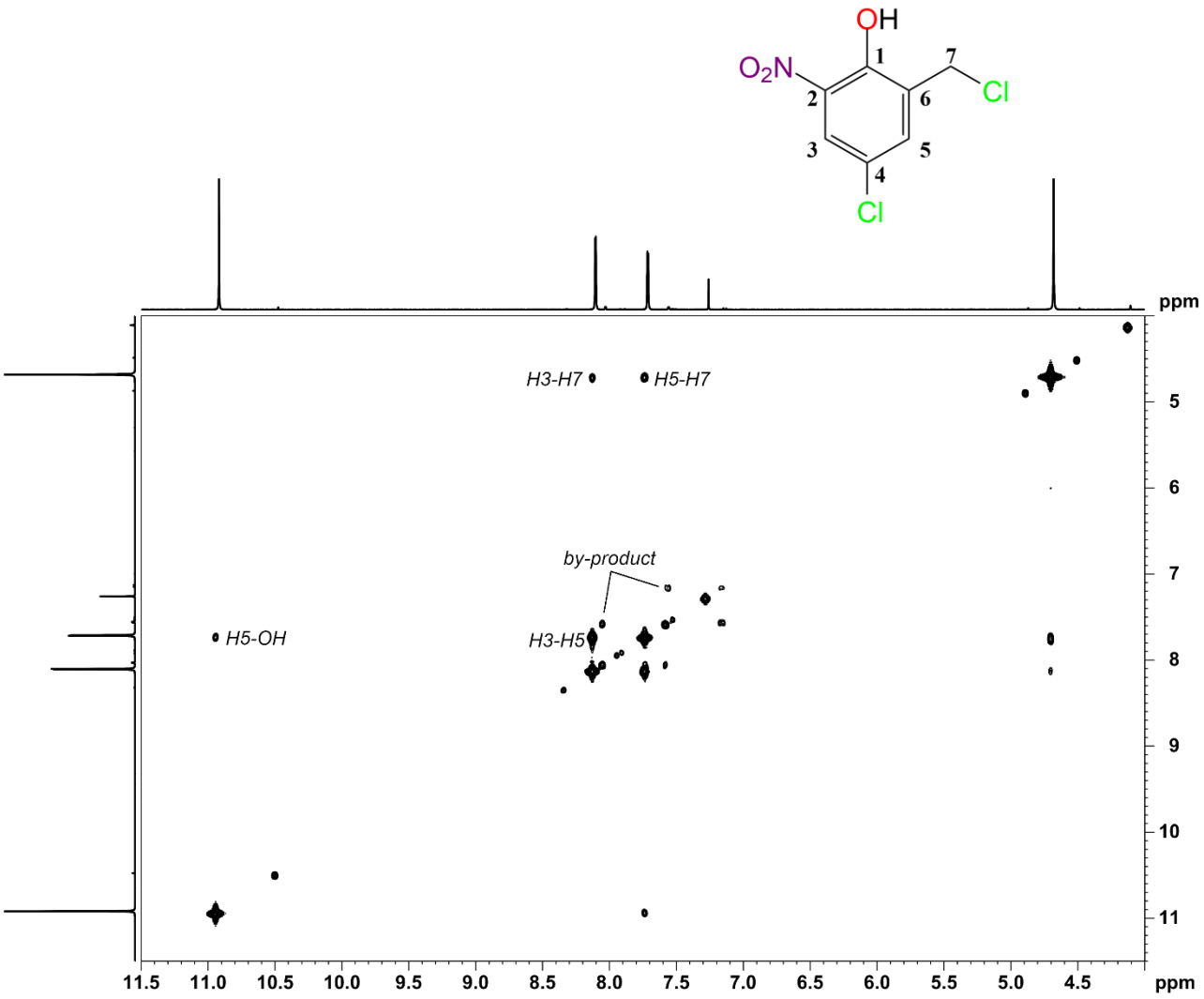

Figure 3.48: Structure and ^{1}H–^{1}H COSY spectrum of $PhClNO_2CH_2Cl$ in $CDCl_3$ between 11.5 ppm and 4.0 ppm (298 K, 400.13 MHz). The labelling of the cross-peaks indicates the ^{1}H–^{1}H coupling (F2,F1). Processing parameters (TopSpin 4.3.0) for F2 (x axis): SI = TD, LB = 1.00 Hz. Processing parameters for F1 (y axis): SI = 2·TD, LB = 0.30 Hz.

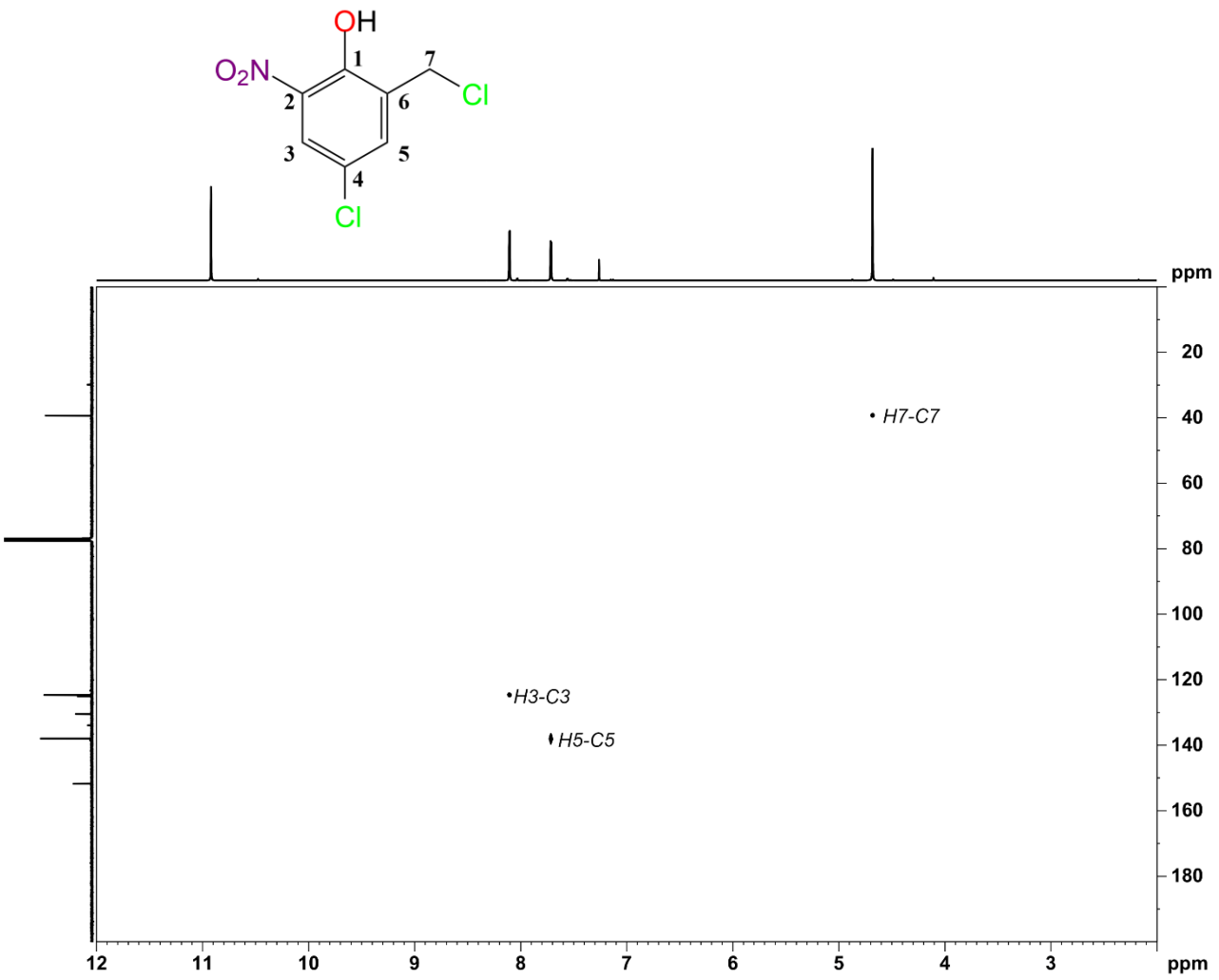

Figure 3.49: Structure and ^{1}H–^{13}C HSQC spectrum of $PhClNO_2CH_2Cl$ in $CDCl_3$ for δ_H = 12.0–6.8 ppm and δ_C =200–0 ppm. The labelling of the cross-peaks indicates the ^{1}H–^{13}C coupling (F2,F1). Processing parameters (TopSpin 4.3.0) for F2 (x axis): SI = 2·TD, LB = 1.00 Hz. Processing parameters for F1 (y axis): SI = 3·TD, LB = 0.30 Hz

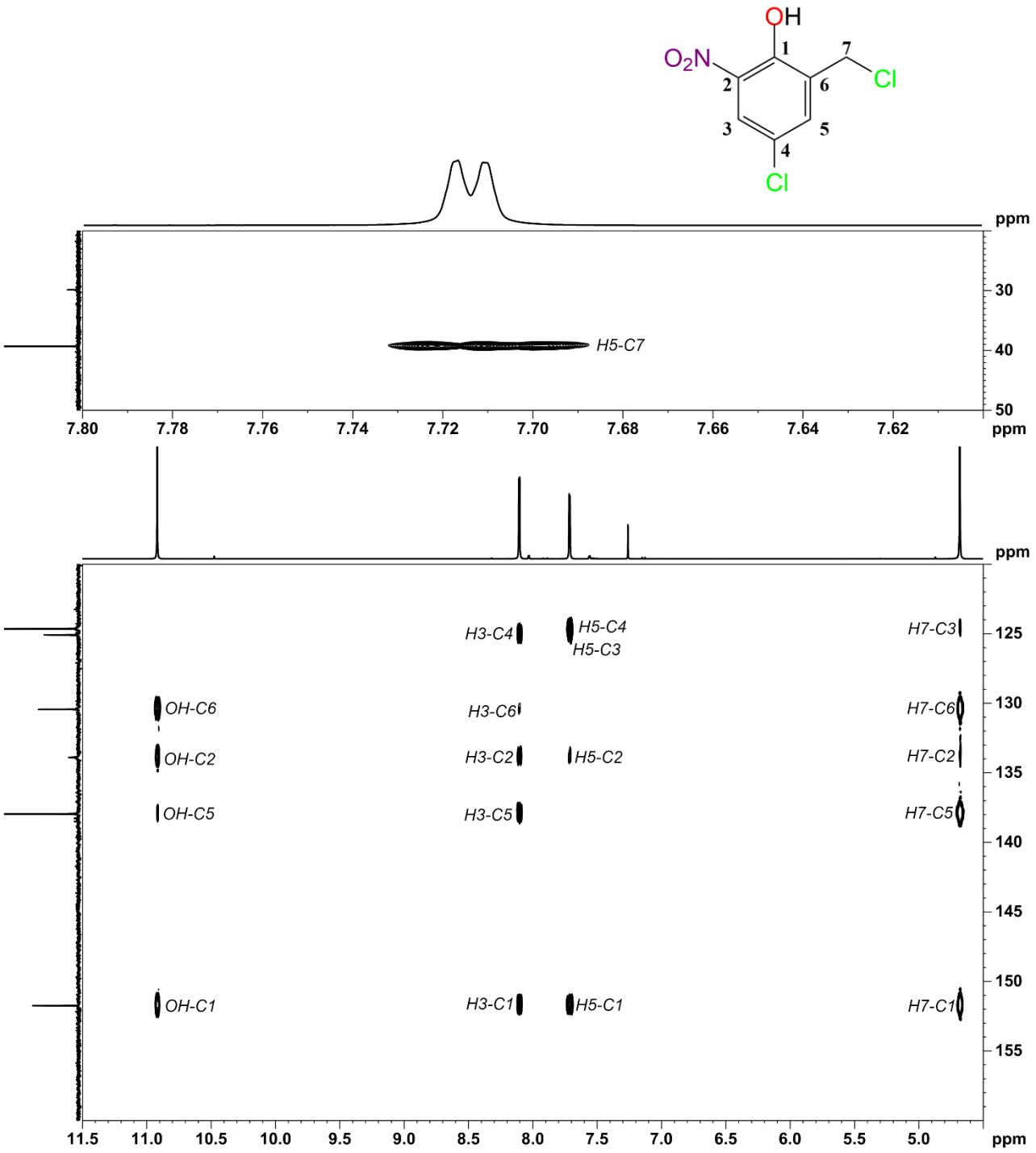

Figure 3.50: Structure and ^{1}H–^{13}C HMBC spectrum of $PhClNO_2CH_2Cl$ in $CDCl_3$ for: bottom δ_H = 11.5–4.5 ppm and δ_C =160–120 ppm, top δ_H = 7.8–7.6 ppm and δ_C = 50–20 ppm (298 K, 400.13 MHz). The labelling of the cross-peaks indicates the ^{1}H–^{13}C coupling (F2,F1). Processing parameters (TopSpin 4.3.0) for F2 (x axis): SI = 2·TD, LB = 1.00 Hz. Processing parameters for F1 (y axis): SI = 3·TD, LB = 0.30 Hz

3.5 Synthesis of TPAs proligands

As discussed in Sections 3.2 and 3.4 we optimized our own synthetic pathways to TPAs precursors PhX_2CH_2Cl, $DPA^{Cl,Cl}$ and $DPA^{F,F}$ theoretically enabling the synthesis of 6 different TPAs ligands, shown in Figure 3.51.

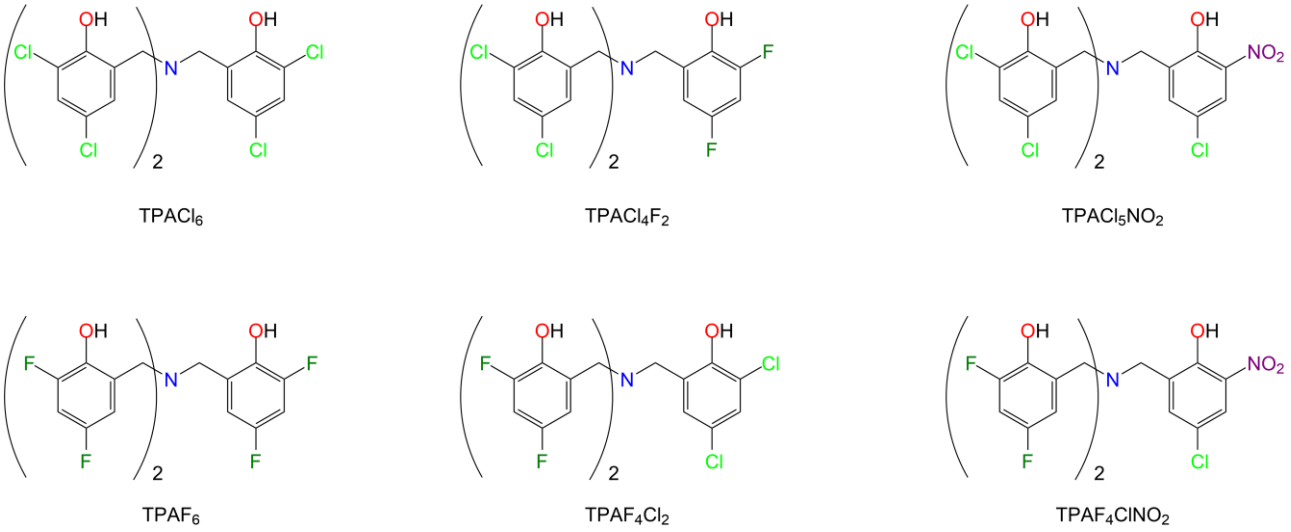

Figure 3.51: Structures of the six possible combinations obtainable from the three PhX_2CH_2Cls and two DPAs synthetized

We started working on the symmetric 6,6',6''-(nitrilotris(methylene))tris(2,4-dichlorophenol) ($TPACl_6$) and 6,6',6''-(nitrilotris(methylene))tris(2,4-difluorophenol) ($TPAF_6$) testing the typical reported procedure[31] (Figure 3.7) for similar substrates. This pathway suggests operating in THF reflux conditions for several hours, using an excess of triethylamine (TEA) as a base. Unfortunately, both $DPA^{Cl,Cl}$ and $DPA^{F,F}$ solubility in THF is very low, and NMR conversions to the corresponding TPAs were poor even extending reaction time to several days. Thus, we tried similar conditions replacing THF with DMSO, a solvent in which DPAs are soluble, obtaining complete conversions and high yields. Therefore, we tried to extend this approach to the synthesis of 6,6'-(((3,5-difluoro-2-hydroxybenzyl)azanediyl)bis(methylene))bis(2,4-dichlorophenol) ($TPACl_4F_2$) and 6,6'-(((3,5-dichloro-2-hydroxybenzyl)azanediyl)bis(methylene))bis(2,4-difluorophenol) ($TPAF_4Cl_2$) giving complete conversions, but obtaining in both cases complicated mixtures, hard to identify through NMR. Luckily, ESI-MS gave clarifying information showing that the raw product was indeed a mixture of the targeted TPA and other "arms" combinations. For example, the raw product obtained starting from $DPA^{F,F}$ showed similar quantities of $TPAF_4Cl_2$ and $TPACl_4F_2$, followed by smaller amounts of $TPAF_6$ and $TPACl_6$. This is reasonable hypothesizing an overalkylation of the desired product ($TPAF_4Cl_2$), forming an unstable quaternary ammonium salt that can decompose to the other

main product ($TPACl_4F_2$) and PhF_2CH_2Cl (Figure 3.52) which can alkylate $DPA^{F,F}$ to form $TPAF_6$. $TPACl_6$ can be formed in a similar way from the overalkylation of $TPACl_4F_2$ by-product.

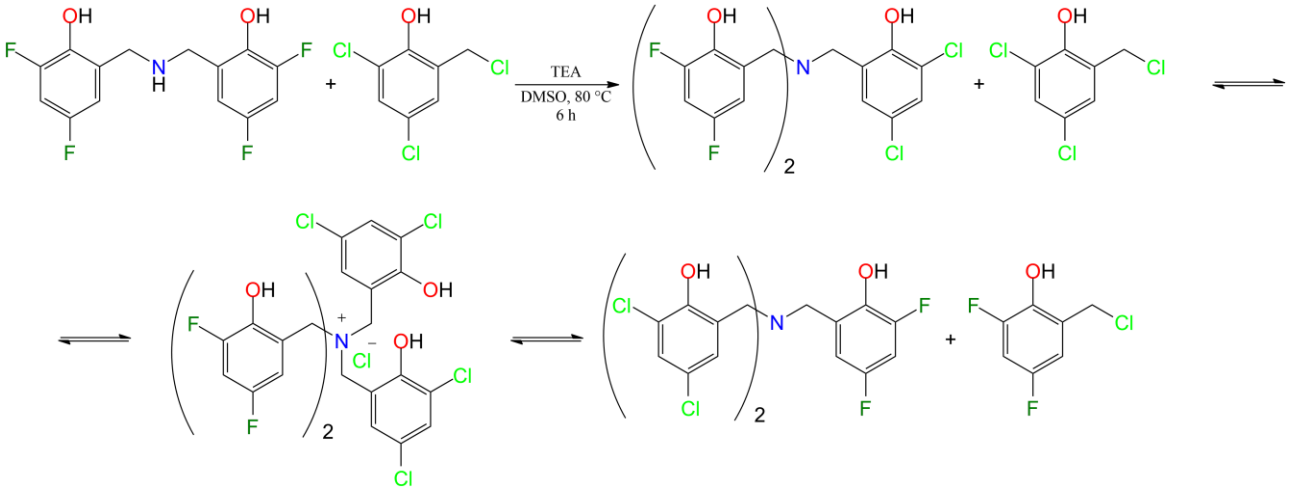

Figure 3.52: Schematic representation of the overalkylation product formation and decomposition giving a different TPA

Decreasing reaction time and testing other bases such as K_2CO_3 and Cs_2CO_3 did not solve this issue. On the other hand, working at rt can significantly improve selectivity toward the desired product, forming ~5-10% of main by-product and non-detectable amounts of the others. Decreasing temperature, however, significantly reduces reaction speed, and thus much longer reaction times are required, up to a week, to achieve conversions similar to the high temperature processes. Purification from residual TEA and PhX_2CH_2Cl (described in Sections 3.8.11–16) is quite easy thanks to their very different solubility in solvents and water, while separation of TPAs by-products from the desired TPA product is extremely hard. In fact, the presence of phenolic and aminic groups, both known to give big tailing problems, makes chromatography impossible, especially considering the extremely low solubility in common solvents of both TPAs and DPAs. Continuous solid-liquid extraction proved to be ineffective, as same TPAs ratios of the raw material were obtained, while recrystallization from DMSO or DMF was impossible, as the solubility in these solvents is too high and just few drops can completely solubilize several hundred milligrams of raw mixture. Selective precipitation slowly increasing pH of a strongly basic water solution also failed, as their pKa are probably too similar. Neither the products nor the impurities showed significant sublimation in 25 °C/760 mmHg – 100 °C/1 mmHg range. Thus, given the shortage of other purification options we decided to accept the purity obtained after removal of residual TEA and PhX_2CH_2Cl (Sections 3.8.11–16), which is in the worst case ~75%, hoping for an easier purification after complexation.

Direct application of the method described for $TPAF_4Cl_2$ and $TPACl_4F_2$ to $PhClNO_2CH_2Cl$ gave no results, as previously discussed (Sections 3.2 and 3.4) $PhClNO_2CH_2Cl$ acidity is significantly higher

than $PhCl_2CH_2Cl$ and PhF_2CH_2Cl ones. $PhClNO_2CH_2Cl$ deprotonation is clearly highlighted by a color change from light yellow to deep red. When TEA is used as a base a quick shift to a red color is observed, meaning that deprotonation occurred, hampering amine alkylation. Thus, several progressively weaker bases were tested, starting from pyridine which generates a very stable ionic couple, shown in Figure 3.53, that we managed to isolate and characterize through ^1H NMR in $CDCl_3$ (Section 3.8.8).

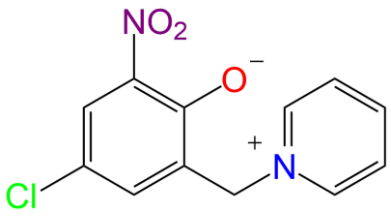

Figure 3.53: Ionic couple generated by $PhClNO_2CH_2Cl$ alkylation of pyridine

Finally, we have been able to avoid deprotonation using KH_2PO_4 as a base, and the reaction proceeded smoothly in the same conditions described above producing slightly higher amounts of impurities, allowing us to obtain 6,6'-(((3-nitro-5-chloro-2-hydroxybenzyl)azanediyl)bis(methylene))bis(2,4-dichlorophenol) ($TPACl_5NO_2$) and 6,6'-(((3-nitro-5-chloro-2-hydroxybenzyl)azanediyl)bis(methylene))bis(2,4-difluorophenol) ($TPAF_4ClNO_2$). Interestingly, in our tests CH_3COOK quickly deprotonated $PhClNO_2CH_2Cl$, setting its pK_a somewhere between 2.14 ($H_3PO_4/H_2PO_4^-$) and 4.76 (CH_3COOH/CH_3COO^-) showing a remarkably high acidity for a phenolic compound, comparable to that of carboxylic acids.

All obtained TPAs ligand were characterized by NMR spectroscopy and ESI-MS spectrometry as shown in Figures 3.54–3.93. Assignments were determined through careful analysis of 1D (^1H, ^{13}C and ^{19}F when applicable) and 2D (^1H–^1H COSY, ^1H–^{13}C HSQC, ^1H–^{13}C HMBC) spectra.

3.5.1 Characterization of 6,6',6''-(nitrilotris(methylene))tris(2,4-dichlorophenol) ($TPACl_6$)

DMSO-d_6 is required for NMR as solubility in other solvents is too low to reach the concentrations necessary for this technique. Figure 3.54 shows the typical ^1H NMR spectrum of $TPACl_6$ purified mixture with two aromatic signals at 7.37 ppm (*H3*) and 7.21 ppm (*H5*), they both should have a small coupling constant of ~2 Hz but are too broad to appreciate that. *H7* signal can be detected only in ^1H–^{13}C HSQC experiment, as it is completely covered by H_2O broad signal at 3.8 ppm, a typical situation when DMSO-d_6 is employed. Major aromatic impurities signals have an area of ~7% of

$TPACl_6$ ones. Signals at 5.36 ppm and 4.89 ppm are very sharp and even if they look of a comparable height with $TPACl_6$ signals their area is ~15% of one product proton. We have not been able to identify the molecule generating these signals, they can be found in all the synthesis performed with $PhCl_2CH_2Cl$ and given the position and constant ratios we hypothesized that they correspond to the benzylic methylenes belonging to the minor aromatic signals, and thus worthy a ~8% of impurities each. Close to residual solvent peak it can be seen non-deuterated DMSO signal, partially retained also after multiple aqueous washing, showing that $TPACl_6$ is contaminated by ~5% of DMSO. Therefore, it should be safe to assume ~80% NMR purity for $TPACl_6$ mixture.

Figure 3.55 shows ^{13}C NMR of $TPACl_6$ with aromatic *C2–C6* signals clustered between 120 and 130 ppm, while phenolic *C1* and benzylic *C7* can be found at 150.9 ppm and 54 ppm respectively. Detection and assignments for *C2–C6* required to use both ^{1}H–^{13}C HSQC (Figure 3.57) and ^{1}H–^{13}C HMBC (Figure 3.58), particularly for *C3* and *C5* which possess surprisingly low intensity for non-quaternary carbons.

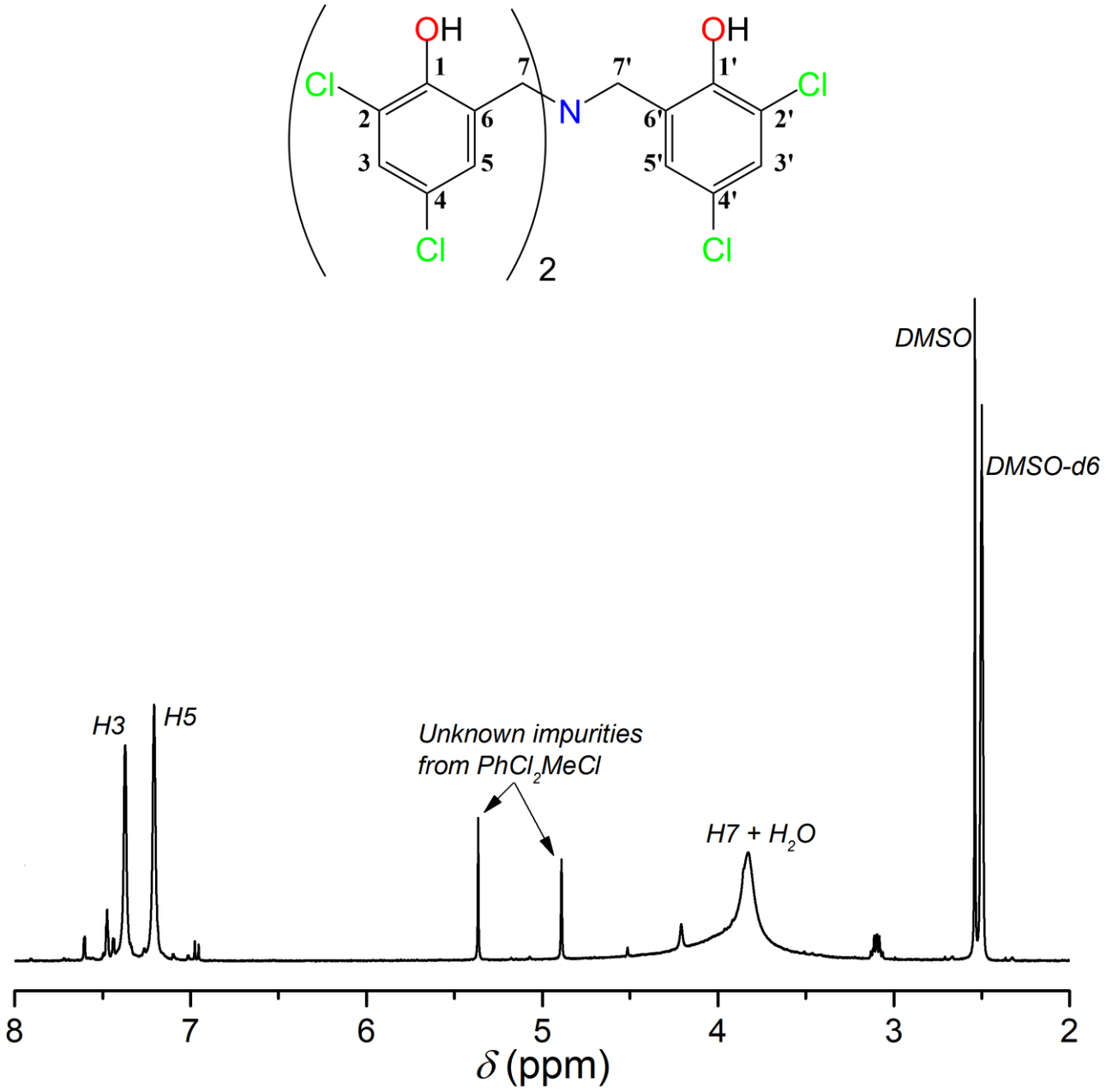

Figure 3.54: Bottom: ^{1}H NMR spectrum of $TPACl_6$ in DMSO-d_6 (298 K, 400.13 MHz). Top: structure of $TPACl_6$. Processing parameters (TopSpin 4.3.0): SI = TD, LB = 0.30 Hz. δ_H (ppm) = 2.50 (residual protons in DMSO-d_6)

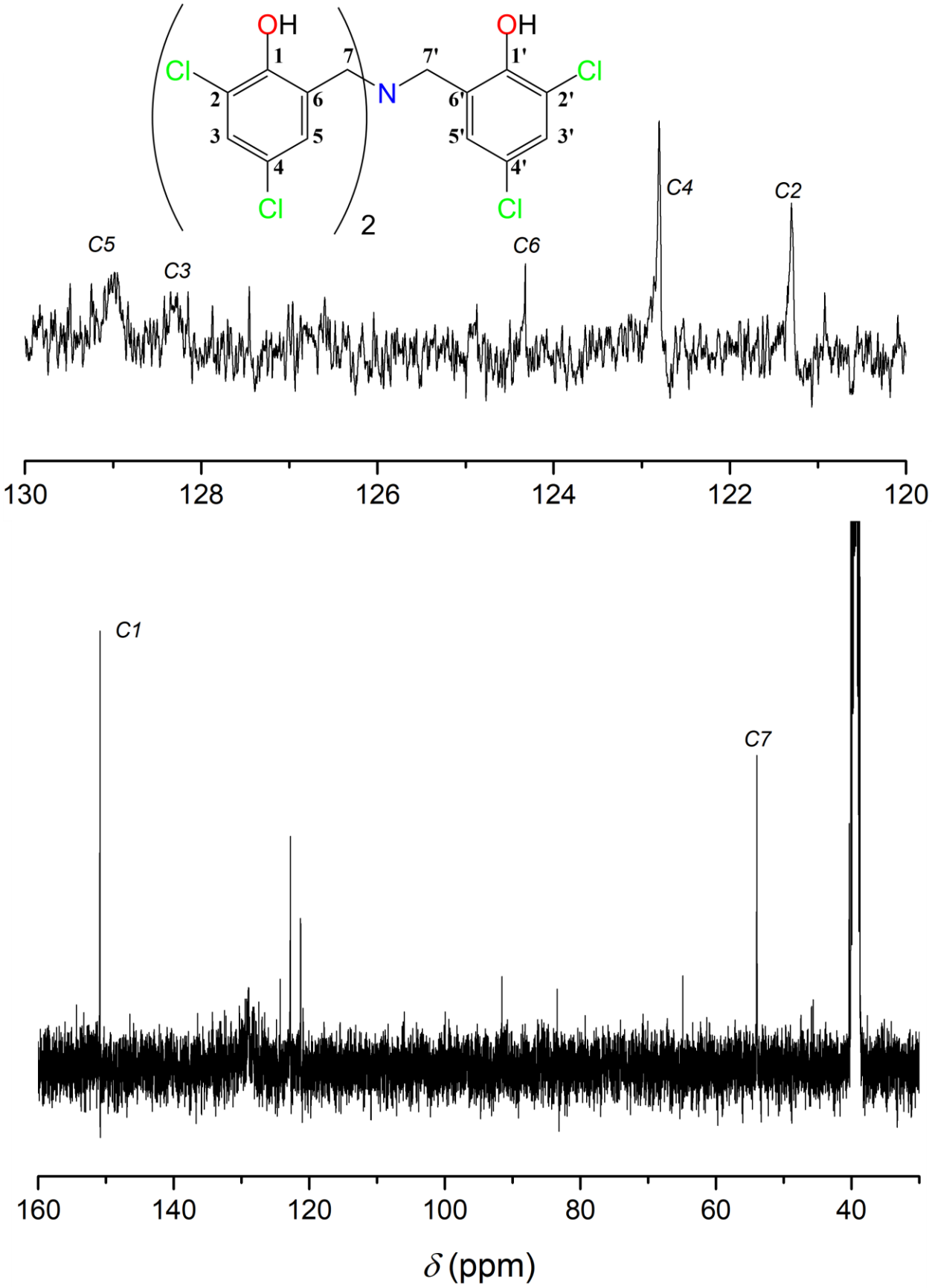

Figure 3.55: Bottom: ^{13}C NMR spectrum of $TPACl_6$ in DMSO-d_6 (298 K, 400.13 MHz). Top: structure of $TPACl_6$ and magnification of the spectrum between 130 ppm and 120 ppm. Processing parameters (TopSpin 4.3.0): SI = TD, LB = 0.30 Hz. δ_C (ppm) = 39.52 (residual carbon in DMSO-d_6)

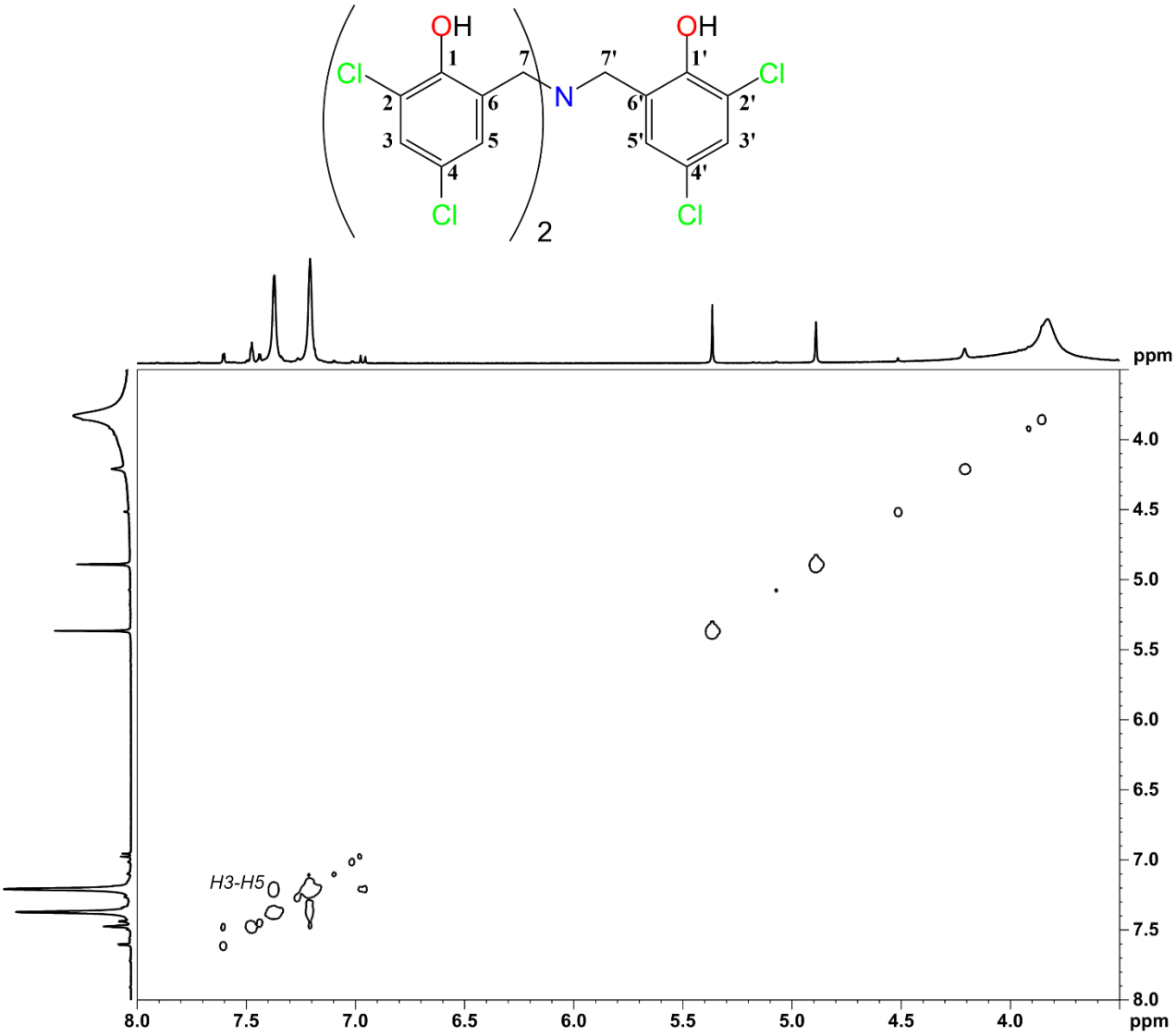

Figure 3.56: Structure and ^{1}H–^{1}H COSY spectrum of $TPACl_6$ in DMSO-d_6 between 8.0 ppm and 3.5 ppm (298 K, 400.13 MHz). The labelling of the cross-peaks indicates the ^{1}H–^{1}H coupling (F2,F1). Processing parameters (TopSpin 4.3.0) for F2 (x axis): SI = TD, LB = 1.00 Hz. Processing parameters for F1 (y axis): SI = 2·TD, LB = 0.30 Hz.

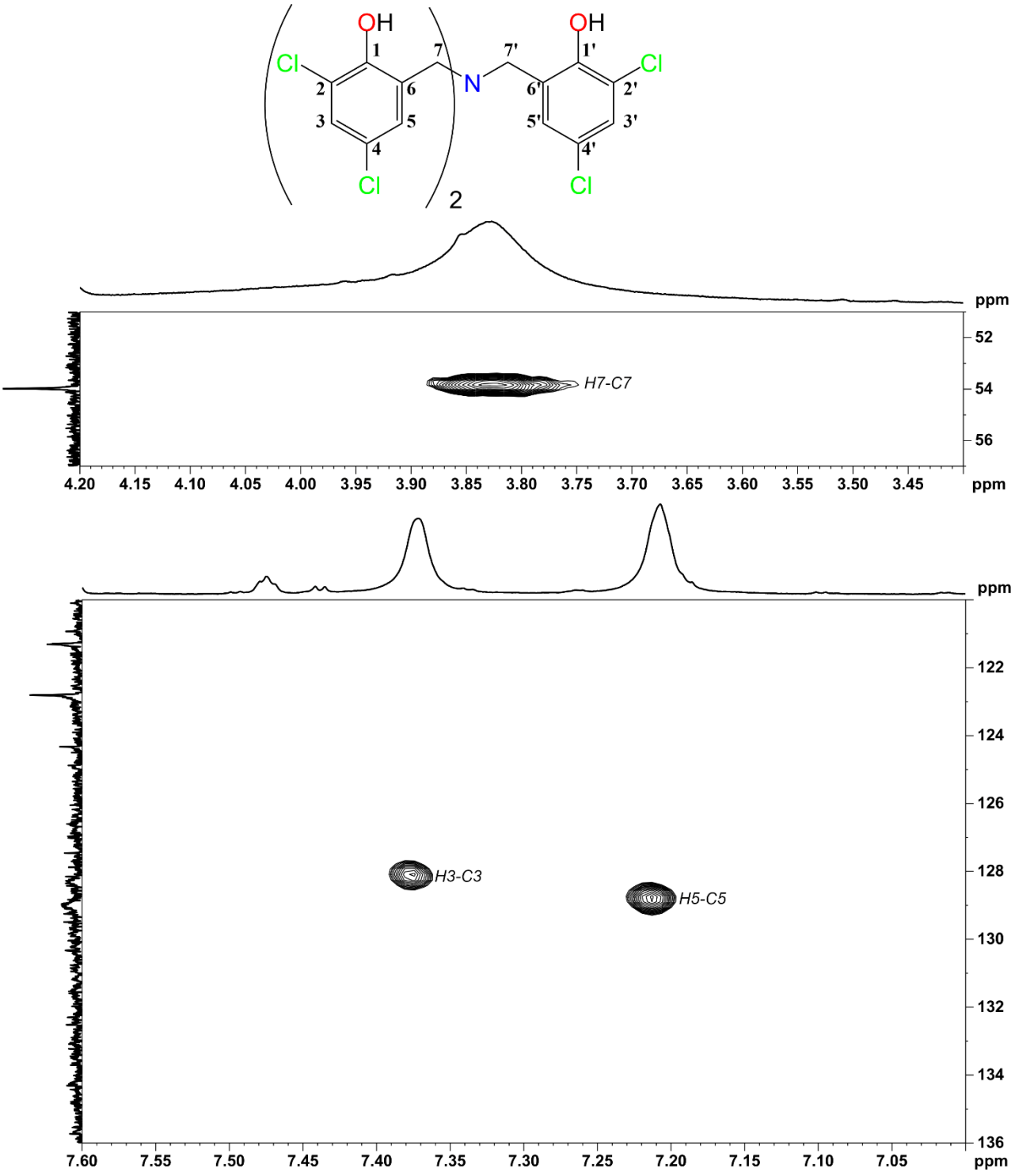

Figure 3.57: Structure and $^{1}H–^{13}C$ HSQC spectrum of $TPACl_6$ in DMSO-d_6 for bottom δ_H = 7.6–7.0 ppm and δ_C = 136–120 ppm, top δ_H = 4.2–3.4 ppm and δ_C = 57–51 ppm. The labelling of the cross-peaks indicates the $^{1}H–^{13}C$ coupling (F2,F1). Processing parameters (TopSpin 4.3.0) for F2 (x axis): SI = 2·TD, LB = 1.00 Hz. Processing parameters for F1 (y axis): SI = 3·TD, LB = 0.30 Hz

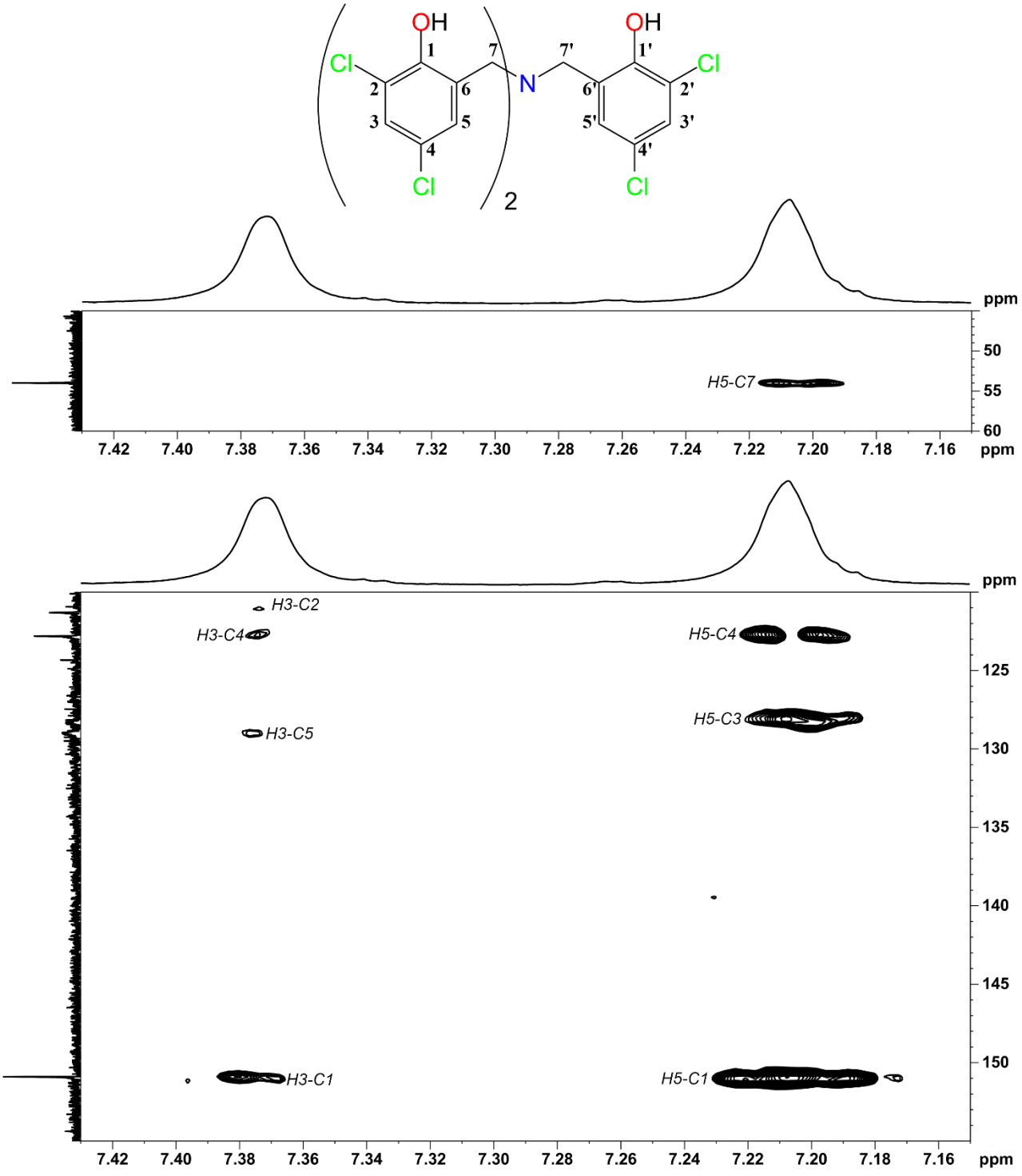

Figure 3.58: Structure and $^{1}H–^{13}C$ HMBC spectrum of $TPACl_6$ in DMSO-d_6 for: bottom δ_H = 7.43–7.15 ppm and δ_C =155–120 ppm, top δ_H = 7.43–7.15 ppm and δ_C = 60–45 ppm (298 K, 400.13 MHz). The labelling of the cross-peaks indicates the $^{1}H–^{13}C$ coupling (F2,F1). Processing parameters (TopSpin 4.3.0) for F2 (x axis): SI = 2·TD, LB = 1.00 Hz. Processing parameters for F1 (y axis): SI = 3·TD, LB = 0.30 Hz

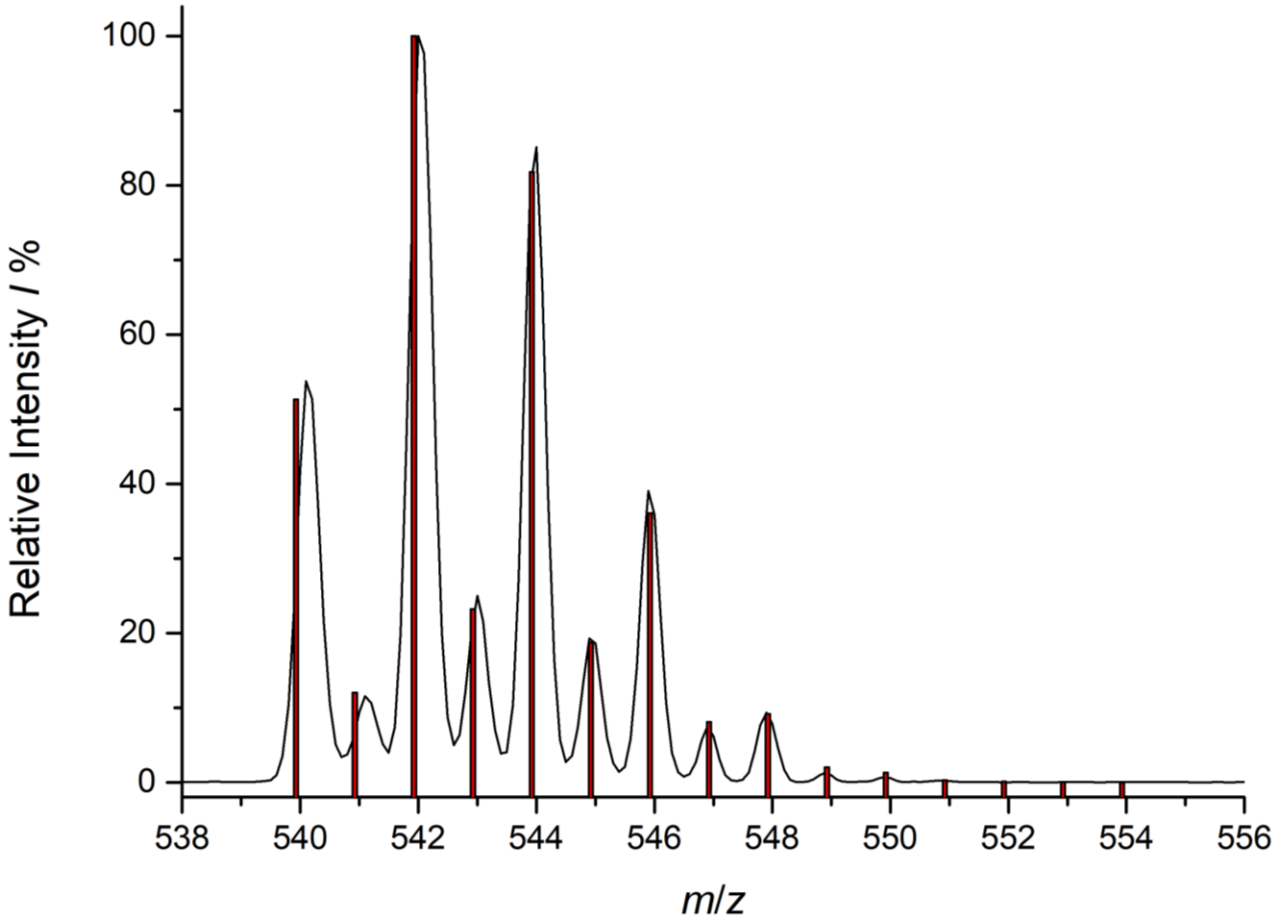

Figure 3.59: Black line: ESI-MS spectrum of $TPACl_6$ (isocratic LC at 80:20 CH_3CN:H_2O (0.1% HCOOH)/Zorbax 30x4.6 mm column, positive ion mode). Red bars: simulated isotopic pattern for $[TPACl_6+H]^+$.

Figure 3.59 displays the experimental ESI-MS spectra of $TPACl_6$ in black, and the simulated isotopic pattern for $[TPACl_6+H]^+$ as red bars, showing a good fit. Concentrations required for ESI-MS are extremely low compared to those needed for NMR, thus it was possible to use CH_3CN even if TPAs are not very soluble in it. $TPACl_6$ is easily recognized by MS thanks to its protonated m/z = 539.92 combined with its very peculiar isotopic pattern given by 6 chloride atoms.

3.5.2 Characterization of 6,6'-(((3,5-difluoro-2-hydroxybenzyl)azanediyl) bis(methylene))bis(2,4-dichlorophenol) ($TPACl_4F_2$)

DMSO-d_6 is required for NMR as solubility in other solvents is too low to reach the concentrations necessary for this technique. Figure 3.60 shows the typical ^{1}H NMR spectrum of $TPACl_4F_2$ purified mixture and it is easy to see that the amount of impurities is negligible, surely much lower than in $TPACl_6$ spectrum, showing a quite clean product. This probably means that PhF_2CH_2Cl is a more selective alkylating reagent than $PhCl_2CH_2Cl$, hypothesis confirmed also by ^{1}H NMR spectra of $TPAF_6$ and $TPAF_4Cl_2$ shown respectively in Sections 3.5.4 and 3.5.5. $TPACl_4F_2$ ^{1}H NMR spectrum (Figure 3.60) shows two sets of two aromatic signals, in area ratio 2 : 1, respectively due to the ligand "Cl branches" and "F branch" both with the expected multiplicity. "Cl branches" signals are doublets with a small $^4J_{H-H}$ of ~2.5 Hz at 7.33 ppm and 7.18 ppm, while "F branch" signals are two poorly resolved double double doublets with different *J*. 7.10 ppm signal has two similar $^3J_{H-F}$ (~10.8 Hz and ~8.8 Hz) and a small $^4J_{H-H}$ of ~2.9 Hz, while 6.92 ppm signal has a big $^3J_{H-F}$ of ~9 Hz and two smaller similar couplings, *i.e.*, $^4J_{H-H}$ (~2.9 Hz) and $^5J_{H-F}$ (~1.5 Hz). In the aliphatic portion of the spectrum the partially overlapped methylene signals are visible as singlets, arising from H_2O signal.

Figure 3.61 shows ^{13}C NMR spectrum, also in this case it is very easy to distinguish between carbons of "Cl branches" and "F branch" as Cl ones stand clearly as singlets, while F ones are barely visible due to the splitting caused by couplings with two fluorides. In particular, detection of *C9*, *C11* and *C13* required ^{1}H–^{13}C HMBC as the first is overlapped with *C6* while intensity of the last two are too low. "Cl branches" signals are clustered between 120 ppm and 130 ppm, except for phenolic and methylenic carbons, which can be found respectively at ~151 ppm and ~54 ppm. "F branch" aromatic signals are all double doublets with different *J*, except for *C12* that is a triplet, having two similar $^2J_{C-F}$, also *C9*, if visible, should have been a triplet with two $^3J_{C-F}$. *C10* signal has a $^2J_{C-F}$ of ~14.6 Hz and a $^4J_{C-F}$ of ~3 Hz, *C11* and *C13* have an *ipso*-F, which generates a wide splitting because of the extremely high coupling constants *C–F* ($^1J_{C-F}$) respectively of ~272 Hz and ~240 Hz while the smaller $^3J_{C-F}$ are ~13 Hz. *C12* has two couplings ($^2J_{C-F}$) of ~25 Hz resulting in a pseudo-triplet signal. *C14* has two quite different coupling constants of ~22 Hz ($^2J_{C-F}$) and ~3 Hz ($^4J_{C-F}$) while *C8* stands as a broad singlet, probably resolution is not good enough to highlight two small $^4J_{C-F}$.

Figure 3.62 shows ^{19}F NMR with two different signals, a triplet at -122 Hz (*F13*) and a doublet at -131 Hz (*F11*) both with $^3J_{H-F}$ of ~10 Hz. This is coherent with both $DPA^{F,F}$ and PhF_2CH_2Cl ^{19}F NMR spectra observations, but with different resolution. In fact, compared to PhF_2CH_2Cl resolution is way lower, as only $^3J_{H-F}$ can be appreciated giving simpler signals. On the other hand, the resolution is way higher than in $DPA^{F,F}$ where the two signals appear as a broad singlet and a poorly resolved

doublet. In $^{1}H–^{13}C$ HMBC (Figure 3.65) it can be noted a coupling between *H7* and *C7'* due to symmetry, *i.e.*, the interaction of the methylenic protons of a "Cl branch" with the methylenic carbon of the other "Cl branch".

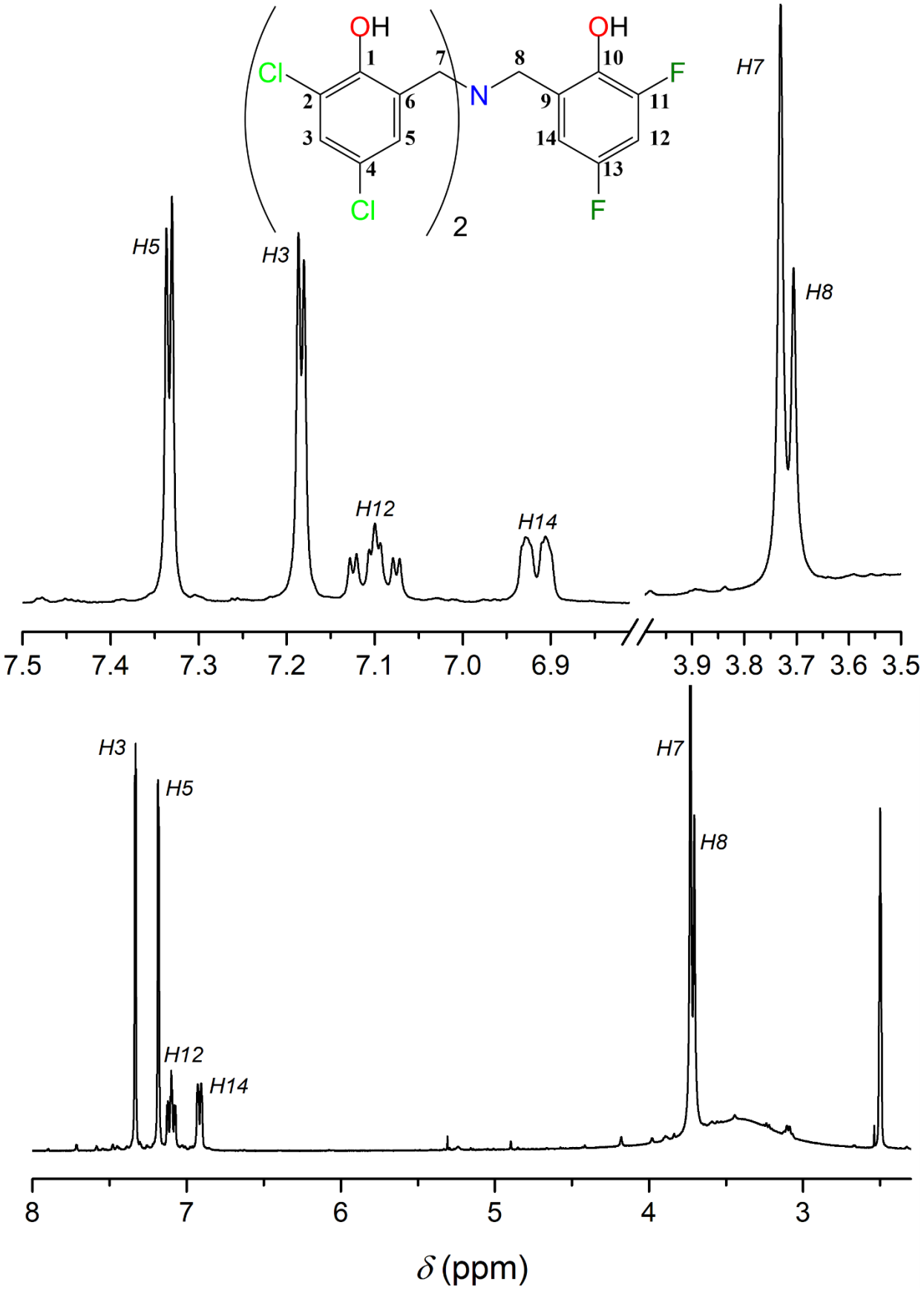

Figure 3.60: Bottom: ^{1}H NMR spectrum of $TPACl_4F_2$ in DMSO-d_6 (298 K, 400.13 MHz). Top: structure of $TPACl_4F_2$ and magnification of the spectrum in 7.5–6.8 ppm and 4.0–3.5 ppm ranges. Processing parameters (TopSpin 4.3.0): SI = TD, LB = 0.30 Hz. δ_H (ppm) = 2.50 (residual protons in DMSO-d_6)

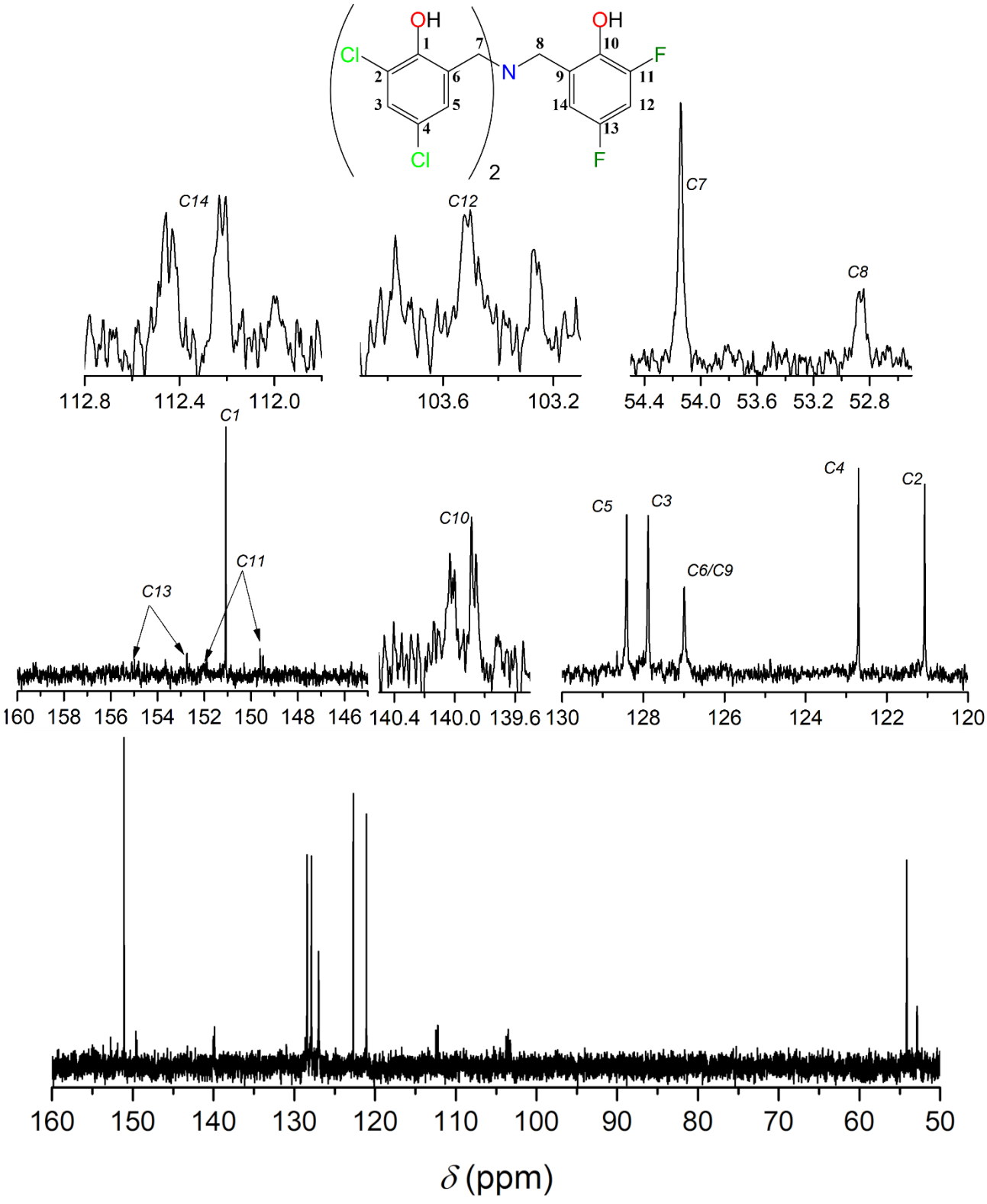

Figure 3.61: Bottom: ^{13}C NMR spectrum of $TPACl_4F_2$ in DMSO-d_6 (298 K, 400.13 MHz). Top: structure of $TPACl_4F_2$ and magnification of the spectrum in 160–145 ppm, 140.5–139.5 ppm, 130–120 ppm, 112.8–111.8 ppm, 104–103 ppm and 54.5–52.5 ppm. Processing parameters (TopSpin 4.3.0): SI = TD, LB = 0.30 Hz. δ_C (ppm) = 39.52 (residual carbon in DMSO-d_6)

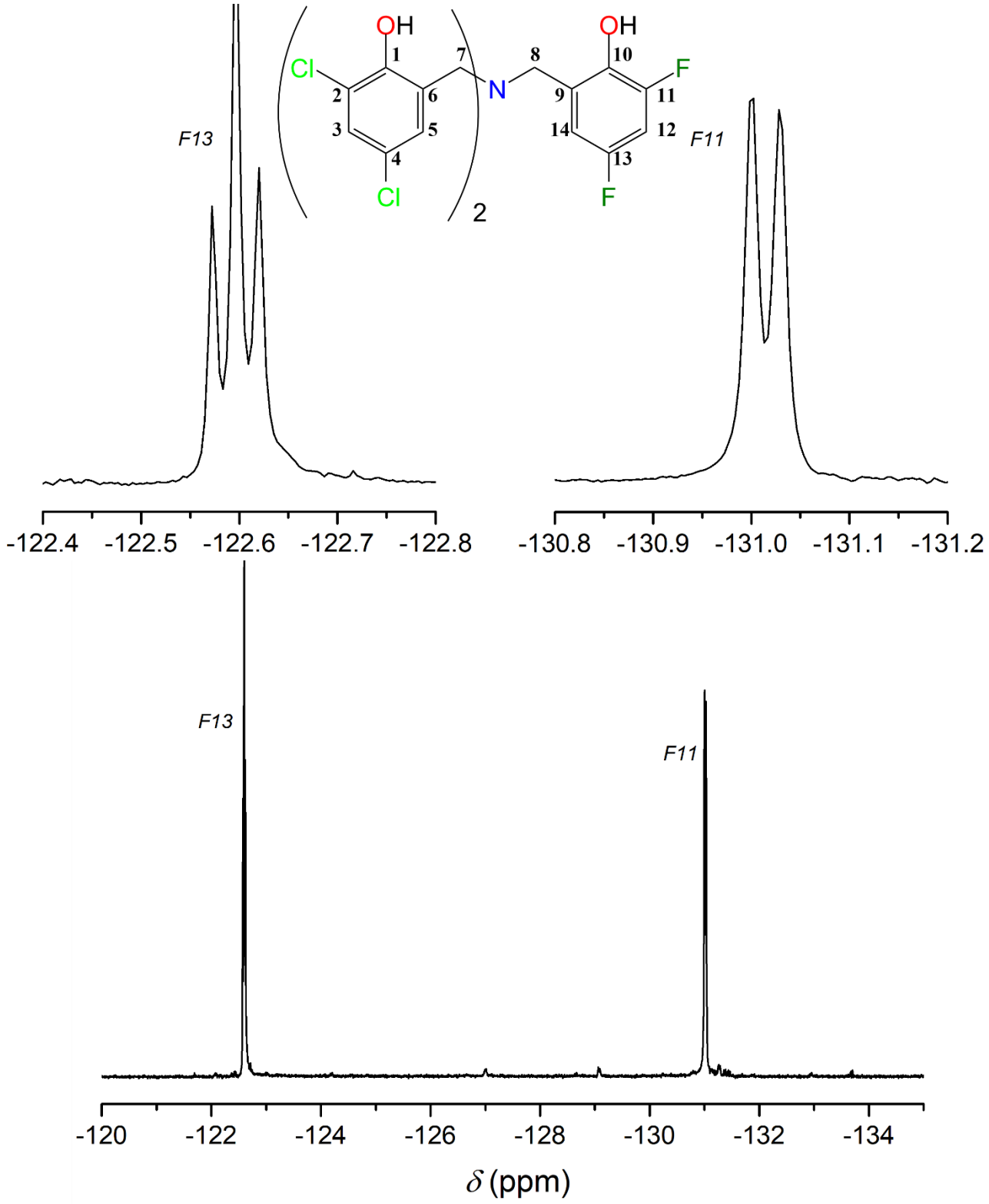

Figure 3.62: Bottom: ^{19}F NMR spectrum of $TPACl_4F_2$ in DMSO-d_6 (298 K, 400.13 MHz). Top: Magnification of the spectrum between −122.4–−122.8 ppm and −130.8–−131.2 ppm and structure of $TPACl_4F_2$. Processing parameters (TopSpin 4.3.0): SI = TD, LB = 0.30 Hz.

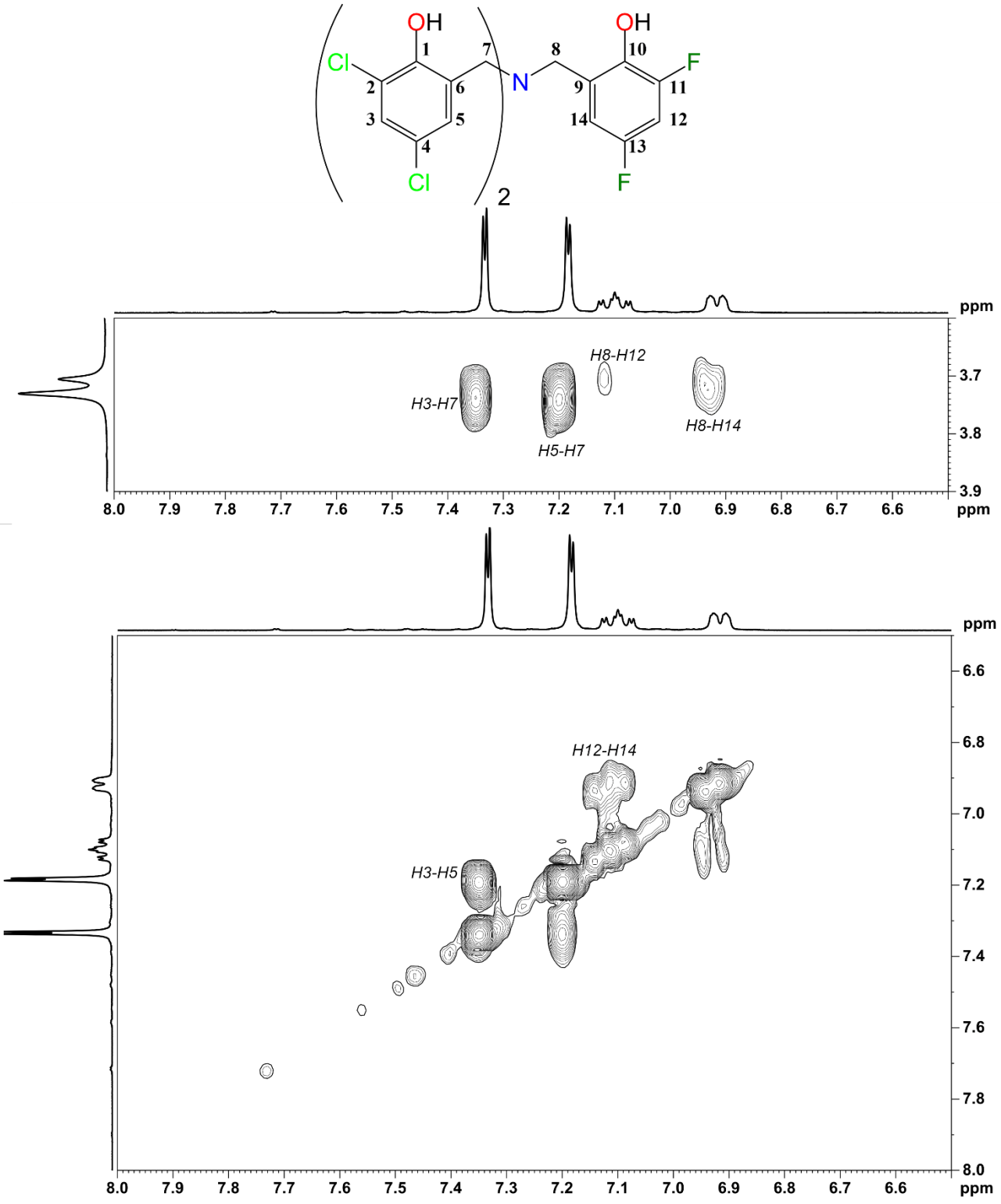

Figure 3.63: Structure and ^{1}H–^{1}H COSY spectrum of $TPACl_4F_2$ in DMSO-d_6 bottom between 8.0 ppm and 6.5 ppm, top between 8.0–6.5 ppm (x) and 3.9–3.6 ppm (y) (298 K, 400.13 MHz). The labelling of the cross-peaks indicates the ^{1}H–^{1}H coupling (F2,F1). Processing parameters (TopSpin 4.3.0) for F2 (x axis): SI = TD, LB = 1.00 Hz. Processing parameters for F1 (y axis): SI = 2·TD, LB = 0.30 Hz.

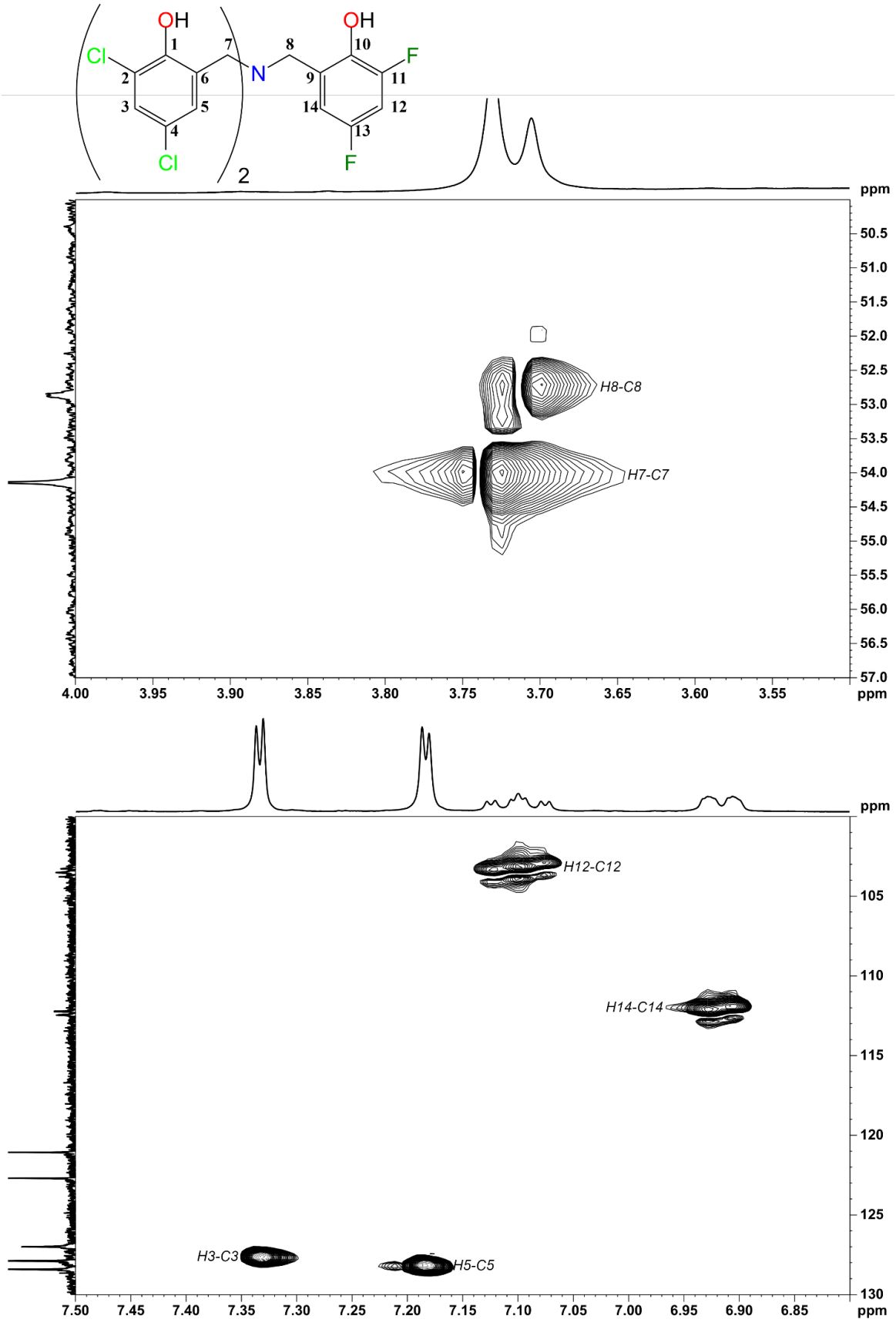

Figure 3.64: Structure and ^{1}H–^{13}C HSQC spectrum of $TPACl_4F_2$ in DMSO-d_6 for bottom δ_H = 7.5–6.8 ppm and δ_C = 130–100 ppm, top δ_H = 4.0–3.5 ppm and δ_C = 57–50 ppm. The labelling of the cross-peaks indicates the ^{1}H–^{13}C coupling (F2,F1). Processing parameters (TopSpin 4.3.0) for F2 (x axis): SI = 2·TD, LB = 1.00 Hz. Processing parameters for F1 (y axis): SI = 3·TD, LB = 0.30 Hz

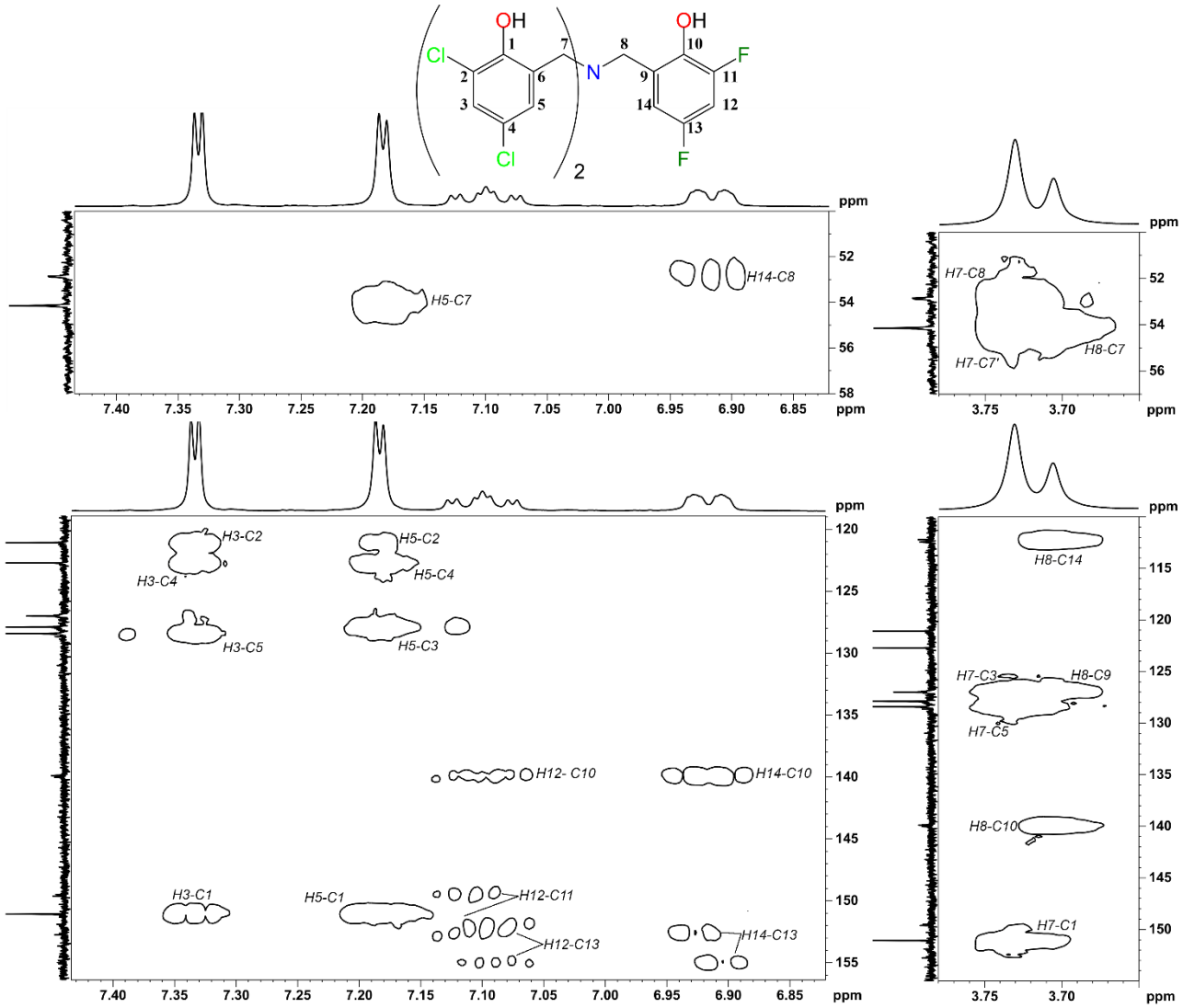

Figure 3.65: Structure and ^{1}H–^{13}C HMBC spectrum of $TPACl_4F_2$ in DMSO-d_6 for: bottom-left δ_H = 7.45–6.80 ppm and δ_C =156–119 ppm, bottom-right δ_H = 3.77–3.65 ppm and δ_C = 155–110 ppm, top-left δ_H = 7.45–6.80 ppm and δ_C = 58–50 ppm, top-right δ_H = 3.77–3.65 ppm and δ_C = 57–50 ppm (298 K, 400.13 MHz). The labelling of the cross-peaks indicates the ^{1}H–^{13}C coupling (F2,F1). Processing parameters (TopSpin 4.3.0) for F2 (x axis): SI = 2·TD, LB = 1.00 Hz. Processing parameters for F1 (y axis): SI = 3·TD, LB = 0.30 Hz

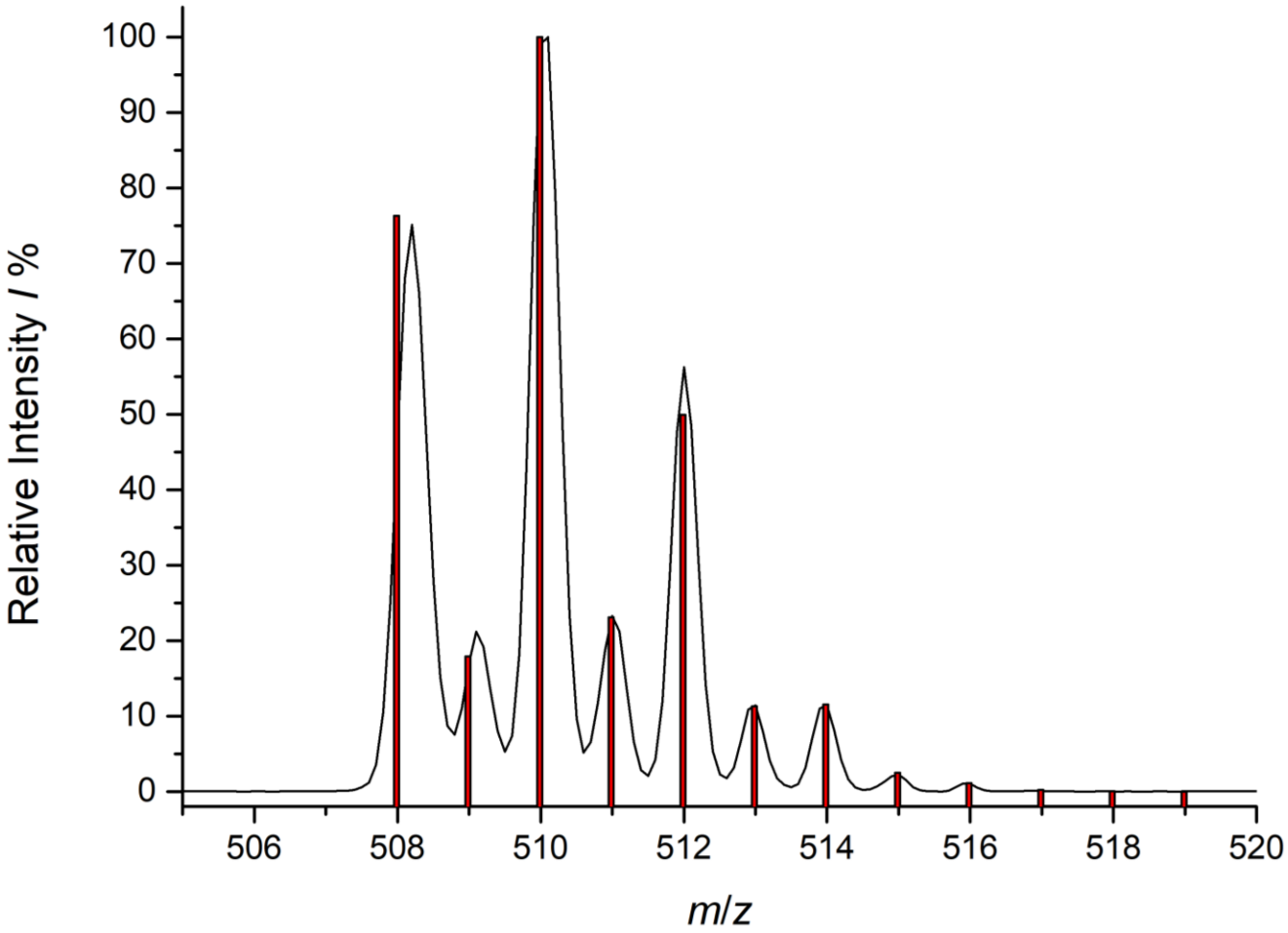

Figure 3.66: Black line: ESI-MS spectrum of $TPACl_4F_2$ (isocratic LC at 80:20 CH_3CN:H_2O (0.1% HCOOH)/Zorbax 30x4.6 mm column, positive ion mode). Red bars: simulated isotopic pattern for $[TPACl_4F_2+H]^+$.

Figure 3.66 displays the experimental ESI-MS spectra of $TPACl_4F_2$ in black, and the simulated isotopic pattern for $[TPACl_4F_2+H]^+$ as red bars, showing a good fit. Concentrations required for ESI-MS are extremely low compared to those needed for NMR, thus it was possible to use CH_3CN even if TPAs are not very soluble in it. $TPACl_4F_2$ is easily recognized by MS thanks to its protonated *m*/*z* = 507.98 combined with its very peculiar isotopic pattern given by 4 chloride atoms.

3.5.3 Characterization of 6,6'-(((3-nitro-5-chloro-2-hydroxybenzyl)azanediyl) bis(methylene))bis(2,4-dichlorophenol) ($TPACl_5NO_2$)

DMSO-d_6 is required for NMR as solubility in other solvents is too low to reach the concentrations necessary for this technique. Figure 3.67 represent the typical ^{1}H NMR spectrum of $TPACl_5NO_2$ purified mixture, showing the worst situation in terms of purity of all the six TPAs synthetized with 40% of an unidentified by-product and some other impurities we estimated to be ~10% of $TPACl_5NO_2$. This observation leads to considerations about reactivity and selectivity of PhX_2CH_2Cls which seems to be in the following order $PhClNO_2CH_2Cl$ > $PhCl_2CH_2Cl$ > PhF_2CH_2Cl, trend also confirmed by TPAs obtained from $DPA^{F,F}$ alkylation. $PhClNO_2CH_2Cl$ higher reactivity was predictable, as NO_2 group greater EWG character surely cause the δ^+ on the benzylic position to be higher and thus a better alkylating agent. On the other hand, it would be expected following the same reasoning a higher reactivity from PhF_2CH_2Cl than $PhCl_2CH_2Cl$ given the higher electronegativity of fluoride, thus there must be other factors to be considered in addition to electronic ones to properly explain these observations. As far as concern ^{1}H NMR of $PhClNO_2CH_2Cl$ (Figure 3.67) resolution is quite poor making all the aromatic signals broad singlets with a 2 : 1 ratio between "Cl branches" (7.33 ppm, 7.19 ppm) and "NO_2 branch" (7.82 ppm, 7.53 ppm). Benzylic signals are distinguishable as decently sharp singlets (4.00 ppm and 3.80 ppm), both partially overlapped to the wide water signal (3.46 ppm). Given the similar area of the main by-product aromatic protons to the "NO_2 branch" ones, proper identification required to combine ^{1}H NMR with ^{1}H–^{13}C HMBC and ^{1}H–^{13}C HSQC information (Figures 3.70 and 3.71).

Figure 3.68 shows ^{13}C NMR spectrum with both branches' aromatic signals clustered between 120 ppm and 140 ppm, with the exception of phenolic and benzylic carbons found at 151.37 ppm, 151.07 ppm and 54.75 ppm, 46.76 ppm respectively, with both "NO_2 branch" signals barely visible and detected through ^{1}H–^{13}C HSQC and ^{1}H–^{13}C HMBC. Finally, in ^{1}H–^{13}C HMBC (Figure 3.71) it can be noted a coupling between *H7* and *C7'* due to symmetry, *i.e.*, the interaction of the methylenic protons of a "Cl branch" with the methylenic carbon of the other "Cl branch".

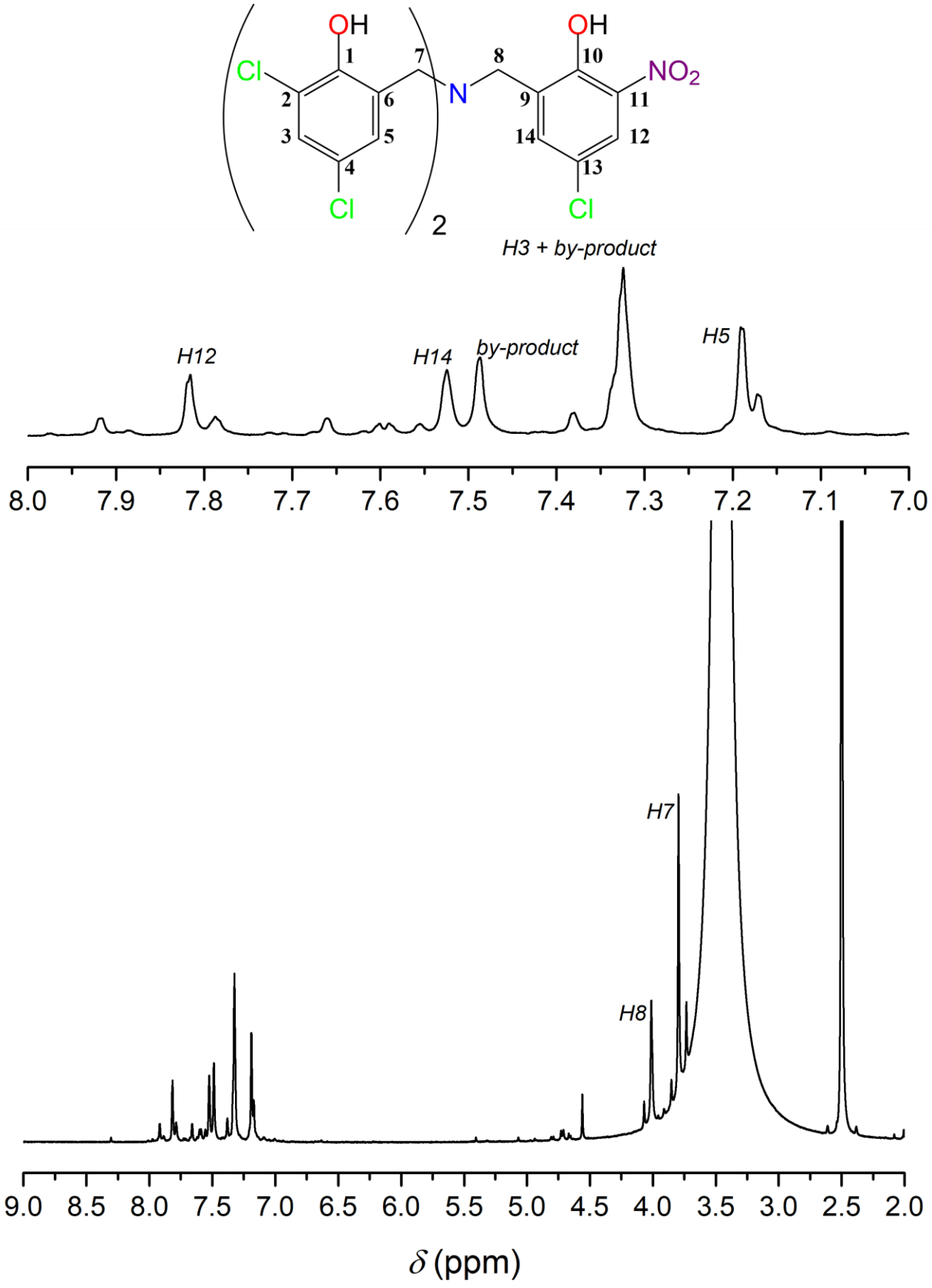

Figure 3.67: Bottom: ^{1}H NMR spectrum of $TPACl_5NO_2$ in DMSO-d_6 (298 K, 400.13 MHz). Top: structure of $TPACl_5NO_2$ and magnification of the spectrum between 8.0 and 7.0 ppm. Processing parameters (TopSpin 4.3.0): SI = TD, LB = 0.30 Hz. δ_H (ppm) = 2.50 (residual protons in DMSO-d_6)

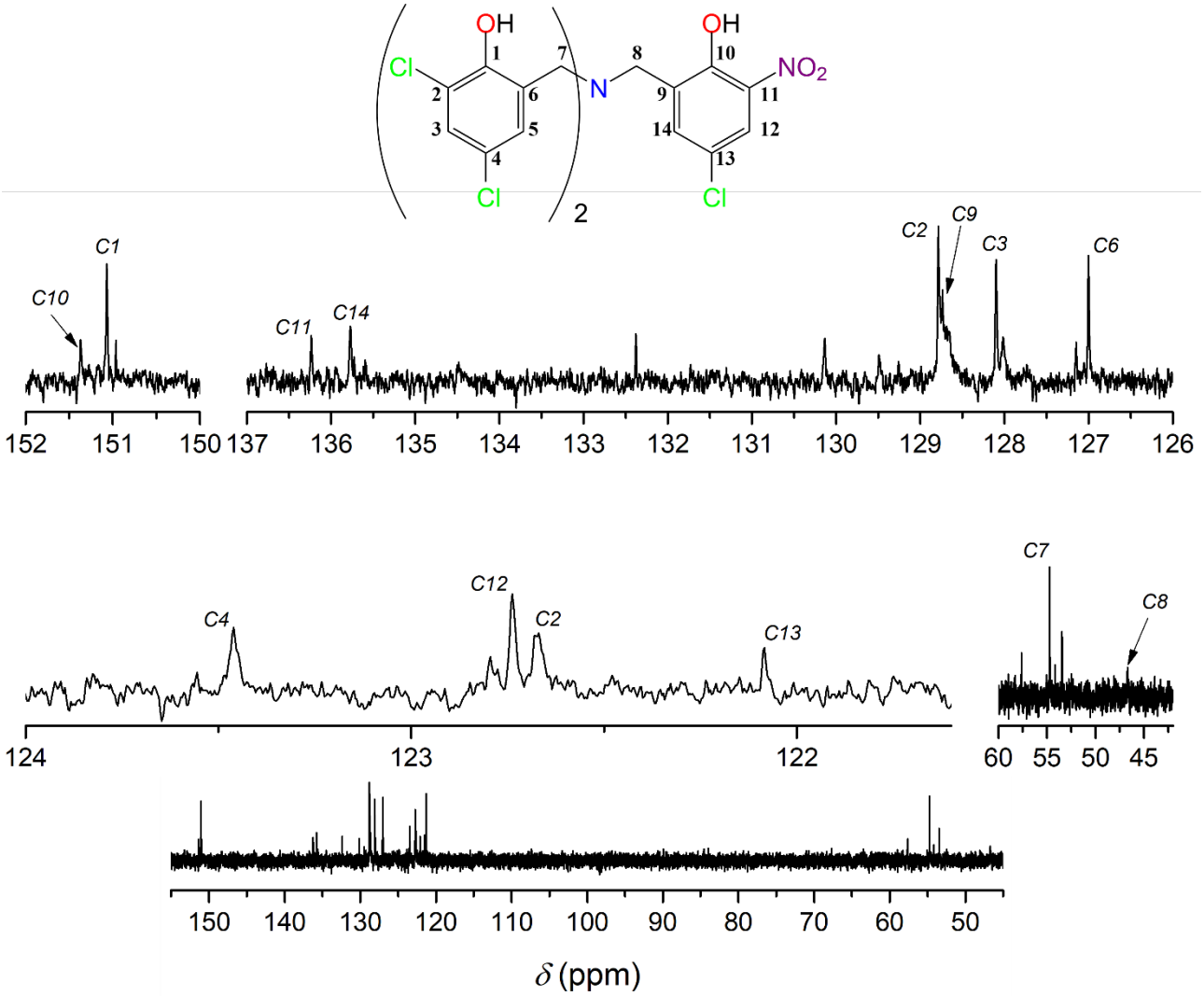

Figure 3.68: Bottom: ^{13}C NMR spectrum of $TPACl_5NO_2$ in DMSO-d_6 (298 K, 400.13 MHz). Top: structure of $TPACl_5NO_2$ and magnification of the spectrum in 152–150 ppm, 137–126 ppm, 124–121 ppm and 60–43 ppm. Processing parameters (TopSpin 4.3.0): SI = TD, LB = 0.30 Hz. δ_C (ppm) = 39.52 (residual carbon in DMSO-d_6)

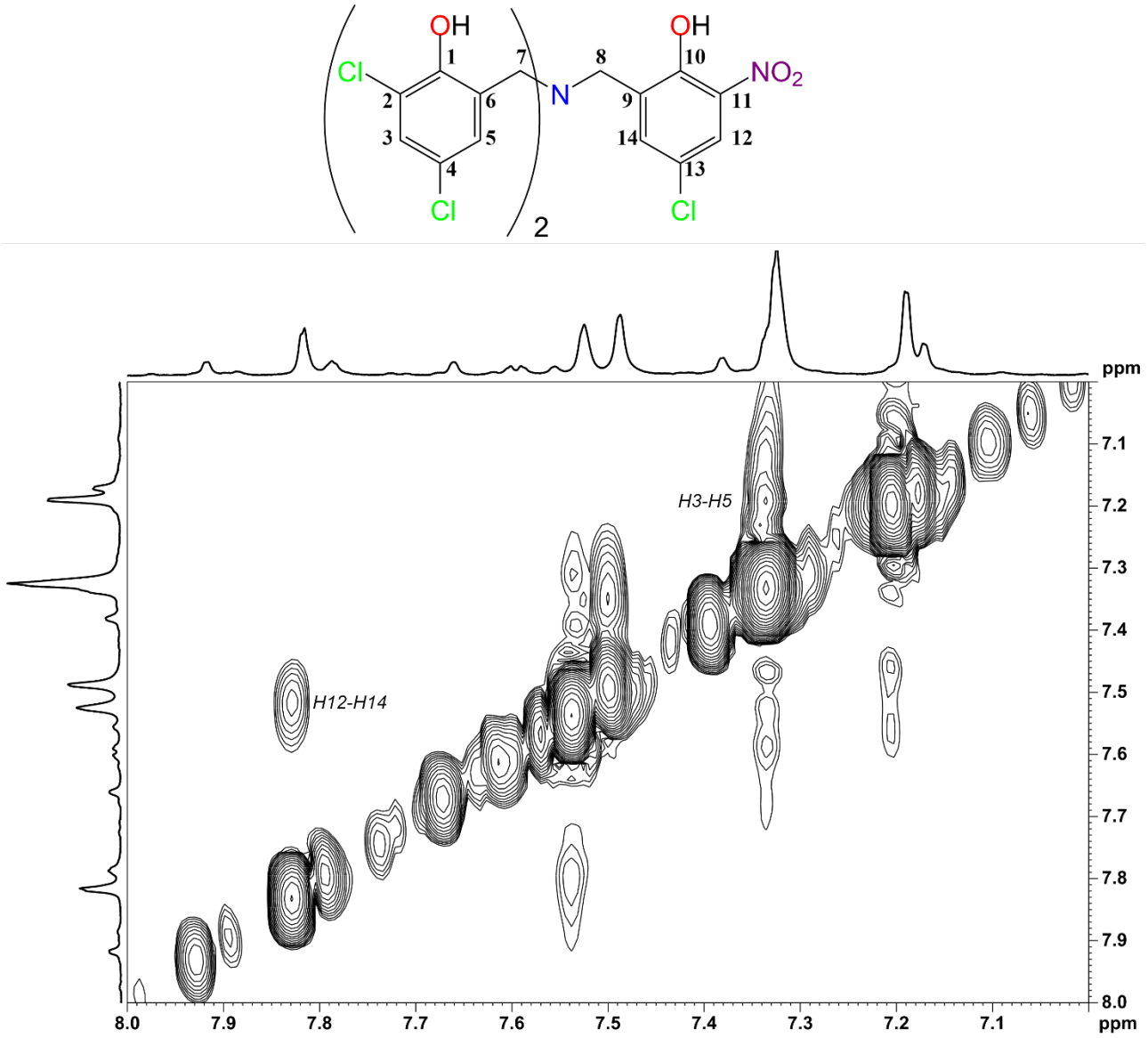

Figure 3.69: Structure and $^{1}H–^{1}H$ COSY spectrum of $TPACl_5NO_2$ in DMSO-d_6 bottom between 8.0 ppm and 7.0 ppm (298 K, 400.13 MHz). The labelling of the cross-peaks indicates the $^{1}H–^{1}H$ coupling (F2,F1). Processing parameters (TopSpin 4.3.0) for F2 (x axis): SI = TD, LB = 1.00 Hz. Processing parameters for F1 (y axis): SI = 2·TD, LB = 0.30 Hz.

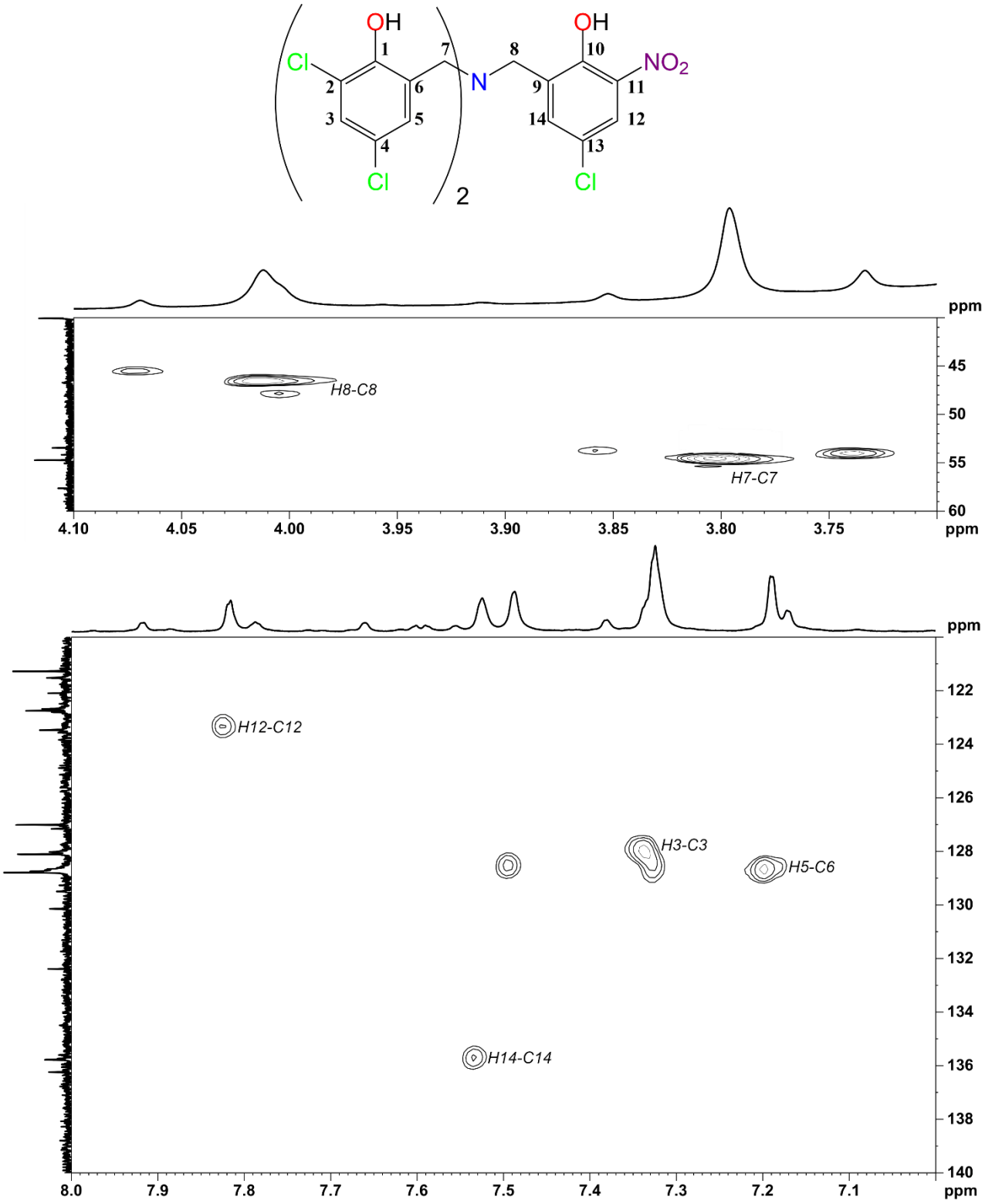

Figure 3.70: Structure and ^{1}H–^{13}C HSQC spectrum of $TPACl_5NO_2$ in DMSO-d_6 for bottom δ_H = 8.0–7.0 ppm and δ_C = 140–120 ppm, top δ_H = 4.1–3.7 ppm and δ_C = 60–40 ppm. The labelling of the cross-peaks indicates the ^{1}H–^{13}C coupling (F2,F1). Processing parameters (TopSpin 4.3.0) for F2 (x axis): SI = 2·TD, LB = 1.00 Hz. Processing parameters for F1 (y axis): SI = 3·TD, LB = 0.30 Hz

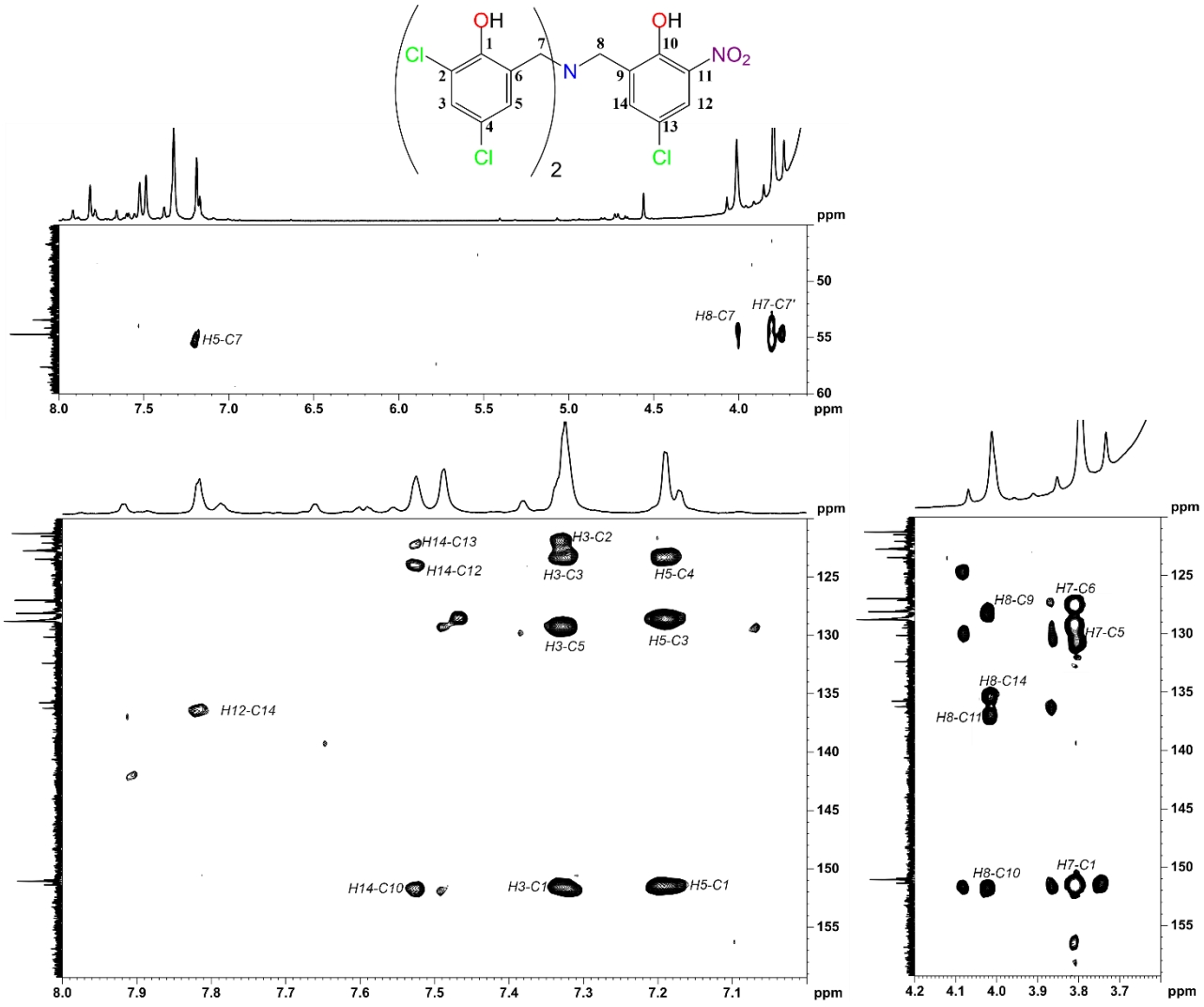

Figure 3.71: Structure and ^{1}H–^{13}C HMBC spectrum of $TPACl_5NO_2$ in DMSO-d_6 for: bottom-left δ_H = 8.0–7.0 ppm and δ_C =160–120 ppm, bottom-right δ_H = 4.2–3.6 ppm and δ_C = 160–120 ppm, top δ_H = 8.0–3.5 ppm and δ_C = 60–45 ppm (298 K, 400.13 MHz). The labelling of the cross-peaks indicates the ^{1}H–^{13}C coupling (F2,F1). Processing parameters (TopSpin 4.3.0) for F2 (x axis): SI = 2·TD, LB = 1.00 Hz. Processing parameters for F1 (y axis): SI = 3·TD, LB = 0.30 Hz

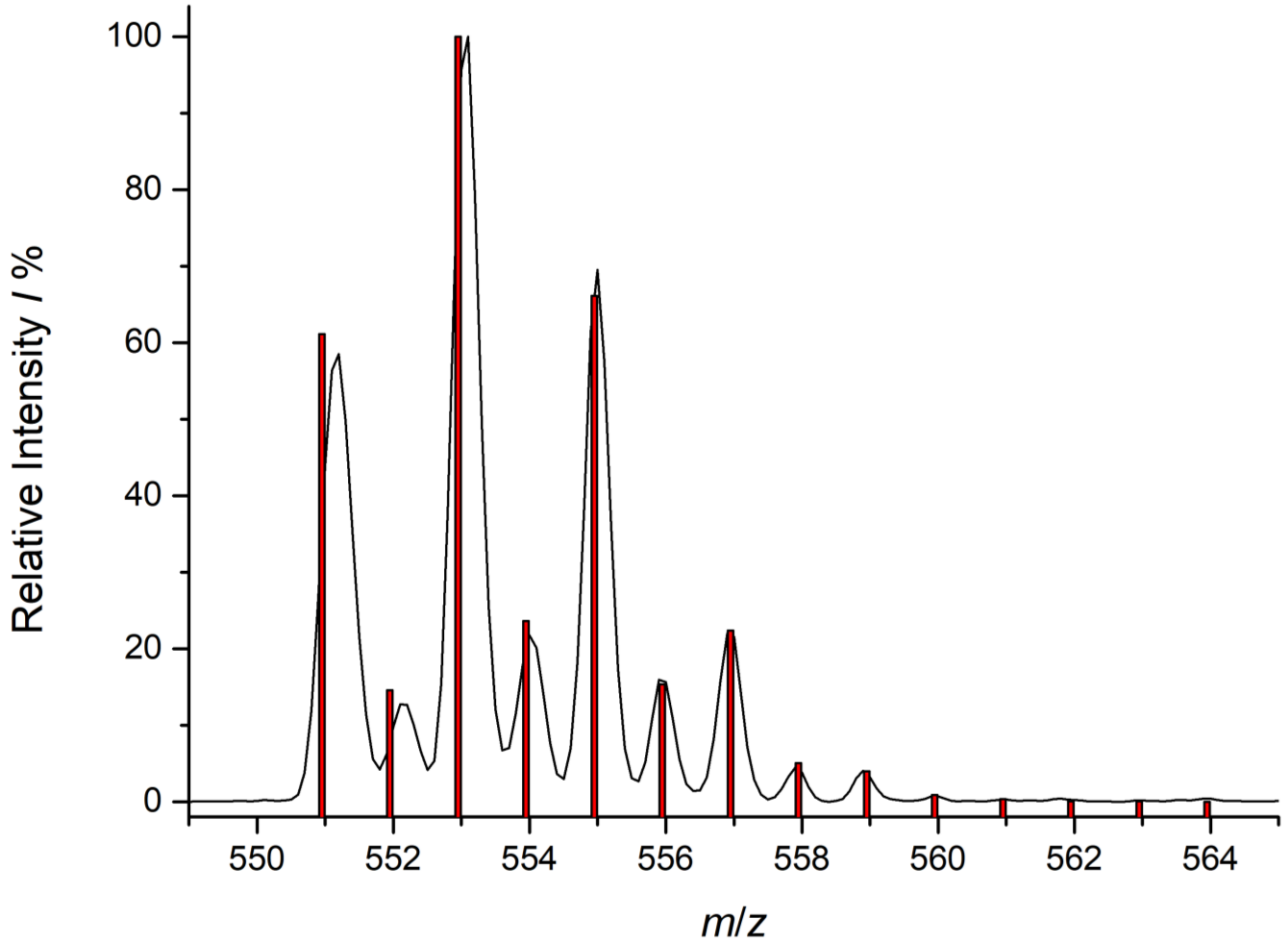

Figure 3.72: Black line: ESI-MS spectrum of $TPACl_5NO_2$ (isocratic LC at 80:20 CH_3CN:H_2O (0.1% HCOOH)/Zorbax 30x4.6 mm column, positive ion mode). Red bars: simulated isotopic pattern for $[TPACl_5NO_2+H]^+$.

Figure 3.72 displays the experimental ESI-MS spectra of $TPACl_5NO_2$ in black, and the simulated isotopic pattern for $[TPACl_5NO_2+H]^+$ as red bars, showing a good fit. Concentrations required for ESI-MS are extremely low compared to those needed for NMR, thus it was possible to use CH_3CN even if TPAs are not very soluble in it. $TPACl_5NO_2$ is easily recognized by MS thanks to its protonated m/z = 550.95 combined with its very peculiar isotopic pattern given by 5 chloride atoms.

3.5.4 Characterization of 6,6',6''-(nitrilotris(methylene))tris(2,4-difluorophenol) ($TPAF_6$)

DMSO-d_6 is required for NMR as solubility in other solvents is too low to reach the concentrations necessary for this technique. Figure 3.73 displays the ^{1}H NMR of $TPAF_6$ purified mixture, showing a very good purity, similar to the results obtained for $TPACl_4F_2$ confirming PhF_2CH_2Cl higher selectivity in this type of reactions. Unfortunately, resolution is quite poor, causing multiplicity to not be appreciable, thus aromatic protons assignation (7.13 ppm, 6.99 ppm) came from ^{1}H–^{13}C HMBC analysis. Interestingly, a very broad signal of area = 3 can be found at ~10 ppm, a very deshielded position for a phenolic OH. While surprising, this behavior was not completely unexpected as we already observed something similar for $PhClNO_2CH_2Cl$ (Section 3.4.3).

Figure 3.74 shows the ^{19}F NMR with two broad singlets, at -122.6 Hz (*F13*) and at -131.9 Hz (*F11*). This is coherent with all the previously described fluorinated products but with poor resolution, thus assignments were based on position comparison with both $DPA^{F,F}$ and PhF_2CH_2Cl, as without visible multiplicity it would be impossible to do it independently.

^{13}C NMR of $TPAF_6$ (Figure 3.75) was acquired performing a much larger number of scans, requiring 15 hours instead of 30 min, and setting different parameters as with the "standard" ^{13}C programme no peaks were detectable. All the signals possess 2 *C–F* couplings giving a set of 7 double doublet signals. *C1* signal has a $^{2}J_{C-F}$ of ~15 Hz $^{4}J_{C-F}$ of ~4 Hz. *C2* and *C4* both have an *ipso*-F, which generates a wide splitting because of the extremely high coupling constants $^{1}J_{C-F}$ respectively of ~240 Hz and ~242 Hz while the smaller $^{3}J_{C-F}$ are both ~12 Hz. *C3* has two couplings ($^{2}J_{C-F}$) of ~27 Hz and ~22 Hz, this is quite surprising as from 2 similar $^{2}J_{C-F}$ a triplet would be predicted. Also *C6* and *C7* have two quite different $^{3}J_{C-F}$ (~9 Hz and ~3 Hz) and $^{4}J_{C-F}$ (~4 Hz and ~2 Hz) respectively. Finally, *C5* has two different coupling constants of ~24 Hz ($^{2}J_{C-F}$) and 4 Hz ($^{4}J_{C-F}$). Lastly, as observed in all DPAs and TPAs, ^{1}H–^{13}C HMBC (Figure 3.78) shows a coupling between *H7* and *C7'* due to symmetry, *i.e.*, the interaction of methylenic protons and methylenic carbon of two different "branches".

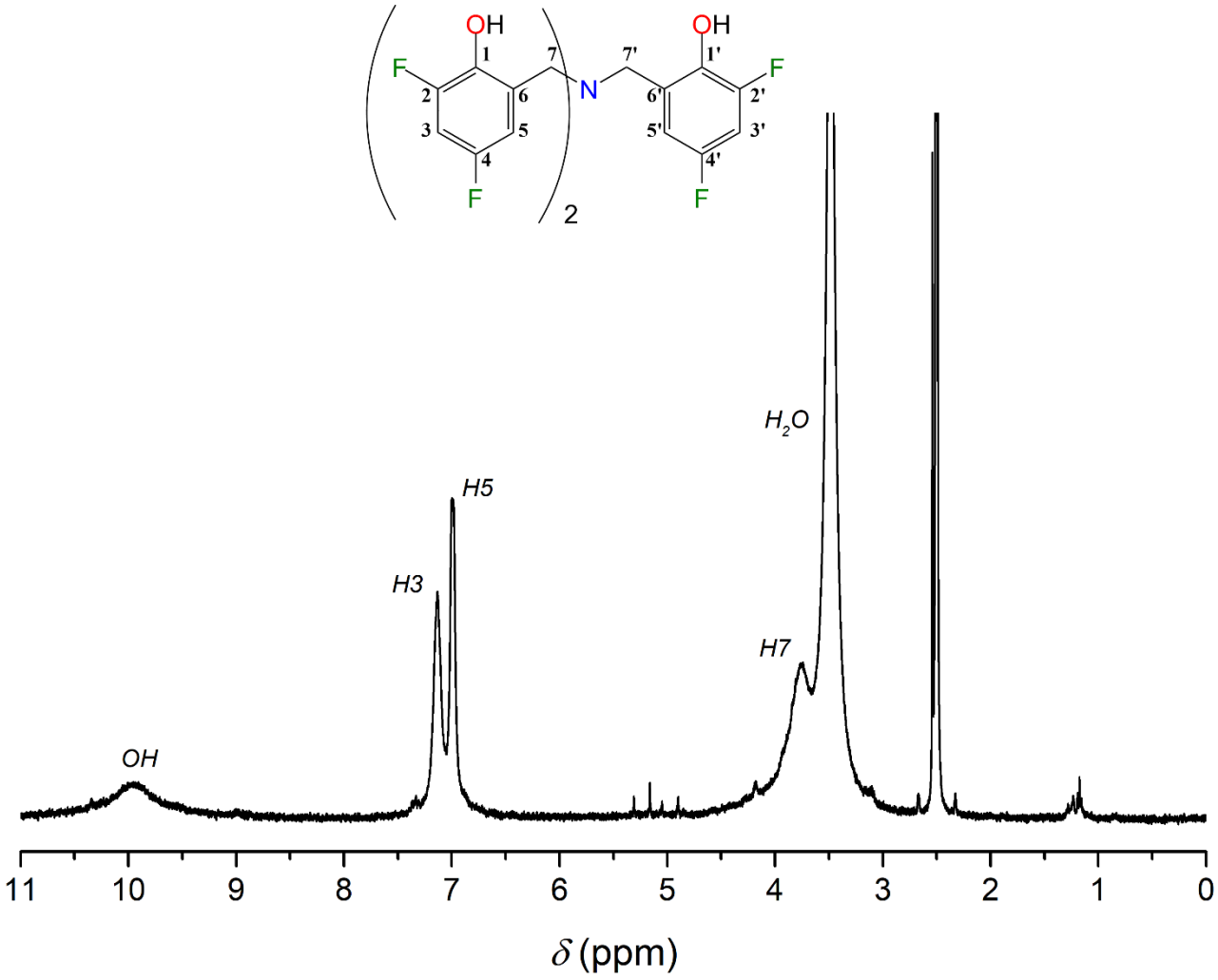

Figure 3.73: Bottom: ^{1}H NMR spectrum of $TPAF_6$ in DMSO-d_6 (298 K, 400.13 MHz). Top: structure of $TPAF_6$. Processing parameters (TopSpin 4.3.0): SI = TD, LB = 0.30 Hz. δ_H (ppm) = 2.50 (residual protons in DMSO-d_6)

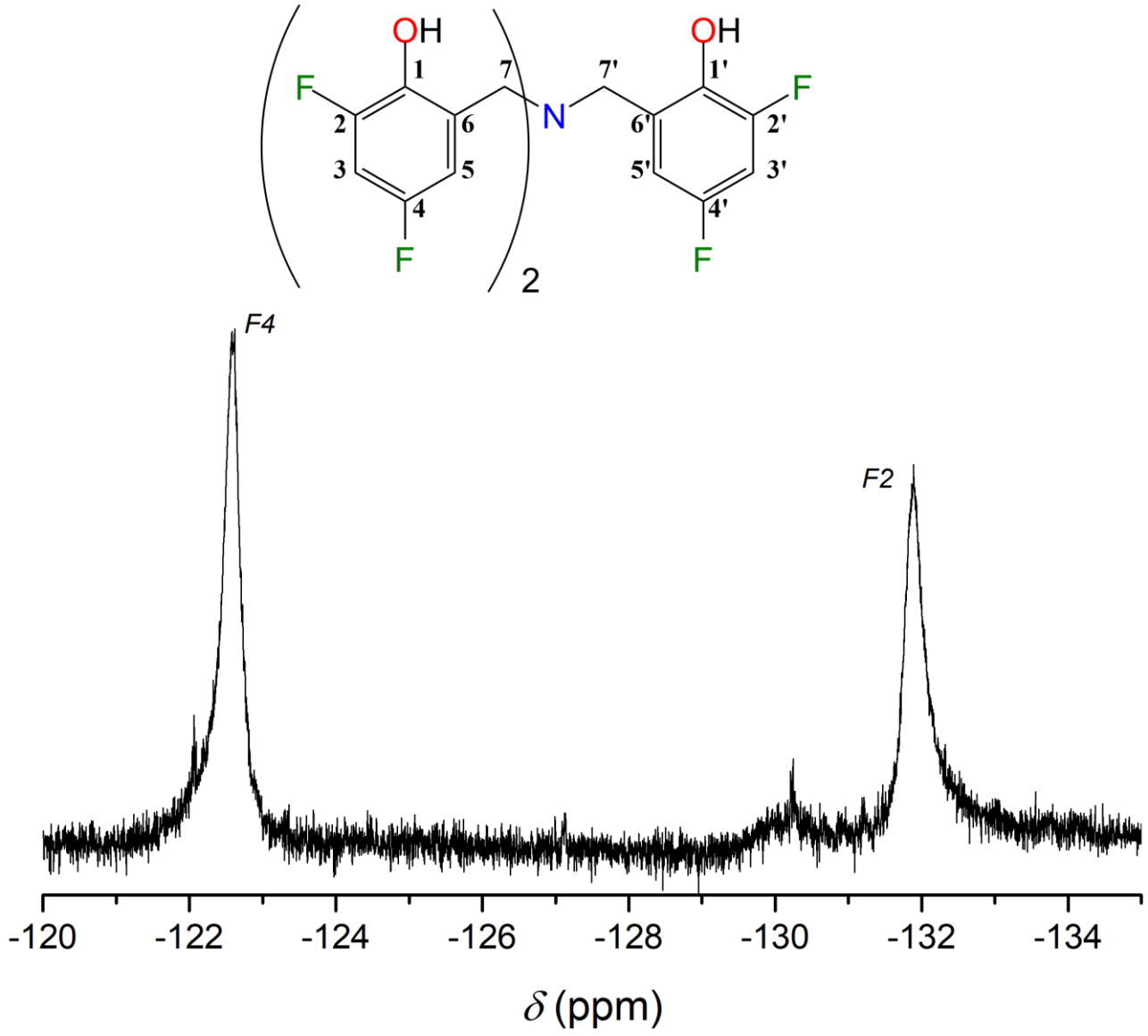

Figure 3.74: ^{19}F NMR spectrum of $TPAF_6$ in DMSO-d_6 (298 K, 400.13 MHz) and structure of $TPAF_6$. Processing parameters (TopSpin 4.3.0): SI = TD, LB = 0.30 Hz.

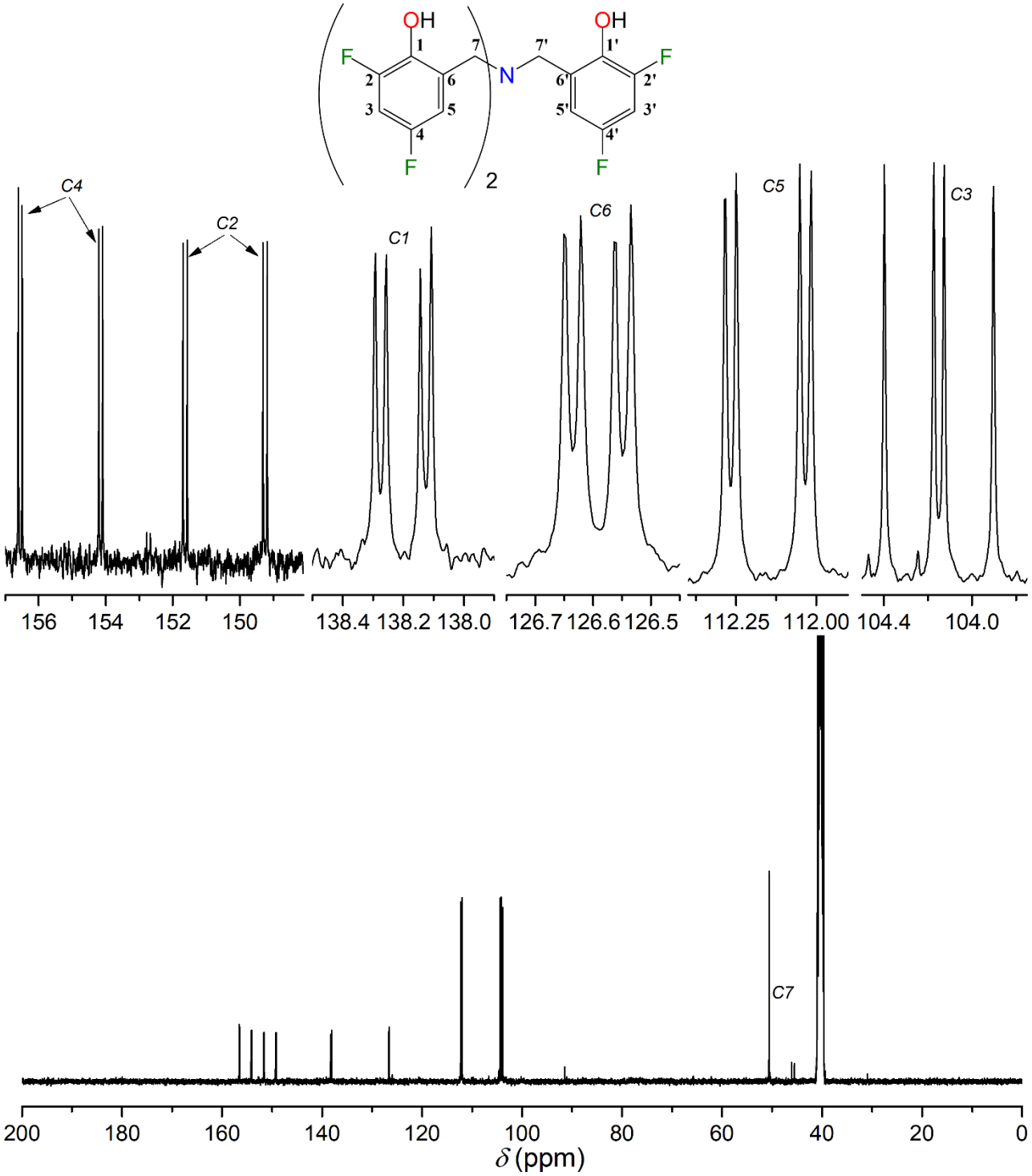

Figure 3.75: Bottom: ^{13}C NMR spectrum of $TPAF_6$ in DMSO-d_6 (298 K, 400.13 MHz). Top: structure of $TPAF_6$ and magnification of the spectrum in 157–148 ppm, 138.6–137.8 ppm, 126.8–126.4 ppm, 112.3–111.9 ppm and 104.5–103.9 ppm. Processing parameters (TopSpin 4.3.0): SI = TD, LB = 0.30 Hz. δ_C (ppm) = 39.52 (residual carbon in DMSO-d_6)

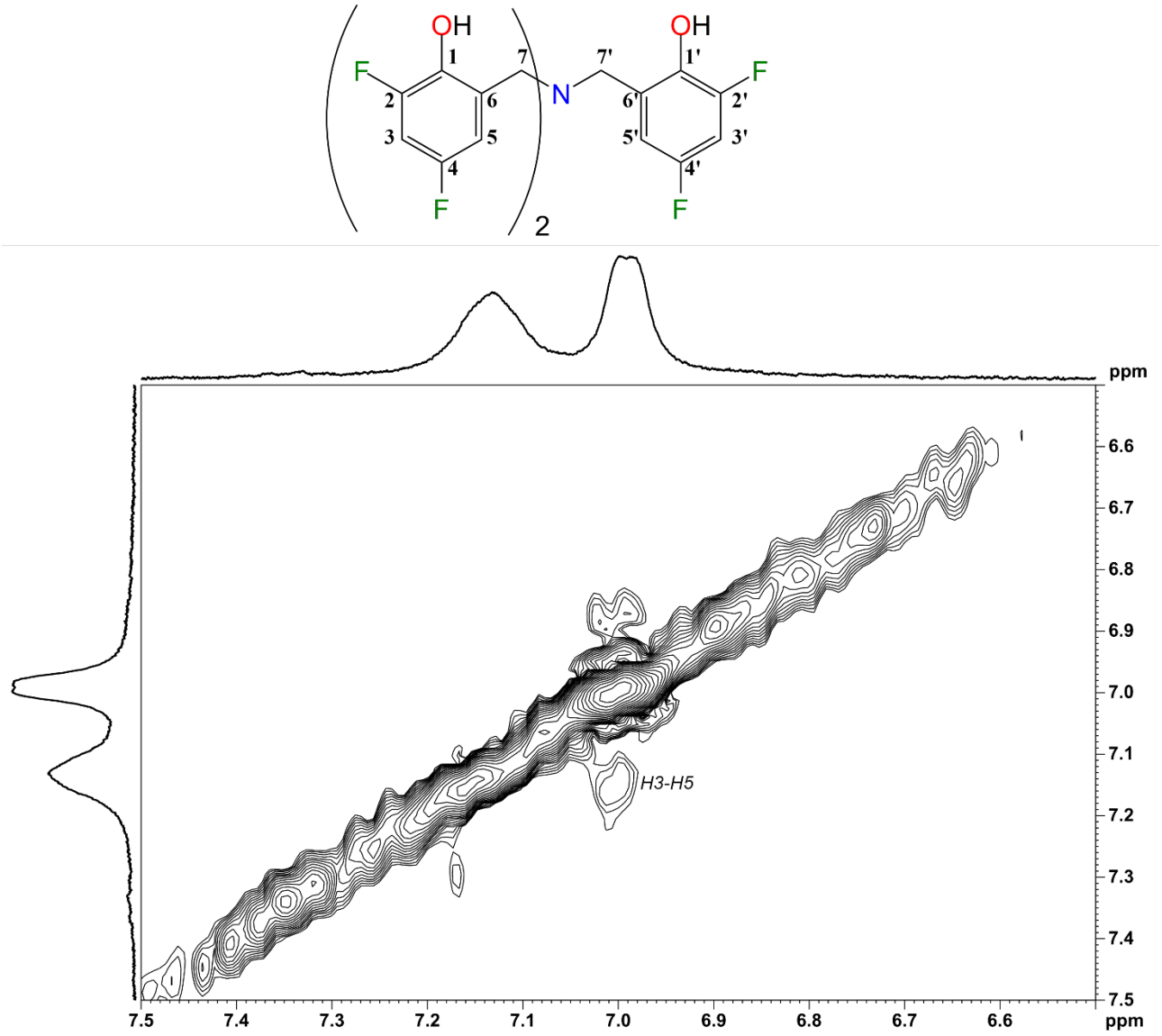

Figure 3.76: Structure and $^{1}H–^{1}H$ COSY spectrum of $TPAF_6$ in DMSO-d_6 bottom between 7.5 ppm and 6.5 ppm (298 K, 400.13 MHz). The labelling of the cross-peaks indicates the $^{1}H–^{1}H$ coupling (F2,F1). Processing parameters (TopSpin 4.3.0) for F2 (x axis): SI = TD, LB = 1.00 Hz. Processing parameters for F1 (y axis): SI = 2·TD, LB = 0.30 Hz.

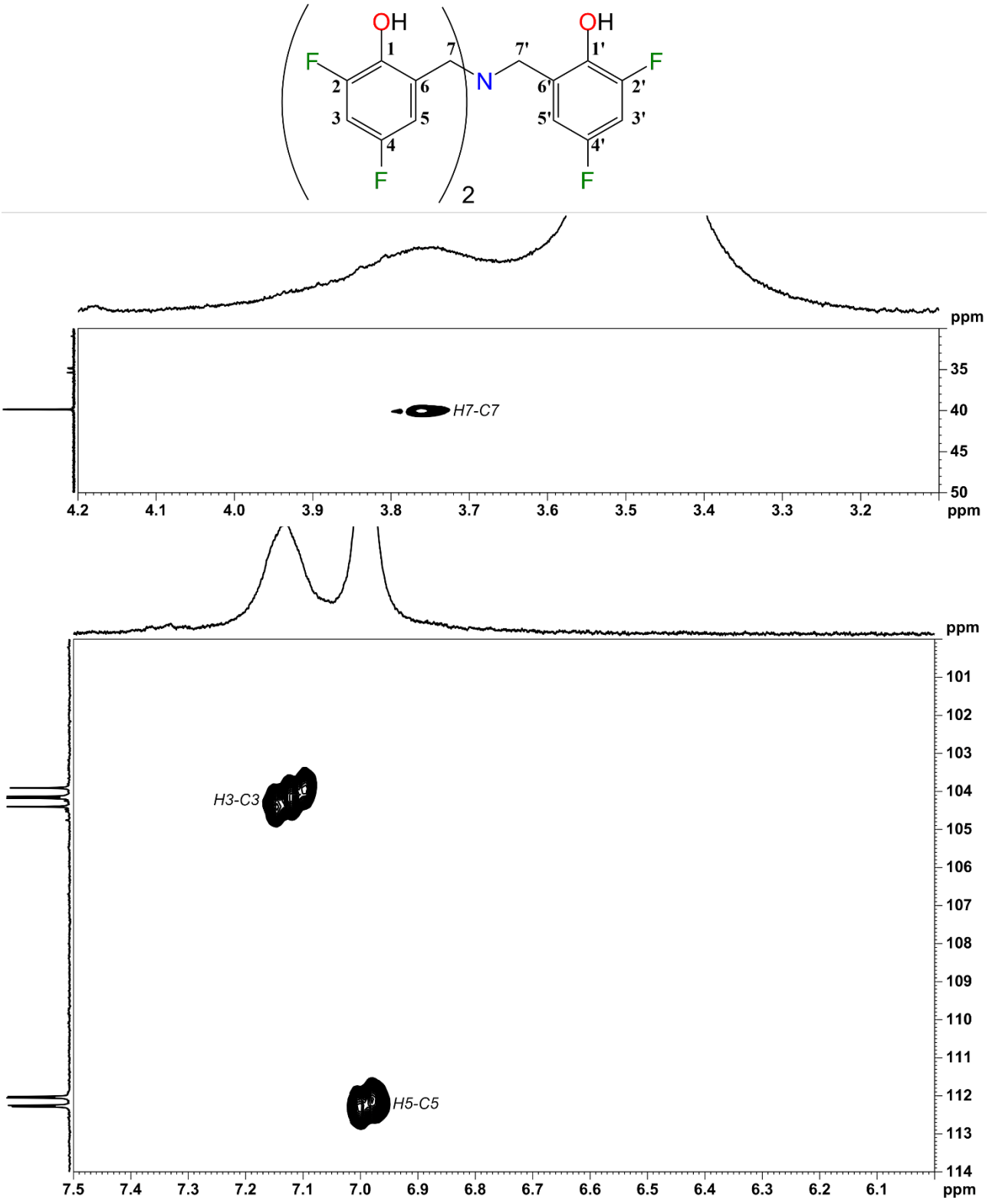

Figure 3.77: Structure and $^{1}H–^{13}C$ HSQC spectrum of $TPAF_6$ in DMSO-d_6 for bottom δ_H = 7.5–6.0 ppm and δ_C = 114–100 ppm, top δ_H = 4.2–3.1 ppm and δ_C = 50–30 ppm. The labelling of the cross-peaks indicates the $^{1}H–^{13}C$ coupling (F2,F1). Processing parameters (TopSpin 4.3.0) for F2 (x axis): SI = 2·TD, LB = 1.00 Hz. Processing parameters for F1 (y axis): SI = 3·TD, LB = 0.30 Hz

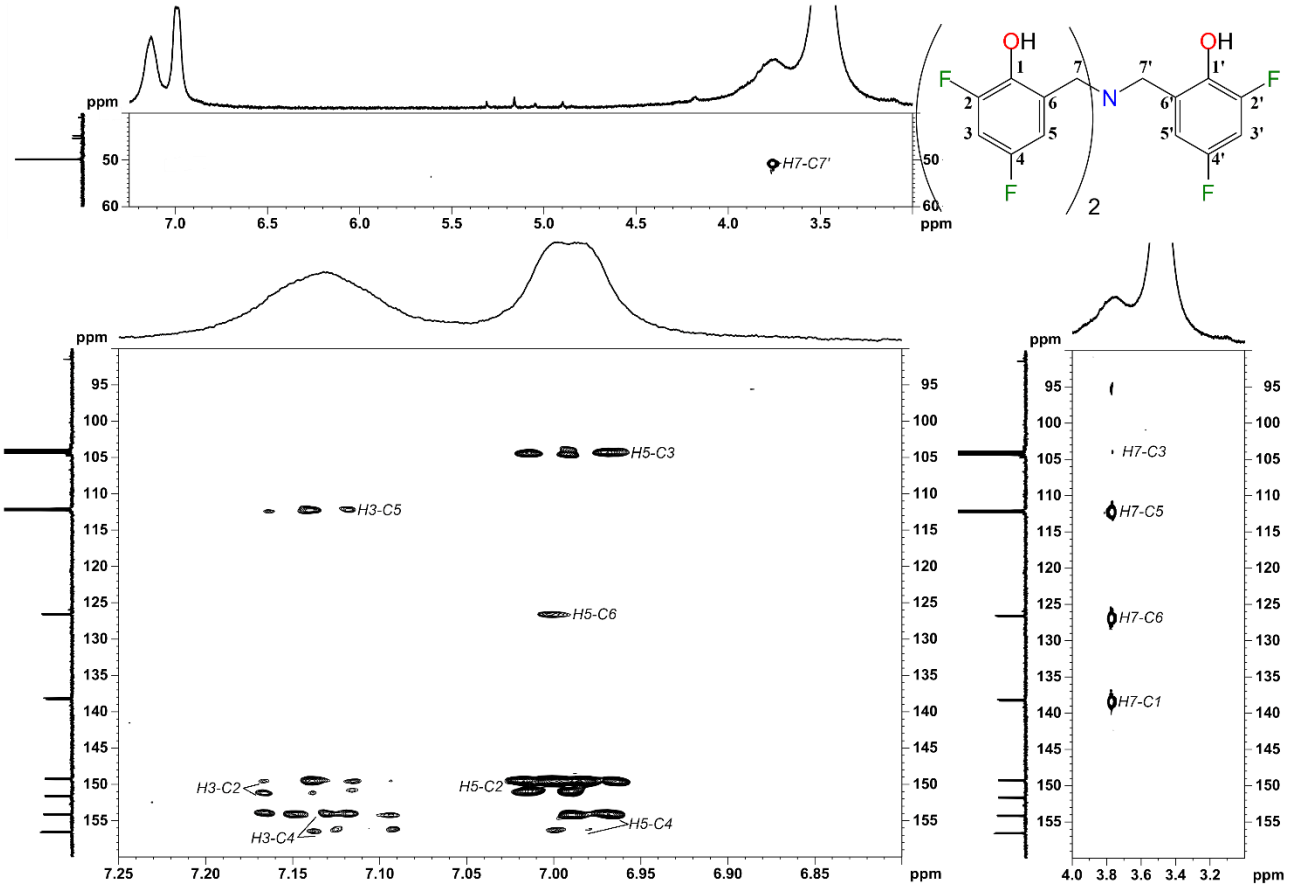

Figure 3.78: Structure and $^{1}H–^{13}C$ HMBC spectrum of $TPAF_6$ in DMSO-d_6 for: bottom-left δ_H = 7.25–6.8 ppm and δ_C =160–90 ppm, bottom-right δ_H = 4.0–3.0 ppm and δ_C = 160–90 ppm, top δ_H = 7.2–3.0 ppm and δ_C = 60–45 ppm (298 K, 400.13 MHz). The labelling of the cross-peaks indicates the $^{1}H–^{13}C$ coupling (F2,F1). Processing parameters (TopSpin 4.3.0) for F2 (x axis): SI = 2·TD, LB = 1.00 Hz. Processing parameters for F1 (y axis): SI = 3·TD, LB = 0.30 Hz

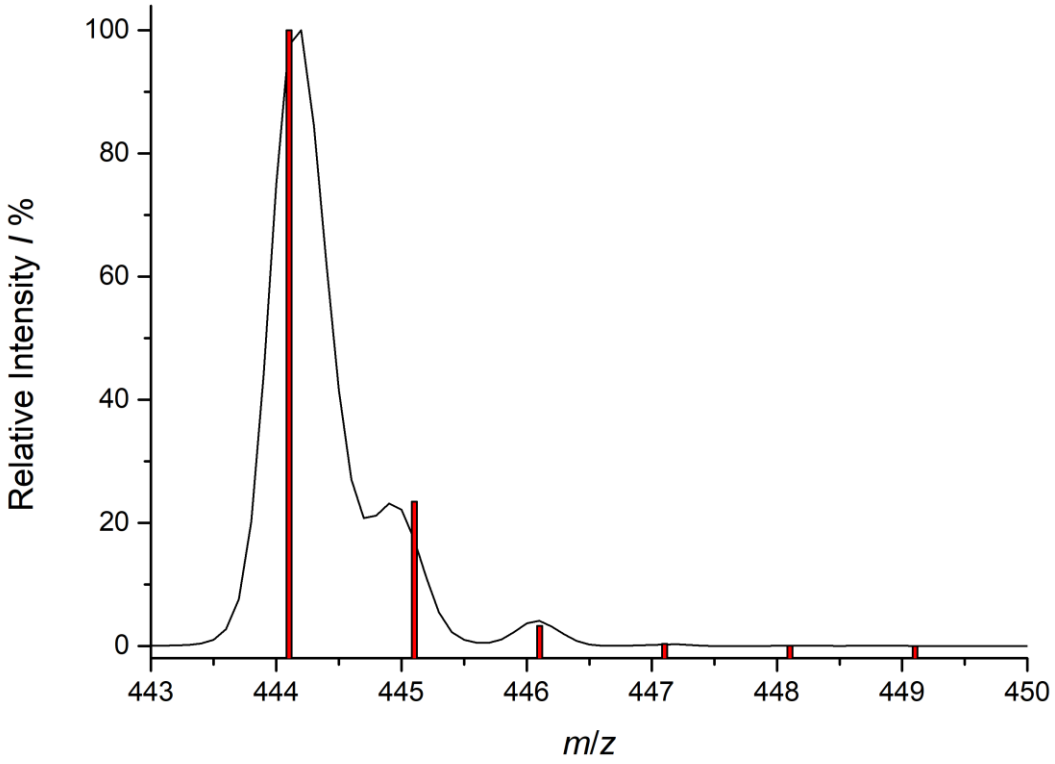

Figure 3.79: Black line: ESI-MS spectrum of $TPAF_6$ (isocratic LC at 80:20 CH_3CN:H_2O (0.1% HCOOH)/Zorbax 30x4.6 mm column, positive ion mode). Red bars: simulated isotopic pattern for $[TPAF_6+H]^+$.

Figure 3.79 displays the experimental ESI-MS spectra of $TPAF_6$ in black, and the simulated isotopic pattern for $[TPAF_6+H]^+$ as red bars, showing a good fit. Concentrations required for ESI-MS are extremely low compared to those needed for NMR, thus it was possible to use CH_3CN even if TPAs are not very soluble in it. $TPAF_6$ can be easily distinguished by MS from other TPAs as it is the only one without chlorides, thus showing the typical isotopic pattern of organic molecules at m/z = 444.1.

3.5.5 Characterization of 6,6'-(((3,5-dichloro-2-hydroxybenzyl)azanediyl) bis(methylene))bis(2,4-difluorophenol) ($TPAF_4Cl_2$)

DMSO-d_6 is required for NMR as solubility in other solvents is too low to reach the concentrations necessary for this technique. Figure 3.80 shows the ^{1}H NMR of $TPAF_4Cl_2$ purified mixture displaying some minor impurities and a major by-product in a ~25% quantity. This by-product, with two aromatic (7.47 ppm, 7.21 ppm) and two aliphatic (5.36 ppm, 4.89 ppm) signals, was also detected in $TPACl_6$ in lower amounts. This set of NMR experiments clearly showed that the four signals belong to the same molecule, as correlation are observed in COSY (shown in Figure 3.83) and in HMBC (not shown) experiments. Regarding $TPAF_4Cl_2$ ^{1}H NMR spectrum the resolution is too low to appreciate smaller coupling constants resulting in broad signals. In particular, two singlets for the "Cl branch" at 7.36 ppm and 7.22 ppm, a triplet and a doublet respectively at 7.12 ppm and 6.95 ppm for the "F branches" with similar $^3J_{H-F}$ of ~7.5 Hz. Benzylic positions are overlapped at 3.75 ppm and partially covered by H_2O broad signal, making impossible to distinguish them from ^{1}H NMR, however, a small shift can be detected in ^{1}H–^{13}C HSQC (Figure 3.84) couplings allowing to define *C7* (3.73 ppm) and *C8* (3.76 ppm) signal positions. Figure 3.81 shows the ^{19}F NMR of $TPAF_4Cl_2$ which is extremely similar to $TPAF_2Cl_4$ both in shape and positions with a shift in δ smaller than 0.1 ppm, resulting in a triplet at −126 ppm (*F4*) and a doublet at −131 ppm (*F2*).

^{13}C NMR of $TPAF_4Cl_2$ is shown in Figure 3.82, *C2* and *C4* are the only "F branches" carbon with the expected multiplicity, *i.e.*, double doublets made by a $^1J_{C-F}$ of ~240 Hz and a $^3J_{C-F}$ of ~12 Hz, respectively at ~150 ppm and ~154 ppm. Phenolics carbons *C1* and *C10* can be found at ~140 ppm (*C1*) as a doublet with a $^3J_{C-F}$ of ~13 Hz and as a singlet at ~151 ppm (*C10*), while *C6*, *C9*, *C11*, *C12*, *C13* and *C14* are clustered as singlets between 130 ppm and 120 ppm. Surprisingly, both non-quaternary *C3* and *C5* are barely visible and can be assigned only through ^{1}H–^{13}C HSQC (Figure 3.84). Finally, *C7* and *C8* stand as singlets at ~53 ppm and ~54 ppm respectively.

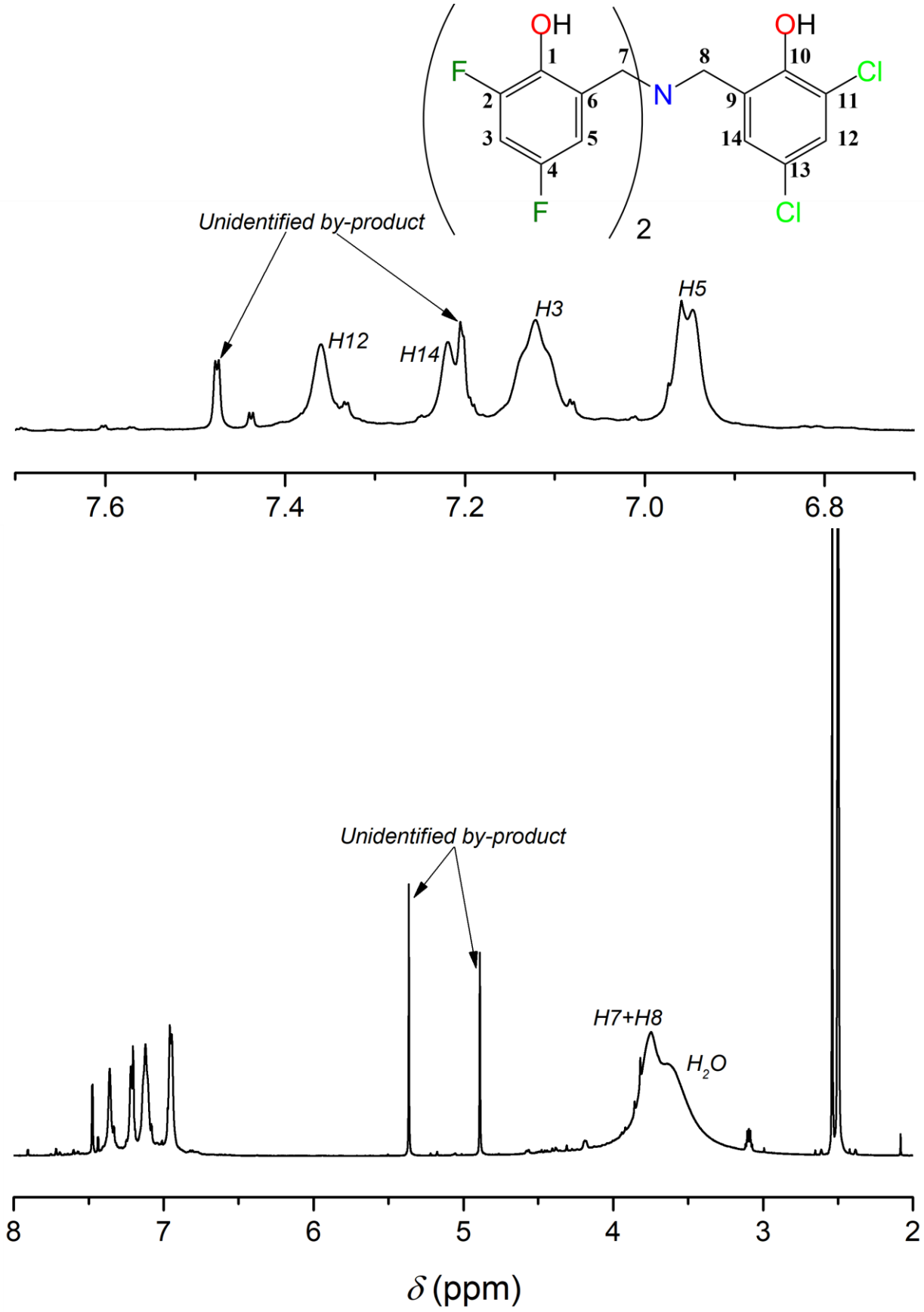

Figure 3.80: Bottom: ^{1}H NMR spectrum of $TPAF_4Cl_2$ in DMSO-d_6 (298 K, 400.13 MHz). Top: structure of $TPAF_4Cl_2$ and magnification of the spectrum between 7.7 ppm and 6.7 ppm. Processing parameters (TopSpin 4.3.0): SI = TD, LB = 0.30 Hz. δ_H (ppm) = 2.50 (residual protons in DMSO-d_6)

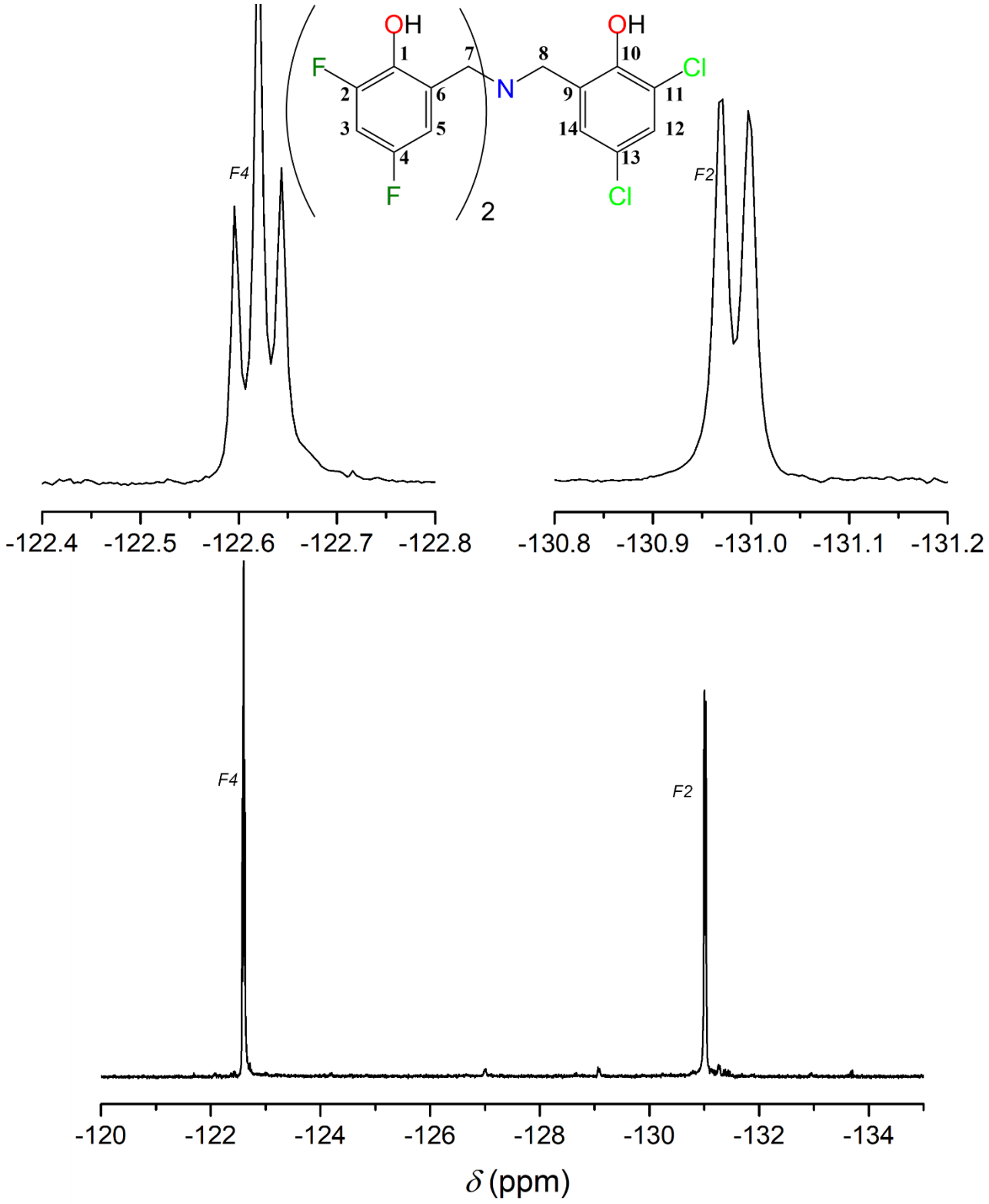

Figure 3.81: Bottom: ^{19}F NMR spectrum of $TPAF_4Cl_2$ in DMSO-d_6 (298 K, 400.13 MHz), top: Magnification of the spectrum in −122.4–−122.8 ppm and −130.8–−131.2 ppm ranges and structure of $TPAF_4Cl_2$. Processing parameters (TopSpin 4.3.0): SI = TD, LB = 0.30 Hz.

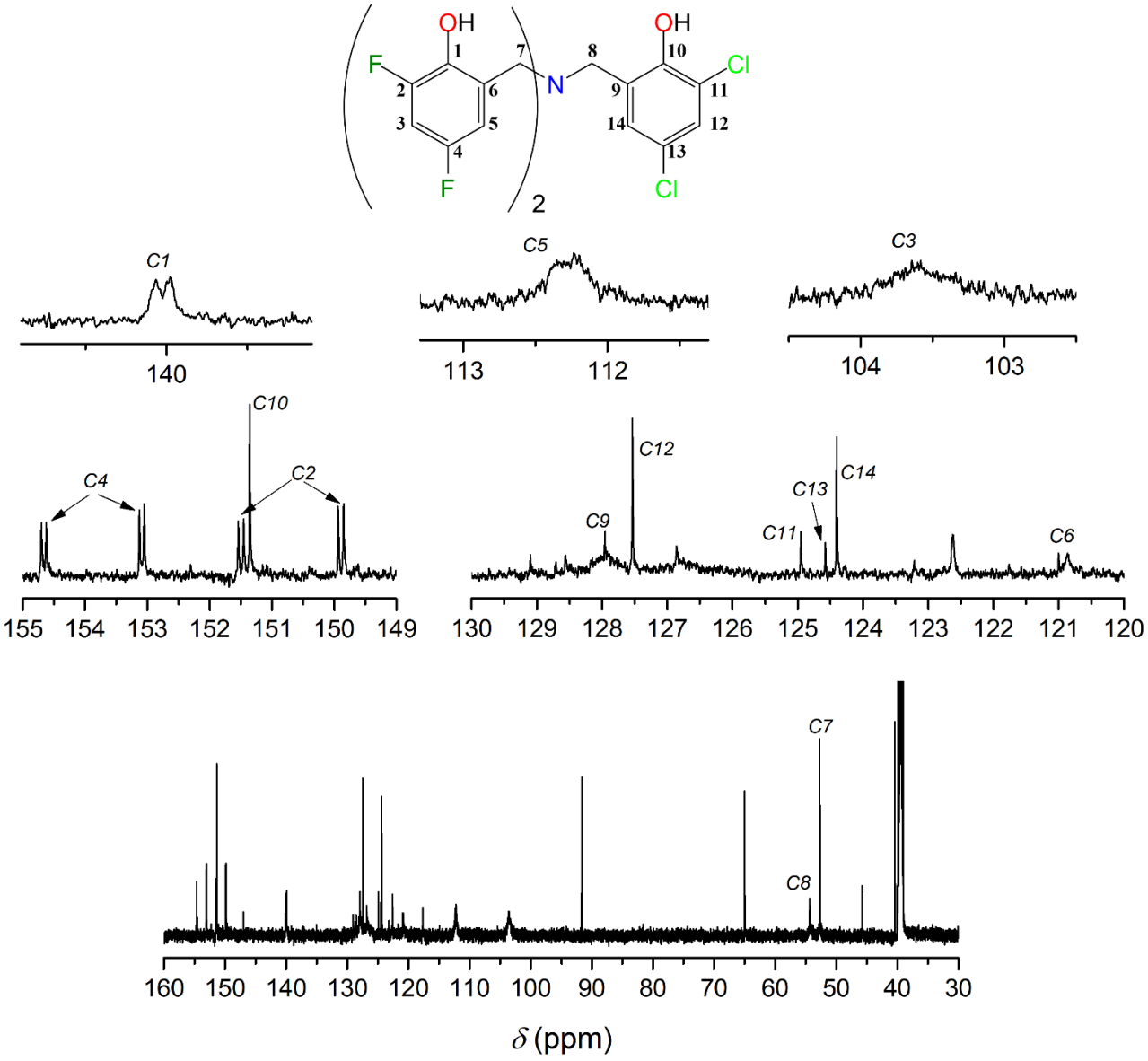

Figure 3.82: Bottom: ^{13}C NMR spectrum of $TPAF_4Cl_2$ in DMSO-d_6 (298 K, 400.13 MHz). Top: structure of $TPAF_4Cl_2$ and magnification of the spectrum in 155–149 ppm, 130–120 ppm, 126.8–126.4 ppm, 142–138 ppm 114–111 ppm and 105–102 ppm. Processing parameters (TopSpin 4.3.0): SI = TD, LB = 0.30 Hz. δ_C (ppm) = 39.52 (residual carbon in DMSO-d_6)

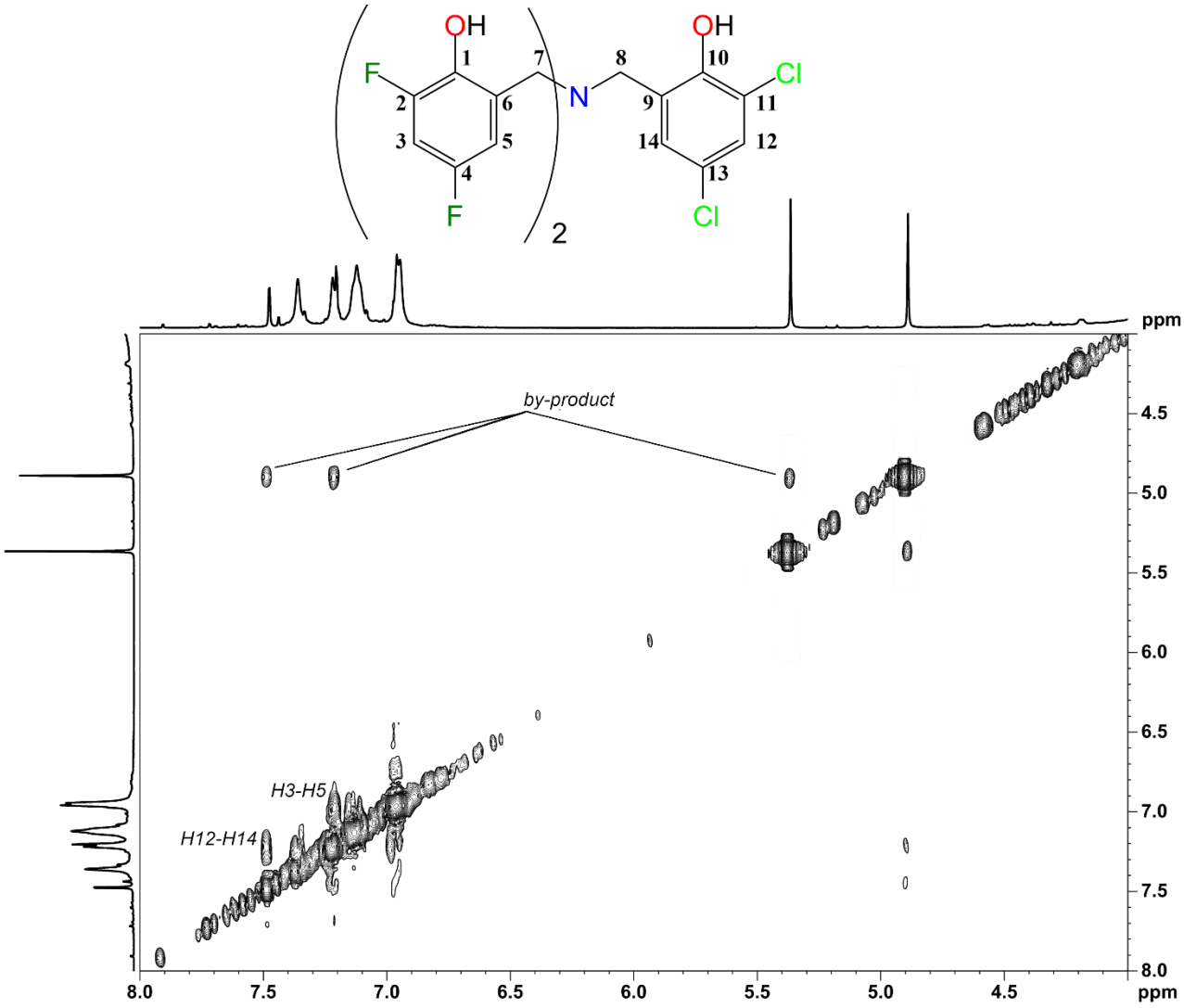

Figure 3.83: Structure and $^{1}H–^{1}H$ COSY spectrum of $TPAF_4Cl_2$ in DMSO-d_6 bottom between 8.0 ppm and 4.0 ppm (298 K, 400.13 MHz). The labelling of the cross-peaks indicates the $^{1}H–^{1}H$ coupling (F2,F1). Processing parameters (TopSpin 4.3.0) for F2 (x axis): SI = TD, LB = 1.00 Hz. Processing parameters for F1 (y axis): SI = 2·TD, LB = 0.30 Hz.

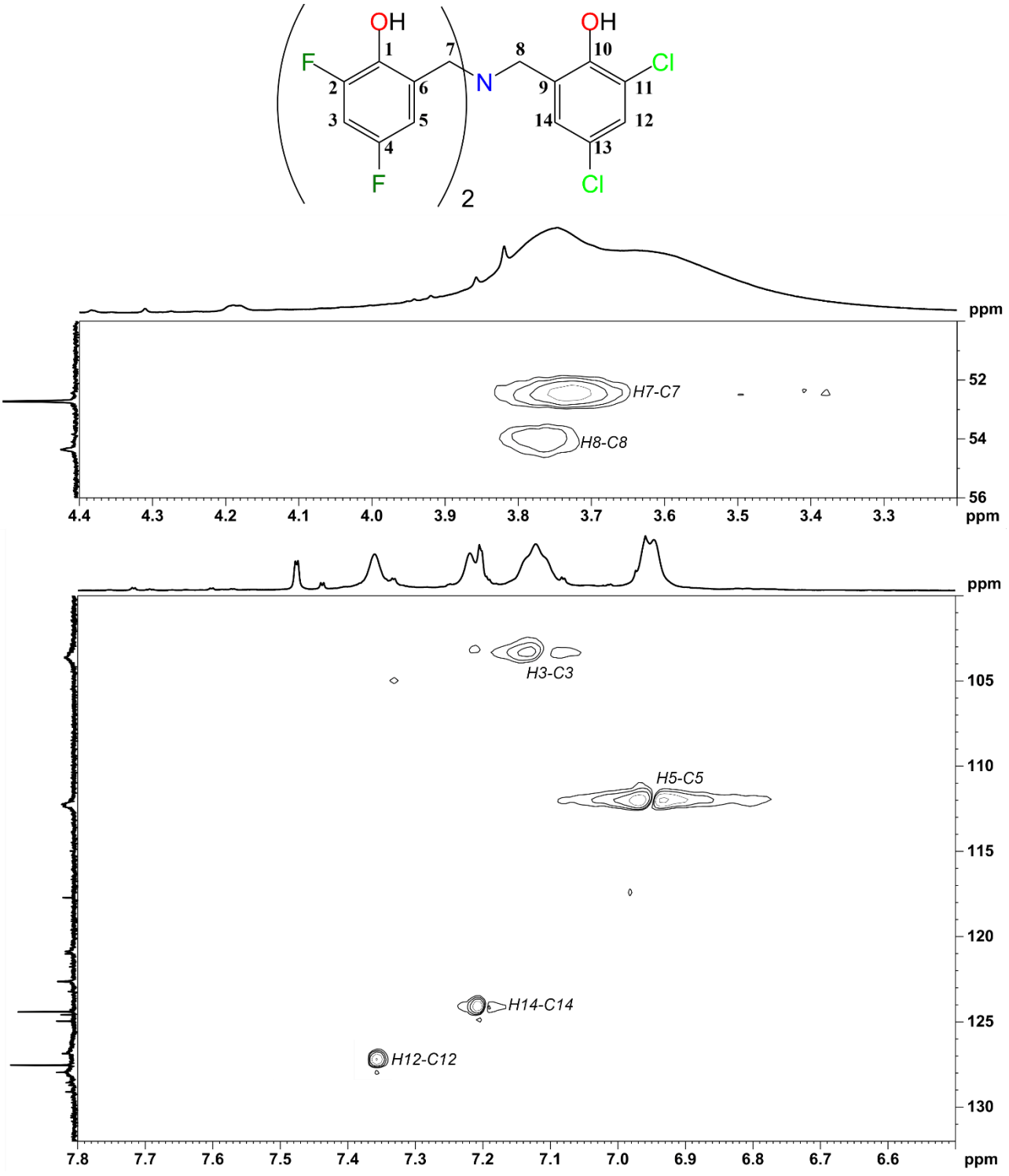

Figure 3.84: Structure and ^{1}H–^{13}C HSQC spectrum of $TPAF_4Cl_2$ in DMSO-d_6 for bottom δ_H = 7.8–6.5 ppm and δ_C = 132–100 ppm, top δ_H = 4.4–3.2 ppm and δ_C = 56–50 ppm. The labelling of the cross-peaks indicates the ^{1}H–^{13}C coupling (F2,F1). Processing parameters (TopSpin 4.3.0) for F2 (x axis): SI = 2·TD, LB = 1.00 Hz. Processing parameters for F1 (y axis): SI = 3·TD, LB = 0.30 Hz

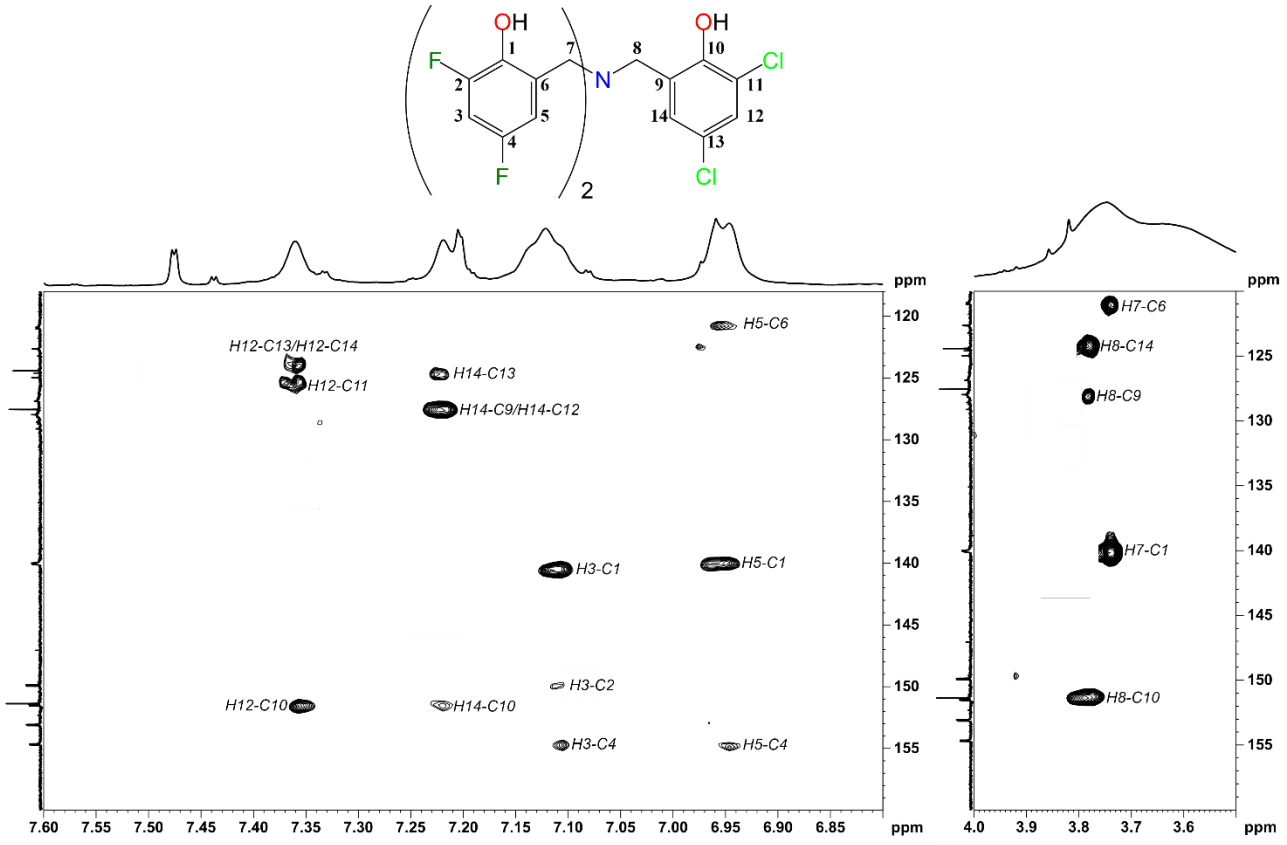

Figure 3.85: Structure and ^{1}H–^{13}C HMBC spectrum of $TPAF_4Cl_2$ in DMSO-d_6 for: left δ_H = 7.6–6.8 ppm and δ_C =160–118 ppm, right δ_H = 4.0–3.5 ppm and δ_C = 160–120 ppm. The labelling of the cross-peaks indicates the ^{1}H–^{13}C coupling (F2,F1). Processing parameters (TopSpin 4.3.0) for F2 (x axis): SI = 2·TD, LB = 1.00 Hz. Processing parameters for F1 (y axis): SI = 3·TD, LB = 0.30 Hz

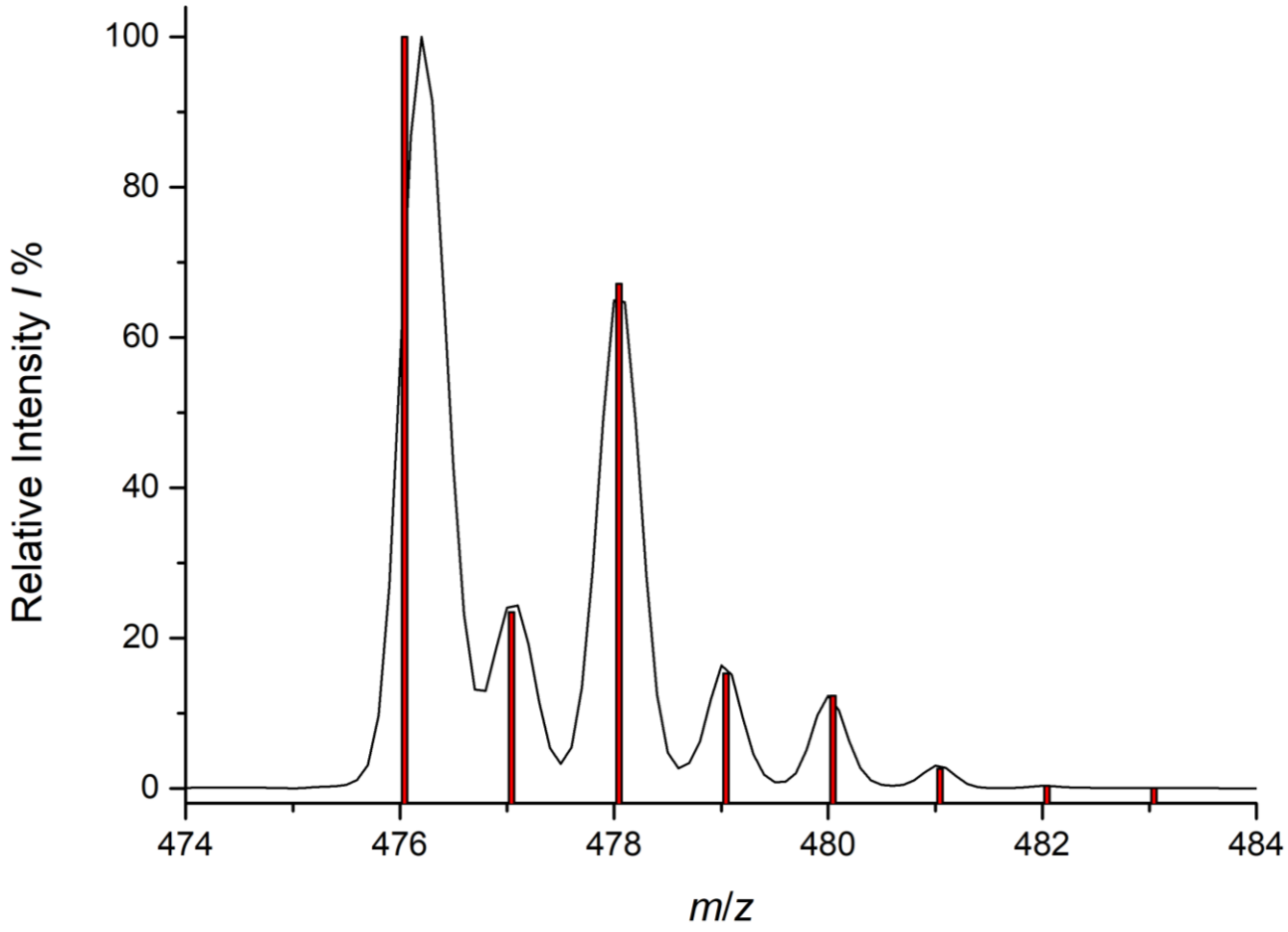

Figure 3.86: Black line: ESI-MS spectrum of $TPAF_4Cl_2$ (isocratic LC at 80:20 CH_3CN:H_2O (0.1% HCOOH)/Zorbax 30x4.6 mm column, positive ion mode). Red bars: simulated isotopic pattern for $[TPAF_4Cl_2+H]^+$.

Figure 3.86 displays the experimental ESI-MS spectra of $TPAF_4Cl_2$ in black, and the simulated isotopic pattern for $[TPAF_4Cl_2+H]^+$ as red bars, showing a good fit. Concentrations required for ESI-MS are extremely low compared to those needed for NMR, thus it was possible to use CH_3CN even if TPAs are not very soluble in it. $TPAF_4Cl_2$ is easily recognized by MS thanks to its protonated *m*/*z* = 476.04 combined with its very peculiar isotopic pattern given by 2 chloride atoms.

3.5.6 Characterization of 6,6'-(((3-nitro-5-chloro-2-hydroxybenzyl)azanediyl) bis(methylene))bis(2,4-difluorophenol) ($TPAF_4ClNO_2$)

DMSO-d_6 is required for NMR as solubility in other solvents is too low to reach the concentrations necessary for this technique. $TPAF_4ClNO_2$ purified mixture ^1H NMR is represented in Figure 3.87, showing a similar purity to $TPAF_4Cl_2$. Even if any major by-product was produced, several medium intensity signals can be found in the aromatic part, coming from two or probably three different impurities, which we estimated to be each ~10% of $TPAF_4ClNO_2$ mixture. $TPAF_4ClNO_2$ ^1H NMR (Figure 3.87) shows two broad singlets at 7.80 ppm (*H12*) and 7.56 ppm (*H14*), a broad triplet (*H3*) and a broad doublet (*H5*) at 7.09 ppm and 6.95 ppm respectively. Probably, resolution is too poor, and *J* lower than $^3J_{H-F}$ of ~ 9 Hz cannot be detected. Both benzylic positions are visible singlets, at 3.82 ppm (*C8)* and 3.75 ppm (*C7*), partially overlapped with H_2O broad signal. Figure 3.88 shows the ^{19}F NMR of $TPAF_4ClNO_2$ which is coherent with the other fluorinated TPAs and DPAs, with two broad signals at −122 ppm and −131 ppm, respectively a triplet (*F4*) and a doublet (*F2*).

^{13}C NMR is shown in Figure 3.89, with the expected 14 signals all visible with proper multiplicity, *i.e.*, singlets for the "NO_2 branch" and double doublets for the "F branches". *C2* (~151 ppm) and *C4* (~154 ppm) have an extremely large *J* due to the *ipso*-fluoride of ~240 Hz and a smaller $^3J_{C-F}$ of ~12 Hz. Phenolic carbons can be found at ~152 ppm (*C10*) and at ~140 ppm (*C1*) with $^2J_{C-F}$ of ~14 Hz and a $^4J_{C-F}$ of ~3 Hz, while *C9*, *C11* and *C14* can be found between 128 ppm and 138 ppm. *C6* should be a triplet with two very similar $^3J_{C-F}$, but for some reason they appear to be quite different, namely of ~8 Hz and ~4 Hz, a similar situation is also found for *C3* with two $^2J_{C-F}$ one of ~27 Hz and the other of ~23 Hz. *C12* and *C13* can be seen between 121 ppm and 124 ppm, while *C5* is at ~112 ppm with a $^2J_{C-F}$ of ~23 Hz and a $^4J_{C-F}$ of ~3 Hz. Finally, both benzylic *C7* and *C8* stand as singlets respectively at 3.75 ppm and 3.82 ppm. Figure 3.90 shows COSY with some unusual long-range couplings between *H8–H12/14* and *H7–H5*. Also in $TPAF_4ClNO_2$ $^1H-^{13}C$ HMBC (Figure 3.92) it can be noted a coupling between *H7* and *C7'* due to symmetry, *i.e.*, the interaction of the methylenic protons of a "F branch" with the methylenic carbon of the other "F branch".

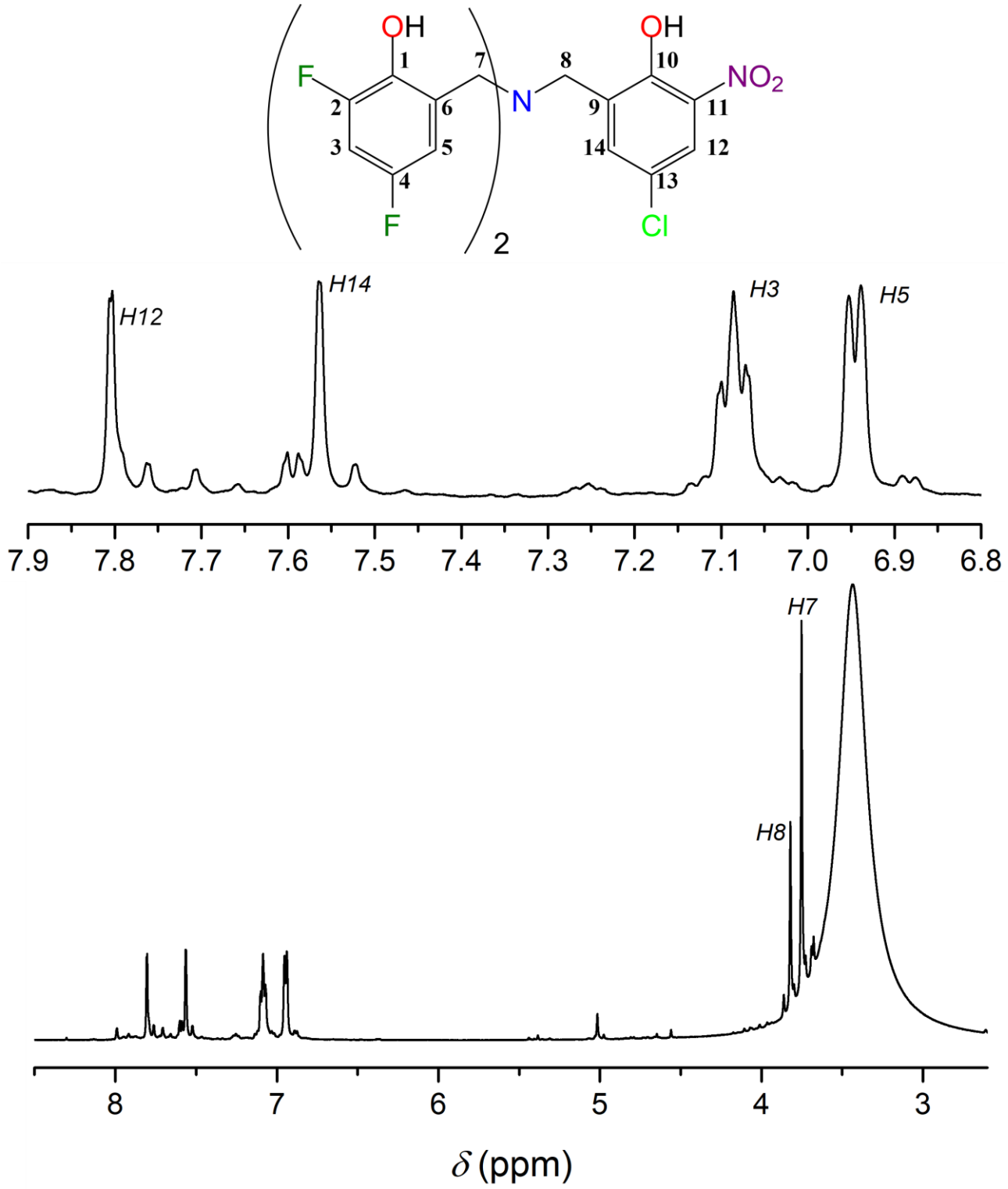

Figure 3.87: Bottom: ^{1}H NMR spectrum of $TPAF_4ClNO_2$ in DMSO-d_6 (298 K, 400.13 MHz). Top: structure of $TPAF_4ClNO_2$ and magnification of the spectrum between 7.9 ppm and 6.8 ppm. Processing parameters (TopSpin 4.3.0): SI = TD, LB = 0.30 Hz. δ_H (ppm) = 2.50 (residual protons in DMSO-d_6)

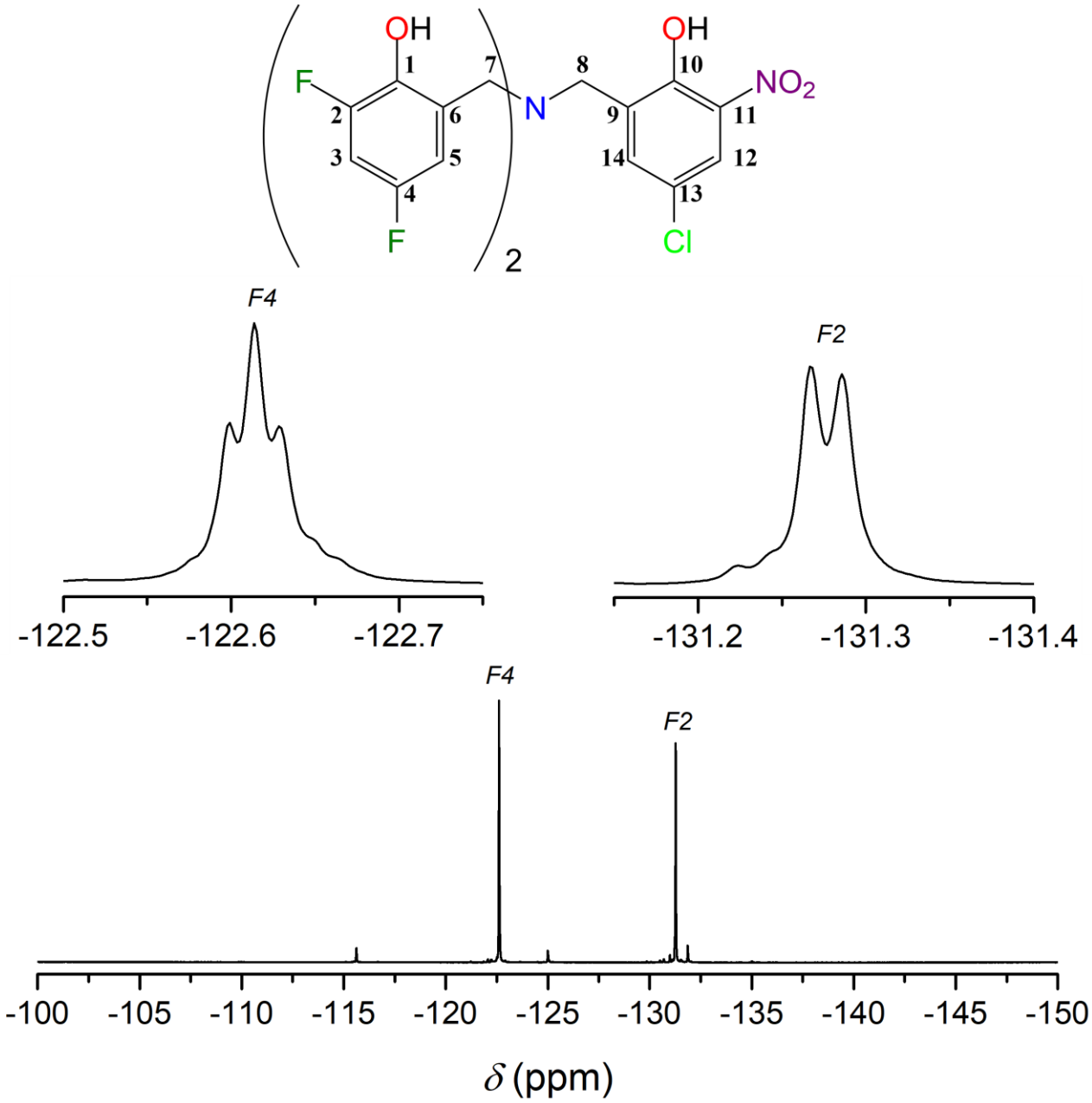

Figure 3.88: Bottom: ^{19}F NMR spectrum of $TPAF_4ClNO_2$ in DMSO-d_6 (298 K, 400.13 MHz), top: Magnification of the spectrum in −122.5–−122.8 ppm and −131.0–−131.4 ppm ranges and structure of $TPAF_4ClNO_2$. Processing parameters (TopSpin 4.3.0): SI = TD, LB = 0.30 Hz.

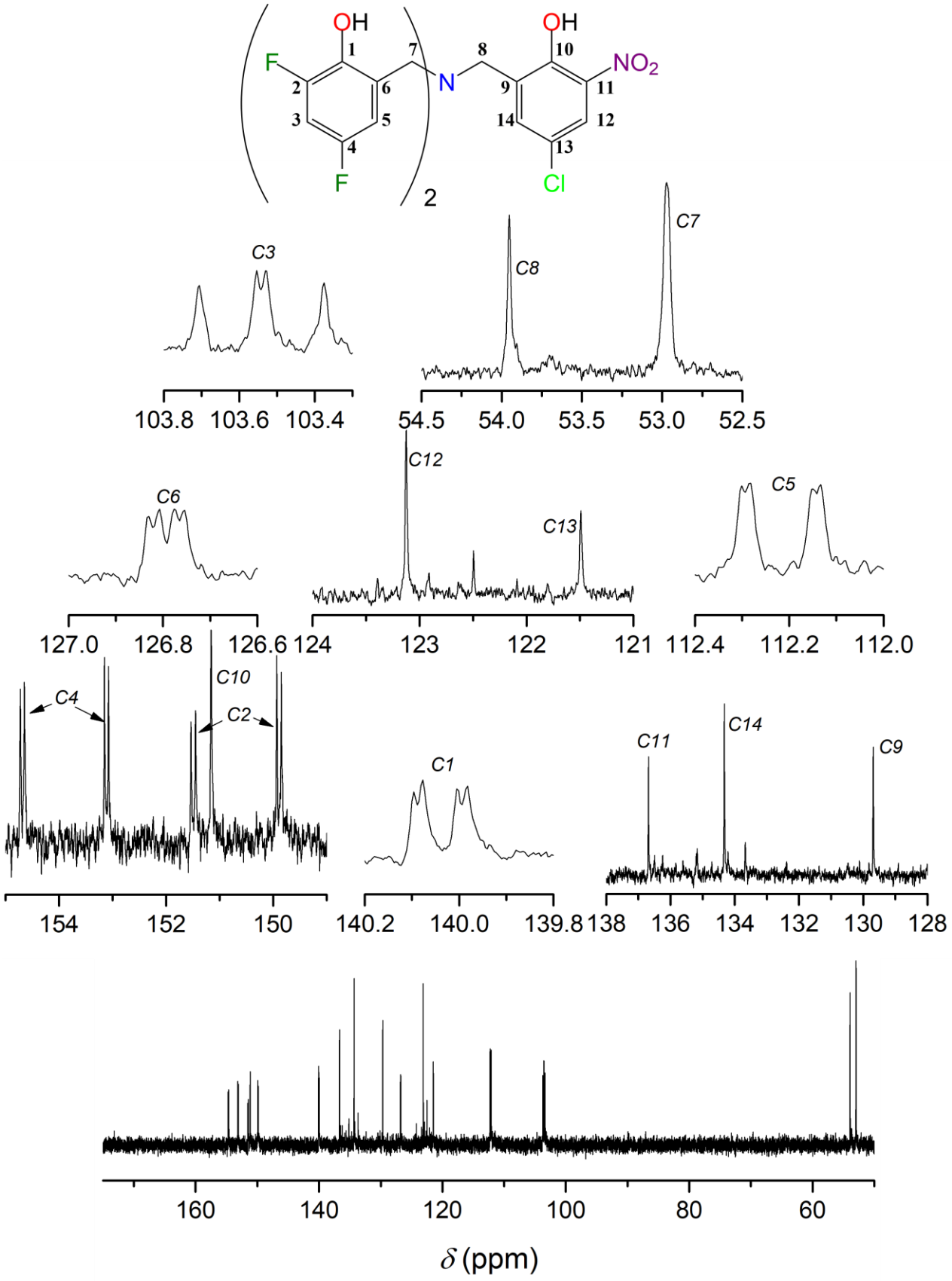

Figure 3.89: Bottom: ^{13}C NMR spectrum of $TPAF_4ClNO_2$ in DMSO-d_6 (298 K, 400.13 MHz). Top: structure of $TPAF_4ClNO_2$ and magnification of the spectrum in 155–149 ppm, 140.2–139.8 ppm, 138–128 ppm, 127.0–126.6 ppm 124–121 ppm, 112.4–112.0 ppm, 103.8–103.3 ppm, and 54.5–52.5 ppm. Processing parameters (TopSpin 4.3.0): SI = TD, LB = 0.30 Hz. δ_C (ppm) = 39.52 (residual carbon in DMSO-d_6)

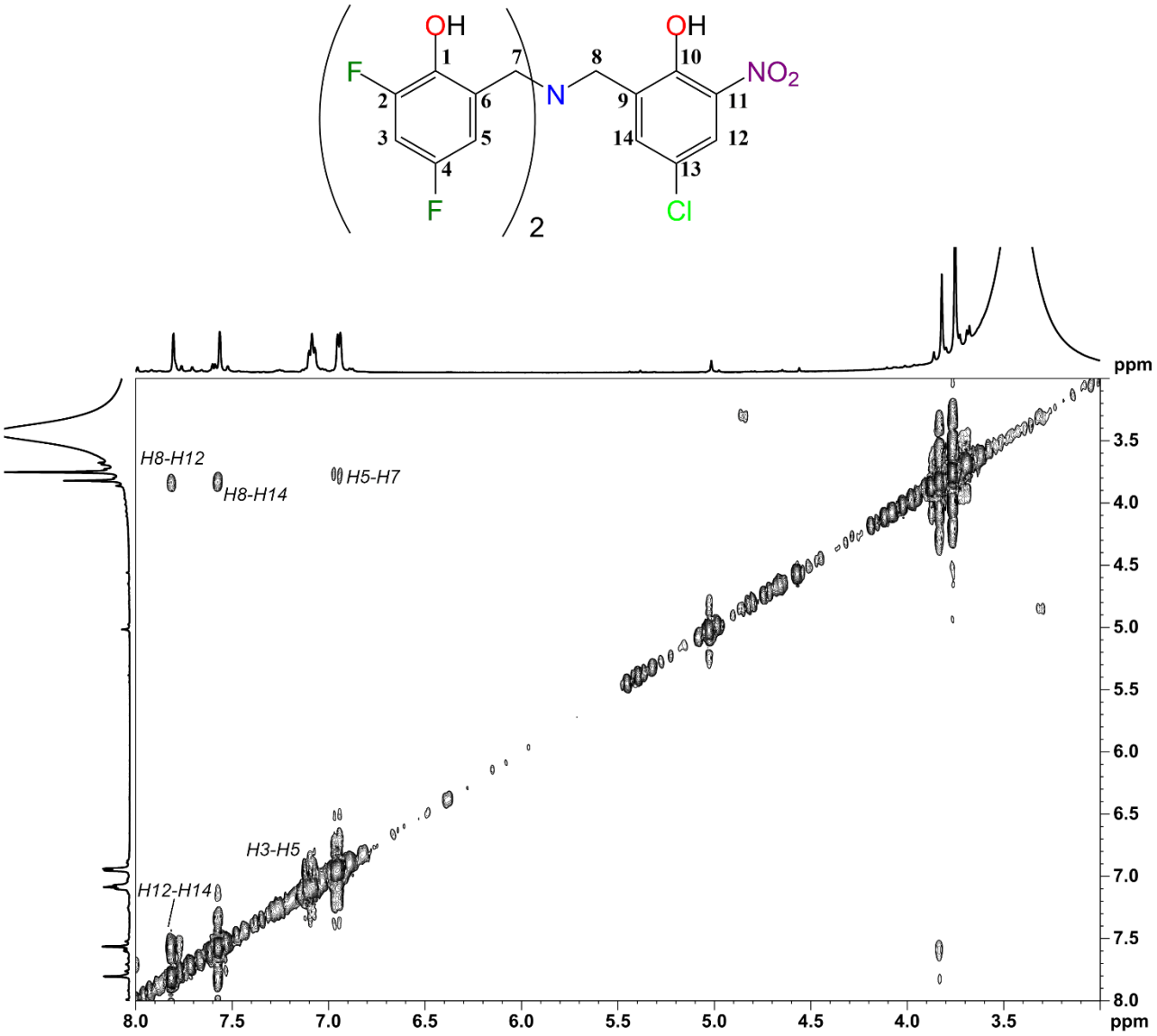

Figure 3.90: Structure and ^{1}H–^{1}H COSY spectrum of $TPAF_4ClNO_2$ in DMSO-d_6 bottom between 8.0 ppm and 3.0 ppm (298 K, 400.13 MHz). The labelling of the cross-peaks indicates the ^{1}H–^{1}H coupling (F2,F1). Processing parameters (TopSpin 4.3.0) for F2 (x axis): SI = TD, LB = 1.00 Hz. Processing parameters for F1 (y axis): SI = 2·TD, LB = 0.30 Hz.

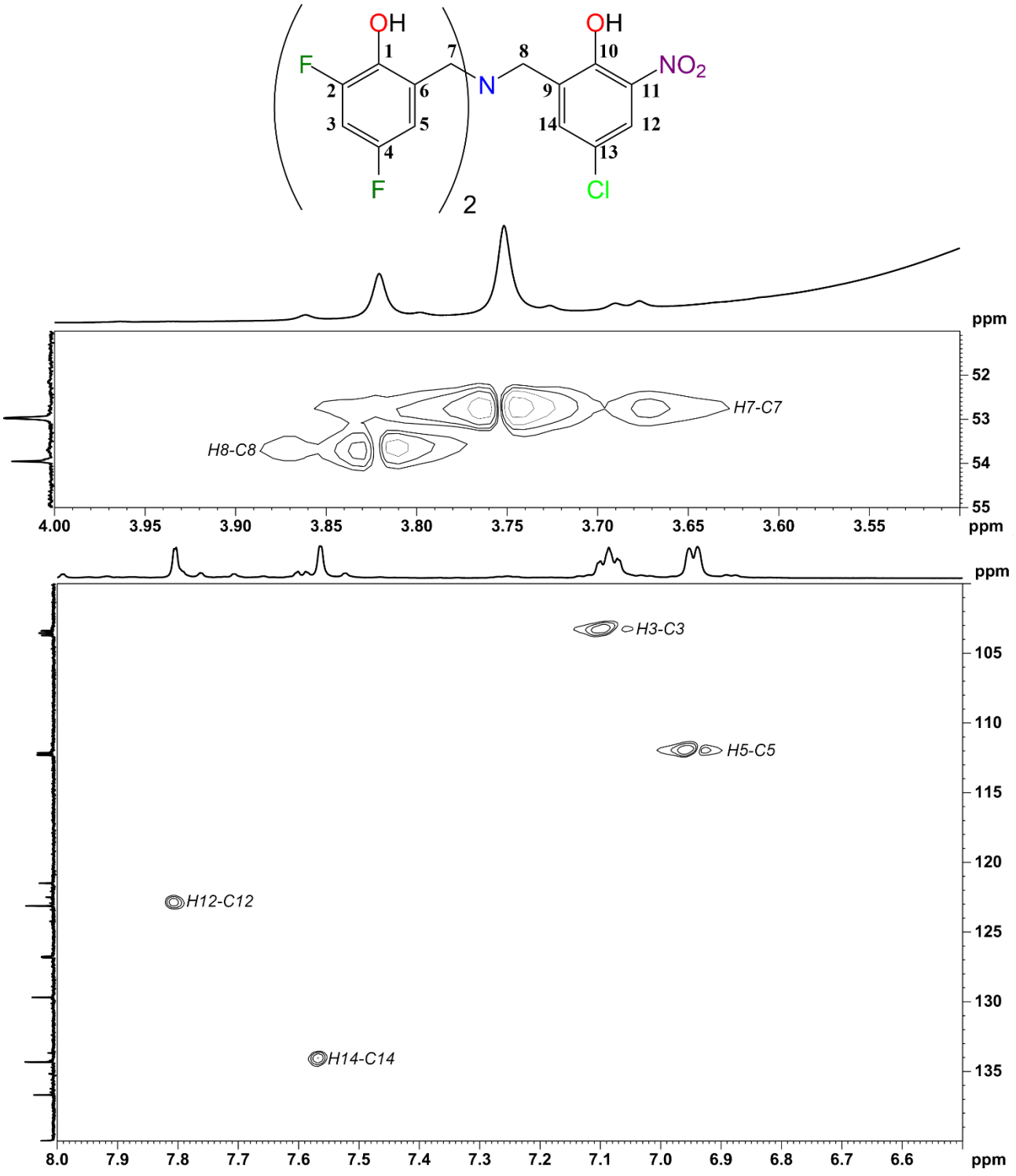

Figure 3.91: Structure and ^{1}H–^{13}C HSQC spectrum of $TPAF_4ClNO_2$ in DMSO-d_6 for bottom δ_H = 8.0–6.5 ppm and δ_C = 140–100 ppm, top δ_H = 4.0–3.5 ppm and δ_C = 55–51 ppm. The labelling of the cross-peaks indicates the ^{1}H–^{13}C coupling (F2,F1). Processing parameters (TopSpin 4.3.0) for F2 (x axis): SI = 2·TD, LB = 1.00 Hz. Processing parameters for F1 (y axis): SI = 3·TD, LB = 0.30 Hz

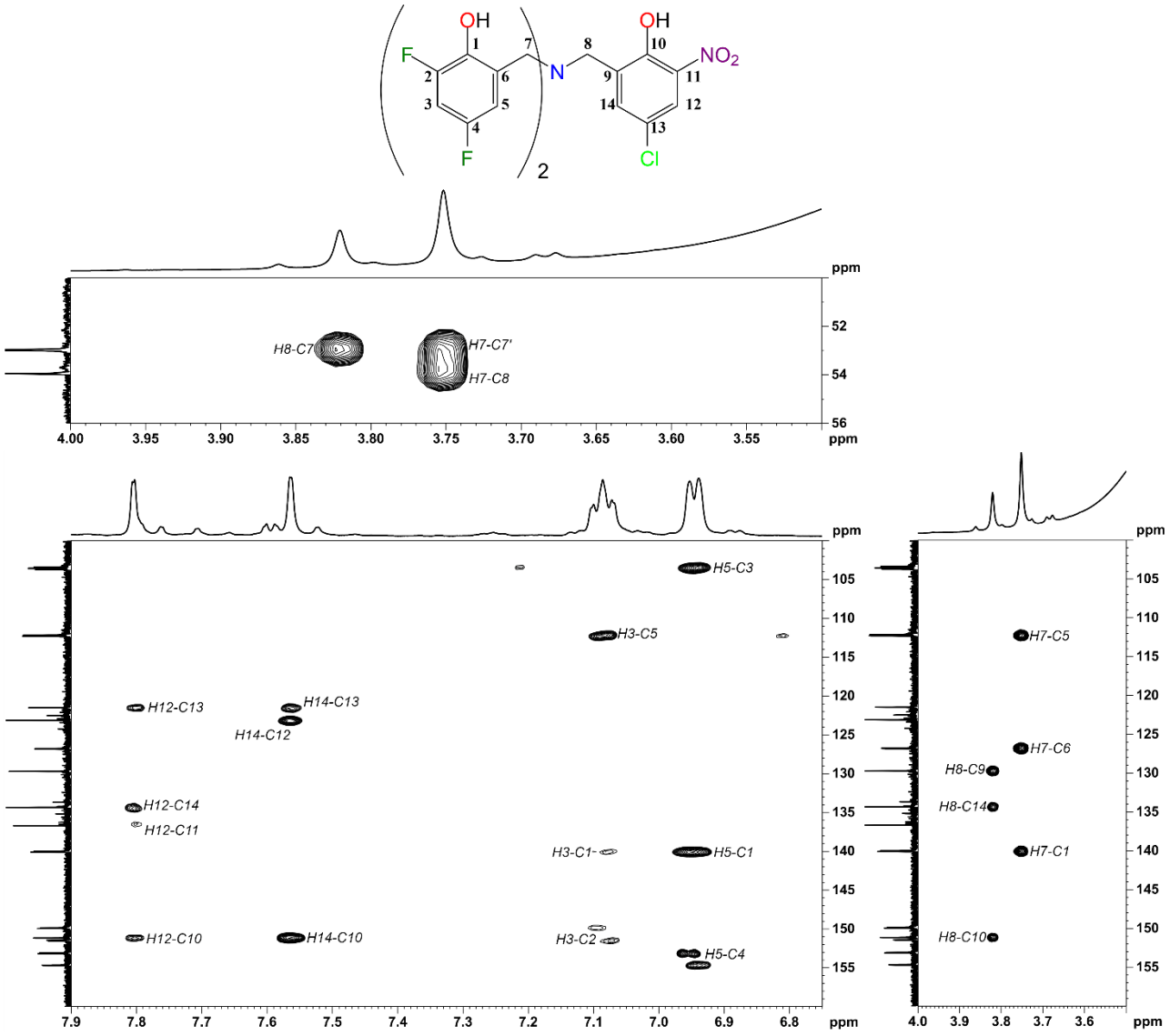

Figure 3.92: Structure and $^{1}H–^{13}C$ HMBC spectrum of $TPAF_4ClNO_2$ in DMSO-d_6 for: bottom-left δ_H = 7.9–6.7 ppm and δ_C =160–100 ppm, bottom-right δ_H = 4.0–3.5 ppm and δ_C = 160–100 ppm, top δ_H = 4.0–3.5 ppm and δ_C = 56–51 ppm. The labelling of the cross-peaks indicates the $^{1}H–^{13}C$ coupling (F2,F1). Processing parameters (TopSpin 4.3.0) for F2 (x axis): SI = 2·TD, LB = 1.00 Hz. Processing parameters for F1 (y axis): SI = 3·TD, LB = 0.30 Hz

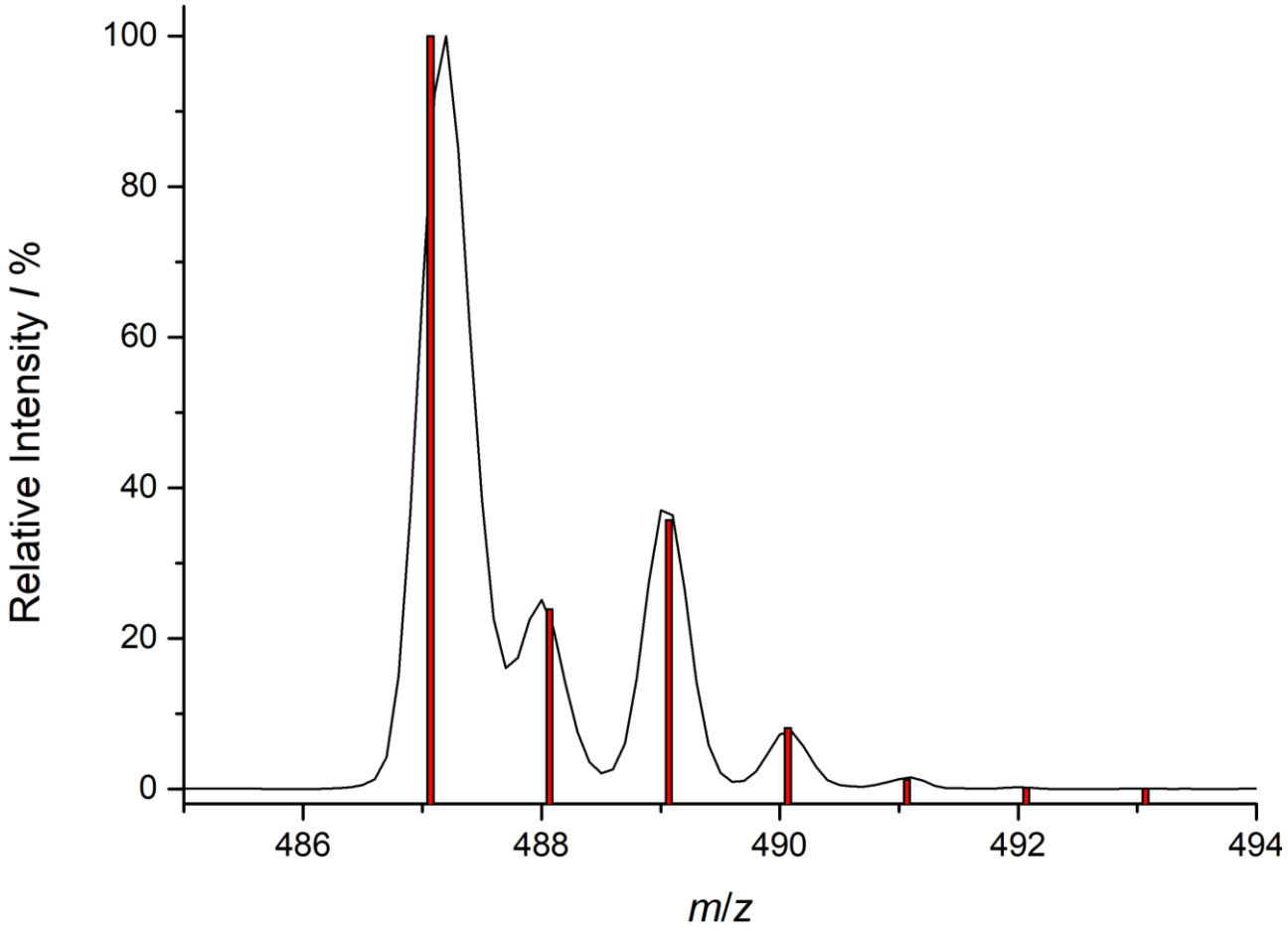

Figure 3.93: Black line: ESI-MS spectrum of $TPAF_4ClNO_2$ (isocratic LC at 80:20 CH_3CN:H_2O (0.1% HCOOH)/Zorbax 30x4.6 mm column, positive ion mode). Red bars: simulated isotopic pattern for $[TPAF_4ClNO_2+H]^+$.

Figure 3.93 displays the experimental ESI-MS spectra of $TPAF_4ClNO_2$ in black, and the simulated isotopic pattern for $[TPAF_4ClNO_2+H]^+$ as red bars, showing a good fit. Concentrations required for ESI-MS are extremely low compared to those needed for NMR, thus it was possible to use CH_3CN even if TPAs are not very soluble in it. $TPAF_4ClNO_2$ is easily recognized by MS thanks to its protonated m/z = 487.07 combined with its very peculiar isotopic pattern given by one chloride atom.

3.6 Preliminary study of TPAs coordination chemistry

As previously mentioned, these TPA proligands were synthesized with the aim to obtain vanadium(V) oxide complexes (VOTPAs) with deactivated rings, theoretically increasing their reduction potential and consequently their activity in cleavage of lignin model compounds C–C bonds. We decided to follow the typical approach to obtain these VOTPAs complexes, briefly discussed in Section 3.1, that is to react TPA proligands in aprotic, non-coordinating solvents, with $VO(O\textit{i}Pr)_3$ which act both as a source of metal and as a base. Reported procedures usually add a solution of TPA to a solution of $VO(O\textit{i}Pr)_3$ under strictly controlled anhydrous conditions but given the solubility issues of our TPAs proligands we decided to invert the addition order, dropping $VO(O\textit{i}Pr)_3$ into a suspension of the proper TPA. We worked all these syntheses in anhydrous DCM, quickly adding neat $VO(O\textit{i}Pr)_3$ to the stirred proligand suspension to minimize $VO(O\textit{i}Pr)_3$ exposure to air humidity as we could not work into a glovebox, and $VO(O\textit{i}Pr)_3$ is extremely sensitive to water, quickly turning from a light-yellow liquid to a red completely insoluble solid. In fact, all the equipment used to manipulate $VO(O\textit{i}Pr)_3$ must be made of Pyrex glass without metallic parts, as the only way to clean this red solid is to treat it several times with aqua regia. The observed behavior upon addition of $VO(O\textit{i}Pr)_3$ to the slurried proligand is more or less the same for each TPAs, that is fast solubilization to obtain a deep blue or purple color which can be recognized only in thin layer as it is extremely dark and in bulk appear as black. VOTPA complexes solutions seem to be quite stable and there is no need to keep them under a controlled atmosphere, as they are not particularly air sensitive. Unfortunately, we have not been able to obtain SC-XRD quality crystals from layering or gas diffusion techniques, nor by slow evaporation. Thus, we adopted as a general purification method after synthesis filtration and precipitation in dry heptane to obtain a VOTPA powder that can be collected, washed with dry pentane and extensively vacuum dried. These solids were used to express a complexation yield, and divided into weighted portions used for solution studies, *i.e.*, ^{1}H NMR, ^{51}V NMR, UV-Vis spectroscopy, Cyclic Voltammetry (CV) and Chronoamperometry combined with UV-Vis spectroscopy. Some literature for ^{51}V NMR and ^{1}H NMR on different VOTPA complexes is available[20,24], while we have not been able to find anything for the other techniques. All these studies were performed in CH_2Cl_2 (CD_2Cl_2 for NMR) on samples of known concentration, results are organized in the following Sections.

3.6.1 NMR Characterization of VOTPAs complexes

$VOTPACl_6$, $VOTPAF_4Cl_2$ and $VOTPACl_4F_2$ ^1H NMR spectra are very similar, with four (or two for $VOTPACl_6$) poorly resolved but well-defined aromatic signals with proper ratios, in slightly different positions in the region between 7.5–6.5 ppm and the benzylic protons forming a broad singlet at 2.61 ppm, with medium amounts of unidentified impurities. Therefore, we decided to report only $VOTPACl_4F_2$ ^1H NMR spectrum (Figure 3.94) as a representative of the three, as reporting all of them would not add much to the discussion.

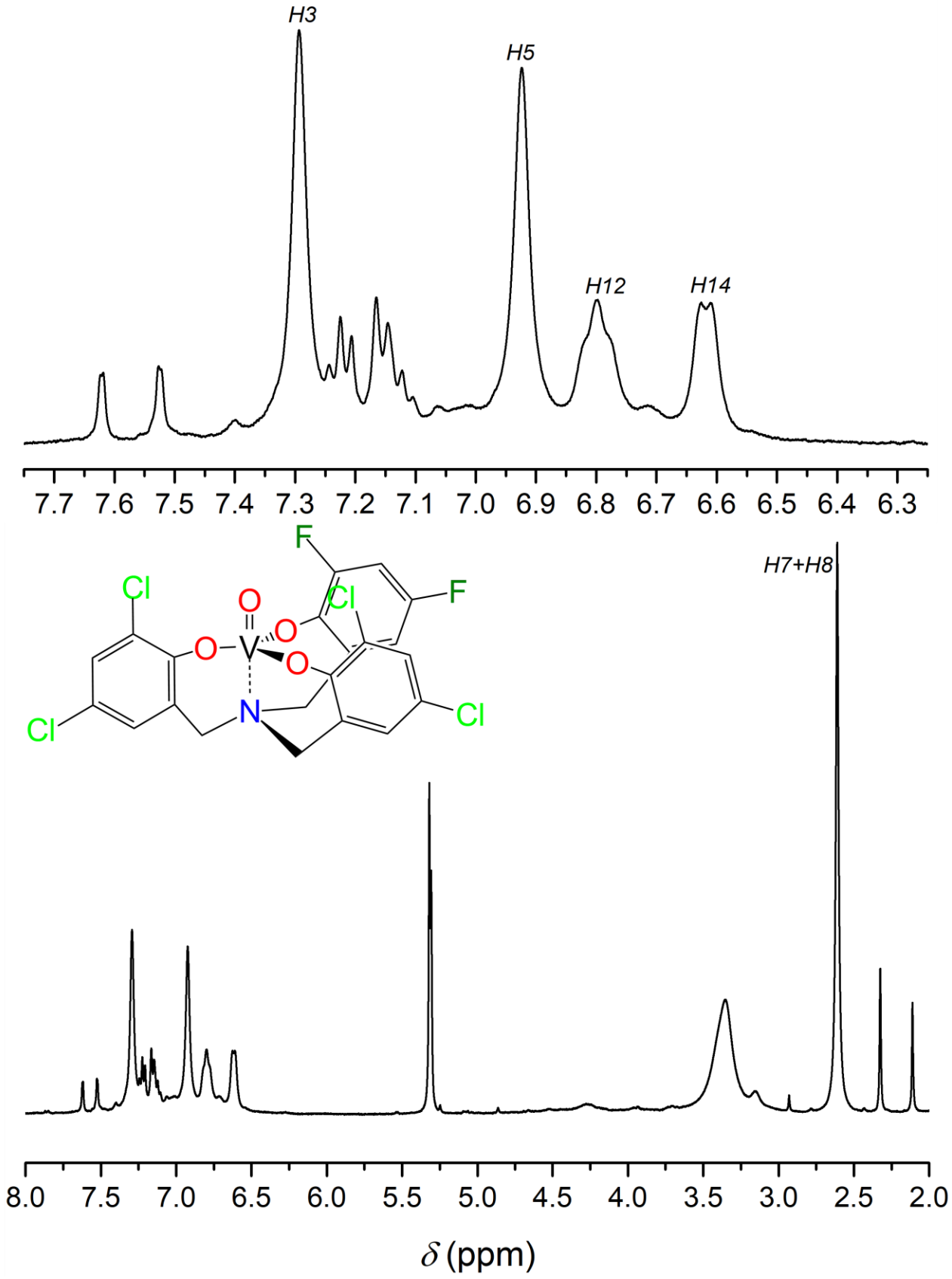

Figure 3.94: Bottom: ^{1}H NMR spectrum of blue $VOTPACl_4F_2$ complex in CD_2Cl_2 (298 K, 400.13 MHz). Top: Hypothetical structure of $VOTPACl_4F_2$ and magnification of the spectrum between 7.8 ppm and 6.2 ppm. Processing parameters (TopSpin 4.3.0): SI = TD, LB = 0.30 Hz. δ_H (ppm) = 5.32 (residual protons in CD_2Cl_2)

Similarity of ^{1}H NMR for the above-mentioned complexes was predictable while we were not expecting particular differences in the other three complexes, whose spectra are reported in comparison with $VOTPACl_4F_2$ in Figure 3.95.

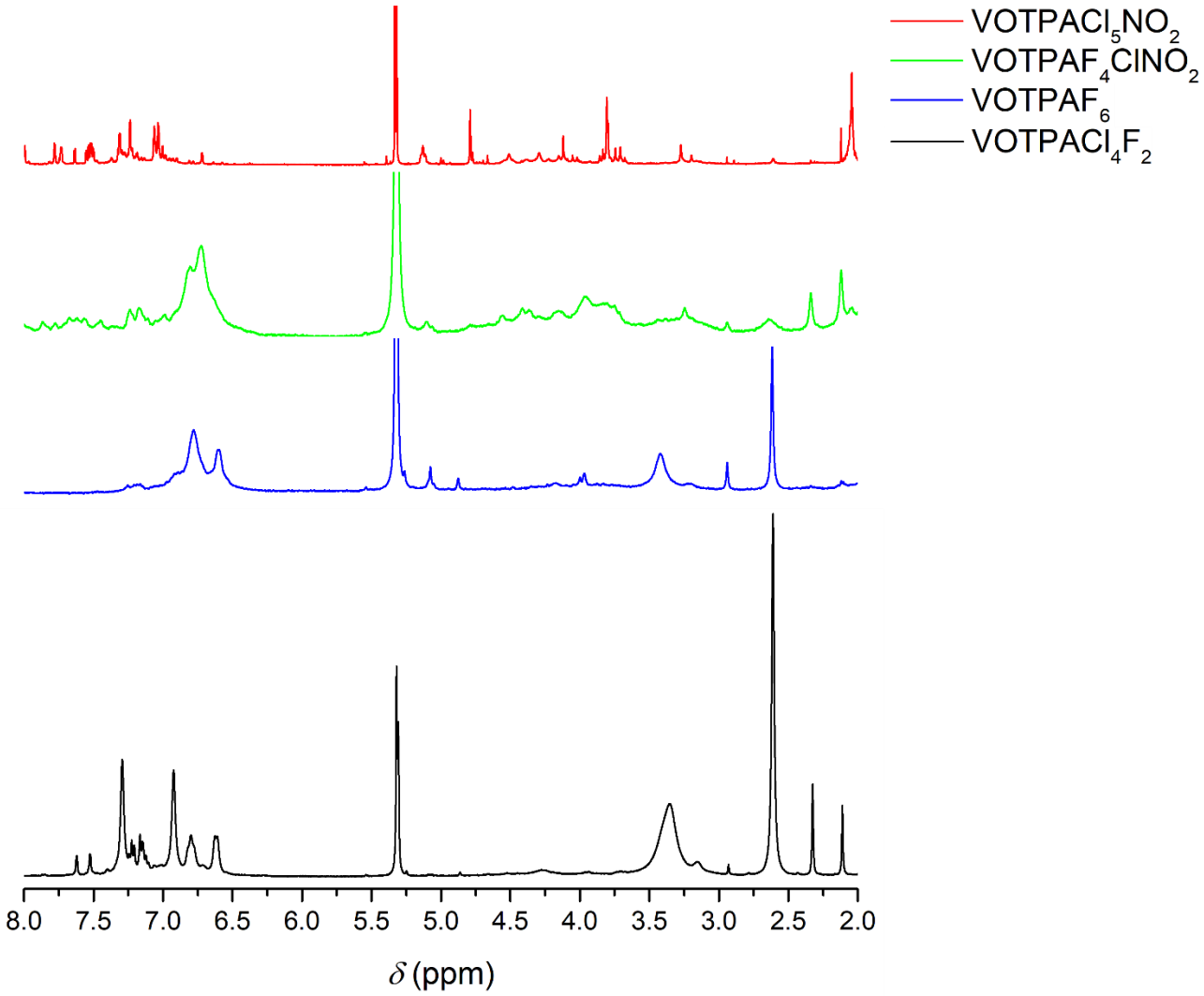

Figure 3.95: ^{1}H NMR superimposition of blue $VOTPACl_4F_2$ complex (black line) and purple complexes $VOTPAF_6$ (blue line), $VOTPAF_4ClNO_2$ (green line) and $VOTPACl_5NO_2$ (red line)

As far as concern $VOTPAF_6$ complex signals are still visible, even if a significant broadening and intensity decrease occurred, while for $VOTPACl_5NO_2$ and $VOTPAF_4ClNO_2$ they are completely missing, particularly obvious looking at methylenic signal (2.61 ppm) which fall in a decently free spectral region. These observations are coherent with the ^{51}V NMR spectra, reported for the 6 VOTPAs superimposed in Figure 3.96, showing well-defined peaks at −432 ppm for $VOTPACl_6$, $VOTPAF_4Cl_2$ and $VOTPACl_4F_2$, a barely visible peak for $VOTPAF_6$ and almost flat baselines for $VOTPACl_5NO_2$, $VOTPAF_4ClNO_2$.

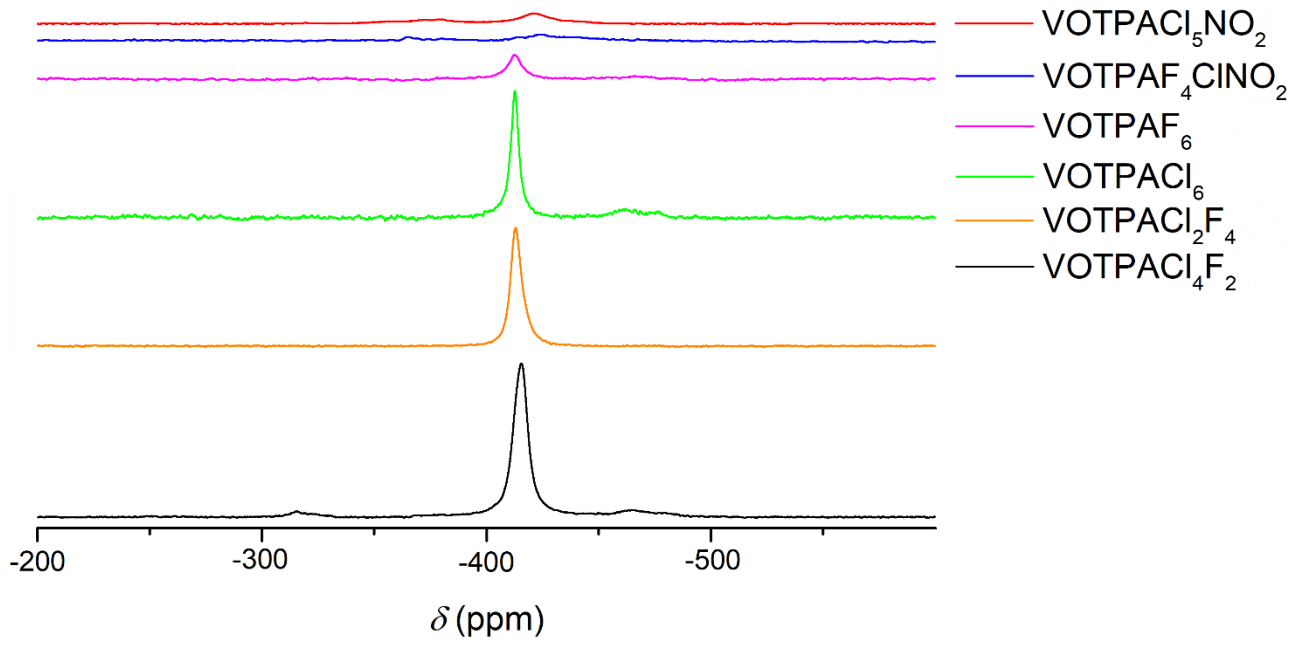

Figure 3.96: ^{51}V NMR superimposition of blue complexes $VOTPACl_4F_2$ (black line), $VOTPAF_4Cl_2$ (orange line), $VOTPACl_6$ (green line) and purple complexes $VOTPAF_6$ (pink line), $VOTPAF_4ClNO_2$ (blue line), $VOTPACl_5NO_2$ (red line)

These data seem to point to a paramagnetic behavior for $VOTPAF_6$, $VOTPACl_5NO_2$ and $VOTPAF_4ClNO_2$ that would mean vanadium in a +4 oxidation state, whose complexes are usually quite air sensitive and easily oxidized to their V^{+5} analogous. This division in two groups with supposedly similar properties, *i.e.*, V^{+5} and V^{+4} complexes is also supported from a macroscopic point of view with $VOTPACl_6$, $VOTPAF_4Cl_2$ and $VOTPACl_4F_2$ being of a deep blue color, while $VOTPAF_6$, $VOTPACl_5NO_2$ and $VOTPAF_4ClNO_2$ being of a deep purple color. Through EPR studies or obtaining a crystal suitable for SC-XRD it would surely be possible to state if our assumption is correct, but due to the lack of time we decided to focalize on techniques (UV-Vis and CV) we have an easier access to in order to obtain some other information to hopefully confirm our hypothesis.

3.6.2 Electrochemical characterization of VOTPAs

Electrochemical studies were conducted using glassy carbon as working electrode and the couple Ag/AgCl as a reference, then reported to SHE for clarity. As far as concern CV, we decided to report and discuss only $VOTPACl_4F_2$ and $VOTPACl_5NO_2$ ones, showed in Figure 3.97, as the other four have very similar profiles, simply with current peak positions slightly shifted. In any case all current peaks are reported in Section 3.8

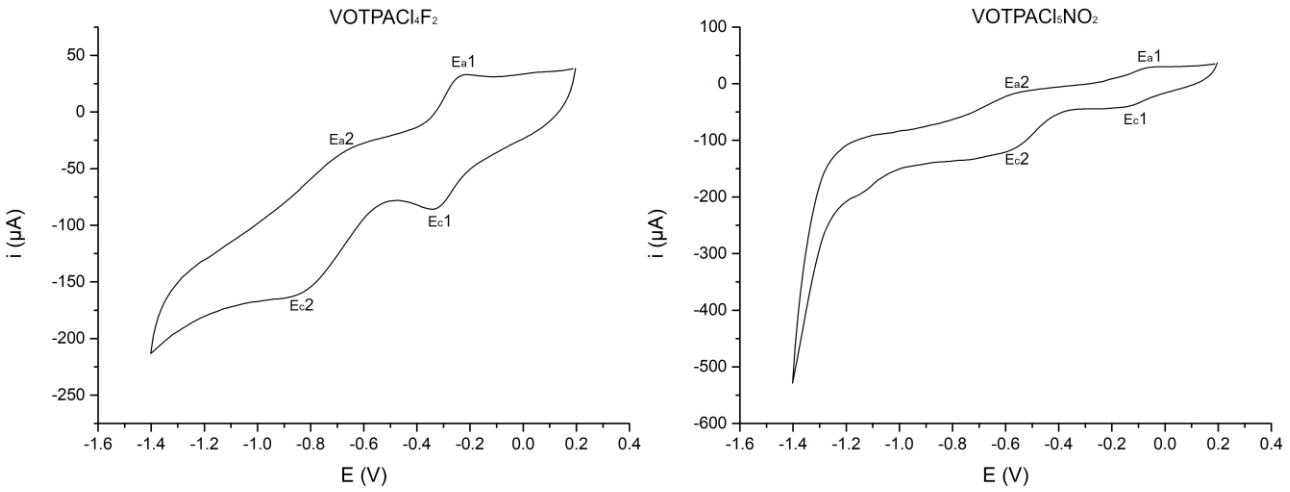

Figure 3.97: Last scan of Cyclic Voltammetries: on the left a blue complex ($VOTPACl_4F_2$), on the right a purple complex ($VOTPACl_5NO_2$), both were recorded at same electrolyte and complex concentration and are reported vs. SHE reference electrode

$VOTPACl_4F_2$ CV shows two cathodic peaks, E_c1 well defined at −0.342 V, while the other, E_c2, is clearly visible as a shoulder at −0.822 V, both processes should be considered as irreversible processes. As far as concern the second transition it is quite clear that the anodic peak E_a2 is much less defined than E_c2 marking it as a not completely reversible process. On the other hand, E_c1 and E_a1 seem quite similar pointing to a fully reversible process, however, E_a1 anodic peak stands at −0.212 V, which means that the cathodic-anodic difference in potential is 0.120 V, more than double the typically accepted 0.057 V value for ideal reversible processes[61]. This means that the barrier to overcome for reoxidation is too big for a fast process to occur, requiring longer time and/or higher potential to be applied, marking the process as a semi-reversible "non-Nernstian" process. This means that the reduced form possesses a natural stability possibly making it recalcitrant to return to the starting form, something we were able to empirically demonstrate with a small chronoamperometric experiment. A potential of −0.4 V was applied to a diluted solution of $VOTPACl_4F_2$ for 30 min, until complete transition from blue to purple color (this will be properly discussed later), few drops of this "reduced solution" were allowed to dry in a Petri capsule, exposed to air while the rest was stored in a vial closed with a screwcap. The initially purple solid slowly turned back to blue in a couple of days while the solution remained purple for several weeks, until it was disposed. From vanadium perspective E_c1 and E_c2 should respectively be the transition from V^{+5} to V^{+4} and the transition from V^{+4} to V^{+3}. This means a hypothetical shift from a double bond to a single bond in VO for the first step, probably forming oxygen radical species that can couple to structure like those predicted by Amadio *et al.*[20] and shown in Figure 3.5. That would probably increase their stability and could partially explain the high ΔE1 causing the process to be "non-Nernstian". Then, with the second step V^{+3} is generated and oxygen released. This is probably making the process non-reversible, as the

conditions for CV are usually strictly anaerobic, working under a layer of Ar with degassed solvents, to avoid oxygen due artefacts. Thus, even if oxygen is released during reduction, O_2 concentration in solution is probably too low for an efficient up-take to restore the V^{+4} form.

Also $VOTPACl_5NO_2$ CV shows two poorly resolved cathodic peaks, E_c1, at −0.112 V, has very low intensity, probably due to the low concentration of V^{+5} complex in solution, while E_c2 is at −0.563 V. A third shoulder can be noted at −1.14 V, possibly linked to complex decomposition as the anodic counterpart is not detectable. First transition is considerable fully reversible, with a $\Delta E1 = 0.05$ V, while the second one seems to be partially irreversible, as the anodic peak is less pronounced, probably for similar reasons to those hypothesized for $VOTPACl_4F_2$. It should be noted that both transitions in $VOTPACl_5NO_2$ happen at less negative potentials than in $VOTPACl_4F_2$ with a difference of 0.230 V for E_c1 and 0.259 V for E_c2, quite big differences considering that these two metal centers should be very similar. This data confirms unambiguously the starting hypothesis that EWG groups on the ligand can significantly improve the reduction potential of the resulting complex, possibly making these more reactive catalysts.

Before delving into UV-Vis characterization of native complexes and of their electrochemically reduced analogues we wanted to describe a peculiar behavior we have observed during preliminary study for CV, while evaluating concentrations and electrolyte. 0.5 mM solutions of native $VOTPACl_5NO_2$ are of a dark purple shaded color, upon addition of tetrabutylammonium tetrafluoroborate ($TBABF_4$) we observed a quick color intensification and definition to a deep purple. However, when to native $VOTPACl_5NO_2$ a different electrolyte, tetrabutylammonium chloride (TBACl), was added color changed to a well-defined blue, the UV-Vis spectra of relevant region are reported in Figure 3.98.

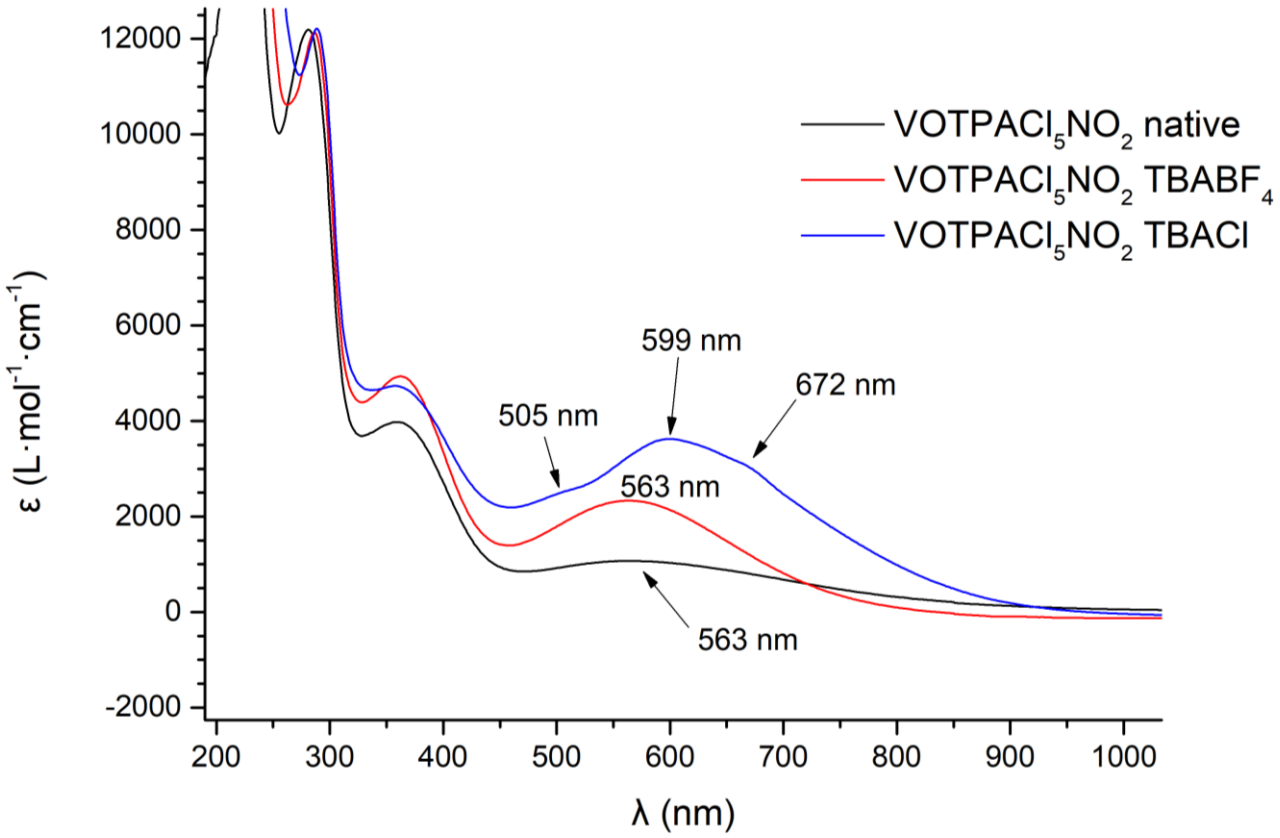

Figure 3.98: Superimposition of UV-Vis-NIR spectra of native $VOTPACl_5NO_2$ (black line) and after addition of $TBABF_4$ (red line) or TBACl (blue line). All spectra were recorded between 190 nm and 2000 nm but only the relevant region was reported

It is quite evident that upon addition of $TBABF_4$ (red line) there is a significant increase and sharpening of 563 nm ε band compared to native (black line). However, when TBACl is added (blue line) the ε increase is combined with a shift of the peak to 599 nm and with the appearance of two shoulders at 505 nm and 672 nm. This difference in behavior must be due to the anion nature, as the cation is the same, in particular, Cl^- is a medium sized anion, slightly coordinating that could both coordinate imposing a different geometry to the V center and stabilize a different oxidation state. On the other hand, BF_4^- is a big sized non-coordinating anion that hardly can be more than a counterion, thus, we believe that in this case ε increase is due to the cation, possibly stabilizing a negatively charged monomeric version of the peroxide dimer reported in Figure 3.5.

3.6.3 UV-Vis Characterization of $VOTPACl_6$

UV-Vis spectra were recorded for the six VOTPA complexes in their native forms, and after application of an appropriate potential, determined from CV experiments, for 1 h to convert native forms to their reduced analogues.

Figure 3.99 shows the superimposed UV-Vis spectra of $VOTPACl_6$ native (black line) and reduced forms. First transition form, that we assume to be V^{+4} was obtained imposing a −0.6 V potential for 1 h, recording the blue spectrum. To verify completeness of this transition and stability of it we kept the −0.6 V potential for another 30 min showing any significant difference in the recorded spectrum (pink line). Then, to the V^{+4} complex solution was applied a −0.9 V potential for 1 h (green line), followed by another 30 min (red line) to generate V^{+3} form and evaluate its stability.

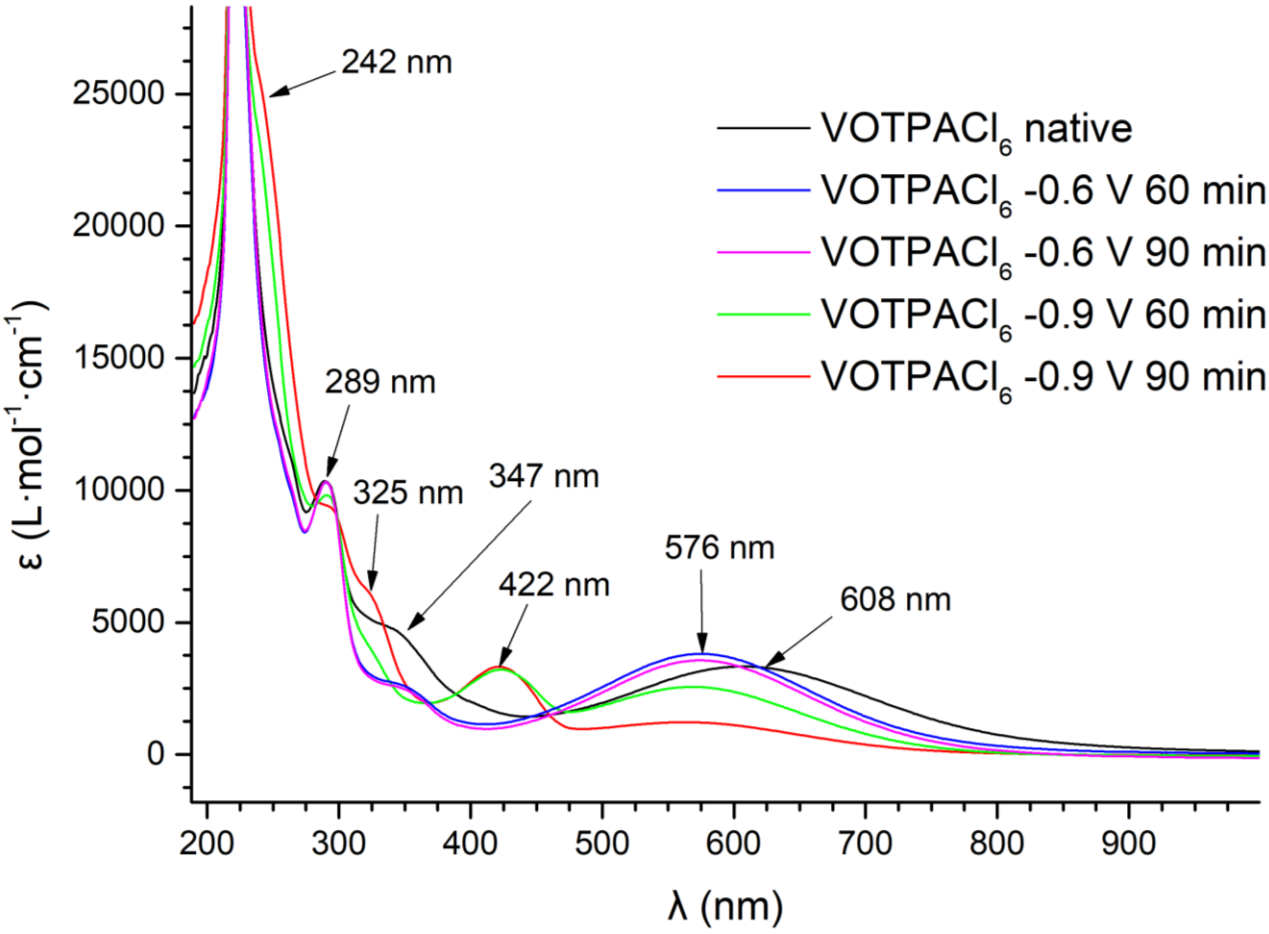

Figure 3.99: Superimposition of UV-Vis-NIR spectra of native $VOTPACl_6$ (black line), after application of a −0.6 V potential for 60 min (blue line), 90 min (pink line), after application of a −0.9 V potential for 60 min (green line) and 90 min (red line). All spectra were recorded between 190 nm and 2000 nm but only the relevant region was reported

Native form color is a deep blue, as demonstrated by the wide band centered at 608 nm. Its spectrum also shows a shoulder in the near-UV, at 347 nm, and two ligand peaks, one at 289 nm while the other falls below DCM cut-off, giving that Lorentzian shape to the peak. V^{+4} form spectra are quite similar to the native form, with a decrease in 347 nm shoulder intensity and shift of the main band from 608 nm to 576 nm, switching the solution color from blue to purple. V^{+4} form seems to be quite stable as the two recorded spectra (blue and pink lines) are almost the same. Further reduction to V^{+3} causes the color to turn to a bright yellow, as demonstrated by the appearance of a peak at 422 nm. V^{+3} form does not seem to be stable, as 422 nm peak stop to increase while the residue of 576 nm band (V^{+4})

is still present, furthermore, maintaining −0.9 V potential cause an increase in two shoulders at 242 nm and 325 nm, while the ligand peak at 289 nm decreases. These observations point to complex decomposition after formation of V^{+3} form, indicating it as a metastable product, and confirming the non-reversibility depicted by CV.

3.6.4 UV-Vis Characterization of $VOTPACl_4F_2$

Figure 3.100 shows UV-Vis spectra of $VOTPACl_4F_2$ native and V^{+4} forms, as application of −0.9 V led directly to decomposition without appearance of the V^{+3} form.

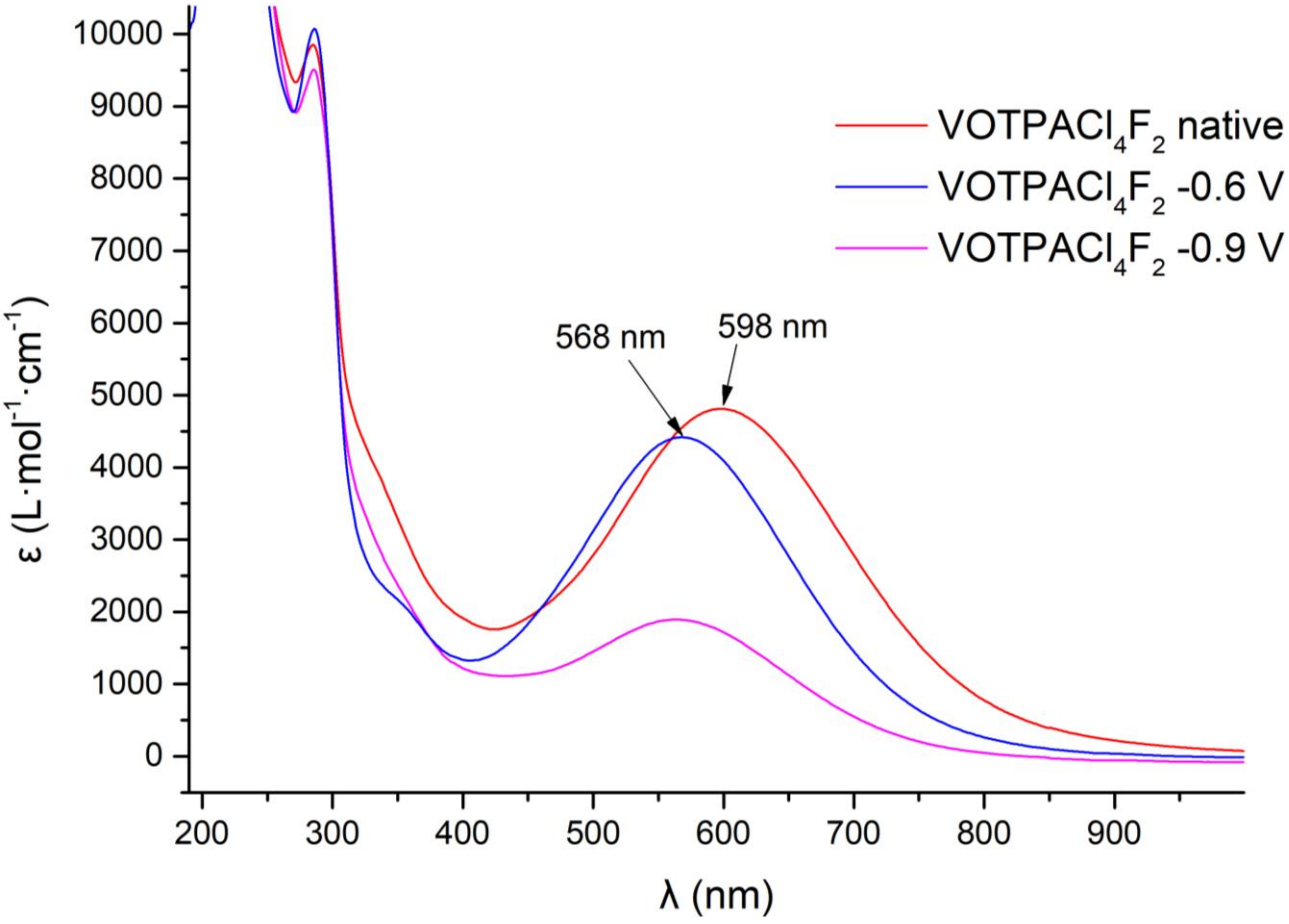

Figure 3.100: Superimposition of UV-Vis-NIR spectra of native $VOTPACl_4F_2$ (red line), after application of a −0.6 V potential for 60 min (blue line) and after application of a −0.9 V potential for 60 min (pink line). All spectra were recorded between 190 nm and 2000 nm but only the relevant region was reported

Similarly to $VOTPACl_6$ complex $VOTPACl_4F_2$ shows two wide bands for native and V^{+4} forms, respectively at 598 nm and 568 nm, making them appear blue and purple. Unfortunately, V^{+3} was not

detected as application of −0.9 V potential led only to an intensity decrease in 568 nm band, with slightly visible decomposition shoulders similar to those observed for $VOTPACl_6$.

3.6.5 UV-Vis Characterization of $VOTPAF_4Cl_2$

$VOTPAF_4Cl_2$ UV-Vis spectra (Figure 3.101) are very similar to $VOTPACl_6$ ones, only with slight shift in band maxima of major bands of the three forms.

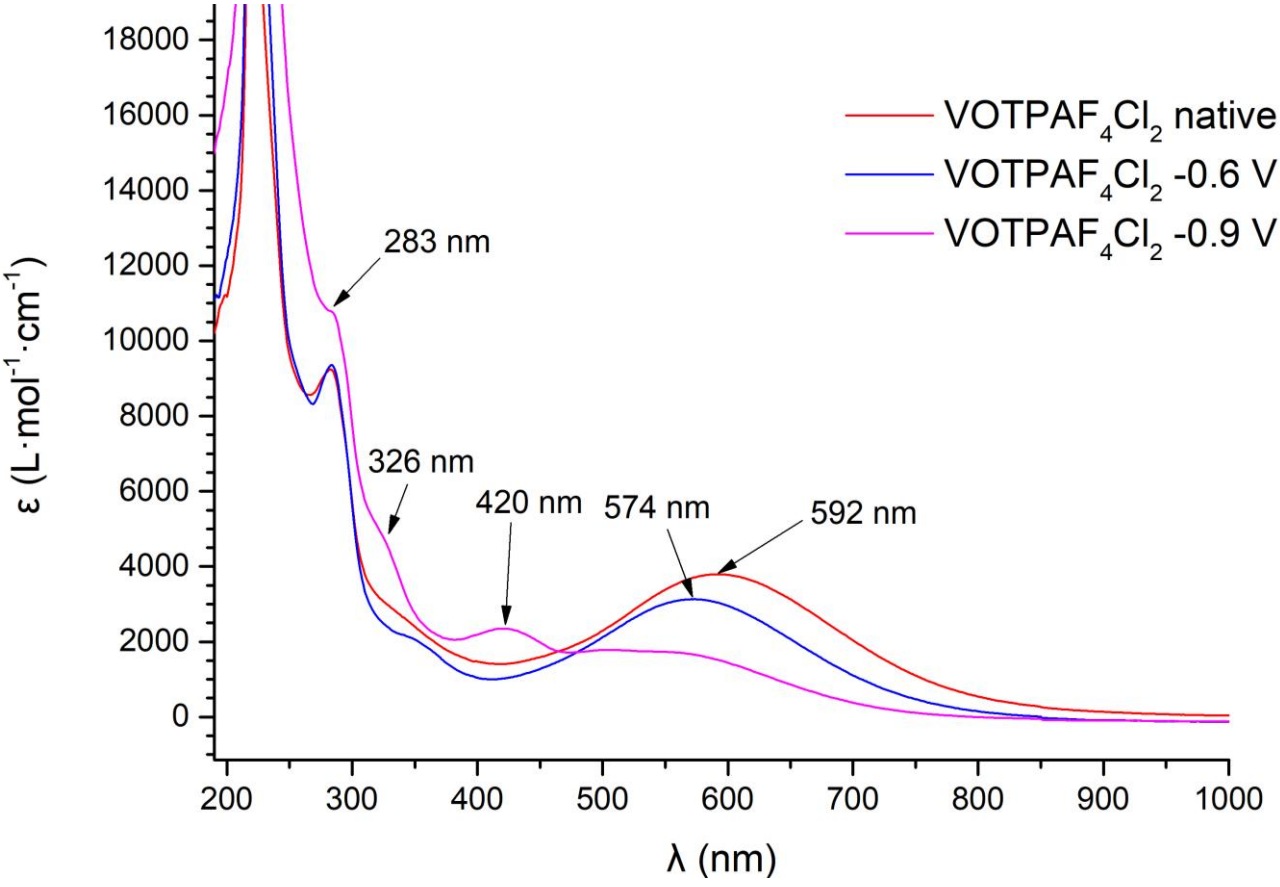

Figure 3.101: Superimposition of UV-Vis-NIR spectra of native $VOTPAF_4Cl_2$ (red line), after application of a −0.6 V potential for 60 min (blue line) and after application of a −0.9 V potential for 60 min (pink line). All spectra were recorded between 190 nm and 2000 nm but only the relevant region was reported

Native form (red line) major band is located at 594 nm, giving to the solution a blue color, while V^{+4} (blue line) is at 574 nm and appear to be purple. As observed for $VOTPACl_6$ V^{+3} form is yellow, with a peak at 420 nm and starts decomposing before reaching complete conversion.

3.6.6 UV-Vis Characterization of $VOTPAF_6$

$VOTPAF_6$ starts as a purple solution, thus if the behavior is similar to the three previous complexes we should assume it to be in its V^{+4} form. Therefore, we applied also sequential positive potentials, up to +0.8 V, as well as the most negative one, hoping to detect transitions to V^{+5} and V^{+3} respectively. Figure 3.102 shows $VOTPAF_6$ spectra, reported in the relevant UV-Vis region.

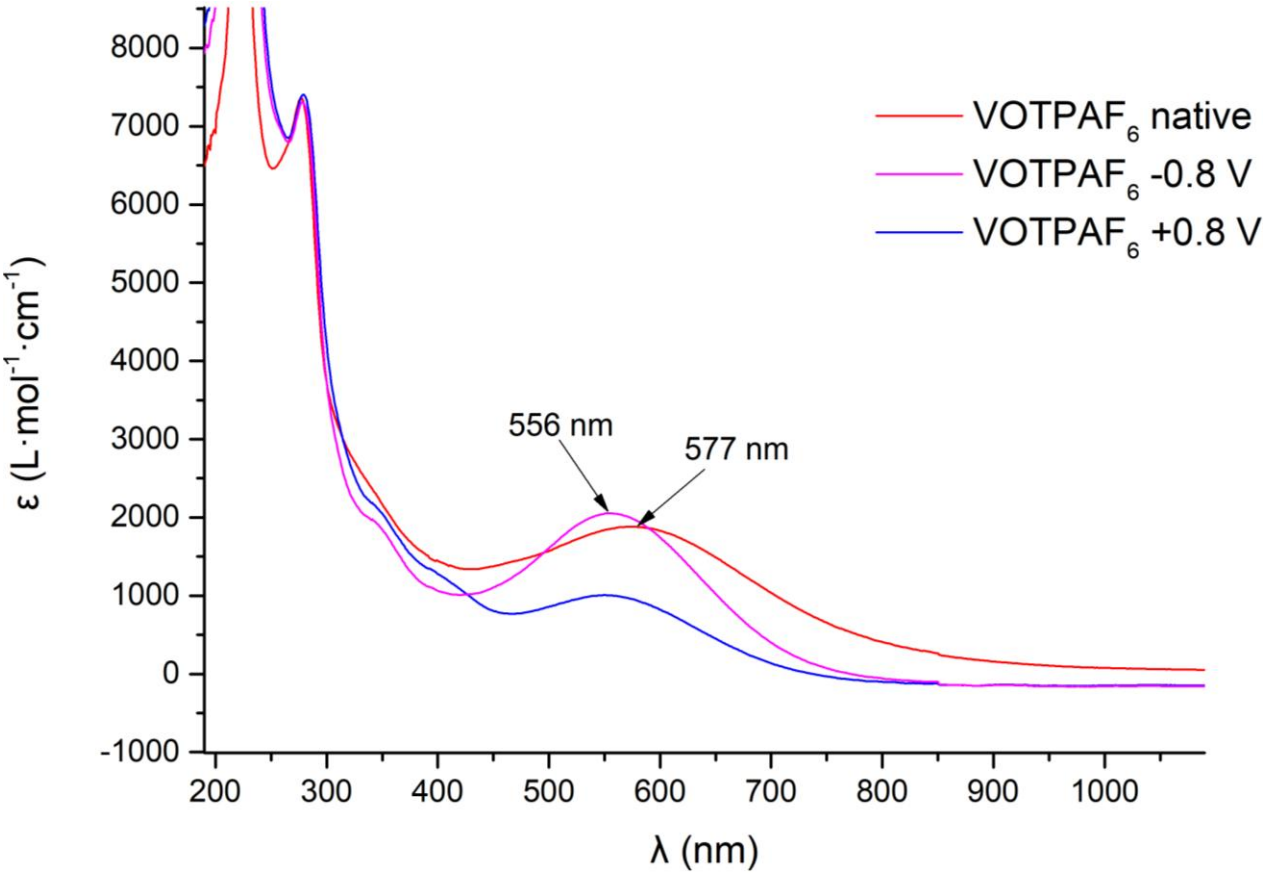

Figure 3.102: Superimposition of UV-Vis-NIR spectra of native $VOTPAF_6$ (red line), after application of a −0.8 V potential for 60 min (pink line) or after application of a +0.8 V potential for 60 min (blue line). All spectra were recorded between 190 nm and 2000 nm but only the relevant region was reported

Unfortunately, $VOTPAF_6$ seems to be quite inert to applied potentials, in fact, the shift in the main band from 577 nm in native form (red line) to 556 nm when reducing potential is applied (pink line) is actually due to the addition of $TBABF_4$ rather than to an actual reduction, similarly to what was shown for $VOTPACl_5NO_2$ in Section 3.6.2. $VOTPAF_6$ also proved to be inert to oxidation showing any differences in spectra recorded (not shown) up to +0.8 V where complex decomposition start (blue line).

3.6.7 UV-Vis Characterization of VOTPACl$_5$NO$_2$

Figure 3.103 shows the UV-Vis spectra of VOTPACl$_5$NO$_2$ native form (black line), after addition of TBABF$_4$ (pink form) and after 1 h application of −0.6 V (blue line).

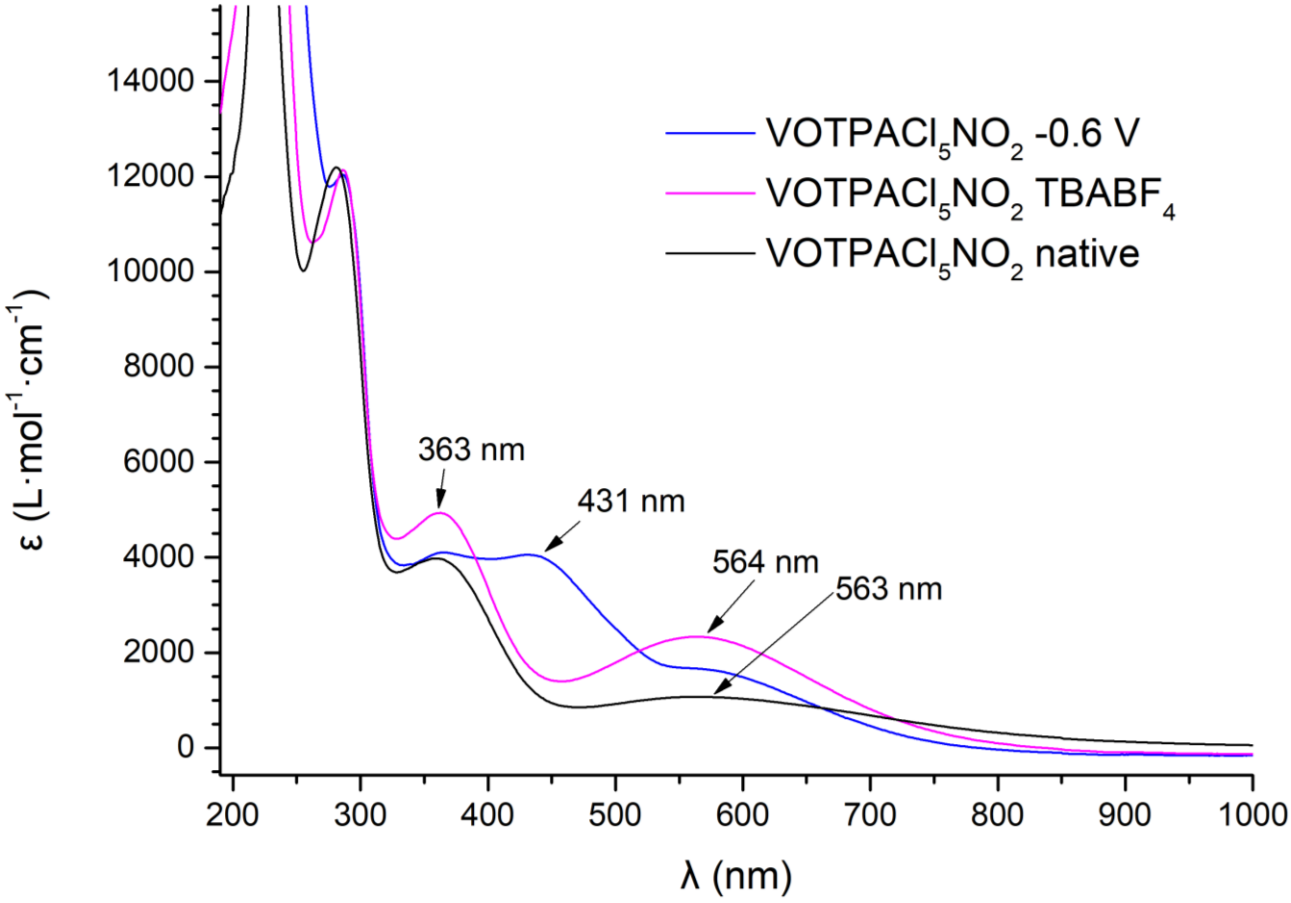

Figure 3.103: Superimposition of UV-Vis-NIR spectra of native VOTPACl$_5$NO$_2$ (black line), after addition of TBABF$_4$ (pink line) and after application of a −0.6 V potential for 60 min (blue line). All spectra were recorded between 190 nm and 2000 nm but only the relevant region was reported

VOTPACl$_5$NO$_2$ starts of a dark color shaded in purple, this can be observed in UV-Vis spectrum (black line) as a broad band of similar intensity between 700 nm and 450 nm, with its maximum at 563 nm. Furthermore, a peak in the UV region is observed, at 363 nm, this has not been detected in previously discussed complexes while it is also present in VOTPAF$_4$ClNO$_2$ making reasonable to think that it is due to the presence of NO$_2$ group. As already mentioned in Section 3.6.2, upon addition of TBABF$_4$ a clean development of purple color is observed, reflected by UV-Vis spectrum (pink line) with a sharpening of the band accompanied by a significant ε increase in 600–500 nm with band maximum retained at 564 nm. When a −0.6 V potential is applied the solution switches from the starting purple to a dark yellow color, this transition is hardly completed as this reduced form does not seem to be stable, similarly to what was observed for other yellow forms. These observations seem to confirm the hypothesis of VOTPACl$_5$NO$_2$ starting as a V^{+4} as when reduced evolves directly

to a yellow unstable form, which is very similar to the situation observed for V^{+3} forms in $VOTPACl_6$ and $VOTPAF_4Cl_2$. Unfortunately, as for $VOTPAF_6$ oxidation failed to give any significant change apart from complex decomposition.

3.6.8 UV-Vis Characterization of $VOTPAF_4ClNO_2$

Figure 3.104 shows UV-Vis spectra of $VOTPAF_4ClNO_2$ in all its possible forms.

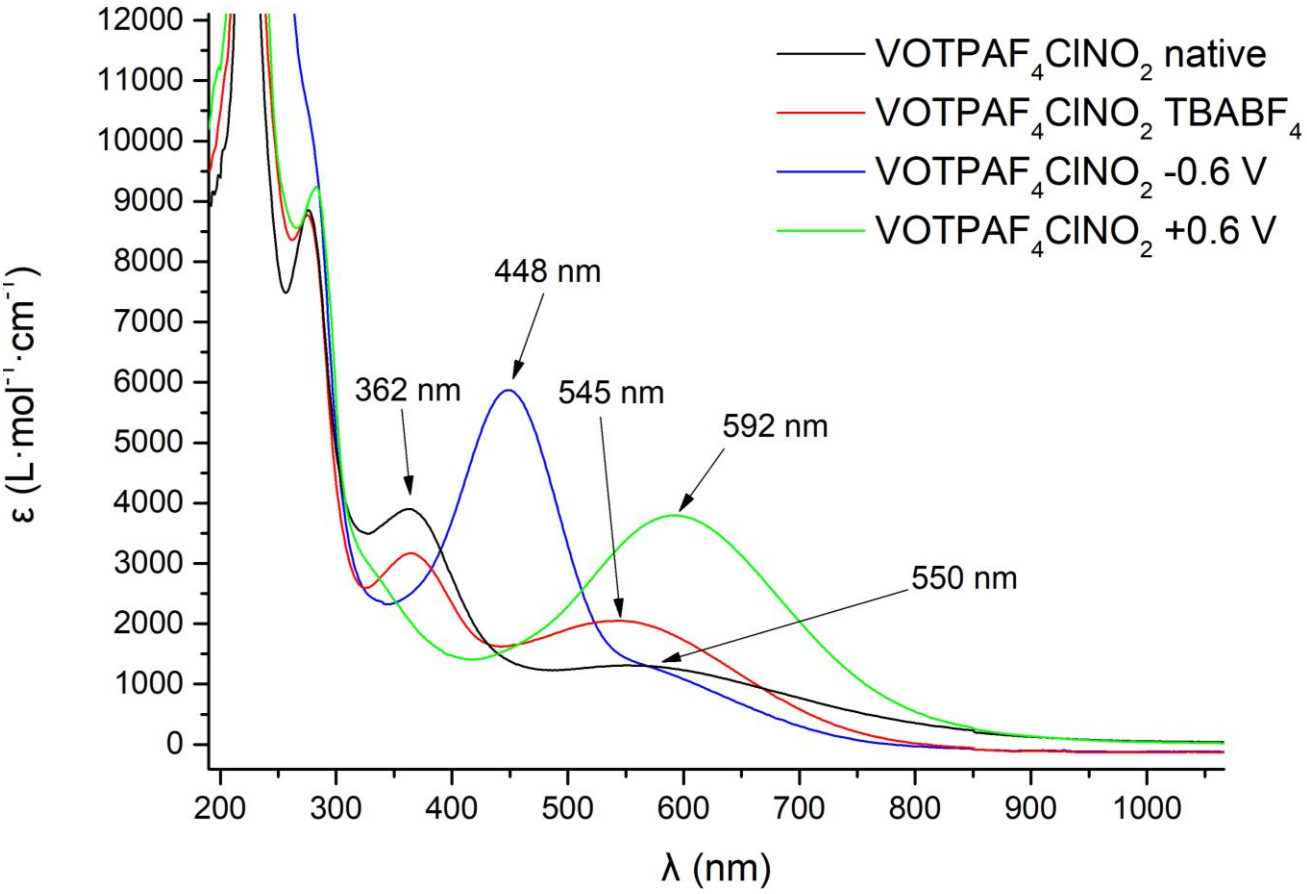

Figure 3.104: Superimposition of UV-Vis-NIR spectra of native $VOTPAF_4ClNO_2$ (black line), after addition of $TBABF_4$ (red line) and after application of a −0.6 V potential for 60 min (blue line) or after application of a +0.6 V potential (green line). All spectra were recorded between 190 nm and 2000 nm but only the relevant region was reported

Similarly to $VOTPACl_5NO_2$ also $VOTPAF_4ClNO_2$ starts as a dark solution, slightly purple, in fact native main bands (black line) are almost the same, with comparable ε values in 700–450 nm range. Also for $VOTPAF_4ClNO_2$ the addition of $TBABF_4$ (red line) causes a sharpening of main band and a small maximum shift to lower wavelengths, making deep purple the perceived color. Applying a reducing potential of −0.6 V causes the solution to turn from purple to a dark yellow, change reflected into the spectrum (blue line) by the rise of a peak at 448 nm. Even tho some decomposition signals

are observed this is by far the most stable yellow form, as it can be seen from the small shoulder at 550 nm representing the remaining starting material. Hoping to confirm what we assumed, that is a native purple complex in V^{+4} form and a reduced yellow complex in V^{+3} form, we tried to oxidize native $VOTPAF_4ClNO_2$. Luckily this time a color change to blue was observed when an oxidizing potential of +0.6 V was applied for 1 h, showing the spectrum (green line) of this oxidized V^{+5} form as a band with its maximum at 592 nm, very similar to native $VOTPAF_4Cl_2$, $VOTPACl_4F_2$ and $VOTPACl_6$. This is a huge confirmation that at least native stabile form of $VOTPAF_4ClNO_2$ is actually a V^{+4} complex. For some reason, 362 nm signal disappears in both oxidized and reduced form, maybe this could be due to a change in coordination geometry.

3.6.9 UV-Vis Characterization Final Remarks and Comparisons

First of all, we want to stress out that given the ε range 1000–5000 $L \cdot mol^{-1} \cdot cm^{-1}$ for the Vis band of each complex these must be absorptions due to ligand to metal charge transfer (LMCT) as they are way too intense to be d-d transitions that rarely are greater than a few hundreds. Furthermore, d-d transitions usually give more defined and sharp peaks, while LMCT are generally broader bands. Even for LMCT Vis absorptions, these ε values are quite big, for comparison $KMnO_4$, which is universally known to be of an extremely intense purple, has an ε for the main band at 525 nm of 3340 $L \cdot mol^{-1} \cdot cm^{-1}$[62]. This would mean that from a photocatalyst perspective these complexes could harvest light in visible-region with good efficiency, possibly requiring lower concentrations to be active.

Another interesting observation, easily visible in Figure 3.105 comparing complexes native forms, is that there is a good linear correlation between 289 nm peak intensity and number of Cl substituents, clearly visible looking at $VOTPAF_4Cl_2$, $VOTPACl_4F_2$ and $VOTPACl_6$, while NO_2 give an even higher contribution. Looking at Figure 3.105 is easy to recognize the similarity between $VOTPAF_4Cl_2$, $VOTPACl_4F_2$ and $VOTPACl_6$ and between $VOTPACl_5NO_2$ and $VOTPAF_4ClNO_2$ both in shape and intensity of the band, while $VOTPAF_6$ stands in the middle.

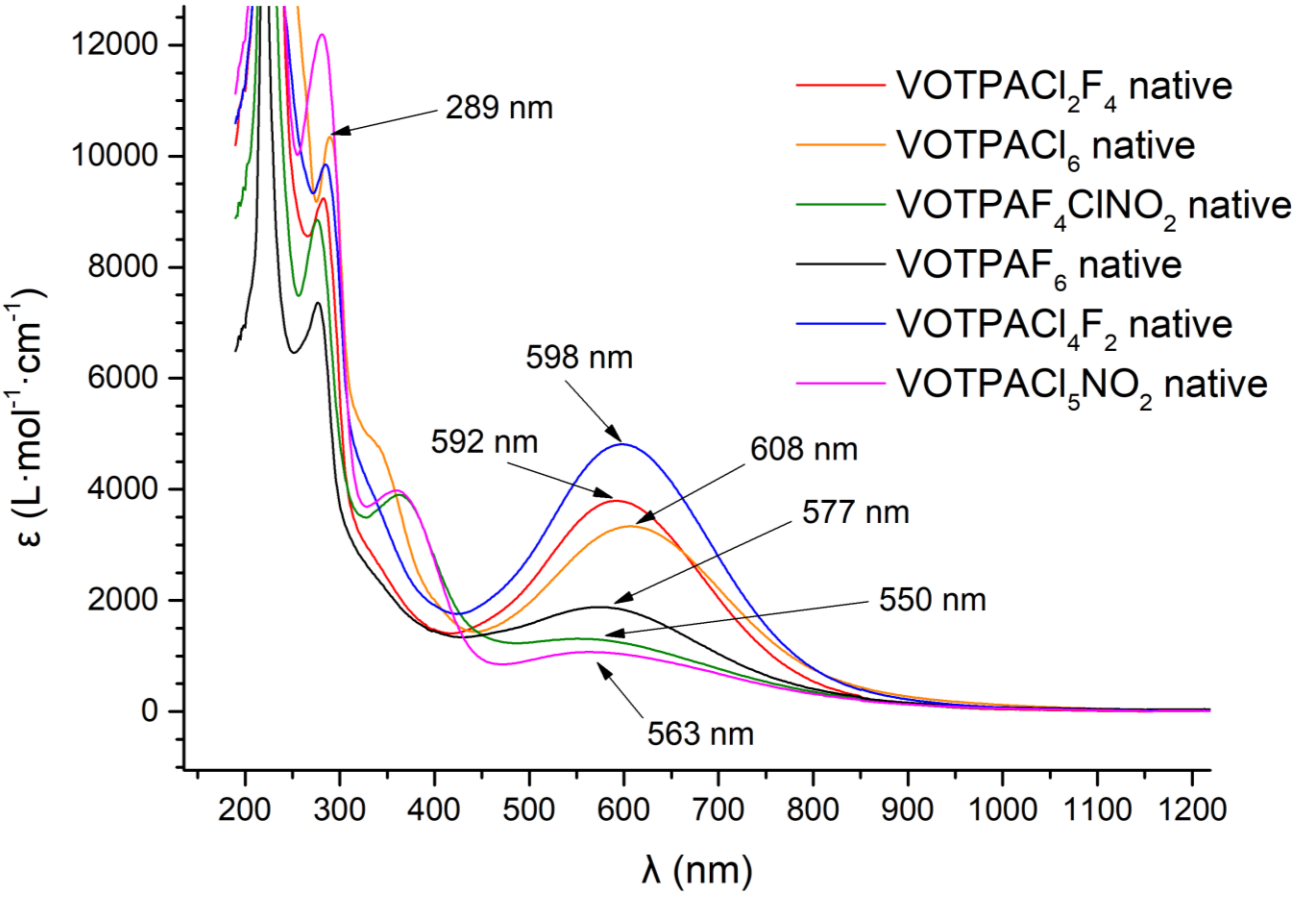

Figure 3.105: Comparison of UV-Vis-NIR spectra of native complexes: $VOTPAF_4Cl_2$ (red line), $VOTPACl_6$ (orange line), $VOTPAF_4ClNO_2$ (dark green line), $VOTPAF_6$ (black line), $VOTPACl_4F_2$ (blue line), $VOTPACl_5NO_2$ (pink line). All spectra were recorded between 190 nm and 2000 nm but only the relevant region was reported

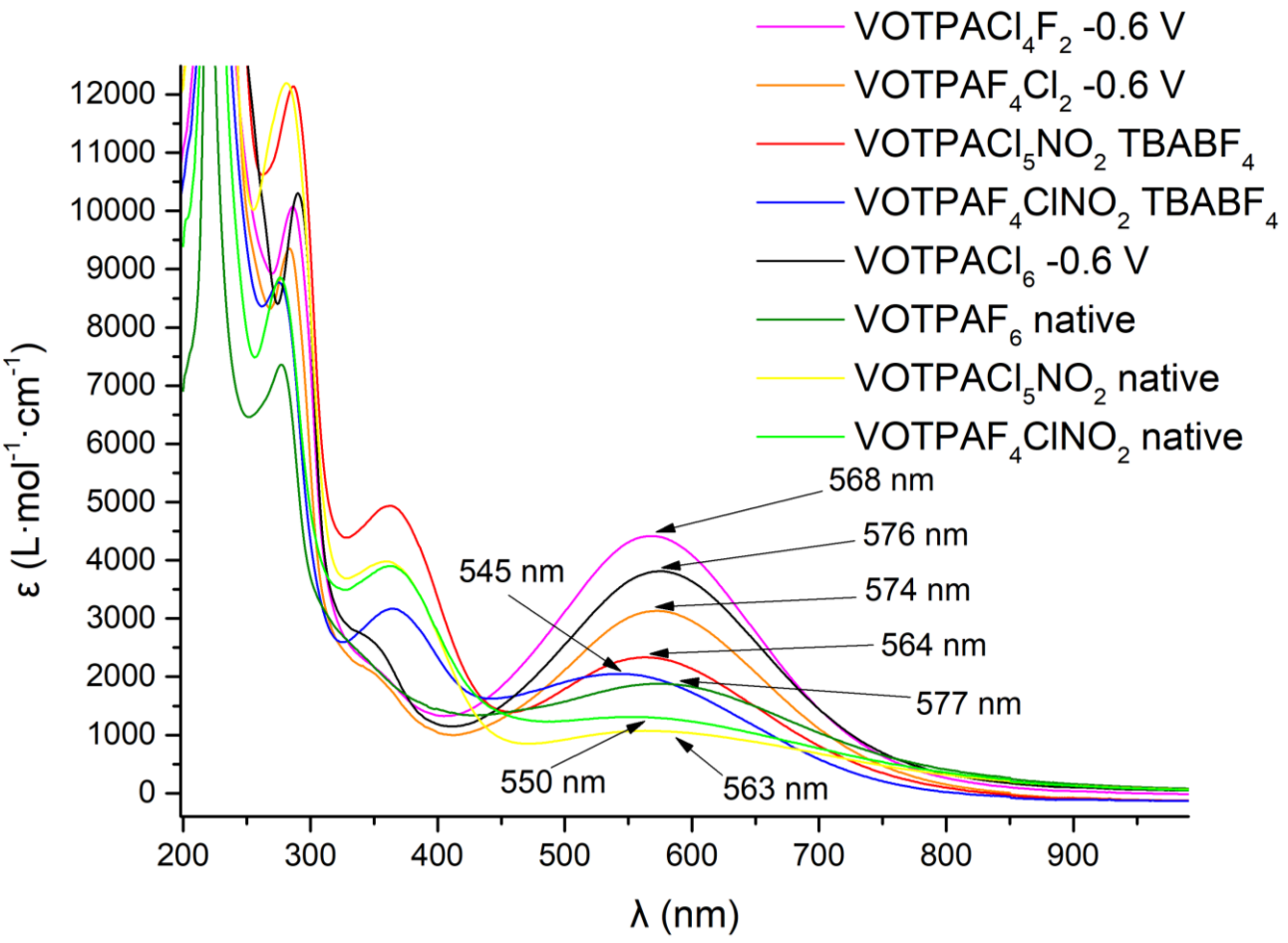

Figure 3.106: Comparison of UV-Vis-NIR spectra of complexes in purple form: $VOTPACl_4F_2$ (pink line), $VOTPAF_4Cl_2$ (orange line), $VOTPACl_5NO_2$ + $TBABF_4$ (red line), $VOTPAF_4ClNO_2$ + $TBABF_4$ (blue line), $VOTPACl_6$ (black line), $VOTPAF_6$ (dark green line), native $VOTPACl_5NO_2$ (yellow line), native $VOTPAF_4ClNO_2$ (green line). All spectra were recorded between 190 nm and 2000 nm but only the relevant region was reported

Figure 3.106 shows an overlap of the purple complexes' spectra native or electrochemically reduced. $VOTPACl_5NO_2$ and $VOTPAF_4ClNO_2$ spectra are reported both for native and with the addition of $TBABF_4$. Excluding intensity of the absorption all the bands are quite similar apart $VOTPACl_5NO_2$ native form and $VOTPAF_4ClNO_2$ in native and $TBABF_4$ form, with the latter being slightly shifted to smaller wavelength, possibly because of an overlap with a secondary, less intense, band around 490 nm. $VOTPACl_5NO_2$ and $VOTPAF_4ClNO_2$ native forms are quite similar, and upon addition of $TBABF_4$ both increase their band intensity paired with a significant sharpening that brings them closer to $VOTPAF_6$ native form spectrum (dark green line). We think that these similarities in Vis spectra of purple complex solutions must be due to the oxidation state of vanadium center. Pairing this information with data collected in CV and the paramagnetic behavior observed in both ^{1}H NMR and ^{51}V NMR of $VOTPACl_5NO_2$, $VOTPAF_4ClNO_2$, and to a minor extent also $VOTPAF_6$ we believe is reasonably safe to assume that these purple complexes all possess a V^{+4} center. This is remarkable, as V^{+4} species are generally easily oxidized to their V^{+5} analogous from air oxygen, while $VOTPACl_5NO_2$, $VOTPAF_4ClNO_2$ and $VOTPAF_6$ are indefinitely stable in these conditions.

Furthermore, V^{+4} complexes are generally obtained directly from V^{+4} sources, like vanadyl acetylacetonate, and as far as we know it is quite unusual to obtain them from V^{+5} sources like $VO(OiPr)_3$. The hypothesis of vanadyl complexes does not seem reasonable with our ligands, as vanadyl is a VO^{2+} while our ligands all possess three negative charges and during synthesis of complexes any cation is generated or already available for charge balance. Therefore, a peroxide dimeric structure like those predicted to form during a catalytic cycle (Figure 3.5) seems more likely as a synthetic outcome, as it would be neutral. However, the situation changes significantly when $TBABF_4$ is added, as TBA^+ becomes available and could stabilize a monomeric vanadyl form, causing a significant change in the chromophore, and possibly justifying the observed UV-Vis spectral changes. Still, two electrons would be required to convert a peroxide dimer to two vanadyl complexes, and solution charge balance would require the generation of other two cations or quenching of two anions. As we cannot identify the electron source in the system, nor what could keep charge balance, this hypothesis seems to be quite weak, even if we do not have a better explanation.

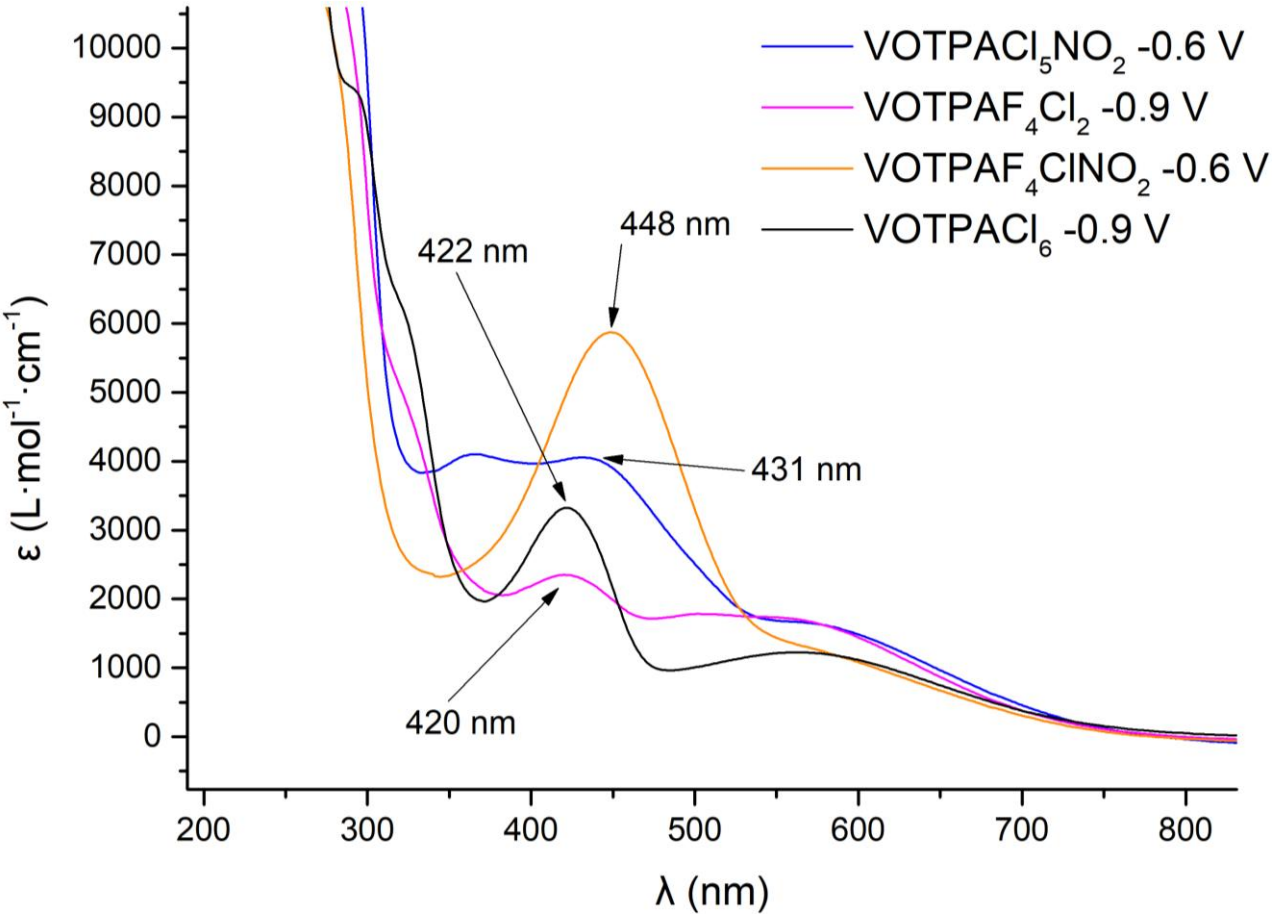

Figure 3.107: Comparison of UV-Vis-NIR spectra of complexes in yellow form: $VOTPACl_5NO_2$ (blue line), $VOTPAF_4Cl_2$ (pink line), $VOTPAF_4ClNO_2$ (orange line), $VOTPACl_6$ (black line). All spectra were recorded between 190 nm and 2000 nm but only the relevant region was reported

Figure 3.107 shows the superimposition of the four complexes we were able to reduce to their yellow form, that are $VOTPACl_5NO_2$, $VOTPAF_4Cl_2$, $VOTPAF_4ClNO_2$ and $VOTPACl_6$. As a straightforward consequence of what has already been discussed for purple forms, it should be clear that these yellow forms must be the V^{+3} complexes. This also explains the poor stability observed for each complex, especially considering the process irreversibility expected for the second transition according to CVs. As far as concern band maximum positions $VOTPAF_4Cl_2$ and $VOTPACl_6$ are extremely close, with a distance of 2 nm, while NO_2 complexes are more distant. However, these gaps are not too big, especially given the broad bands, and that some shift could occur upon complete depletion of the starting forms.

3.7 Conclusions and future outlooks

In this work we developed a reliable convergent synthetic pathway to triphenolamine (TPAs) proligands synthetizing two precursors from the same starting material, an *o-, p*-disubstituted phenol. These precursors are diphenolamines (DPAs) and chloromethylated phenols, in particular, we obtained 2 different DPAs and 3 different chloromethylated phenols, giving us the chance to obtain 6 different TPAs. All these 11 organic molecules were obtained in good to high yield and characterized through NMR spectroscopy and ESI-MS if possible. Both DPAs and TPAs coordination chemistry were investigated with preliminary studies on Ti, Co and V, obtaining 9 complexes, 3 were crystallized and characterized through SC-XRD, while the other 6 were unable to give crystals and thus solution studies were performed. $DPA^{Cl,Cl}$ Ti complex was found to be an interesting example of a low nuclearity Ti oxo-isopropoxide complex, whose structure forced the ligand into a bent position, bringing the aromatic rings into π-stacking range. Co complexes obtained with $DPA^{Cl,Cl}$ ligand were two, a monomer made by a Co^{3+} sandwiched between two ligand molecules with a protonated DBU as a counterion, and a square planar cluster of 4 Co^{2+}, surprisingly stable under air atmosphere. VOTPAs complexes were studied in solution, through ^{1}H NMR, ^{51}V NMR, CV and UV-Vis spectroscopy, these characterization showed a peculiar division in the products between V^{+4} and V^{+5} complexes according to the EWG character of ligand substituents. This is a remarkable and unexpected result as V^{+4} complexes are usually quite unstable in air atmosphere and hardly synthetized from V^{+5} sources. A further confirmation of this difference could come from EPR studies, and they should be planned as soon as possible. Unfortunately, we were not able to obtain crystals of these complexes, and future work should start from this, in order to clarify their structure. Due to lack of time, we did not start catalytic studies to assess these complexes performances in oxidative

cleavage of lignin model compounds, these should be performed both in ordinary and photocatalytic conditions, as the very high ε values imply a possibly high photocatalytic efficiency.

3.8 Experimental

3.8.1 Materials and Methods

Reagents and solvents were purchased by Sigma-Aldrich and used as received unless stated otherwise. All reactions were performed in standard glassware under air atmosphere. ESI-MS measurements were conducted on a 6310A Ion Trap LC-MS(n) instrument (Agilent Technologies) performing an isocratic LC at 80:20 CH_3CN:H_2O (0.1% HCOOH) through a Zorbax 30x4.6 mm column, in positive ion mode. The one- and two-dimensional NMR spectra (^{1}H, ^{13}C, ^{19}F, ^{51}V, ^{1}H–^{1}H COSY, ^{1}H–^{13}C HSQC, ^{1}H–^{13}C HMBC and ^{1}H–^{19}F HMBC) were recorded at 298 K in $CDCl_3$, DMSO-d_6 or CD_2Cl_2, using a Bruker Avance400 FT-NMR spectrometer (400.13 MHz). The chemical shifts are expressed in ppm downfield from Me_4Si as external standard, by setting the residual ^{1}H (^{13}C) signal of $CDCl_3$, DMSO-d_6 or CD_2Cl_2 at 7.26 ppm (77.16 ppm), 2.50 ppm (39.52 ppm) and 5.32 ppm respectively. Spectrum analysis was carried out with TopSpin 4.3.0 software. Electrochemical experiments were conducted with a PalmSens4™ potentiostat equipped with a glassy carbon rod (diameter = 1,96 mm, length = 2,5 cm) as the working electrode, a Pt wire as the counter electrode (diameter = 0,50 mm, length = 4 cm) and an Ag/AgCl/saturated KCl electrode as the reference electrode. The software used to operate the potentiostat, record and process data was PSTrace 5.9. Cyclic Voltammetry (CV) curves were recorded in CH_2Cl_2 with complex concentrations of 1.0 mM, working with Tetrabutylammonium tetrafluoroborate ($TBABF_4$) as electrolyte in 0.1 M concentration from −1.4 V to +0.2 V potential range, at a potential scan rate of 100 mV/s. Before any measurement the solution was degassed by bubbling nitrogen for 3 minutes, and both working and counter electrode were cleaned by flame heating to red-hot. All potential were converted to SHE reference potentials. Bulk electrolyses were performed over 2 mL of $2.7 \cdot 10^{-4}$ M complex solutions, with a $TBABF_4$ concentration of 0.1 M in CH_2Cl_2 in an undivided-cell setup for 60 minutes at a fixed potential depending on the complex. The electronic spectra in CH_2Cl_2 solution were recorded up to 2000 nm on a double beam UV-Vis-NIR Jasco V-570 spectrometer, using a quartz cuvette sealed with an airtight Teflon® cap (optical path length l = 0.1 cm).

3.8.2 Synthesis of $PhCl_2MeOH$

$PhCl_2$ (1.0 g; 6.13 mmol), KOH (400 mg; 7.12 mmol), aqueous CH_2O 37% solution (450 µL; 6.05 mmol) and 10 mL of H_2O were added to a 25 mL round bottom flask and heated to 60 °C for 7 days. The obtained yellow solution was acidified by HCl 37%, the resulting light-yellow suspension was directly extracted with 3x10 mL of DCM. The organic phase was mixed with 1.0 g of SiO_2 and vacuum dried. The resulting solid was placed on top of a short (~10 cm) column of SiO_2 and eluted with 95 : 5 Petroleum Ether : Et_2O up to complete removal of residual $PhCl_2$, than eluted with DCM to recover the product. After vacuum drying 638 mg (yield = 55 %) of a pale-yellow solid were collected and analyzed through ^1H NMR in $CDCl_3$, showing the desired product was obtained.

^1H NMR ($CDCl_3$, 400.13 MHz): δ_H (ppm) = 7.29 (1H, d, J = 2.45 Hz), 7.13 (1H, d, J = 2.45 Hz), 6.64 (1H, bs), 4.78 (2H, s).

3.8.3 Synthesis of PhF_2MeOH

PhF_2 (370 µL; 3.87 mmol), KOH (249 mg; 4.45 mmol), aqueous CH_2O 37% solution (290 µL; 3.90 mmol) and 5 mL of H_2O were added to a 10 mL round bottom flask and heated to 60 °C for 7 days. The obtained red solution was acidified by HCl 37%, the resulting light-red suspension was directly extracted with 3x5 mL of DCM. The organic phase was mixed with 0.5 g of SiO_2 and vacuum dried. The resulting solid was placed on top of a short (~10 cm) column of SiO_2 and eluted with 95 : 5 Petroleum Ether : Et_2O up to complete removal of residual PhF_2, than eluted with DCM to recover the product. After vacuum drying 247 mg (yield = 40 %) of a light-brown solid were collected and analyzed through ^1H NMR in $CDCl_3$, showing the desired product was obtained.

^1H NMR ($CDCl_3$, 400.13 MHz): δ_H (ppm) = 6.80 (1H, ddd, J = 2.88, 8.22, 10.85 Hz), 6.73 (1H, ddd, J = 1.65, 2.88, 8.52 Hz), 6.39 (1H, bs), 4.81 (2H, s).

3.8.4 Synthesis of $PhCl_2CH_2Cl$ starting from $PhCl_2MeOH$

$PhCl_2MeOH$ (627 mg, 3.25 mmol) and 5 mL of DCM were added to a 10 mL round bottom flask. $SOCl_2$ (630 µL, 8.68 mmol) were slowly added under vigorous stirring, the flask was closed and left to stir at rt overnight. The yellow solution was quenched with water, the organic layer was recovered and vacuum dried obtaining 680 mg (yield = 99 %) of a light-brown solid which was analyzed through ^1H NMR in $CDCl_3$, showing the desired product was obtained.

^{1}H NMR ($CDCl_3$, 400.13 MHz): δ_H (ppm) = 7.32 (1H, d, J = 2.50 Hz), 7.28 (1H, d, J = 2.50 Hz), 5.77 (1H, bs), 4.62 (2H, s).

3.8.5 Synthesis of PhF_2CH_2Cl starting from PhF_2MeOH

PhF_2MeOH (115 mg, 0.72 mmol) and 2 mL of DCM were added to a 5 mL round bottom flask. $SOCl_2$ (140 µL, 1.92 mmol) were slowly added under vigorous stirring, the flask was closed and left to stir at rt overnight. The yellow solution was quenched with water, the organic layer was recovered and vacuum dried obtaining 127 mg (yield = 99 %) of a light-brown solid which was analyzed through ^{1}H NMR in $CDCl_3$, showing the desired product was obtained.

^{1}H NMR ($CDCl_3$, 400.13 MHz): δ_H (ppm) = 6.91 (1H, ddd, J = 2.04, 2.86, 8.65 Hz), 6.84 (1H, ddd, J = 2.86, 8.06, 10.19 Hz), 5.46 (1H, bs), 4.63 (2H, s).

3.8.6 Synthesis of $PhCl_2CH_2Cl$ starting from $PhCl_2$

$PhCl_2$ (2.0 g, 12.27 mmol), paraformaldehyde (560 mg, 18.67 mmol), 10 mL HCl 37% and 3 mL H_2SO_4 98% were added to a 25 mL round bottom flask and stirred at 70 °C overnight. The limpid, colorless solution obtained started cropping white solid upon cooling. Still, it was extracted as is with 3x15 mL DCM and vacuum dried, obtaining 2.5 g (yield = 96 %) of a white solid, that was fully characterized through NMR.

^{1}H NMR ($CDCl_3$, 400.13 MHz): δ_H (ppm) = 7.32 (1H, d, J = 2.50 Hz), 7.28 (1H, d, J = 2.50 Hz), 5.77 (1H, bs), 4.62 (2H, s). δ_C (ppm) = 148.32, 129.38, 128.87, 126.49, 125.6, 120.9, 40.50.

3.8.6 Synthesis of PhF_2CH_2Cl starting from PhF_2

PhF_2 (1.6 mL, 16.72 mmol), paraformaldehyde (560 mg, 18.67 mmol), 10 mL HCl 37% and 3 mL H_2SO_4 98% were added to a 25 mL round bottom flask and stirred at 70 °C overnight. The limpid, colorless solution obtained started cropping white solid upon cooling. Still, it was extracted as is with 3x15 mL DCM and vacuum dried, obtaining 2.5 g (yield = 82 %) of a amber liquid, that was fully characterized through NMR.

^{1}H NMR ($CDCl_3$, 400.13 MHz): δ_H (ppm) = 6.91 (1H, ddd, J = 2.04, 2.86, 8.65 Hz), 6.84 (1H, ddd, J = 2.86, 8.06, 10.19 Hz), 5.46 (1H, d, J = 4.2 Hz), 4.63 (2H, s). δ_C (ppm) = 155.38 (1C, dd, J = 11.59, 241.96 Hz), 150.46 (1C, dd, J = 12.54, 240.22 Hz), 138.20 (1C, dd, J = 3.57, 15.01 Hz), 126.59 (1C,

dd, J = 2.79, 8.71 Hz), 112.15 (1C, dd, J = 3.52, 23.45 Hz), 104.15 (1C, dd, J = 22.45, 27.17 Hz), 39.84 (1C, dd, J = 1.59, 3.65 Hz). δ_F (ppm) = − 120.07 (dt, J = 1.52, 8.45 Hz), − 135.80 (dq, J = 10.2, 4.2, 2.04, 1.52 Hz).

3.8.7 Synthesis of $PhClNO_2CH_2Cl$

$PhClNO_2$ (1.0 g, 6.37 mmol), paraformaldehyde (412 mg, 13.72 mmol) and NaCl (6.0 g, 102.7 mmol) were grinded together in a mortar and carefully transferred in a 250 mL round bottom flask. An over dimensioned flask is required to avoid stopper ejection, as the reaction develops gases and needs to be closed to work properly. In a dropping funnel 1.2 mL of water and 14 mL of H_2SO_4 98% are mixed and very slowly added to the powder mixture. If the addition is too fast the pressure will increase in the vessel and the cork will be ejected, leading to HCl gas to be lost. After addition, the yellow mixture is left to stir at rt for 5 days, after which it assumes green shades. The mixture is carefully quenched with 20 mL of H_2O slowly added, and then extracted with 3x15 mL of DCM, the organic phase is extracted yielding 1.3 g (yield = 98 %) of a bright yellow solid that was fully characterized through NMR and ESI-MS.

^{1}H NMR ($CDCl_3$, 400.13 MHz): δ_H (ppm) = 10.92 (1H, s), 8.10 (1H, d, J = 2.57 Hz), 7.71 (1H, d, J = 2.57 Hz), 4.68 (2H, s). δ_C (ppm) = 151.82, 137.96, 133.89, 130.44, 125.10, 124.61, 39.30.

3.8.8 Synthesis of $PhClNO_2CH_2Cl$-py adduct

$PhClNO_2CH_2Cl$ (50 mg, 0.225 mmol) was added to pyridine (1 mL, 12.4 mmol) in a 5 mL round bottom flask and the solution immediately became of a bright orange color. It was stirred at rt overnight and then carefully vacuum dried yielding 59 mg (yield = 99%) of a bright orange solid that was characterized by ^{1}H NMR.

^{1}H NMR ($CDCl_3$, 400.13 MHz): δ_H (ppm) = 9.74 (2H, d, J = 6.05 Hz), 8.87 (1H, d, J = 2.57 Hz), 8.42 (1H, t, J = 7.75 Hz), 8.16 (1H, d, J = 2.57), 8.03 (2H, t, J = 6.90 Hz), 6.59 (2H, s).

3.8.9 Synthesis of $DPA^{Cl,Cl}$

$PhCl_2$ (4.0 g, 24.5 mmol), HMTA (565 mg, 4.02 mmol) and *p*-TsOH (20.6 mg, 0.109 mmol) were mixed in a Schlenk Tube with a screw cap. The tube was completely submerged in a bath at 110 °C and left stirring for 40 h. The obtained product is a block of rock like yellow solid, very hard to

remove from the tube. Trituration with boiling $CHCl_3$ was necessary to recover, by filtration a row product. This was dissolved in a NaOH water solution, and re-precipitated slowly adding H_2SO_4 98% obtaining a solid, that after filtration and drying gave 4.0 g (yield = 91 %) of a beige solid that was fully characterized through NMR and ESI-MS.

^{1}H NMR (DMSO-d_6, 400.13 MHz): δ_H (ppm) = 7.48 (2H, d, J = 2.03 Hz), 7.32 (2H, d, J = 2.03 Hz), 4.01 (4H, s). δ_C (ppm) = 151.41, 128.71, 128.60, 125.47, 122.61, 121.51, 46.75. ESI-MS (80:20 CH_3CN:H_2O (0.1% HCOOH)), m/z $[DPA^{Cl,Cl}+H]^+$ = 365.95

3.8.10 Synthesis of $DPA^{F,F}$

PhF_2 (4.3 g, 32.8 mmol), HMTA (713 mg, 5.09 mmol) and *p*-TsOH (36.8 mg, 0.193 mmol) were mixed in a Schlenk Tube with a screw cap. The tube was completely submerged in a bath at 110 °C and left stirring for 40 h. The obtained product is a block of rock like yellow solid, very hard to remove from the tube. Trituration with boiling $CHCl_3$ was necessary to recover, by filtration a row product. This was dissolved in a NaOH water solution, and re-precipitated slowly adding H_2SO_4 98% obtaining a solid, that after filtration and drying gave 4.2 g (yield = 91 %) of a white solid that was fully characterized through NMR.

^{1}H NMR (DMSO-d_6, 400.13 MHz): δ_H (ppm) = 6.77 (2H, ddd, J = 3.24, 8.92, 11.20 Hz), 6.64 (2H, ddd, J = 1.57, 3.14, 9.32 Hz), 3.58 (4H, s). δ_C (ppm) = 153.20 (2C, dd, J = 10.30, 205.06 Hz), 150.70 (2C, dd, J = 10.40, 233.09 Hz), 148.40 (2C, d, J = 23.15 Hz), 130.38 (2C, dd, J = 5.17, 7.66 Hz), 111.22 (2C, dd, J = 2.77, 20.75 Hz), 102.31 (2C, t, J = 25.0 Hz), 47.66 (2C, s). δ_F (ppm) = − 130.15 (bs), − 133.47 (d, J = 10.2 Hz). ESI-MS (80:20 CH_3CN:H_2O (0.1% HCOOH)), m/z $[DPA^{F,F}+H]^+$ = 302.1

3.8.11 Synthesis of $TPACl_6$

$PhCl_2CH_2Cl$ (200 mg, 0.946 mmol), $DPA^{Cl,Cl}$ (316 mg, 0.861 mmol), Et_3N (200 µL, 1.43 mmol) and 2 mL of DMSO were added to a 5 mL round bottom flask and stirred for 7 days. To the orange solution obtained were added 25 mL of water and NaOH 50% solution up to complete solubilization of the previously formed precipitate. This solution is extracted with 3x10 mL of DCM to remove solvent soluble impurities, then H_2SO_4 98% is added until product precipitation. The solid is filtered, washed several times with water and carefully dried, giving 436 mg (yield = 94 %) of a white solid that was fully characterized through NMR and ESI-MS.

^{1}H NMR (DMSO-d_6, 400.13 MHz): δ_H (ppm) = 7.37 (3H, s), 7.21 (3H, s), 3.83 (6H, s). δ_C (ppm) = 150.92, 129.01, 128.35, 124.34, 122.31, 121.81, 54.00. ESI-MS (80:20 CH_3CN:H_2O (0.1% HCOOH)), *m/z* $[TPACl_6+H]^+$ = 539.9

3.8.12 Synthesis of $TPACl_4F_2$

PhF_2CH_2Cl (200 mg, 1.12 mmol), $DPA^{Cl,Cl}$ (374 mg, 1.02 mmol), Et_3N (200 µL, 1.43 mmol) and 2 mL of DMSO were added to a 5 mL round bottom flask and stirred for 7 days. To the orange solution obtained were added 25 mL of water and NaOH 50% solution up to complete solubilization of the previously formed precipitate. This solution is extracted with 3x10 mL of DCM to remove solvent soluble impurities, then H_2SO_4 98% is added until product precipitation. The solid is filtered, washed several times with water and carefully dried, giving 472 mg (yield = 91 %) of a white solid that was fully characterized through NMR and ESI-MS.

^{1}H NMR (DMSO-d_6, 400.13 MHz): δ_H (ppm) = 10.17 (3H, bs), 7.33 (2H, d, *J* = 2.53 Hz), 7.18 (2H, d, *J* = 2.53 Hz), 7.10 (1H, ddd, *J* = 2.95, 8.75, 10.84 Hz), 6.92 (1H, ddd, *J* = 1.43, 2.95, 9.01 Hz) 3.73 (4H, s), 3.71 (2H, s). δ_C (ppm) = 153.83 (1C, dd, *J* = 13.06, 240.51 Hz), 151.08 (2C, s), 150.78 (1C, dd, *J* = 13.06, 272.6 Hz), 139.94 (1C, dd, *J* = 3.08, 14.64 Hz), 128.41 (1C, s), 127.88 (1C, s), 127.0 (3C, m), 122.70 (2C, s), 121.07 (2C, s), 112.33 (1C, dd, *J* = 2.93, 22.56 Hz), 103.52 (1C, t, *J* = 25.5 Hz), 54.15 (2C, s), 52.87 (1C, s). δ_F (ppm) = − 122.59 (t, *J* = 8.65 Hz), − 131.3 (d, *J* = 10.56 Hz). ESI-MS (80:20 CH_3CN:H_2O (0.1% HCOOH)), *m/z* $[TPACl_4F_2+H]^+$ = 508.0

3.8.13 Synthesis of $TPACl_5NO_2$

$PhClNO_2CH_2Cl$ (187 mg, 0.842 mmol), $DPA^{Cl,Cl}$ (281 mg, 0.766 mmol), KH_2PO_4 (281 mg, 2.06 mmol) and 2 mL of DMSO were added to a 5 mL round bottom flask and stirred for 7 days. To the orange solution obtained were added 25 mL of water and NaOH 50% solution up to complete solubilization of the previously formed precipitate. This solution is extracted with 3x10 mL of DCM to remove solvent soluble impurities, then H_2SO_4 98% is added until product precipitation. The solid is filtered, washed several times with water and carefully dried, giving 336 mg (yield = 79 %) of a yellow solid that was fully characterized through NMR and ESI-MS.

^{1}H NMR (DMSO-d_6, 400.13 MHz): δ_H (ppm) = 7.82 (1H, s), 7.53 (1H, s), 7.33 (2H, s), 7.19 (2H, s), 4.00 (2H, s), 3.80 (4H, s). δ_C (ppm) = 151.37 (1C, s), 151.07 (2C, s), 136.24 (1C, s), 135.77 (1C, s), 128.79 (2C, s), 128.74 (1C, s), 128.1 (2C, s), 127.0 (2C, s), 123.45 (1C, s), 123.45 (2C, s), 122.74

(2C, s), 122.09 (1C, s), 54.75 (2C, s), 46.76 (1C, s). ESI-MS (80:20 CH_3CN:H_2O (0.1% HCOOH)), *m*/*z* $[TPACl_5NO_2+H]^+$ = 550.9

3.8.14 Synthesis of $TPAF_6$

PhF_2CH_2Cl (200 mg, 1.12 mmol), $DPA^{F,F}$ (307 mg, 1.02 mmol), Et_3N (200 µL, 1.43 mmol) and 2 mL of DMSO were added to a 5 mL round bottom flask and stirred for 7 days. To the orange solution obtained were added 25 mL of water and NaOH 50% solution up to complete solubilization of the previously formed precipitate. This solution is extracted with 3x10 mL of DCM to remove solvent soluble impurities, then H_2SO_4 98% is added until product precipitation. The solid is filtered, washed several times with water and carefully dried, giving 352 mg (yield = 68 %) of a white solid that was fully characterized through NMR and ESI-MS.

^1H NMR (DMSO-d_6, 400.13 MHz): δ_H (ppm) = 9.96 (3H, bs), 7.13 (3H, bs), 6.99 (3H, bs), 3.75 (6H, bs). δ_C (ppm) = 155.38 (3C, dd, *J* = 11.59, 241.96 Hz), 150.46 (3C, dd, *J* = 12.54, 240.22 Hz), 138.20 (3C, dd, *J* = 3.57, 15.01 Hz), 126.59 (3C, dd, *J* = 2.79, 8.71 Hz), 112.15 (3C, dd, *J* = 3.52, 23.45 Hz), 104.15 (3C, dd, *J* = 22.45, 27.17 Hz), 52.06 (3C, dd, *J* = 1.59, 3.65 Hz). δ_F (ppm) = − 122.63 (bs), − 131.96 (bs). ESI-MS (80:20 CH_3CN:H_2O (0.1% HCOOH)), *m*/*z* $[TPAF_6+H]^+$ = 444.1

3.8.15 Synthesis of $TPAF_4Cl_2$

$PhCl_2CH_2Cl$ (200 mg, 0.946 mmol), $DPA^{F,F}$ (251 mg, 0.833 mmol), Et_3N (200 µL, 1.43 mmol) and 2 mL of DMSO were added to a 5 mL round bottom flask and stirred for 7 days. To the orange solution obtained were added 25 mL of water and NaOH 50% solution up to complete solubilization of the previously formed precipitate. This solution is extracted with 3x10 mL of DCM to remove solvent soluble impurities, then H_2SO_4 98% is added until product precipitation. The solid is filtered, washed several times with water and carefully dried, giving 340 mg (yield = 83 %) of a white solid that was fully characterized through NMR and ESI-MS.

^1H NMR (DMSO-d_6, 400.13 MHz): δ_H (ppm) = 10.23 (3H, bs), 7.36 (1H, bs), 7.22 (1H, bs), 7.12 (2H, bt, *J* = 7.54 Hz), 6.95 (2H, bd, *J* = 7.85 Hz), 3.76 (1H, s), 3.73 (2H, s). δ_C (ppm) = 153.95 (2C, dd, *J* = 11.62, 237.23 Hz), 151.35 (1H, s), 150.67 (2C, dd, *J* = 12.77, 241.98 Hz), 140.08 (2C, d, *J* = 12.97 Hz), 127.96 (1C, s), 127.5 (1C, s), 124.95 (1C, s), 124.58 (1C, s), 124.4 (1C, s), 120.88 (2C, bs), 112.33 (2C, bs), 103.58 (2C, bs), 54.36 (1C, s), 52.73 (2C, s). δ_F (ppm) = − 122.62 (t, *J* = 8.65

Hz), − 130.96 (d, J = 10.56 Hz). ESI-MS (80:20 CH_3CN:H_2O (0.1% HCOOH)), m/z $[TPAF_4Cl_2+H]^+$ = 476.1

3.8.16 Synthesis of $TPAF_4ClNO_2$

$PhClNO_2CH_2Cl$ (187 mg, 0.842 mmol), $DPA^{F,F}$ (231 mg, 0.767 mmol), KH_2PO_4 (313 mg, 2.30 mmol) and 2 mL of DMSO were added to a 5 mL round bottom flask and stirred for 7 days. To the orange solution obtained were added 25 mL of water and NaOH 50% solution up to complete solubilization of the previously formed precipitate. This solution is extracted with 3x10 mL of DCM to remove solvent soluble impurities, then H_2SO_4 98% is added until product precipitation. The solid is filtered, washed several times with water and carefully dried, giving 309 mg (yield = 83 %) of a yellow solid that was fully characterized through NMR and ESI-MS.

^1H NMR (DMSO-d_6, 400.13 MHz): δ_H (ppm) = 7.80 (1H, bs), 7.56 (1H, bs), 7.09 (2H, bt, J = 9.04 Hz), 6.95 (2H, bd, J = 8.46 Hz), 3.82 (2H, s), 3.75 (4H, s). δ_C (ppm) = 153.91 (2C, dd, J = 11.45, 237.29 Hz), 151.57 (1C, s), 150.68 (2C, dd, J = 12.74, 241.85 Hz), 140.04 (2C, dd, J = 2.88, 14.04 Hz), 136.73 (1C, s), 134.33 (1C, s), 129.80 (1C, s), 123.12 (1C, s), 121.49 (1C, s), 112.23 (2C, dd, J = 2.74, 22.74 Hz), 103.55 (2C, dd, J = 23.03, 26.65 Hz), 53.96 (1C, s), 52.98 (2C, s). δ_F (ppm) = − 122.61 (t, J = 8.65 Hz), − 131.32 (d, J = 10.56 Hz). ESI-MS (80:20 CH_3CN:H_2O (0.1% HCOOH)), m/z $[TPAF_4ClNO_2+H]^+$ = 487.1

3.8.17 Synthesis of oxo-isopropoxo Ti $DPA^{Cl,Cl}$ complex

$DPA^{Cl,Cl}$ (50 mg, 0.136 mmol) was suspended in a 5 mL round bottom flask with 2 mL of DCM. $Ti(O^iPr)_4$ (40 µL, 0.136 mmol) was quickly added to the mixture, that was then stirred to rt for 1 h. The orange solution was then filtered, reduced to half its volume under vacuum, and layered under 9 mL of *n*-hexane in a 10 mL tube. After 2 weeks orange crystals appeared, some were collected and analyzed through SC-XRD. All details can be found in Tables 3.1–3.4.

3.8.18 Synthesis of Co $DPA^{Cl,Cl}$ monomer

$DPA^{Cl,Cl}$ (50 mg, 0.136 mmol), DBU (24 µL, 0.163 mmol) and 2 mL of THF were added to a round bottom flask and stirred at rt overnight. Then $CoCl_2$ (18 mg, 0.138 mmol) was added and stirring continued for 4 h. The dark red solution obtained was filtered, reduced to half its volume under

vacuum, and layered under 9 mL of *n*-hexane in a 10 mL tube. After 2 weeks dark red crystals appeared, some were collected and analyzed through SC-XRD. All details can be found in Tables 3.5–3.8.

3.8.19 Synthesis of Co DPA^{Cl,Cl} tetramer

DPA^{Cl,Cl} (50 mg, 0.136 mmol), $CoCl_2$ (18 mg, 0.138 mmol) were added in a 5 mL round bottom flask to 2 mL of a 0.04 M NaOH water solution (3.2 mg, 0.08 mmol). The mixture was stirred at 80 °C for 4 hours. The system appeared as a bright green suspension, this was filtered, the solution extracted 10x1 mL with DCM. The green colored organic phase was then reduced to ~1 mL under vacuum and layered under 9 mL of *n*-hexane in a 10 mL tube. After 2 weeks green crystals appeared, some were collected and analyzed through SC-XRD. All details can be found in Tables 3.9–3.12.

3.8.20 Synthesis of VOTPACl$_6$

$TPACl_6$ (50 mg, 0.0928 mmol) were suspended in 2 mL of DCM, $VO(OiPr)_3$ (22 µL, 0.0932 mmol) was added and the system quickly turned to an extremely dark color. The mixture was left stirring at rt for 4 h, then it was filtered and added to 25 mL of stirring heptane, causing precipitation and complete color fading. This solid was recovered by filtration, washed 3x0.5 mL with pentane and carefully dried in vacuum yielding 42 mg (yield = 75 %) of an almost black solid. This was characterized through ^{1}H NMR, ^{51}V NMR, CV, and UV-Vis.

^{1}H NMR (CD_2Cl_2, 400.13 MHz): δ_H (ppm) = 7.33 (3H, bs), 6.96 (3H, bs), 2.61 (6H, bs). δ_V (ppm) = − 423.45. E_c1 = − 0.333 V, E_a1 = − 0.163 V, E_c2 = − 0.920 V, E_a2 = n.d. λ_{max} (ε) = 289 nm ($1.0 \cdot 10^4$ $L \cdot mol^{-1} \cdot cm^{-1}$), 608 nm ($3.3 \cdot 10^3$ $L \cdot mol^{-1} \cdot cm^{-1}$).

3.8.21 Synthesis of VOTPACl$_4$F$_2$

$TPACl_4F_2$ (50 mg, 0.0986 mmol) were suspended in 2 mL of DCM, $VO(OiPr)_3$ (23 µL, 0.0975 mmol) was added and the system quickly turned to an extremely dark color. The mixture was left stirring at rt for 4 h, then it was filtered and added to 25 mL of stirring heptane, causing precipitation and complete color fading. This solid was recovered by filtration, washed 3x0.5 mL with pentane and carefully dried in vacuum yielding 56 mg (yield = 99 %) of an almost black solid. This was characterized through ^{1}H NMR, ^{51}V NMR, CV, and UV-Vis.

^{1}H NMR (CD_2Cl_2, 400.13 MHz): δ_H (ppm) = 7.29 (2H, bs), 6.92 (2H, bs), 6.8 (1H, bt, J = 7.88 Hz), 6.62 (1H, bd, J = 6.30 Hz), 2.61 (6H, bs). δ_V (ppm) = − 419.72. E_c1 = − 0.342 V, E_a1 = − 0.212 V, E_c2 = − 0.822 V, E_a2 = − 0.692 V. λ_{max} (ε) = 285 nm ($9.8 \cdot 10^3$ L·mol^{-1}·cm^{-1}), 598 nm ($4.8 \cdot 10^3$ L·mol^{-1}·cm^{-1}).

3.8.22 Synthesis of $VOTPACl_5NO_2$

$TPACl_5NO_2$ (50 mg, 0.0910 mmol) were suspended in 2 mL of DCM, VO(O*i*Pr)$_3$ (22 µL, 0.0932 mmol) was added and the system quickly turned to an extremely dark color. The mixture was left stirring at rt for 4 h, then it was filtered and added to 25 mL of stirring heptane, causing precipitation and complete color fading. This solid was recovered by filtration, washed 3x0.5 mL with pentane and carefully dried in vacuum yielding 34 mg (yield = 61 %) of an almost black solid. This was characterized through ^{1}H NMR, ^{51}V NMR, CV, and UV-Vis, but no NMR data are available due to its paramagnetic behavior.

E_c1 = − 0.112 V, E_a1 = − 0.0628 V, E_c2 = − 0.563 V, E_a2 = − 0.552 V. λ_{max} (ε) = 281 nm ($1.2 \cdot 10^4$ L·mol^{-1}·cm^{-1}), 360 nm ($4.0 \cdot 10^3$ L·mol^{-1}·cm^{-1}), 563 nm ($1.1 \cdot 10^3$ L·mol^{-1}·cm^{-1}).

3.8.23 Synthesis of $VOTPAF_6$

$TPAF_6$ (50 mg, 0.113 mmol) were suspended in 2 mL of DCM, VO(O*i*Pr)$_3$ (25 µL, 0.106 mmol) was added and the system quickly turned to an extremely dark color. The mixture was left stirring at rt for 4 h, then it was filtered and added to 25 mL of stirring heptane, causing precipitation and complete color fading. This solid was recovered by filtration, washed 3x0.5 mL with pentane and carefully dried in vacuum yielding 28 mg (yield = 49 %) of an almost black solid. This was characterized through ^{1}H NMR, ^{51}V NMR, CV, and UV-Vis.

^{1}H NMR (CD_2Cl_2, 400.13 MHz): δ_H (ppm) = 6.78 (3H, bs), 6.60 (3H, bs), 2.62 (6H, bs). δ_V (ppm) = − 421.88. E_c1 = − 0.323 V, E_a1 = − 0.253 V, E_c2 = − 0.762 V, E_a2 = − 0.523 V. λ_{max} (ε) = 277 nm ($7.4 \cdot 10^3$ L·mol^{-1}·cm^{-1}), 577 nm ($1.9 \cdot 10^3$ L·mol^{-1}·cm^{-1}).

3.8.24 Synthesis of $VOTPAF_4Cl_2$

$TPAF_4Cl_2$ (50 mg, 0.0920 mmol) were suspended in 2 mL of DCM, VO(O*i*Pr)$_3$ (22 µL, 0.0932 mmol) was added and the system quickly turned to an extremely dark color. The mixture was left stirring at

rt for 4 h, then it was filtered and added to 25 mL of stirring heptane, causing precipitation and complete color fading. This solid was recovered by filtration, washed 3x0.5 mL with pentane and carefully dried in vacuum yielding 34 mg (yield = 68 %) of an almost black solid. This was characterized through ^{1}H NMR, ^{51}V NMR, CV, and UV-Vis.

^{1}H NMR (CD_2Cl_2, 400.13 MHz): δ_H (ppm) = 7.32 (1H, d, J = 2.63 Hz), 6.93 (1H, d, J = 2.63 Hz), 6.82 (2H, ddd, J = 3.05, 8.52, 10.46 Hz), 6.62 (2H, ddd, J = 1.72, 3.05, 8.52 Hz), 2.62 (6H, bs). δ_V (ppm) = − 422.47. E_c1 = − 0.302 V, E_a1 = − 0.213 V, E_c2 = − 0.772 V, E_a2 = − 0.622 V. λ_{max} (ε) = 283 nm ($9.2 \cdot 10^3$ L·mol^{-1}·cm^{-1}), 592 nm ($3.8 \cdot 10^3$ L·mol^{-1}·cm^{-1}).

3.8.25 Synthesis of $VOTPAF_4ClNO_2$

$TPAF_4ClNO_2$ (50 mg, 0.103 mmol) were suspended in 2 mL of DCM, $VO(O\textit{i}Pr)_3$ (25 µL, 0.106 mmol) was added and the system quickly turned to an extremely dark color. The mixture was left stirring at rt for 4 h, then it was filtered and added to 25 mL of stirring heptane, causing precipitation and complete color fading. This solid was recovered by filtration, washed 3x0.5 mL with pentane and carefully dried in vacuum yielding 38 mg (yield = 67 %) of an almost black solid. This was characterized through ^{1}H NMR, ^{51}V NMR, CV, and UV-Vis, but no NMR data are available due to its paramagnetic behavior.

E_c1 = n.d., E_a1 = n.d., E_c2 = − 0.293 V, E_a2 = − 0.213 V. λ_{max} (ε) = 276 nm ($8.9 \cdot 10^3$ L·mol^{-1}·cm^{-1}), 360 nm ($4.0 \cdot 10^3$ L·mol^{-1}·cm^{-1}), 550 nm ($1.3 \cdot 10^3$ L·mol^{-1}·cm^{-1}).

3.9 Bibliography

[1] J. J. Bozell, B. R. Hames, D. R. Dimmel, *J. Org. Chem.* **1995**, *60*, 2398–2404.

[2] B. Biannic, J. J. Bozell, T. Elder, *Green Chem.* **2014**, *16*, 3635–3642.

[3] J. Liu, S. C. Lorraine, B. S. Dolinar, J. M. Hoover, *Inorg. Chem.* **2022**, *61*, 6008–6016.

[4] A. Haikarainen, J. Sipilä, P. Pietikäinen, A. Pajunen, I. Mutikainen, *Bioorg. Med. Chem.* **2001**, *9*, 1633–1638.

[5] Y. Tsai, C. Chen, Y. Hsieh, M. Tsai, *Eur. J. Inorg. Chem.* **2019**, *2019*, 4637–4646.

[6] V. P. McCaffrey, O. Q. Conover, M. A. Bernard, J. T. Yarranton, N. R. Lessnau, J. P. Hempfling, *Polyhedron* **2021**, *205*, 115268.

[7] S. D. Springer, J. He, M. Chui, R. D. Little, M. Foston, A. Butler, *ACS Sustain. Chem. Eng.* **2016**, *4*, 3212–3219.

[8] X. Zhou, *Environ. Prog. Sustain. Energy* **2015**, *34*, 1120–1128.

[9] V. Sippola, O. Krause, T. Vuorinen, *Journal of Wood Chemistry and Technology* **2004**, *24*, 323–340.

[10] X.-F. Zhou, *Drewno. Prace Naukowe, Doniesienia, Komunikaty = Wood. Research Papers, Reports, Announcements* **2013**, *56*, 5–17.

[11] X.-F. Zhou, *Polish Journal of Chemical Technology* **2014**, *16*, 91–96.

[12] T. Elder, J. J. Bozell, D. Cedeno, *Physical Chemistry Chemical Physics* **2013**, *15*, 7328.

[13] K. Tang, X.-F. Zhou, *Theoretical Foundations of Chemical Engineering* **2015**, *49*, 877–883.

[14] P. Zucca, A. Rescigno, A. C. Rinaldi, E. Sanjust, *J. Mol. Catal. A Chem.* **2014**, *388–389*, 2–34.

[15] I. Artaud, K. Ben-Aziza, D. Mansuy, *J. Org. Chem.* **1993**, *58*, 3373–3380.

[16] G. Labat, B. Meunier, *J. Org. Chem.* **1989**, *54*, 5008–5011.

[17] S. K. Hanson, R. Wu, L. A. “Pete” Silks, *Angew. Chem. Int. Ed.* **2012**, *51*, 3410–3413.

[18] B. Sedai, C. Díaz-Urrutia, R. T. Baker, R. Wu, L. A. “Pete” Silks, S. K. Hanson, *ACS Catal.* **2013**, *3*, 3111–3122.

[19] B. Sedai, C. Díaz-Urrutia, R. T. Baker, R. Wu, L. A. “Pete” Silks, S. K. Hanson, *ACS Catal.* **2011**, *1*, 794–804.

[20] E. Amadio, J. González-Fabra, D. Carraro, W. Denis, B. Gjoka, C. Zonta, K. Bartik, F. Cavani, S. Solmi, C. Bo, G. Licini, *Adv. Synth. Catal.* **2018**, *360*, 3286–3296.

[21] D. Y. Bae, Y. Kim, J. Cha, E. Lee, *Coord. Chem. Rev.* **2020**, *419*, 213402.

[22] S. Groysman, I. Goldberg, Z. Goldschmidt, M. Kol, *Inorg. Chem.* **2005**, *44*, 5073–5080.

[23] C. Miceli, J. Rintjema, E. Martin, E. C. Escudero-Adán, C. Zonta, G. Licini, A. W. Kleij, *ACS Catal.* **2017**, *7*, 2367–2373.

[24] M. Mba, M. Pontini, S. Lovat, C. Zonta, G. Bernardinelli, P. E. Kündig, G. Licini, *Inorg. Chem.* **2008**, *47*, 8616–8618.

[25] C. Redshaw, M. A. Rowan, D. M. Homden, S. H. Dale, M. R. J. Elsegood, S. Matsui, S. Matsuura, *Chem. Comm.* **2006**, 3329.

[26] T. Kajiwara, R. Wagner, E. Bill, T. Weyhermüller, P. Chaudhuri, *Dalton Trans.* **2011**, *40*, 12719.

[27] S. Gazi, M. Đokić, A. M. P. Moeljadi, R. Ganguly, H. Hirao, H. Sen Soo, *ACS Catal.* **2017**, *7*, 4682–4691.

[28] A. Chandrasekaran, R. O. Day, R. R. Holmes, *J. Am. Chem. Soc.* **2000**, *122*, 1066–1072.

[29] S. Groysman, I. Goldberg, M. Kol, E. Genizi, Z. Goldschmidt, *Adv. Synth. Catal.* **2005**, *347*, 409–415.

[30] D. Y. Bae, G. S. Park, N. Ko, K. Son, E. Lee, *Dalton Trans.* **2019**, *48*, 9617–9624.

[31] T. R. Forder, M. F. Mahon, M. G. Davidson, T. Woodman, M. D. Jones, *Dalton Trans.* **2014**, *43*, 12095.

[32] J. D. Chartres, A. Dahir, P. A. Tasker, F. J. White, *Inorg. Chem. Commun.* **2007**, *10*, 1154–1158.

[33] C. J. Whiteoak, N. Kielland, V. Laserna, F. Castro-Gómez, E. Martin, E. C. Escudero-Adán, C. Bo, A. W. Kleij, *Chemistry – A European Journal* **2014**, *20*, 2264–2275.

[34] E. Y. Tshuva, I. Goldberg, M. Kol, Z. Goldschmidt, *Inorg. Chem.* **2001**, *40*, 4263–4270.

[35] Q. Sun, Y. Wang, D. Yuan, Y. Yao, Q. Shen, *Dalton Trans.* **2015**, *44*, 20352–20360.

[36] R. van Gorkum, J. Berding, A. M. Mills, H. Kooijman, D. M. Tooke, A. L. Spek, I. Mutikainen, U. Turpeinen, J. Reedijk, E. Bouwman, *Eur. J. Inorg. Chem.* **2008**, *2008*, 1487–1496.

[37] E. Safaei, T. Weyhermüller, E. Bothe, K. Wieghardt, P. Chaudhuri, *Eur. J. Inorg. Chem.* **2007**, *2007*, 2334–2344.

[38] R. K. Dean, S. L. Granville, L. N. Dawe, A. Decken, K. M. Hattenhauer, C. M. Kozak, *Dalton Trans.* **2010**, *39*, 548–559.

[39] S. Kannan, K. N. Kumar, R. Ramesh, *Polyhedron* **2008**, *27*, 701–708.

[40] A. Lehtonen, R. Sillanpää, *Inorg. Chem.* **2004**, *43*, 6501–6506.

[41] S. VenkatRamani, N. B. Huff, M. T. Jan, I. Ghiviriga, K. A. Abboud, A. S. Veige, *Organometallics* **2015**, *34*, 2841–2848.

[42] R. R. Choudhury, R. Chitra, *CrystEngComm* **2010**, *12*, 2113.

[43] R. H. Duncan Lyngdoh, H. F. Schaefer, R. B. King, *Chem. Rev.* **2018**, *118*, 11626–11706.

[44] N. Y. Turova, *Russian Chem. Rev.* **2004**, *73*, 1041–1064.

[45] R. J. Kern, *Journal of Inorganic and Nuclear Chemistry* **1962**, *24*, 1105–1109.

[46] K. Szalewicz, in *Encyclopedia of Physical Science and Technology*, Elsevier, **2003**, pp. 505–538.

[47] L. Pauling, *Proceedings of the National Academy of Sciences* **1976**, *73*, 4290–4293.

[48] X. Liu, Y. Wang, L. Liu, G. Chen, *Medicinal Chemistry Research* **2018**, *27*, 1971–1983.

[49] Y. L. Hu, M. Lu, Q. Ge, P. Cheng Wang, S. Bin Zhang, T. T. Lu, *Journal of the Chilean Chemical Society* **2010**, *55*.

[50] J. Qiu, Q. Zhou, Y. Zhang, M. Guan, X. Li, Y. Zou, X. Huang, Y. Zhao, W. Chen, X. Gu, *Eur. J. Med. Chem.* **2020**, *205*, 112581.

[51] Y. Fang, Y. Deng, Q. Ren, J. Huang, S. Zhang, B. Huang, K. Zhang, *Chin. J. Chem. Eng.* **2008**, *16*, 357–360.

[52] F. B. Mallory, K. E. Butler, A. C. Evans, E. J. Brondyke, C. W. Mallory, C. Yang, A. Ellenstein, *J. Am. Chem. Soc.* **1997**, *119*, 2119–2124.

[53] M. Uyanik, K. Ishihara, H. Yamamoto, *Org. Lett.* **2006**, *8*, 5649–5652.

[54] L. Burroughs, L. Eccleshare, J. Ritchie, O. Kulkarni, B. Lygo, S. Woodward, W. Lewis, *Angew. Chem. Int. Ed.* **2015**, *54*, 10648–10651.

[55] Deepa, Mohd. J. Aalam, P. Kumar, S. Singh, *Tetrahedron Lett* **2023**, *116*, 154343.

[56] M. Movsisyan, T. S. A. Heugebaert, R. Dams, C. V. Stevens, *ChemSusChem* **2016**, *9*, 1945–1952.

[57] D. Li, X. Bao, J. Pang, X. Hu, L. Wang, J. Wang, Z. Yang, L. Xu, S. Wang, Q. Weng, S. Cui, T. Hou, *J. Med. Chem.* **2022**, *65*, 15710–15724.

[58] A. H. Wadsworth, K. W. M. Lawrie, *J. Labelled Comp. Radiopharm.* **2007**, *50*, 500–501.

[59] Q. Wang, C. Wilson, A. J. Blake, S. R. Collinson, P. A. Tasker, M. Schröder, *Tetrahedron Lett* **2006**, *47*, 8983–8987.

[60] R. J. Abraham, M. Mobli, *Magnetic Resonance in Chemistry* **2007**, *45*, 865–877.

[61] A. Bard, *Electrochemical Methods: Fundamentals and Applications*, **1980**.

[62] S. T. McBeath, D. P. Wilkinson, N. J. D. Graham, *Chemosphere* **2020**, *251*, 126626.